CRANFIELD UNIVERSITY

S. HARDACRE

CONTROL OF COLOCATED GEOSTATIONARY SATELLITES

COLLEGE OF AERONAUTICS

PhD THESIS

CRANFIELD UNIVERSITY

COLLEGE OF AERONAUTICS

PhD THESIS

Academic Year 1995-6

S. HARDACRE

CONTROL OF COLOCATED GEOSTATIONARY SATELLITES

SUPERVISOR : T. BOWLING

OCTOBER 1996

This thesis is submitted in partial fulfilment for the degree of Doctor of Philosophy.

ABSTRACT

Control of the inter-satellite distances within a cluster of colocated satellites located in the same GEO window is examined with regards to the close approaches between pairs of satellites.

Firstly, the orbital evolution and station keeping control of a single GEO satellite is examined and a new IBM PC based software program capable of performing both these functions autonomously from initial values of the orbital position and date is detailed and validated.

Cluster design ideas are then examined in detail and the propagation software is used to generate data for a cluster of four satellites. Two test cases are examined to quantify the frequency of close approaches between individual satellite pairs, each test case using a different orbital element separation strategy but the same station keeping control scheme. The results of the study are then compared with previous research and discussions are presented on the advantages of each method.

Finally, a cluster geometry correction manoeuvre, based on Hill's equations of relative motion, is presented which requires only those thrusters used by typical station keeping. This manoeuvre is integrated into the computer software and the two test cases noted previously are again propagated and the close approach results analysed to demonstrate the reduction in the number of close approaches below 5 km.

CONTENTS

1 : INTRODUCTION..... 1
1.1 : Colocation of Geostationary Satellites..... 1
1.1.1 : General..... 1
1.1.2: The GEO Window..... 2
1.2 : Reasons to Colocate..... 3
1.2.1 : ITU regulations..... 3
1.2.2 : Modular Growth Capability..... 4
1.2.3 : Redundancy..... 5
1.3 : Thesis Summary..... 5
1.4 : Original Contribution..... 7
1.5 : Programming Methodology..... 8
1.5.1 : Overview..... 8
1.5.2 : Operating Environment and Commercial Software..... 10
1.5.3 : Modular Programming..... 10
1.5.4 : General Operation and Software Interactions..... 11

2 : COLOCATION STRATEGIES..... 13
2.1 : Overview..... 13
2.2 : Introduction to Relative Motion..... 14
2.2.1 : Hill's Equations of Relative Motion..... 14
2.3.2 : The 2D Eccentricity and Inclination Vectors..... 14
2.3 : Orbital Element Separation..... 16
2.3.1 : Uncoordinated Strategy (CONTROL)..... 16
2.3.2 : Mean Longitude Separation (MLS)..... 16
2.3.3 : Eccentricity Separation (ES)..... 17
2.3.4 : Inclination Separation (IS)..... 18
2.3.5 : Eccentricity and Inclination Separation (EIS)..... 18
2.4 : Discussions..... 21
2.4.1 : Synchronous Vs. Asynchronous Manoeuvres..... 21

2.4.2 : Orbital Element Separation and Fuel Penalties..... 21

3 : LITERATURE REVIEW..... 23
3.1 : Overview..... 23
3.2 : Literature Review..... 23
3.2.1 : Cluster Design Concepts..... 23
3.2.2 : Collision Probabilities..... 24
3.2.3 : Cluster geometry Maintenance..... 26
3.2.4 : Colocation Implementation..... 27
3.3 : Discussions..... 31

4 : SATELLITE ORBIT PROPAGATION..... 33
4.1 : Introduction..... 33
4.1.1 : Overview..... 33
4.1.2 : Need for Propagation Program..... 33
4.1.3 : Propagation Program Validation..... 34
4.1.4 : Time..... 35
4.1.5 : Chapter Summary..... 36
4.2 : Perturbation Methods..... 37
4.2.1 : Fundamentals..... 37
4.2.2 : Solution Methods..... 38
4.2.3 : Cowell's Method..... 39
4.2.4 : Encke's Method..... 40
4.2.5 : The Variation of Parameters Method..... 41
4.3 : Numerical Integration Methods..... 46
4.3.1 : Fundamentals..... 46
4.3.2 : Single Step Methods..... 47
4.3.3 : Multi-Step Methods..... 49
4.3.4 : Active Step Size Control..... 51
4.4 : Perturbation Acceleration Models..... 53
4.4.1 : Fundamentals..... 53

4.4.2 : The Non-Spherical Earth..... 53
4.4.3 : Solar Gravity Perturbations..... 59
4.4.4 : Solar Radiation Perturbations..... 61
4.4.5 : Lunar Gravity Perturbations..... 62
4.5 : Software Implementation..... 64

5 : STATION KEEPING..... 69
5.1 : Introduction..... 69
5.1.1 : Corrective Manoeuvres..... 69
5.1.2 : Mean Orbital Elements..... 70
5.1.3 : Chapter Summary..... 70
5.2 : EW Station Keeping..... 71
5.2.1 : Overview..... 71
5.2.2 : Longitude Control..... 72
5.2.3 : Eccentricity Control..... 81
5.2.4 : Software Implementation of EW Station Keeping..... 90
5.3 : NS Station Keeping..... 100
5.3.1 : Overview..... 100
5.3.2 : Uncontrolled Inclination Evolution..... 102
5.3.3 : NS Manoeuvres, The Effect On The Inclination Vector..... 107
5.3.4 : NS Station Keeping Strategy..... 110
5.3.5 : Software Implementation of NS Station Keeping..... 114
5.4 : Station Keeping Error Analysis..... 117
5.4.1 : Overview..... 117
5.4.2 : Quantification of Errors..... 117
5.4.3 : Simulation of Errors..... 120
5.4.4 : Error Control Methods..... 122
5.4.5 : Software Implementation and Overall Results..... 128

6 : SATELLITE CLUSTER SIMULATION AND RELATIVE MOTION..... 133
6.1 : Overview..... 133

6.2 : Cluster Simulation and Control Options..... 134
6.2.1 : Synchronous Vs. Asynchronous Station Keeping..... 134
6.2.2 : Ground Based Tracking Vs Satellite to Satellite Tracking.....135
6.2.3 : Selected Control Strategy..... 137
6.3 : Accuracy of First Order Relative Motion Equations..... 138
6.3.1 : Evaluation Procedure..... 139
6.3.2 : Comparison Test Cases..... 139
6.3.3 : Summary..... 146
6.4 : Orbit element Separation Strategies..... 147
6.4.1 : Selection of Retained Strategies..... 147
6.4.2 : MLS and EIS Perpendicular Implementation Definitions.....151
6.5 : Cluster Simulation Results With No Geometry Control..... 153
6.5.1 : Approach Frequency Analysis..... 153
6.5.2 : MLS Cluster Results..... 154
6.5.3 : EIS Perpendicular Cluster Results..... 156

7 : COLLISION AVOIDANCE AND RECOVERY..... 161
7.1 : Overview..... 161
7.2 : Solution of Relative Equations..... 162
7.2.1 : Hill's Equations Basics..... 162
7.2.2 : Single Burn recovery for Uncoupled 'K' Axis..... 163
7.2.3 : Three Burn Recovery for Coupled 'R' and 'L' Axes.....164
7.3 : Application Method..... 170
7.3.1 : method of Examination..... 170
7.3.2 : Recovery Optimisation..... 170
7.3.3 : Summary of Application Method..... 178
7.4 : Validation of Procedure and Stability of Solution..... 179
7.4.1 : Validation of Proposed recovery procedure..... 179
7.4.2 : Stability of Solution..... 181
7.5 : Cluster Simulation results with Autonomous Geometry Control.....184
7.5.1 : Implementation Issues..... 184

7.5.2 : Single Satellite Deviation Results..... 185
7.5.3 : MLS Cluster Results..... 187
7.5.4 : EIS Cluster Results..... 189

8 : DISCUSSION AND CONCLUSIONS..... 194
8.1 : Discussions..... 194
8.1.1 : Orbit Propagation..... 194
8.1.2 : Autonomous Station Keeping..... 195
8.1.3 : Cluster Simulation and Relative Motion Control.....197
8.2 : Conclusions..... 200

9: REFERENCES..... 202

APPENDICES

APPENDIX A : TOPICS IN APPLIED MATHEMATICS..... 208
A.1 : Axis and Variable Set Definitions..... 209
A.1.1 : Equinoctial Elements..... 209
A.1.2 : Rectangular Geocentric Inertial Axes..... 210
A.1.3 : Spherical Polar Variables..... 210
A.1.4 : Rectangular Orbital Axes..... 211
A.1.5 : Rectangular Radial/Longitudinal/Latitudinal Axes.....212
A.2 : Axis and Variable Set Transformations..... 214
A.2.1 : Equinoctial to Classical Elements..... 214
A.2.2 : Inertial Position to Orbital Axes and Vice-Versa..... 214
A.2.3 : Equinoctial to Inertial and Vice-Versa..... 215
A.2.4 : Inertial to Radial/Longitudinal/Latitudinal and Vice-Versa.....218
A.2.5 : Polar Variables to Inertial Position..... 219
A.2.6 : Equinoctial Variables to Polar Variables..... 220
A.3 : Curve Fitting..... 221

A.3.1 : Multiple Linear Regression Theory..... 221
A.3.2 : Specific Cases..... 223
A.3.3 : Software Implementation..... 225

APPENDIX B : COMPUTER SOFTWARE..... 226
B.1 : Overview of Validation Procedure..... 227
B.2 : Theoretical Validation..... 231
B.2.1 : Test 1: Ideal GEO (Test Name : *IDEAL1*)..... 231
B.2.2 : Test 2: Near GEO (Test Name : *IDEAL2*)..... 233
B.2.3 : Test 3: Earth Harmonics (Test Name : *EH*)..... 235
B.2.4 : Test 4: Solar Gravity Test (Test Name : *SG*)..... 244
B.2.5 : Test 5: Lunar Gravity Test (Test Name : *LG*)..... 252
B.2.6 : Test 6: Solar Pressure Test (Test Name : *SP*)..... 262
B.3 : Comparison with Second Propagator..... 271

APPENDIX C : DERIVATION OF HILL'S EQUATIONS.....274
C.1 : Overview..... 275
C.2 : Orbital Element Derivation.....276
C.3 : Position and Velocity Derivation.....278
C.4 : Three Burn RL Recovery.....282

APPENDIX D : ORBIT PROPAGATOR LISTINGS..... 290
D.1 : Overview..... 290
D.2 : Variable Definition Module..... 291
D.3 : Perturbation Force Module..... 292
D.4 : Main Orbit Integration Module..... 295

NOTATION

In naming variables the convention has been to use the same symbols as those in the standard astrodynamical references as much as possible. Sometimes this leads to different variables being referred to by the same symbol and where this occurs clarification is provided in the text. Due to the large number of variables used, this is inevitable. The variables listed have been grouped under different headings for clarity.

Variables used in the text in addition to those listed above are defined the first time they are used in the text..

VECTORS

VECTOR	DESCRIPTION	UNITS
$[r,\alpha,\phi]$	geocentric radial, right ascension, declination polar co-ordinates.	[m,rad,rad]
[X,Y,Z]	geocentric inertial co-ordinates.	m
$[x_1,y_1,z_1]$	rectangular orbital axes, origin at centre of satellite.	m
$[x_2,y_2,z_2]$	geocentric rectangular axes, radial, longitudinal, latitudinal.	m
$[V_X,V_Y,V_Z]$	geocentric inertial velocity components.	m
$[a_i,a_j,a_k]$	acceleration components along axes referred to in subscripts.	m
$[\underline{\hat{r}},\underline{\hat{u}},\underline{\hat{k}}]$	unit vectors in $[x_1,y_1,z_1]$ axis frame.	m
$\underline{a_d}$	perturbing acceleration vector, short-hand notation	m/s
$\underline{r_{osc}}$	osculating/reference orbit vector used in Encke's method.	m
$\underline{\delta}$	deviation of actual orbit vector from $\underline{r_{osc}}$ in Encke's method.	m
$\underline{e}$	eccentricity vector.	
$\underline{e_\rho}$	eccentricity vector relative to centre of controlled eccentricity circle.	

CLASSICAL AND EQUINOCTIAL ORBITAL ELEMENTS

ELEMENT	DESCRIPTION	UNITS
a	semi-major axis.	m
e	eccentricity.	
i	inclination.	rad
f	true anomaly.	rad
ω	argument of perigee.	rad

Ω	right ascension of the ascending node.	rad
L	true longitude.	rad
l	mean longitude.	rad
P1	equinoctial element equal to y axis component of 2D 'e' vector.	
P2	equinoctial element equal to x axis component of 2D 'e' vector.	
Q1	equinoctial element equal to y axis component of 2D.	
Q2	equinoctial element equal to x axis component of 2D.	
M	mean anomaly.	rad
E	eccentric anomaly.	rad
K	eccentric longitude.	rad
λ	Greenwich longitude	rad

TIME VARIABLES

VARIABLE	DESCRIPTION	UNITS
t	time.	sec
UT	universal time.	sec
DT	dynamic time.	sec
JD	Julian date.	
Tu	Julian centuries since 2000.0 epoch.	
T_i	station keeping cycle length, subscript refers to NS or EW cycles.	sec
t_{step}	integration time step for numerical integration.	sec
t_{init}	initial value of 't' measured from some reference point.	sec

MISCELLANEOUS VARIABLES

SYMBOL	DESCRIPTION	UNITS
r	radial distance, geocentric centre of Earth to satellite.	m
h	orbit angular momentum.	m^2/s
n	mean orbital angular velocity.	r/s
G	Greenwich sidereal angle.	rad
V	orbital velocity.	m/s
V_E	gravitational potential of Earth.	m^2/s^2
e_c	radius of controlled eccentricity circle.	
e_n	radius of natural eccentricity circle.	
A	satellite surface area normal to solar pressure vector.	m^2
M	satellite mass.	kg
R	surface reflectance coefficient.	
ε, σ	error variables.	
$[\alpha_i,\beta_i,\gamma_i]$	curve fitting variables used to approximate a variables mean motion.	VARIES

CONSTANTS

CONSTANTS	DESCRIPTION	VALUE	UNITS
Re	mean radius of The Earth.	6371000	m
μ_E	gravitational constant of Earth.	3.986005×10^{14}	m^3/s^2
μ_S	gravitational constant of Sun.	1.327124×10^{20}	m^3/s^2
μ_l	gravitational constant of Moon.	4.902794×10^{12}	m^3/s^2
a_S	semi-major axis of Earth orbit about Sun	1.495979×10^{11}	m
a_E	ideal semi-major axis of unperturbed GEO satellite.	42164172	m
G	solar radiation pressure constant.	9.1×10^{-6}	N/m^2

SUBSCRIPTS

SUBSCRIPT	DESCRIPTION
E	Earth related variable.
S	Sun related variable.
l	Moon related variable.
o	value of variable at t = 0.
G	ideal GEO values.

COLOCATION SEPARATION STRATEGY ACRONYMS

ACRONYM	DESCRIPTION
CONTROL	No strategy, satellites operate as single entities.
MLS	Mean Longitude Separation.
ES	Eccentricity Separation.
IS	Inclination Separation.
EIS	Eccentricity plus Inclination Separation.

MISCELLANEOUS ACRONYMS

ACRONYM	DESCRIPTION
TPW	Borland Turbo Pascal for Windows 1.5.
VB	Microsoft Visual Basic 3.0.
PC5	fifth order predictor-corrector.
RK5	fifth order Runge-Kutta.
EH	Earth Harmonics perturbations.
SG	Solar Gravity perturbations.
SP	Solar Pressure perturbations.
LG	Lunar Gravity perturbations.
GEO	Geostationary Orbit.
NS	North-South.
EW	East-West.
WARC	World Administrative Radio conference.
RARC	Regional Administrative Radio conference.
ITU	International Telecommunication Union.
DBSS	Direct Broadcast Satellite Services.
IFRB	International Frequency registration Board.
GMT	Greenwich Mean Time.
ISL	Inter-Satellite Links.

SST	Satellite to Satellite Tracking.
2D	Two Dimensional.
3D	Three Dimensional.

ACKNOWLEDGEMENTS

I would like to thank my supervisor, Tom Bowling for his help throughout the research, especially for providing the hardware which sat on my desk for two years and without which the programming element of this the research would have been problematic to say the least.

I would also like to thank my parents and all those people who put up with me throughout the last two years, a period during which I was frequently irritable and at times anti-social.

1 : INTRODUCTION

1.1 : Colocation of Geostationary Satellites

1.1.1 : General

The geostationary orbit is a unique resource providing invaluable facilities for communications and Earth observation purposes. Because of this there is a high demand for orbital positions in GEO and as a consequence, the concept of satellite *colocation* has been developed. In this context to *colocate* (or *cluster*) satellites means to position more than one satellite in a GEO window which is usually only reserved for one satellite. Alternatively, it can be said that *colocated* satellites all share the same GEO window.

Two satellites positioned in the same GEO window tend to follow almost identical orbital paths under optimal single satellite control methods, even if each satellite is controlled by a different agency. In practice this can produce interference between satellites due to the high probability of close approaches, and even collision risks. To avoid these problems a co-ordinated control approach is required to separate the satellites physically in space whilst still maintaining both within the nominal window.

Various approaches to the separation of colocated satellites are possible, such as introducing a time interval between the application of station keeping manoeuvres for each satellite (e.g. one week), operating each satellite in a slightly non-GEO orbit by separating the orbital elements of each satellite (e.g. using a slightly different eccentricity or inclination), or a combination of the two.

The usefulness of each method changes as the size of the cluster increases. Generally the conceptually simple schemes become less effective as the number of satellites increases, however even with the 'best' methods the requirement for all the satellites to remain within the same GEO window coupled with the presence of non-zero tracking and orbital control errors means that close approach risks can only be reduced and not eliminated.

The subject of this thesis is to demonstrate that these close approach risks can be further reduced by the application of an avoidance or relative motion correction manoeuvre. To this end a computer software program, which is detailed in this document, has been written to model the motion of a cluster of GEO satellites operating under the influence of realistic perturbation effects. Both standard station keeping manoeuvres and control algorithms which provide relative motion corrections are applied autonomously by the software for an initial cluster configuration which is user specified.

To aid in the development of usable cluster concepts and to analyse the simulation data various software based design tools have been created and these too are detailed in this document.

Reference has already been made to the GEO window, in which a cluster of satellites must remain, and due to its importance the concept will now be defined.

1.1.2 : The GEO Window

An ideal GEO satellite would orbit the Earth at a fixed Greenwich longitude, 'λ_i' , with a constant latitude of zero. Perturbation effects cause the satellite to deviate from the ideal and so a GEO window with a centre at 'λ_i' radians longitude and zero radians latitude, is defined and the satellite must remain within $\pm\Delta\lambda$ radians longitude and $\pm\Delta\phi$ radians latitude of these values (cross-coupling between longitudinal and radial motions make the definition of a radial deadband unnecessary). The extent of the *deadbands* is determined by a combination of regulatory body and mission requirements. The resulting window can be visualised as a 'box' with EW dimensions '$2a_G\Delta\lambda$' and NS dimensions '$2a_G\Delta\phi$' as shown in figure 1.1.

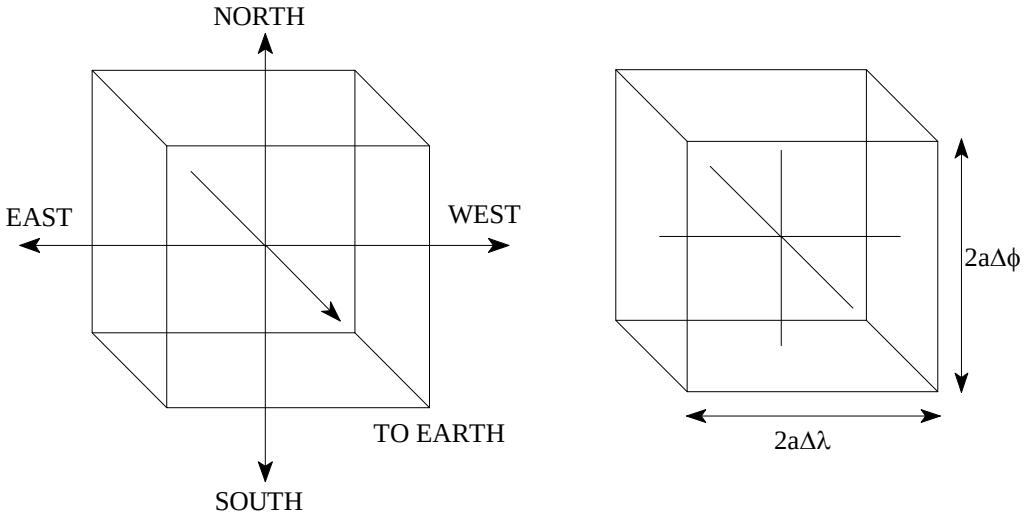

Figure 1.1: GEO Station Keeping Window

A typical GEO window could have longitudinal and latitudinal deadbands of ±0.°1 about the nominal values, although for some applications this could be increased to about ±0.°5.

1.2 : Reasons to Colocate

1.2.1 : ITU Regulations

The allocation of radio frequencies, orbital position and window deadband in the geostationary orbit for direct broadcast satellite services (DBSS) is dealt with by the International Telecommunications Union (ITU). The ITU is an agency of the United Nations and membership is open to all countries.

Regulations and constitutional changes are dealt with by administrative conferences for which a two tier system exists. World Administrative Radio Conferences (WARC's) deal with issues globally whilst Regional Administrative Radio Conferences (RARC's) consider single regions, the globe being divided into three region. Region 1 covers Europe, Africa and northern Asia, region 2 covers the Americas and region 3 covers the remainder. Administrative conferences are usually called to discuss a specific issue, (e.g. in 1987 the WARC reviewed mobile space telecommunications) however every twenty years a general

WARC is held to consider the entire frequency spectrum, the most recent of these taking place in 1979.

Of relevance to colocation was WARC77 which discussed DBSS and it is this class of satellite that is the most common in GEO. A 'plan' was adopted for regions 1 and 3 comprising a list of reserved frequencies and nominal orbital positions in GEO, each separated by 6° in longitude and extending ±0.1° in longitudinal deadband. Amongst other things the plan made the date of registration with the international frequency registration board no longer important, ending the 'first come, first served' rule for DBSS applications and granting member countries the right to place satellites at certain locations even if they currently were not in a position to do so. Due to the number of countries involved, the same longitude position was often allocated multiple times (e.g. in the case of 19.0° W, thirteen countries were allocated the same ±0.°1 window). The restriction of individual countries on where they can place satellites in GEO leads to several locations where colocation has or probably will, occur.

More details on the ITU and GEO orbital allocations and can be found in Morgan et al [30].

1.2.2 : Modular Growth Capability

The growth trend in telecommunications could soon exceed the capabilities of present and planned launch vehicles to satisfy payload requirements since the development cycle of launch vehicles is considerably longer than the rate of increase in payloads. In particular the current demand for more satellite television services could accelerate the process.

Colocation provides a solution to this problem by dividing the payload into several segments which are launched separately. This form of colocation implies single agency controlled clusters are likely to occur in addition to the multi-agency clusters described in section 1.2.1.

In addition to this driving force there are advantages to modular growth. The ability to add on-station capability (the entire cluster can be regarded as a single communications medium from the point of view of an end user) within the lifetime of current satellites is particularly appealing. Lower specification satellites (possibly of the shelf) can also be used since individual satellites are not expected to satisfy the total cluster requirements at the end of their life (for single satellites it is common to include an unused capability at the beginning of life to allow for increased requirements at end of life). Thus the cost of individual satellites in a cluster can be reduced.

1.2.3 : Redundancy

A single satellite in a GEO window is a single point failure system. Although total failure is unlikely it is not unheard of, the OLYMPUS satellite being a good example which will be discussed in reference to colocation at 19.0°W in chapter 3.

Multiple platforms can avoid this problem if backup transponders are included on each satellite in the cluster to prevent a single satellite failure from affecting the communications traffic of the overall cluster. The same method can be used to temporarily cope with the total traffic when a satellite reaches the end of life and is removed from the cluster, to be replaced afterwards by a new satellite.

1.3 : Thesis Summary

Since colocation is a specialist subject the basics are described in chapter 2 which hopefully allows the literature review of chapter 3 to be understandable by someone unfamiliar with the topic. The remainder of the thesis is then divided into self contained chapters which describe various parts of the research. Each chapter will now be summarised, including the reasons why it is present.

Since an orbit propagator is fundamental to the simulation of any satellite orbit it is the first highly mathematical subject addressed and this is done in chapter 4. Numerical integration schemes and orbit perturbation models are discussed and a software

implementation of orbit propagation based on these is detailed. Software validation is essential for simulation results to be meaningful and so to supplement chapter 4, appendix B contains details of the validation process followed. As part of this validation a comparison is performed between the software detailed in chapter 4 and a segment of orbit propagation data from ESA.

For the propagator to be useful in the long term for the simulation of a single GEO satellite it must possess the ability to autonomously control the satellite via station keeping manoeuvres and this subject is addressed in chapter 5. Included is a discussion and derivation of an EW and NS station keeping control scheme along with a section on control errors and how they can be simulated in software. By way of validation, results are presented showing that the motion of a single satellite at a specific location in GEO over multiple station keeping cycles remains within a prescribed GEO window.

With validated software for orbit propagator and station keeping simulation the relative motion of colocated satellites can be examined and this subject is described in chapter 6. Firstly, to approximate the motion of satellites with respect to each other, the accuracy of Hill's equations of relative motion is established for colocation by comparing the predicted relative motion with the actual motion as produced by the orbit propagation software. Secondly, cluster design concepts based on the descriptions in chapter 2 and the motion as described by Hill's equations are examined and the available strategies are reduced to two. These are then implemented as two four satellite clusters which are simulated for extended periods to produce data on the close approach probabilities between individual satellite pairs.

Under the cluster simulation conditions described in chapter 6, the resulting close approach probabilities are shown to be unacceptably high and chapter 7 addresses this issue by introducing the concept of a cluster geometry recovery manoeuvre which is applied when a given satellite deviates too far from its nominal relative orbit. With this correction in place the two cluster configurations described in chapter 6 are again simulated and the close approach frequencies are analysed to demonstrate the

effectiveness of the system. To supplement chapters 6 and 7 appendix C contains two derivations of Hill's first order equations of relative motion.

To conclude the main text chapter 8 presents discussions and conclusions along with details of possible extensions to the research.

Appendices A and D have so far not been mentioned. Appendix A contains several mathematical methods which are referred to throughout the text, specifically co-ordinate frame and variable set definitions, conversions between co-ordinate frames equations and multiple regression curve fitting algorithms. Appendix D contains a listing of the main elements of the propagation software core program.

1.4 : Original Contribution

In chapter 5 concerning the evolution of an autonomous station keeping scheme, although packages capable of performing this function already exists as in-house software with the major operators, the implementation described in chapter 5 was written without reference to these and as such may be considered original work. Also in this chapter, software based cluster design tools are developed which aid in the positioning of individual satellites in longitude, eccentricity and inclination to obtain maximum usage of the GEO window without violating the deadband restrictions.

In chapter 6, the concept of a *phantom satellite* is introduced as a position with respect to which the relative motion of all the clustered satellites are measured. Consider the path of a optimised satellite operating alone in the GEO window. Due to perturbation effects station keeping manoeuvres will be required to correct the motion and if these are applied *with no errors* the resulting orbital motion can be described as an *ideal perturbed GEO orbit*. The *phantom satellite* is defined as a satellite describing this path. In physical terms this satellite does not exist, however its location is useful as the centre of the relative motion frame since its position is always ideal and hence correction manoeuvres calculated using relative motion equations are simplified since the correction applied to the phantom satellite is always zero.

In chapter 7, Hill's equations are used to formulate two cluster geometry correction manoeuvres. The first derivation requires that velocity increments can be applied along a combination of the radial, longitudinal and normal (or NS) axes where-as the second derivation requires thruster capability along only those axes used for EW and NS station keeping, i.e. the longitudinal and normal axes. Both the derivations and the use of Hill's equations to calculate cluster correction manoeuvres is thought to be original.

1.5 : Programming Methodology

1.5.1 : Overview

In the course of the research a substantial amount of computer software was generated for the simulation and analysis of colocated satellites. This will be referred to as, *the software*, or *the evolved software* throughout this thesis and is represented both descriptively and graphically using operational flow charts and screenshots of the software in operation where relevant.

As an example of the last, figure 1.2 illustrates two screenshots, showing aspects of the text and graph handling aspects of the software. In the top diagram the built-in text editor shows two open files. In the background is an orbit propagation data file in classical orbital elements (see appendix A for definition) and in the foreground is the corresponding initialisation data file which contains all the relevant information concerning the initial conditions for the same propagation. In the lower diagram the graph window shows the evolution over time (in days) of an orbit eccentricity. The data used to generate this graph was read directly from the orbit propagation data file from the top diagram.

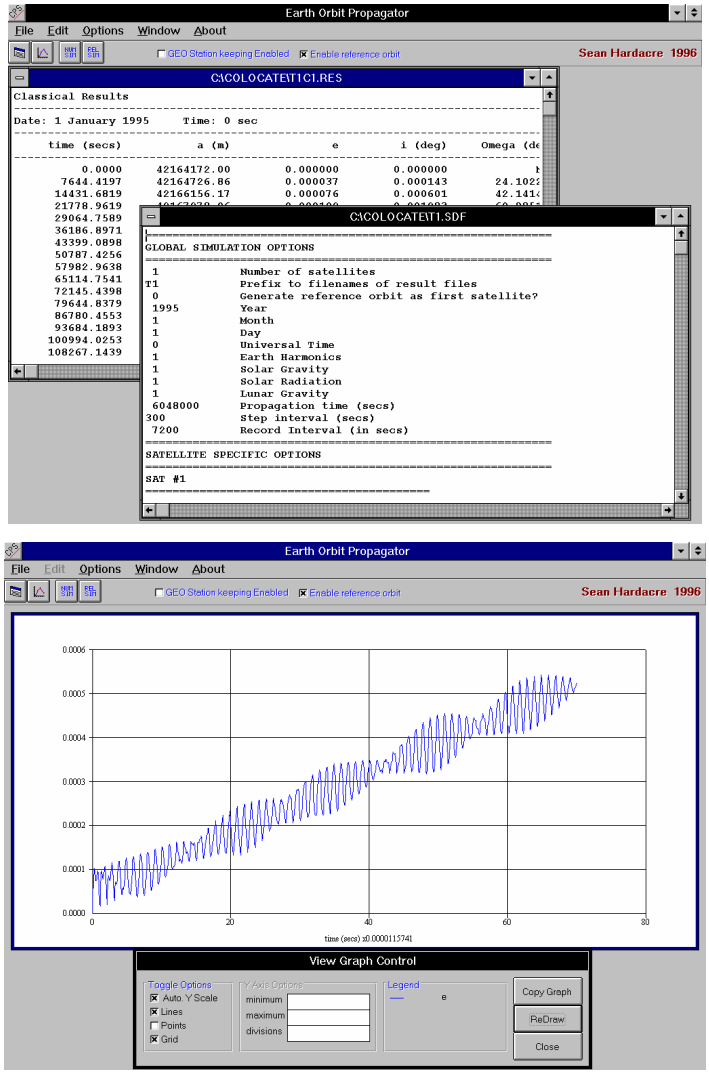

Figure 1.2 : Software Screenshot Examples

Although it is impractical to include a complete program listing, as already noted a small section concerning the main elements of the orbit propagator upon which everything else operates is included as appendix D.

The hardware and commercial software with which the software was constructed, the programming methodology employed and the general operation of the software, will now be discussed.

1.5.2 : Operating Environment and Commercial Software

The software was written on an *IBM compatible PC*, running the *Microsoft Windows for Workgroups 3.11®* operating system using the following commercial software packages to perform the programming and analysis tasks,

- *Microsoft Visual Basic 3.0 (Professional edition)®* (VB).
- *Borland Turbo Pascal for Windows 1.5®* (TPW).
- *The Student Edition of MATLAB 4.0®* (MATLAB).

A minimum of an Intel 486DX2 PC running at 66 MHz with 8 Mb of RAM is required to use all aspect of the software, however an Intel Pentium class machine or greater is recommended to reduce orbit propagation times.

1.5.3 : Modular Programming

A series of sub-programs or modules were written to accomplish specific tasks (e.g. orbit propagation) with no attempt being made to integrate all the code into one single executable program. This was done to avoid problems with 'unexpected' interaction between various aspects of the code which would necessitate the entire code being re-validated every time a change was made or a module was added. The approach thus allowed individual modules to be debugged independently, shortening (in theory) the debugging/validation process.

Each module was written in a way that enabled them all to be launched from a common graphical user interface (GUI) for usability. Inputs are recorded by the GUI and user requests launch the relevant task specific sub-program. Results generated are then stored in standard ASCII text file format enabling them to be accessed later by either the GUI launch program or some other software package. Since the modules are physically separate from each other there was no need to program the entirety in a single language, allowing the most appropriate tool to be used for each task.

Microsoft Visual Basic® is an interpreted language which was originally intended for rapid applications development (RAD) and database work. As such using VB it is very

simple to create a complex GUI relatively quickly. The main disadvantage of the language is speed (on average an interpreted program runs about ten times slower than a compiled one) which is a problem for mathematically intensive operations such as orbit propagation. Based on this the GUI, including certain analysis and pre-processing tools which were not mathematically complex, were programmed in VB.

Borland Turbo Pascal® produces compiled code and is thus much faster at run-time than VB, in use however it is difficult to produce a complex GUI. Based on this the mathematically intensive tasks, such as orbit propagation, station keeping and axis conversion were programmed in TPW.

To supplement both VB and TPW the student version of MathCad MATLAB® was used for some of the post-simulation analysis of the data and all the graphs presented in this thesis were generated using it. To simplify data transfers between programs, the evolved software has options enabling various results files to be generated in a file format which can be directly read by MATLAB.

1.5.4 : General Operation and Software Interactions

The main program elements are illustrated in figure 1.3. The TPW software is controlled from the VB launch program which can assess all the modules shown that are bordered by solid lines. At a lower level, various separate modules exist in the TPW code and these can also interact with each other as shown by the arrows.

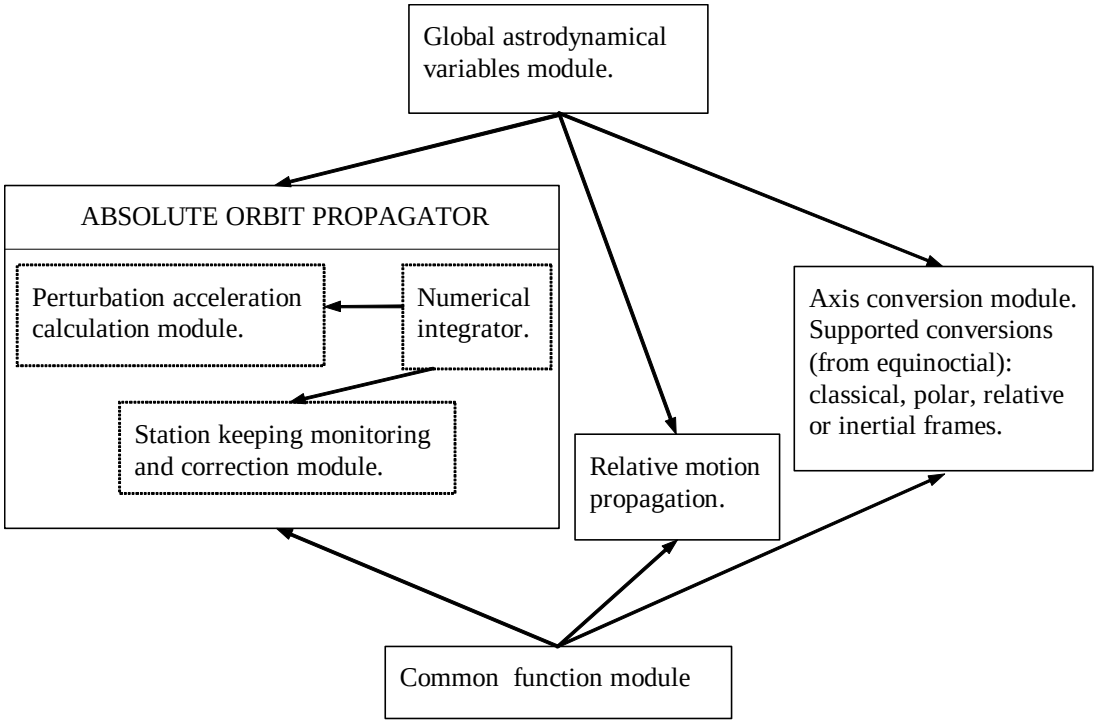

1.3 : TPW Modules Interaction

Of the modules shown in figure 1.3, the perturbation acceleration calculation and the numerical integrator modules are the most critical. These two define the model of the environment within which the simulated satellite(s) are moving and must therefore produce realistic results. It is the validation of these that is included in appendix B.

2 : COLOCATION STRATEGIES

2.1 : Overview

There are two categories of separation methods between colocated satellites; those involving synchronous station keeping manoeuvres, and those involving asynchronous manoeuvres (in which each satellite follows a different station keeping schedule).

The synchronous method all involve separating the orbital elements of the satellites (excluding the semi-major axis which is fixed by the orbital period requirement) and a description of the methods commonly used are discussed in section 2.3. For visualisation purposes Hill's relative equations (also known as the Clohessy-Wiltshire equations) are used to describe each method and these are introduced in section 2.2. Later in this thesis a more comprehensive discussion of relative motion will be given.

The asynchronous method can be applied in two forms. When used independently of 'planned' orbit separation methods relative distances are maintained by the fact that the orbital elements are expected to drift during the cycle, thus if each satellite is at a different point in the cycle there exists a natural separation in elements. The second form involves combining asynchronous manoeuvres with planned orbital element separation. Since asynchronous manoeuvres are conceptually simple a section describing them is not required.

A discussion of the effectiveness of the different schemes, in terms of maintaining inter-satellite distances and fuel consumption, is included in section 2.4.

2.2 : Introduction to Relative Motion

2.2.1 : Hill's Equations of Relative Motion

Separation strategies are often referred to in terms of the position of one satellite relative to another. In defining a relative co-ordinate system one satellite is used as the origin and the position of a second is given along the following three axes.

R	Radial separation (from centre of Earth), positive outwards.
L	Longitudinal separation, positive Eastwards.
K	Latitudinal separation, positive Northwards

The last two axes are strictly arc lengths, however since relative separations are usually small compared to the GEO radius, linear assumptions are usually reasonable. Starting from a pure Newtonian orbit model motion along these three directions to first order can be written as,

$$\begin{aligned} R &= -\frac{2}{3}E_2 + E_3\mathrm{Cos}\left(n_G\left(t-t_0\right)\right) + E_4\mathrm{Sin}\left(n_G\left(t-t_0\right)\right) \\ L &= E_1 + E_2 n_G\left(t-t_0\right) - 2E_3\mathrm{Sin}\left(n_G\left(t-t_0\right)\right) + 2E_4\mathrm{Cos}\left(n_G\left(t-t_0\right)\right) \\ K &= E_5\mathrm{Cos}\left(n_G\left(t-t_0\right)\right) + E_6\mathrm{Sin}\left(n_G\left(t-t_0\right)\right) \end{aligned} \tag{2.1}$$

where the 'E_i' variables are found in terms of the equinoctial orbital elements as,

$$\begin{aligned} E_1 &= a_G\Delta\lambda_0 \\ E_2 &= -\frac{3}{2}\Delta a \\ E_3 &= -a_G\Delta P2 \\ E_4 &= -a_G\Delta P1 \\ E_5 &= -2a_G\Delta Q1 \\ E_6 &= 2a_G\Delta Q2 \end{aligned} \tag{2.2}$$

A full derivation of equations (2.1) and (2.2) is included in appendix C.

2.2.2 : The 2D Eccentricity and Inclination Vectors

Two useful concepts for visualising orbital element separation strategies are the 2D eccentricity and inclination vectors, which are related to the projection of the 3D versions onto the equatorial plane. Unlike the 3D form however, different authors use different definitions. Since the equinoctial orbital element set is used extensively in this thesis the choice here reflects this and is again non-standard. The vectors are defined in equations (2.3).

$$\begin{aligned} \underline{e} &= e\begin{bmatrix} \mathrm{Cos}(\Omega+\omega) \\ \mathrm{Sin}(\Omega+\omega) \end{bmatrix} = \begin{bmatrix} P2 \\ P1 \end{bmatrix} \\ \underline{i} &= \mathrm{Tan}(i/2)\begin{bmatrix} \mathrm{Cos}(\Omega) \\ \mathrm{Sin}(\Omega) \end{bmatrix} = \begin{bmatrix} Q2 \\ Q1 \end{bmatrix} \end{aligned} \tag{2.3}$$

The selection is made to simplify the inclination and eccentricity plane diagrams which illustrate the 2D vectors graphically. These are shown in figure 2.1.

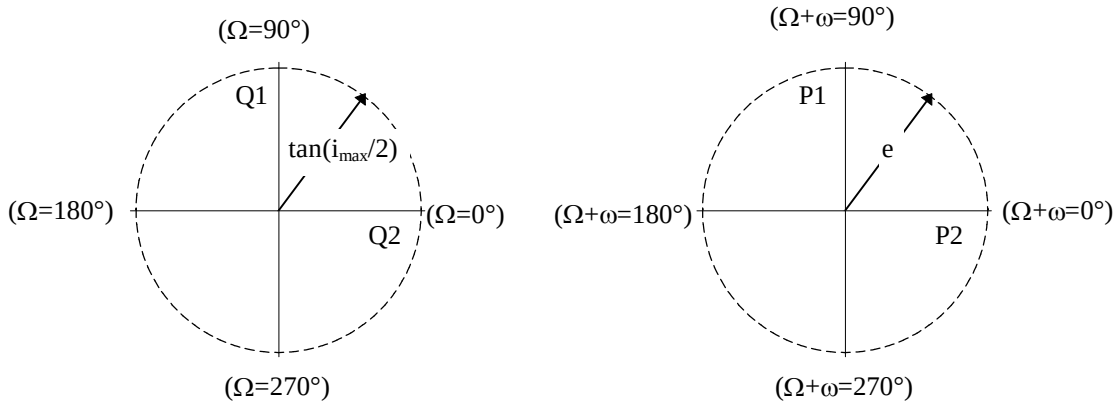

Figure 2.1 : Inclination and Eccentricity Plane Diagrams

Drift across the 'i' plane is approximately linear and motion in the 'e' plane, circular (the radius of the control circle being selectable to a certain degree). A more detailed discussion of both planes is given in chapter 5. In terms of equations (2.1) and (2.2), the *relative* 2D eccentricity vector is directly related to 'E_3' and 'E_4', and similarly the *relative* 2D inclination vector is directly related to 'E_5' and 'E_6'.

2.3 : Orbital Element Separation

2.3.1 : Uncoordinated Strategy (CONTROL)

The CONTROL scheme is not suggested as a viable means of colocating, however it is useful as a baseline comparison for the other methods. For this strategy each satellite is independently controlled and possesses the same nominal orbital parameters. Separation is achieved from inaccuracies in the station keeping burns and, if different control centres are used for each satellite, differences in operational practice. In terms of equations (2.2) all the E_i (i=1 to 6) elements are nominally zero.

2.3.2 : Mean Longitudinal Separation (MLS)

Using MLS the mean longitude of each satellite is unique to that satellite. Two satellite MLS is shown in figure 2.2 below. In the diagram '$\Delta\lambda$' is the separation between satellites.

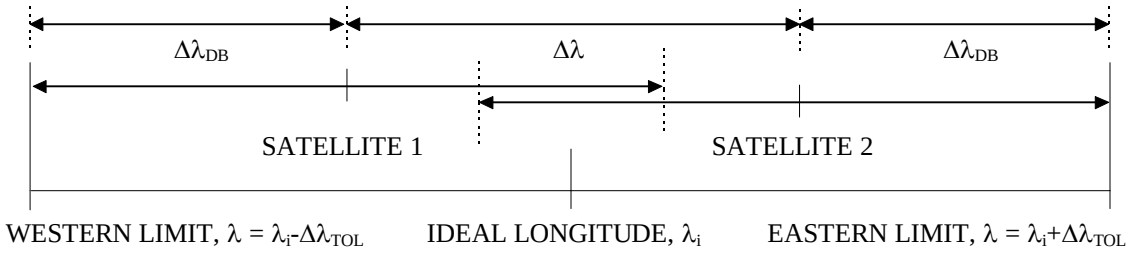

Figure 2.2 : EW Deadband for MLS Strategy

To use the entire deadband the following relationship, $2\Delta\lambda_{TOL} = \Delta\lambda + 2\Delta\lambda_{DB}$ must be satisfied. Alternatively, if the reduced deadband, '$\Delta\lambda_{DB}$' is selected to equal '$\Delta\lambda/2$', the satellites will be entirely separated in longitude with no region of overlap. This configuration is often referred to as the 'necklace' geometry, and allows each satellite to be considered independently - the only impact colocation has on nominal operations is a reduction in the allowable EW deadband. The main advantage of this is that co-operation between control centres for different satellites should not be necessary. The main disadvantage is a fuel penalty due to more frequent EW manoeuvres. As the number of satellites increases so too does this penalty.

In terms of equations (2.1) and (2.2) only the 'E_1' variable is non-zero. The nominal relative motion is thus a constant separation along the 'L' axis with no 'R' and 'K' separation.

2.3.3 : Eccentricity Separation (ES)

An ideal GEO orbit has zero eccentricity, however a non-zero value is acceptable provided the daily libration effect in the longitudinal direction does not cause an EW deadband violation. By separating the eccentricity vectors of two colocated satellites the 'E_3' and 'E_4' variables in equations (2.1) become non-zero and the relative motion is elliptical, with separation along both 'R' and 'L' axes.

Maximum separation is obtained by selecting non-overlapping eccentricity control circles on the 'e' plane, however this also produces the largest eccentricity correction fuel penalty. The 'e' plane and resulting motion in the RL plane for this configuration is shown in figure 2.3.

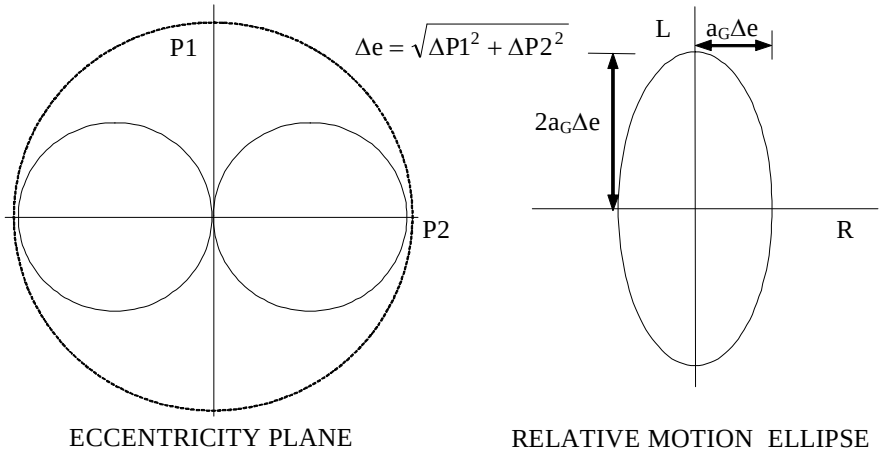

Figure 2.3 : EW Deadband for ES Strategy

Over the course of one year the radius vector of the individual 'e' control circles will describe a complete circle, with the tip of the vectors pointing in the direction of the Sun *as seen from the origin*. At each point the angle between these vectors and the 'P2' axis will be identical for both satellites, leaving the relative ellipse unaffected.

Unlike MLS the inter-satellite distance varies, however two dimensions of the window are utilised making ES more effective for large clusters. The disadvantage is that satellite eclipses can occur, causing possible rf interference problems.

2.3.4 : Inclination Separation (IS)

Separating the inclination vectors results in non-zero 'E_5' and 'E_6' elements, producing a sinusoidal motion along the 'K' axis, which is shown in figure 2.4. To first order the nominal separation along 'R' and 'L' axes is zero.

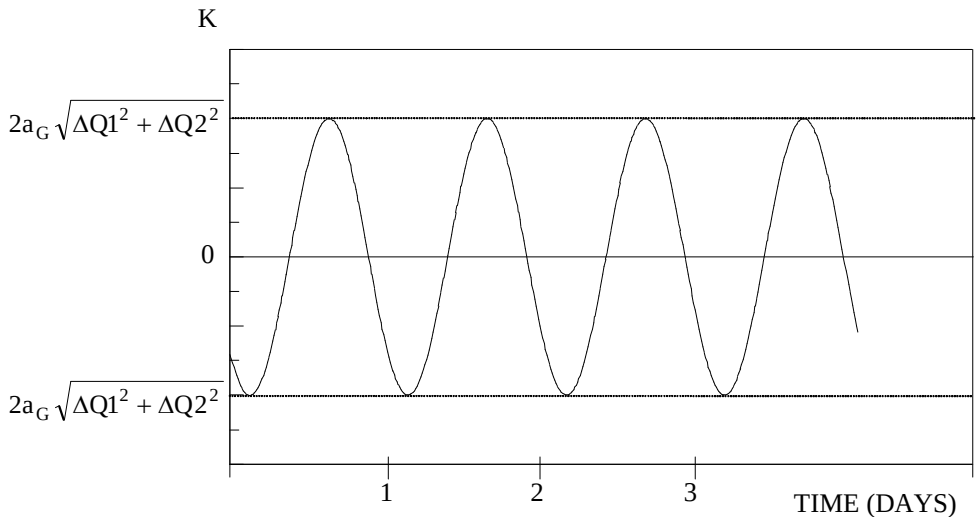

Figure 2.4 : Motion along the 'K' Axis With the IS Strategy

Note that the minimum separation is zero twice per orbit, making pure IS inadvisable.

2.3.5 : Eccentricity and Inclination Separation (EIS)

Combining ES and IS results in EIS separation. Although there is no requirement for a specific relationship between the eccentricity and inclination vectors in EIS three such cases are of interest; namely parallel, perpendicular and circular. Each will be described in turn along with the 'general' EIS scheme.

EIS Parallel

If the relative eccentricity and inclinations vectors are parallel then equations (2.1) can be rewritten as,

$$R = -a_G\sqrt{\Delta P1^2 + \Delta P2^2}\,Sin\left(n_G t + \phi\right)$$
$$L = -2a_G\sqrt{\Delta P1^2 + \Delta P2^2}\,Cos\left(n_G t + \phi\right)$$
$$K = -2a_G\sqrt{\Delta Q1^2 + \Delta Q2^2}\,Cos\left(n_G t + \phi\right)$$

and the motion along [R,L,K] axes is shown in figure 2.5.

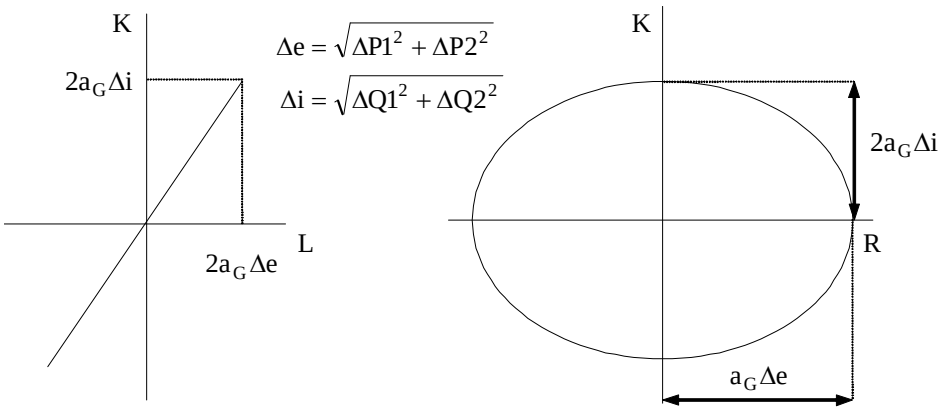

Figure 2.5 : EIS Parallel Separation

The semi-major and semi-minor axes of the relative ellipse are then, $2a_G\sqrt{\Delta i^2 + \Delta e^2}$ and $a_G\Delta e$. Thus the semi-*major* axis has been increased above the value obtained from pure ES.

EIS Perpendicular

If the relative eccentricity and inclinations vectors are perpendicular then equations (2.1) can be rewritten as,

$$R = -a_G\sqrt{\Delta P1^2 + \Delta P2^2}\,Sin\left(n_G t + \phi\right)$$
$$L = -2a_G\sqrt{\Delta P1^2 + \Delta P2^2}\,Cos\left(n_G t + \phi\right)$$
$$K = 2a_G\sqrt{\Delta Q1^2 + \Delta Q2^2}\,Sin\left(n_G t + \phi\right)$$

and the motion along [R,L,K] axes is shown in figure 2.6.

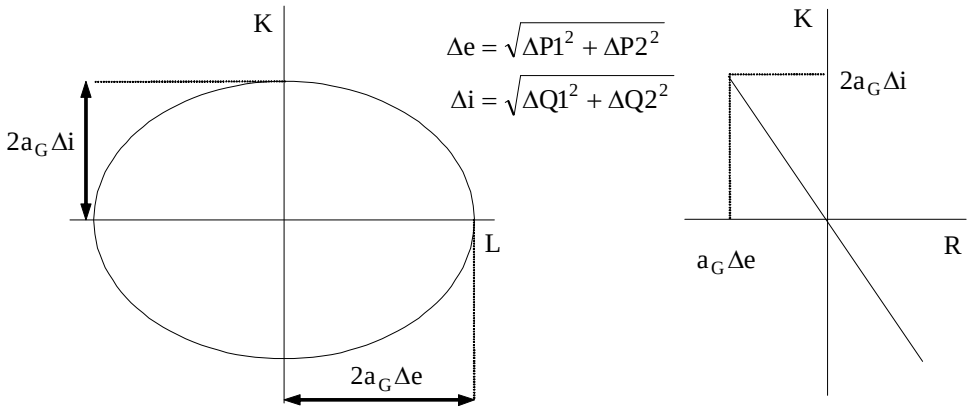

Figure 2.6 : EIS Perpendicular Separation

The semi-major and semi-minor axes of the relative ellipse are then, $a_G\sqrt{4\Delta i^2 + \Delta e^2}$ and $2a_G\Delta e$. Thus the semi-*minor* axis has been increased above the value obtained from pure ES. Theoretically EIS perpendicular is superior to parallel in that the minimum separation distance is increased and, as seen from the Earth, satellite eclipses do not occur. In practice however parallel is 'better' at maintaining separation distances when manoeuvre errors are considered.

EIS Circular ('tilted circle')

Using EIS perpendicular, if 'Δi' is selected such that $\Delta i = \left(\sqrt{3}/2\right)\Delta e$ then the relative ellipse will be circular. This configuration is sometimes referred to as the 'tilted circle' or EIS circular and is particularly useful if SST is used since the 'look' angles between satellites are then constant.

Other EIS Schemes

Other EIS schemes are possible with the relationship between the inclination and eccentricity vectors at some intermediary value. These are 'compromise' configurations selected mainly to avoid the eclipses which occur using EIS parallel whilst providing larger separation distances in the presence of manoeuvre errors than occur using EIS perpendicular. One example of a cluster operating such a scheme is the ASTRA cluster at 19°.0E. This example will be discussed in detail in the next chapter.

2.4 : Discussions

2.4.1 : Synchronous Vs. Asynchronous Manoeuvres

Since the orbital paths followed using only asynchronous manoeuvres as a method of separation are identical to the path followed by an optimally controlled single satellite in the same window (the only difference is that the station keeping cycles begin and end at different times) there is no fuel penalty associated with this form of colocation. Unfortunately as the number of satellites in the cluster increases the method becomes increasingly less effective as nominal separation distances diminish. The biggest problem is that only a relatively small region of the available GEO window is being utilised.

Conversely synchronous manoeuvres are more demanding to implement (especially if the satellites are controlled from different ground stations) and incur a fuel penalty due to the need to separate the orbital elements of individual satellites (see section 2.4.3). However for preserving the internal cluster geometry, which may be a requirement for some SST systems, synchronous manoeuvres are advantageous and can maintain mean inter-satellite distances above those of the asynchronous scheme. Most of the reports detailing separation strategies suggest synchronous manoeuvres as the preferred solution.

The third option is a hybrid of the first two and has advantages both operationally and practically. Specifically, the ground station workload is less intense and the mean separation distances increase (although by an amount less than obtainable purely from orbital element separation). The disadvantage for SST systems is the changing internal geometry of the cluster, which also makes relative orbit visualisation difficult.

2.4.2 : Orbital Element Separation and Fuel Penalties

The separation in orbital elements resulting in the use of more than one dimension of the GEO window are more effective at maintaining large inter-satellite distances. As an example of this ES results in larger theoretical separations than MLS since both radial and longitudinal distances vary with respect to the ideal GEO position instead of just longitudinal, however there are other factors to consider. In particular, separating the eccentricity control circles as shown in figure 2.3 necessitates smaller 'e' circle radii. This may or may not reduce the EW station keeping interval from some desired value but it will mean an increase in the velocity increment needed for eccentricity correction. Whether this affects the overall EW station keeping fuel budget is determined from the triaxiality correction velocity requirement (station keeping is discussed in detail in chapter 5).

The NS manoeuvre is relatively unaffected by the use of orbital element separation methods even if this includes an inclination offset. To obtain 'tighter' control on the inclination plane shorter NS cycles may be required, however the inclination drift is approximately linear and so the overall NS velocity requirement for the mission lifetime will be relatively unaffected. Periodic oscillations superimposed on the linear drift of 'i' cause slight increases however, particularly if the inclination tolerance is very tight (Soop [31]).

As an example of the incurred fuel penalty, consider an extreme case in which the area to mass ratio is about 0.05 (more usually this is >0.02), the maximum 'e' tolerance is 0.00042, the EW cycle is 14 days, and the nominal Greenwich longitude is 0°. The eccentricity control penalty dominates, resulting in a 0.264 m/s EW velocity requirement every cycle for a single satellite. If the number of satellites is increased to two however and either MLS with $\Delta\lambda$=0.°05 or ES/EIS using the configuration shown in figure 2.3 (which halves the 'e' control circle radius) is used this requirement increases to 0.356 m/s. Over a 10 year lifespan the increased fuel requirement is 24 m/s, which is equivalent to approximately a 4 month shortening of the operational lifetime of each satellite (taking into account NS manoeuvres).

3 : LITERATURE REVIEW

3.1 : Overview

Research into colocation is relatively new and only really became an issue after the WARC77 plan for DBSS made it clear that the clustering of satellites in the same GEO window was inevitable. As a result, there is limited research on the subject and even fewer cases of actual colocation implementations.

The literature reviewed here can be divided into four categories; cluster design concepts, interference analysis (of which only collision risks will be examined), the need for internal cluster geometry maintenance and colocation implementation papers. The last of these is a subset of the total and details the history and implementation of the clusters at 19°W and 19°E.

3.2 : Literature Review

3.2.1 : Cluster Design Concepts

This first category focuses on the design of the relative orbits between colocated satellites with the aim of providing a cluster geometry which maintains inter-satellite distances above some minimum value. Each paper proposes several strategies, discusses their relative advantages and in some cases demonstrates their feasibility via Monte-Carlo simulation.

Walker [1] discussed three separation strategies; ES, EIS circular and a hybrid EIS circular/MLS scheme. For each it is assumed SST is used and the suitability of each is based on look angles between satellites, computed from Hill's equations. Simulations using actual orbital dynamics are not discussed.

Hubert & Swale [2] considers a large 0.6° in longitude, 0.2° in latitude GEO window in which satellites are controlled in one of three ways; with no considerations for the other satellites in the cluster, using MLS to separate each satellite, or using MLS to separate

groups of satellites - each group being confined to a 'sub-box' of the overall longitude deadband with EIS separating individual satellites in a group. A simulation using three satellites in two sub-boxes is detailed which includes the effects of NS burn cross-coupling errors. The results are favourable, however the size of the window compared to the number of satellites in it make the results unrepresentative of most GEO positions.

Murdoch et al [3] uses the MLS strategy and examines in detail the requirements of SST, concluding that further development of the concept should not be a high priority and that other methods would be more economical (an example being the TV signal ranging of Agostini et al [20]). The need for numerical simulation to establish both collision probabilities and an examination of synchronous and asynchronous station keeping is suggested as an extension to the research.

Tanaka et al [4] discusses a two satellite cluster within a ±0.1° longitudinal window. Dividing the longitude deadband in two and using MLS with synchronous and asynchronous manoeuvres are examined as separation methods. Of the three, MLS with synchronous manoeuvres was preferred, based partially on the reduction in station keeping cycle time required by the first method.

In comparison Carlini & Graziani [5] describe a pure ES separation strategy for three satellites, each satellite occupying the apex of a triangle which is centred on the eccentricity plane. Hill's equations are used to define the motion and the concept of multiple clusters in the same window is introduced. For this configuration the authors propose each cluster is controlled by an individual agency which is allocated a region of the eccentricity plane. In this respect the sub-division of the window is similar to Hubert & Swale [2] and Tanaka et al [4], although in these the longitudinal deadband was sub-divided. Neither simulations nor station keeping errors are mentioned.

3.2.2 : Collision Probabilities

The second class of papers concern the probability of close approaches between clustered satellites. Different separation strategies are simulated using Monte Carlo

methods which include the effects of manoeuvre and tracking errors to demonstrate the effectiveness of the strategy to 'real' situations.

Fusco & Buratti [6] consider the risks of collisions between active-inactive satellites and active-active satellites. The approach is analytical in nature and uses Hill's equations with the assumption that the relative orbital elements will be randomly distributed about some nominal relative orbit to compute statistical probabilities of close approaches. The conclusion is that close approach probabilities between active-inactive satellites are negligible but those between active-active satellites require a change from single satellite control methods when operating a cluster.

Härting et al [7, 8] assess the risks of close approaches between two identical satellites at 19°W ±0.1° via computer simulations using a simplified orbit propagator (to speed computation). Manoeuvre/tracking errors are included. The station keeping cycle comprises 2 EW manoeuvres (separated by 1/2 a sidereal day) every 14 days and one NS manoeuvre conducted at 4-6 week intervals. The EW manoeuvres are performed two days after the NS to allow for control of the NS cross-coupling effect.

Six strategies are simulated, each for a 500 year propagation period, and histograms are presented to illustrate the minimum approach distances. The conclusions presented are that EIS parallel is the most efficient in minimising the close approach risks but incurs a 5% fuel penalty (due to the reduction in the eccentricity control circle radius) over the simpler MLS scheme. The use of MLS is advocated for 2 satellites and EIS for larger clusters where reductions to the length of the EW cycle make MLS unreasonable.

Rajasingh [9] again considers the case of colocation at 19°W (prior to it actually occurring) and analyses possible separation strategies with regard to the minimum separation distances generated over 140 lifetimes of 7 years each. Simulations are performed for pairs of satellites, including error modelling, and the results are illustrated via histograms of 980 minimum approach distances.

A CONTROL, MLS, ES and EIS scheme are simulated using synchronous manoeuvres and a CONTROL, and EIS scheme for asynchronous manoeuvres. The conclusions are that with four satellites EIS parallel is preferred due to its higher mean minimum separation distances. Additionally, although the asynchronous scheme provides a more evenly distributed ground station workload, the lower minimum approach distances (a 2000 m instead of 6000 m mean) makes the asynchronous manoeuvre method unacceptable.

Maisonobe & Dejoie [10] consider colocation of two identical satellites again using a simplified orbit propagator with simulated tracking and manoeuvre errors to establish characteristic curves for close approaches over multiple lifetimes. The separation methods used are; EW manoeuvre offset of 1 week, ES separation, and EIS parallel with and without simultaneous manoeuvres. An attempt is made to fit statistical distribution laws to a sample of the minimum approach distances, thus quantifying the close approach probabilities analytically. Use of these equations to single lifetimes is questionable due to the low event probability of discrete minimum approach distances.

3.2.3 : Cluster Geometry Maintenance

The third class of papers review popular separation strategies and their implementation and then discusses the need to maintain the internal geometry of the cluster. To do this, a second set of station keeping manoeuvres are proposed in addition to the usual set which are used to maintain the cluster centre within a given window tolerance.

Murdoch & Pocha [11] consider MLS, EIS and hybrid schemes with particular reference to ISL's. They conclude that an EIS circular scheme is desirable since this makes the view angle of one satellite from another constant (using Hill's equations and provided synchronous station keeping is assumed) which simplifies the implementation of SST considerably. A simulation of the scheme is presented to show that identical station keeping for each satellite, based on the requirements of the cluster centre with regard to the window restrictions, cause a gradual degeneration of the internal geometry. To overcome this a second set of manoeuvres are proposed which are to follow the 'normal'

station keeping burns. Analytical expressions and simulations demonstrating these are not discussed. The master-slave concept is also mentioned briefly.

Murdoch [12] deals specifically with the MLS necklace geometry in a ±0.1° longitude window using simultaneous manoeuvres on all satellites. Again the NS cross-coupling error is considered as the main cause of disruptions to the internal cluster geometry and the author proposes either reducing the NS cycle time (which he admits will become untenable as the cluster size increases) or initiating relative orbit corrective manoeuvres as soon as possible after the NS manoeuvres. SST coupled with on-board processing is discussed as a way to monitor and control the internal geometry. Analytical expressions for the average velocity requirements of the relative orbit corrections per NS cycle are also given, however numerical simulations are not detailed.

Blumer [13] expands on the ideas of the previous two papers, including a more detailed discussion of the master-slave configuration with SST and numerical simulation results showing the feasibility of a relative orbit correction strategy. Specifically, the internal geometry of the cluster is maintained by the master satellite autonomously using ranging data from laser tracking to establish the relative orbit and thus the manoeuvres required to correct the motion with respect to the master. Overall cluster station keeping is calculated based on ground station tracking of the master satellite orbit and only this satellite is directly controlled from the ground.

Simulations are detailed based on true orbit propagation including errors using a modified form of Hill's equations (which are solved numerically not analytically) as control laws to monitor and correct the slave satellites when required. Some problems were reported with the implementation but these appear minor and correctable.

3.2.4 : Colocation Implementation

Papers in this category can be divided into two; those detailing with the history and operation of the multi-agency controlled cluster at 19°W, and those dealing with the

single agency controlled cluster at 19°E. Each sub-category is discussed in turn, referring to individual papers in chronological order to place them in historical context.

Colocation at 19° West; Multi-Agency Control

WARC77 allocated the GEO window at 19°W to 14 agencies; 8 European, 5 African and ESA. Each was given the right to place its satellites in the window, making it potentially one of the most crowded in the GEO ring. To date colocation has been attempted by three co-operating agencies; CNES, DLR and ESA with a total of four satellites involved.

The first satellite positioned in the window was the French communications satellite TDF1, controlled by CNES Toulouse, and placed at 19.0°W ±0.1° in December 1988. Initially single satellite control procedures were followed, however it was thought that by the end of 1990 there would be four satellites in the window and so a series of meetings between the three agencies were organised to determine a multi-satellite control method. During these it was agreed that a co-ordinated strategy using the EIS parallel method with synchronised manoeuvres was to be used for the final cluster, and that each agency would perform orbit determination of its satellite(s) and then exchange information with the others using a common 'interface telex' format. In addition, an analysis of the tracking systems used by each agency was initiated to assess the attainable orbit determination and calibrate the differences between the different tracking systems. These topics are discussed by Eckstein et al [14] which was published following the arriving on station of the second satellite OLYMPUS in August 1989.

With OLYMPUS a major obstacle to the synchronised station keeping strategy appeared due to the limited number of NS manoeuvres that this satellite was capable of. While studies were being made to overcome the difficulty the German Bundespost announced that TV-SAT 2 (the third satellite of the cluster) would be positioned at 19.2°W ±0.1° in order to avoid the consequences of colocation. Following this announcement CNES and ESOC agreed on a preliminary separation strategy for TDF1 and OLYMPUS in which the two would be separated using a modified form of EIS parallel which included manoeuvre offsets of one week. Again this is discussed in Eckstein et al [14].

The third satellite, at the new position of 19.2°W ±0.1°, followed quickly in the form of the German TV-SAT 2 satellite also in August 1989 (controlled initially by GSOC until the Deutsche Telecommunications took over in mid 1991). The resultant three satellite cluster (two separated by EIS and one by MLS) remained in place for under a year during which period close approaches between TDF1 and OLYMPUS were responsible for a decision to move TDF1 to 19.1°W ±0.1°, creating a three satellite cluster separated by MLS.

The final satellite, the second French communications satellite TDF2, was added one year later in August 1990. This was introduced into the MLS strategy at 18.8°W ±0.1° where it was later joined by TDF1 and the two CNES satellites were then separated using EIS parallel with one week station keeping offsets, thus freeing two non-overlapping windows for the GSOC and ESOC satellites at 19.2°W ±0.1° and 19.0°W ±0.1° respectively.

Co-operation between agencies at 19°W is now reduced to exchanges of data and the only cases of close approaches following the move of TDF1 to 19.1°W were caused by the failure of OLYMPUS in April and June 1991. In these two instances OLYMPUS entered the TDF window in an uncontrolled way and since the CNES control centre was informed of the violation too late no attempt was made to move the TDF satellites, instead a suggestion by CNES for the best 'come-back' through the TDF window was all that was done. These topics and the colocation of TDF1/2 following the move to 18.8°W ±0.1° are discussed in Dufor [15] which also lists the manoeuvre costs for each change in position of TDF1. Adding these, the overall cost is equivalent to an approximately four and a half month reduction in TDF1's operational lifespan.

Colocation at 19° East; Single Agency Control

The ASTRA satellite cluster at 19.2°E ±0.1° currently consists of six satellites, ASTRA 1A-1F. The cluster is controlled from a single ground station in Betzdorf, Luxembourg operated by the Société Européenne des Satellites (SES). The channel capacity of the cluster has increased modularly with each ‘new’ satellite adding around 20 transponders,

making SES the largest provider of satellite channels available in Europe via one antenna. The last three satellites of the cluster provide full redundancy in the event of transponder failure or end-of-lifetime of the earlier models.

ASTRA 1A first became operational in February 1989, 1B followed in March 1991 and the two satellites were separated using MLS. This strategy changed prior to the addition of ASTRA 1C in May 1993 to an EIS scheme and the cluster has remained EIS to date.

With the knowledge that three more satellites after 1C were to be added (1D in November 1994, followed by 1E in November 1995 and 1F in May 1996) an operational plan stating exactly how the additional satellites would be incorporated into the window was prepared. Basically, with the addition of each satellite, the eccentricity and inclination vectors of the present satellites were changed such that the eccentricity and inclination plane diagrams showed regular polygons with a satellite at each apex and one apex 'empty'. The new satellite was then inserted at this position. The scheme has worked successfully for all the satellites following ASTRA 1B with no close approaches being reported between any satellites in the cluster.

The ASTRA cluster was originally designed using a colocation simulation program based on an orbit propagator written by SES, generating results which were automatically entered into the ESA *GeoControl station keeping system* orbital database (Pietrass et al [16]). This program then produced results concerning the relative motion of the cluster, including events of interest such as close approaches. Details of the SES software are presented in Francken & Wauthier [17].

The EIS method used (part way between parallel and perpendicular) and the method of incorporating 'new' satellites into the cluster are described in Wauthier et al [18] and Wauthier & Francken [19]. Station keeping is performed simultaneously on pairs of satellites (the final groupings being 1A/1C, 1E/1F and 1D/1B). The manoeuvres are separated by either 4 or 5 days (the overall station keeping cycle being 14 days long)

resulting in a non-constant cluster geometry. Since SST is not used this is not an problem operationally.
SES use a single ground station and single tracking antenna (tracking one satellite for a specified length of time and then moving on to the next in the cluster) for angular measurements which is supplemented by a TV signal ranging system adapted from Agostini et al [20]. The complete system has the advantages of cost, response time to individual satellite problems (since all operations are conducted at the same control centre), and simplification of tracking error assessment (one antenna means there is no need for calibration between separate tracking systems and provides identical bias errors, meaning that the relative orbit between cluster members is more accurately known) when compared with the multi-satellite cluster at 19°W.

3.3 : Discussions

From the papers reviewed several general comments on colocation can be made.

All the papers agree that a co-ordinated control strategy is needed for colocation. For two satellite clusters the MLS scheme is preferred for its simplicity and depending on the size of the window, asynchronous station keeping provides a more evenly distributed ground station workload. For larger clusters however the EIS strategy is preferred, commonly in the parallel configuration although EIS circular has the advantage of constant look angles between satellites which could be important for SST systems (synchronous station keeping also seems to be required for this). Since EIS uses more of the available window than MLS (latitude and radial distance in addition to longitudinal) the efficiency of the strategy increases along with the number of satellites.
The need for realistic orbit modelling including control errors to assess cluster design concepts is also recognised. The 'gas' molecule model of relative positions proposed by Fusco & Buratti [6] appears to be unsatisfactory.

Concerning SST the consensus of option is less clear. Blumer [13] demonstrates that such a system is feasible via extensive simulation, however Murdoch [9] suggests more cost effective ways of controlling a cluster are possible and SST should be given a low

research priority. From an operational point of view the topic appears problematic with several major disadvantages,

1. For operators such as SES who purchase, 'off the shelf', satellites the increased cost of including non-standard SST hardware (including integration and testing costs) could be considerable.
2. In the case of satellites controlled by multiple agencies the issue of who controls the master satellite is raised.
3. One of the main advantages of colocation is the redundancy offered by multiple platforms which are indistinguishable to the end user and can take over certain key functions in the event of failure of a single satellite (a feature offered by the ASTRA cluster). Using a master-slave SST configuration a single point failure exists at the master satellite, removing this advantage.
4. The inclusion of non-suitable satellites into a master-slave cluster could be difficult. As GEO becomes more crowded control schemes for new satellites will be restricted by the limitations of existing satellites in the window which probably do not possess the required SST hardware. A possible solution exists in Carlini & Graziani [5] in the proposed sub-division of the window in longitude, eccentricity and inclination. This however leads to non-optimal use of the available space.

Logistically there are two forms of satellite clusters, those controlled by a single agency and those controlled by multiple agencies. The example of 19°W given in section 3.2.4 illustrates the main operational disadvantages of the latter, particularly when the failure of OLYMPUS caused an incursion into the TDF1/2 window at 19.1°W. In the event no collision occurred however the breakdown in communications during an important incident is worrying for the future of multiple agency colocation.

The example of single agency control at 19°E illustrates the main advantages of colocation, specifically modular growth, increased redundancy and 'smooth' end-of-life transitions. Multiple agency control of clusters however is likely to become the most common form of colocation (due to the ITU window allocations) unless agreements between operators allow one control centre to monitor one cluster, which seems

unlikely. Since the industry is relatively inexperienced in the area of co-operation between control centres control of multiple agency clusters should improve.

4 : ORBIT PROPAGATION

4.1: Introduction

4.1.1 : Overview

Orbit propagation is the art of estimating the future orbit of a satellite based on what is known of the current orbit. The orbits of interest for GEO colocation are Earth centred, with low eccentricity and inclination and this chapter deals specifically with this type. Some of the analysis presented is valid for other orbits, however this should not be assumed unless stated in the text.

For applications requiring limited accuracy over short time periods a Newtonian conic section can be used to calculate an approximate orbit. The method treats both the satellite and The Earth as point gravitational sources, ignores other perturbations, and results in equation that can be solved analytically. There is significant literature devoted to this and the subject will not be covered in depth, for more information the reader is directed to references Pocha [29], Soop [31], Wertz et al [35], and Bate et al [33].

In the case of GEO satellites the orbit must usually be controlled within very tight limits (e.g. typically, the longitude must not exceed ±0.1° about some nominal value) and this necessitates a more accurate method of orbit prediction which takes account of perturbation sources such as The Moon, The Sun and the non-spherical nature of The Earth. The methods involved in computing an orbit this way can be quite complex and invariably produce non-analytical solutions that must be solved numerically by computer simulation. It is this subject that will be addressed here.

4.1.2 : Need for Propagation Program

The astrodynamics of colocation can be simplified by assuming that the clustered satellites experience the same perturbation forces, leading to analytical equations for the motion of the cluster relative to some reference point (Hill's equations). If this technique is used in a *Monte Carlo* simulation using mathematical models of position, velocity and thruster burn errors to initiate the relative orbits and the simulation is reset at the

end of the propagation period then useful results for colocation using different control strategies can be obtained (e.g. Hardacre [21]).

Although this method results in simple equations which are easy to visualise and implement in software the technique suffers from the limitations of the mathematical approximations and as a consequence, there is a loss in accuracy as the inter-satellite distances and the propagation period increase. Successful control schemes under this technique are not therefore guaranteed to work as well as might be expected in practice.

To assess the usability of such control schemes an orbit propagation program, capable of computing absolute orbits (relative to the Earth), is therefore desirable.

Later in this document relative motion equations will be used to compute close approach avoidance and cluster geometry recovery manoeuvres which can be incorporated into the propagator to access their viability.

4.1.3 : Propagation Program Validation

'Show me a program with more than ten lines of
code and I'll show you a program with a bug in it.'
Anonymous

For any piece of software of reasonable complexity debugging is a vital part of the programming process to ensure that the software is producing reasonable results. In the case of the orbit propagator this is doubly important since it forms the test-bed on which various colocation station keeping and maintenance schemes will be tried.

For the validation process the propagator results have been compared both with simplified analytical models of the orbit and data obtained from a second, independent, orbit propagator. The 'tests' performed are outlined below.

- Five comparisons were performed in which a simulated orbit was compared with an analytical, general perturbation, solution. The first test included no perturbation effects (allowing the basic integration scheme to be examined) and the remaining four included effects from individual perturbation sources (allowing each perturbation model to be examined in isolation).
- After completing the analytical comparisons the propagator output was compared with similar data from an ESA orbit propagator.

The analytical comparisons are primarily useful for software debugging since by disabling all but one perturbation (or for the first test, all the perturbations) the segment of code in which a particular error lies can be localised. Additionally, unlike comparisons with the second propagator in which the limitations of the comparison data are not known, deviations from the analytical solutions should all be accountable for.

The details of the propagator validation process are included in appendix B.

4.1.4 : Time

In most situation, and for most applications the concept of time is taken for granted. However in astrodynamics small effects, such as the non-uniform rotational rate of the Earth about its axis, cause problems with certain definitions. Of the many definitions of time most will not be mentioned here, for a detailed discussion of the concept as used in astronomy see Green [23], a fair introduction to some of the problems with time can also be found in Buglia [38].

The basis of civilian time it the rotation of the Earth. The most popular definition is *universal time* (UT) and relates to the motion of the Sun as observed from the Greenwich meridian, however since the Earth does not revolve uniformly UT is not strictly uniform either. Astrodynamics needs a system of time that is uniform, and for this reason the concept of *dynamic time* (TDT) was introduced in 1984 (prior to this *ephemeris time* (ET) which is slightly different was used). TDT is based on the atomic clock and the primary unit is the SI second, defined as the duration of 9192631770

periods of the radiation corresponding to the transition between two hyperfine levels of the ground state of the caesium 133 atom. In most cases the difference between time systems can be ignored and TDT = UT = ET.

In this chapter the difference between TDT and UT has been ignored. In terms of calculating the position of the Sun and Moon from the Julian date (which is based on UT) this will result in positional errors. As an indicator to the effect of this by the year 2000 the difference between TDT and UT is expected to be between 60 and 70 seconds.

In the remainder of this chapter periodic reference will be made to UT in relation to calculating certain time dependant variables empirically. It is important to note that the value actually used in the calculations is TDT which, as stated, is an approximation.

4.1.5 : Chapter Summary

The first section after this introduction details methods used to propagate perturbed orbits and explains how the method selected for the propagator was chosen. Next numerical integration methods are considered, both single and multi-step, and again a strategy is selected. The problem of perturbation modelling is then discussed and equations are presented to model the four main sources affecting GEO satellites, namely Earth harmonics, Solar gravitation, Solar pressure and Lunar gravitation. Finally, the software implementation of the selected approach is discussed and a summary of the user inputs required and calculation order followed, detailed.

4.2 : Perturbation Methods

4.2.1 : Fundamentals

'An unperturbed existence leads to dullness of spirit and mind'

Quoted from Bate et al [33]

A perturbation is a deviation from some desired or predicted motion. In astrodynamical terms this can be applied to say a perturbation is something that causes an orbit to deviate from the motion predicted by Newton's inverse square law. There are two types of perturbation sources, those which are natural - for example the non-spherical effects of the Earth, and those which are man-made - specifically those from controlled manoeuvres for purposes such as station keeping (covered in chapter 5).

In dealing with perturbations there are two categories of method, *special perturbations* and *general perturbations*. All numerical methods fall into the first category which employs direct numerical integration of the equations of motion to propagate the orbit. In this category the three mostly commonly used methods will be discussed for use in the orbit propagator and one will be selected. The second category deals with the analytical integration of series expansions which represent each orbital element. This category is more complicated, however it can lead to a better understanding of the perturbed orbit. Although not used for the orbit propagator a general perturbation technique (as already noted) has been employed during the validation procedure, in this case integrating differential expressions for the equinoctial elements (defined in appendix A and discussed later in this chapter) to represent the approximate perturbed orbit. Details of this are included in appendix B.

4.2.2 : Solution Methods

The relative motion of two bodies when acted on by perturbing accelerations can be written as,

$$\frac{d^2\underline{r}}{dt^2} + \frac{\mu_E}{r^3}\underline{r} = \underline{a_d} \tag{4.1}$$

Providing the perturbation terms on the right hand side of the equation can be calculated this results in six unknowns (three positional, three velocity) in six differential equations which can be found by numerical integration to fully specify the orbit at any particular time.

Alternatively these unknowns can be written in terms of six other variables (e.g. the *classical element set*). Re-arranging equation (4.1) then leads to a second set of six first order differential equations that when integrated, either analytically or numerically, make it easier to visualise the orbit.

A second option is to rewrite the equation into the summation of the 'best fit' Newtonian approximation to the starting conditions and some much smaller, deviation terms. Rearranging the equations this time leads to six differential equations in the deviation elements which can again be integrated and added to the analytical solution to the 'best fit' Newtonian orbit to find the actual orbit.

The advantage of the alternative methods is that unlike absolute position and velocity the new elements can be chosen to vary much less with time, thus increasing the acceptable time step used in numerical integration, decreasing the accumulation of round-off errors and shortening the computation time for a given propagation period.

The three methods outlined are known as *Cowell's method*, *the variation of parameters*, and *Encke's method* respectively. These will now be discussed individually in more detail.

4.2.3 : Cowell's Method

For *Cowell's method* the equations of motion of a satellite are integrated directly. The six variables required by equation (4.1) are composed of three positional components and three velocity components. Usually the method is applied in a rectangular co-ordinate frame and for geocentric inertial co-ordinates the resulting six first order differential equations to be solved are,

$$\begin{aligned} \dot{X} &= V_X \\ \dot{Y} &= V_Y \\ \dot{Z} &= V_Z \\ \dot{V}_X &= a_X - (\mu / r^3)X \\ \dot{V}_Y &= a_Y - (\mu / r^3)Y \\ \dot{V}_Z &= a_Z - (\mu / r^3)Z \end{aligned} \tag{4.2}$$

There are two main advantages of Cowell's method, its conceptual simplicity (excluding the equations for the perturbing accelerations equations (4.2) are easily implemented) and the fact that it can successfully deal with all types of conic section orbits (circular, elliptical, parabolic and hyperbolic).

The main disadvantage of the method is its requirement for small step intervals during numerical integration which necessitates a longer period to propagate the orbit than the other methods discussed. This is a result of the position and velocity elements being a function of the total acceleration acting on the satellite, causing them to vary quickly when near a large gravitational body such as the Earth. Some improvement to the method can be made if a polar axis frame is used in place of the Cartesian. In such a frame "r" varies much slower than Cartesian position and velocity, reducing the problem somewhat.

In addition by increasing the number of steps the accumulation of round-off errors also increases and the propagated orbit becomes unreliable much more quickly.

4.2.4 : Encke's Method

For *Encke's method* the position vector of a satellite is written as:

$$\underline{r} = \underline{r}_{osc} + \underline{\delta} \tag{4.3}$$

where $\underline{r}_{osc}$ is the position vector of an unperturbed Newtonian orbit, commonly referred to as the osculating orbit. Initially at some time t_{init} the true orbit and osculating orbit are identical. As time progresses the difference between $\underline{r}$ and $\underline{r}_{osc}$ increases due to perturbation accelerations. The geometry is illustrated in figure 4.1 below.

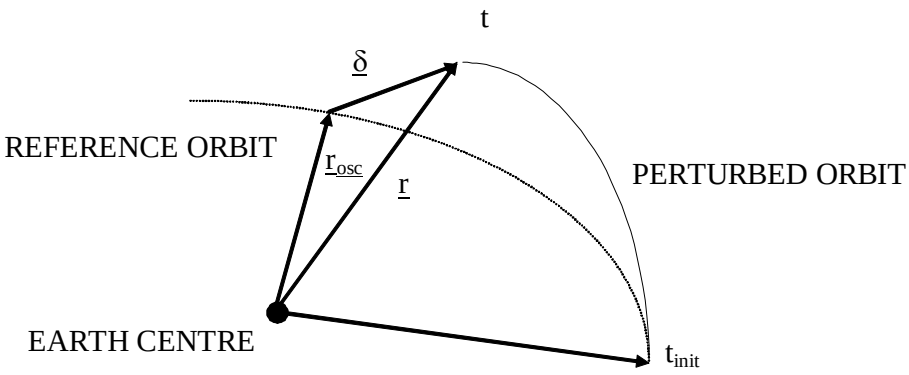

Figure 4.1 : Deviation of Perturbed Orbit from Osculating Orbit

Substituting equation (4.3) into equation (4.1) and re-arranging gives,

$$\frac{d^2\underline{\delta}}{dt^2} + \frac{\mu}{r_{osc}^3}\underline{\delta} = -\frac{\mu}{r_{osc}^3} f(q)\underline{r} + \underline{a}_d \tag{4.4}$$

where, $f(q) = q.\dfrac{3 + 3q + q^2}{1 + (1+q)^{3/2}}$ and, $q = \dfrac{\underline{\delta} \cdot (\underline{\delta} - 2\underline{r})}{\underline{r} \cdot \underline{r}}$

Integration of equation (4.4) results in the deviation vector $\underline{\delta}$ of the actual orbit from the osculating orbit. Since the osculating orbit can be computed analytically the actual orbit can now be evaluated via equation (4.3).

The advantage of Encke's method lies in the fact that the deviation vector changes much slower than the position vector of the satellite and its derivatives, allowing larger step intervals to be used during integration than in Cowell's method. This in turn reduces the computational load.

The main disadvantage of the method lies in its complexity. As $(t-t_{init})$ increases the actual and osculating orbits diverge, necessitating the periodic rectification of the osculating orbit so that it again coincides with the actual orbit. In programming terms Encke's method is difficult to implement, requiring the integration procedure to be interrupted periodically whilst a new oscillating orbit is calculated, adding to the complexity of the program and making it much more likely to contain bugs.

4.2.5 : The Variation of Parameters Method

The *Variation of parameters method* may be thought of as a form of Encke's method in which rectification of the osculating orbit is performed continuously rather than at discrete and separate instants of time.

The original position and velocity vectors of the satellite motion are transformed to a set of six orbital elements via Lagrange's matrix (for details see reference Battin [34]). Through careful selection of these elements the resulting equations will have the same advantages as Encke's method without the need for periodically computing a new reference orbit.

A popular choice of orbital elements are the *classical elements* [f, e, i, M, ω, Ω], how these relate to the orbit geometry is illustrated in figure 4.2.

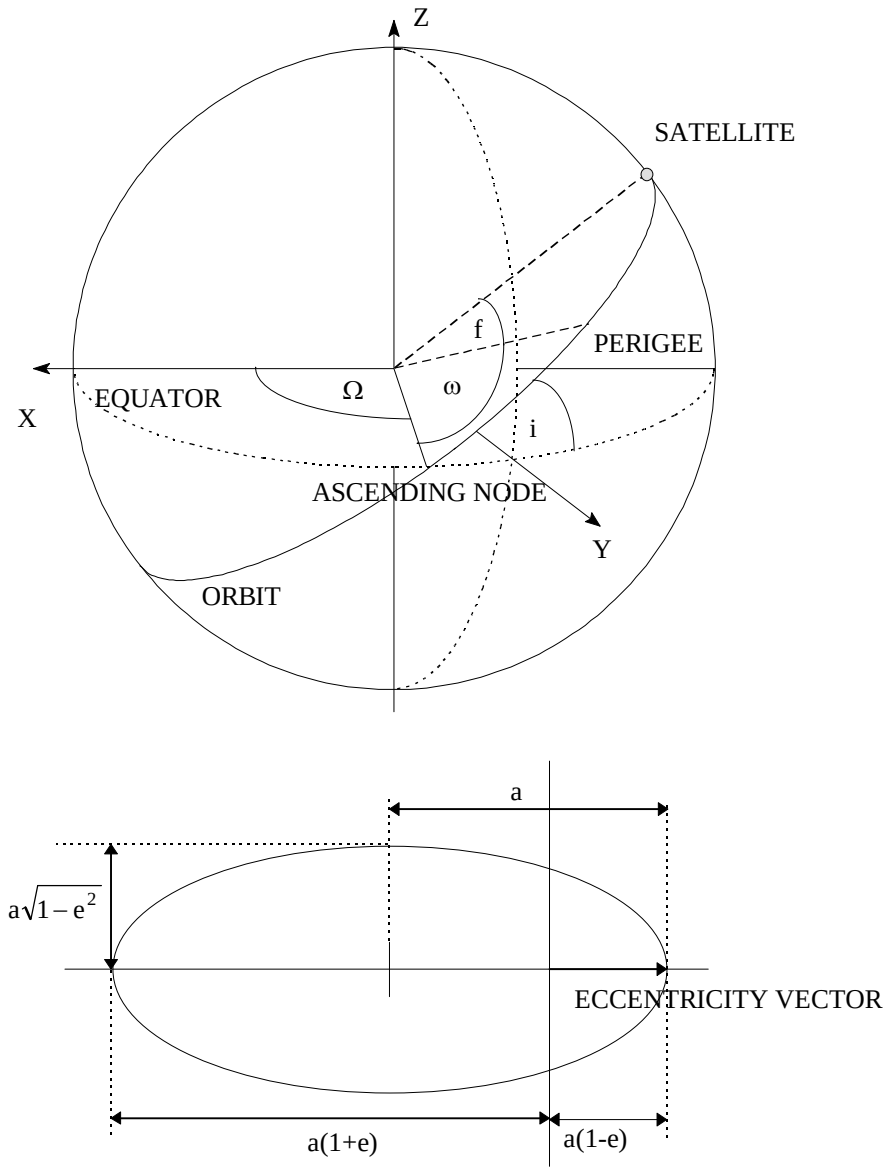

Figure 4.2 : The Classical Elements

The corresponding six differential equations, correspond to the perturbed orbit, can be found by solving Lagrange's planetary equations and are given below without proof (a full treatment is given in Battin [34]).

$$
\begin{aligned}
\frac{da}{dt} &= \frac{2a^2}{h}\left[eSin(f)a_{x_1} + \frac{p}{r}a_{y_1}\right] \\
\frac{de}{dt} &= \frac{1}{h}\left[pSin(f)a_{x_1} + \left((p+r)Cos(f) + re\right)a_{y_1}\right] \\
\frac{di}{dt} &= \frac{rCos(\omega + f)}{h}a_{z_1} \\
\frac{d\omega}{dt} &= \frac{1}{he}\left[-pCos(f)a_{x_1} + (p+r)Sin(f)a_{y_1}\right] - \frac{rSin(\omega + f)Cos(i)}{hSin(i)}a_{z_1} \\
\frac{d\Omega}{dt} &= \frac{rSin(\omega + f)}{hSin(i)}a_{z_1} \\
\frac{dM}{dt} &= n - \frac{b}{ahe}\left[\left(pCos(f) - 2re\right)a_{x_1} - (p+r)Sin(f)a_{y_1}\right]
\end{aligned}
\tag{4.5}
$$

where : $p = a\left(1 - e^2\right)$; $b = a\sqrt{1 - e^2}$;

and the perturbation acceleration components $\underline{a}_d = \left[a_{x_1}, a_{y_1}, a_{z_1}\right]^T$ are in orbital axes (see appendix A for definition).

As part of the integration process Kepler's equation must be solved to find the eccentric anomaly, E and Gauss' equation then used to find the true anomaly, f . Specifically,

$$
\begin{aligned}
M &= E - eSin(E) \\
Tan\left(\frac{f}{2}\right) &= \sqrt{\frac{1+e}{1-e}}Tan\left(\frac{E}{2}\right)
\end{aligned}
\tag{4.6}
$$

An alternative is to replace the sixth equation for mean anomaly with the equivalent for true anomaly, namely

$$
\frac{df}{dt} = \frac{h}{r^2} + \frac{1}{eh}\left[pCos(f)a_{X_1} - (p+r)Sin(f)a_{Y_1}\right]
$$

This however does not remove the need for equation (4.6) which must then be used in reverse to relate the orbit to some specific time.

Unfortunately in GEO the line of nodes and orbit perigee do not exist, consequently the elements [ω,Ω,f] are undefined causing singularities to occur in equations (4.5). Even in near GEO conditions (e ≈ i ≈ 0) where these elements do exist they change rapidly, negating the advantage of the variation of parameters method over Cowell's method.

A more suitable set of orbital elements is referred to as the *Equinoctial set* (Battin [34]) and can be written in terms of the classical elements as:

$$\begin{aligned} P1 &= e\mathrm{Sin}(\Omega+\omega) \\ P2 &= e\mathrm{Cos}(\Omega+\omega) \\ Q1 &= \tan(i/2)\mathrm{Sin}(\Omega) \\ Q2 &= \tan(i/2)\mathrm{Cos}(\Omega) \\ a &= a \\ l &= (\Omega+\omega)+M \\ L &= (\Omega+\omega)+f \end{aligned} \tag{4.7}$$

Where 'L' is referred to as the true longitude of the satellite and 'l', the mean longitude. The relationship between mean and true longitude is akin to that between mean and true anomaly.

In this element set singularities only occur when the angular momentum of the orbit equals zero or the orbit inclination equals π - neither of which occur in near GEO orbits. The corresponding six perturbed differential equations are quoted below from Battin [34].

$$
\begin{aligned}
\frac{dl}{dt} &= n - \frac{r}{h}\left[\begin{array}{l}\left(\frac{a}{a+b}\left(\frac{p}{r}\right)\left(P1Sin(L)+P2Cos(L)\right)+\frac{2b}{a}\right)a_{X_1} \\ +\frac{a}{a+b}\left(1+\frac{p}{r}\right)\left(P1Cos(L)-P2Sin(L)\right)a_{Y_1}+\left(Q1Cos(L)-Q2Sin(L)\right)a_{Z_1}\end{array}\right] \\
\frac{da}{dt} &= \frac{2a^2}{h}\left[\left(P2Sin(L)-P1Cos(L)\right)a_{x_1}+\left(\frac{p}{r}\right)a_{y_1}\right] \\
\frac{dP1}{dt} &= \frac{r}{h}\left[-\left(\frac{p}{r}\right)Cos(L)a_{x_1}+\left[P1+\left(1+\left(\frac{p}{r}\right)\right)Sin(L)\right]a_{y_1}-P2\left(Q1Cos(L)-Q2Sin(L)\right)a_{z_1}\right] \\
\frac{dP2}{dt} &= \frac{r}{h}\left[\left(\frac{p}{r}\right)Sin(L)a_{x_1}+\left[P2+\left(1+\left(\frac{p}{r}\right)\right)Cos(L)\right]a_{y_1}+P1\left(Q1Cos(L)-Q2Sin(L)\right)a_{z_1}\right] \\
\frac{dQ1}{dt} &= \frac{r}{2h}\left(1+Q1^2+Q2^2\right)Sin(L)a_{z_1} \\
\frac{dQ2}{dt} &= \frac{r}{2h}\left(1+Q1^2+Q2^2\right)Cos(L)a_{z_1}
\end{aligned}
\tag{4.8}
$$

Again an intermediary step is needed to find true longitude from mean longitude. In this case the variable is eccentric longitude, K and the relevant equations are,

$$
\begin{aligned}
l &= K + P1Cos(K) + P2Sin(K) \\
Sin(L) &= \frac{a}{r}\left[\left(1-\frac{a}{a+b}P2^2\right)Sin(K)+\frac{a}{a+b}P1P2Cos(K)-P1\right] \\
Cos(L) &= \frac{a}{r}\left[\left(1-\frac{a}{a+b}P1^2\right)Cos(K)+\frac{a}{a+b}P1P2Sin(K)-P2\right]
\end{aligned}
\tag{4.9}
$$

The first of these must be solved iteratively and both Sin(L) and Cos(L) are required to remove an inverse tangent ambiguity which arises when solving for L in terms of K.

The main advantages of this form of the variation of parameters method are the same as those for Encke's method, however unlike the latter periodic rectification is not required.

The main disadvantage again is complexity, however once the orbital elements have been defined and the resulting six first order differential equations of motion constructed the implementation is much simpler than Encke's method. A second, minor problem, is the physical interpretation of the equinoctial elements, however this is overcome by transforming the results into a more 'usable' element set (such as the classical elements) after propagation.

Bearing in mind the increased speed of orbit propagation when compared to Cowell's method, coupled with less complex implementation than Encke's method, the *variation of parameters method* was selected, using the equinoctial elements, for use in the orbit propagator.

4.3 : Numerical Integration Methods

4.3.1 : Fundamentals

There are many excellent texts of the subject of numerical integration and it is not the purpose of this section to consider the topic in any detail. However, it is useful to illustrate what methods were considered before programming began to help explain how the method used was chosen. Since the selected method is required to integrate a series of first order differential equations only this class of equation will be referred to here.

It is worth noting that for any set of six orbital elements used in orbit propagation all six must be known simultaneously to enable the calculation of the next set of values.

Numerical integration methods can be divided into two main categories; single step and multi-step. For single step methods only the information relating to the last known *mesh point* is required to estimate the next set of values where-as for multi-step methods, information about a series of previous mesh points is required, necessitating a *boot-up* procedure to obtain sufficient information to initially start the multi-step procedure.

In the first category, the Runge-Kutta family of methods are commonly used, and in the second, predictor-corrector techniques (in the case of the variation of parameters, the Adams-Bashford and Adams-Moulton methods are preferred). In each case the accuracy of the method is determined by its 'order', which refers to the number of successive terms in the original Taylor expansion series (upon which all the methods are based) that were retained when the numerical solution was derived (e.g. a fourth order method will include terms upto and including 'm^4' where 'm' is the element being integrated). Of course increasing the accuracy adversely affects the speed and makes the resulting

implementation more complex. Speed, truncation error and stability are all important when considering which technique to use, table 4.1 (Pocha [29]) summarises these parameters for several common fourth order methods. The results can easily be extrapolated to higher order methods also.

METHOD	TRUNCATION ERROR (LOCAL)	SPEED	STABILITY	ERROR ACCUMULATION
Single Step				
Runge-Kutta	t_{step}^{5}	Slow	Stable	Satisfactory
Runge-Kutta-Gill	t_{step}^{5}	Slow	Stable	Satisfactory
Multi-Step				
Milne	t_{step}^{5}	Very fast	Unstable	Poor
Adams-Moulton	t_{step}^{5}	Very fast	Unconditionally stable	Satisfactory

Table 4.1: Fourth Order Method Characteristics

Both categories of numerical integration will now be considered in more detail.

4.3.2 : Single-Step Methods

Single-step methods require more computation at each point in the integration than the equivalent multi-step, however they are much simpler to implement in a computer program, leading to less chance of programming error, clearer code and shorter (theoretically) debugging time. The most commonly used single-step methods belong to the Runge-Kutta family for which 8^{th} order solutions exist (Battin [34]). Under this heading the fourth and fifth order Runge-Kutta methods will be discussed here. The first because it is the most commonly used integration scheme of any type on digital computers and the second, because it is included as the boot-up procedure in the propagator.

Each equation in equations (4.8) can be approximated to,

$$\frac{dy}{dt} = f(t, y) \tag{4.10}$$

Time 't' is not explicitly used in (4.8), however it is used by the propagator to calculate 'l' and then 'L' which is explicitly used. 'y' is the element in question, i.e. one of the equinoctial variables.

The fourth order Runge-Kutta solution for the $(i+1)^{st}$ mesh point, given the i^{th} mesh point value, to (4.10) is,

$$y_{i+1} = y_i + \frac{1}{6}\left(k_1 + 2k_2 + 2k_3 + k_4\right) \tag{4.11}$$

where $[k_1, k_2, k_3, k_4]$ are calculated as,

$$\begin{aligned} k_1 &= t_{step} \times f\left(t_i, y_i\right) \\ k_2 &= t_{step} \times f\left(t_i + \frac{t_{step}}{2}, y_i + \frac{k_1}{2}\right) \\ k_3 &= t_{step} \times f\left(t_i + \frac{t_{step}}{2}, y_i + \frac{k_2}{2}\right) \\ k_4 &= t_{step} \times f\left(t_{i+1}, y_i + k_3\right) \\ t_{step} &= t_{i+1} - t_i \end{aligned} \tag{4.12}$$

The fifth order Runge-Kutta algorithms are,

$$y_{i+1} = y_i + \frac{16}{135}k_1 + \frac{6656}{12825}k_3 + \frac{28561}{56430}k_4 - \frac{9}{50}k_5 + \frac{2}{55}k_6 \tag{4.13}$$

and $[k_1, k_2, k_3, k_4, k_5, k_6]$ are,

$$
\begin{aligned}
k_1 &= t_{step} \times f(t_i, y_i) \\
k_2 &= t_{step} \times f\left(t_i + \frac{t_{step}}{4}, y_i + \frac{k_1}{4} \right) \\
k_3 &= t_{step} \times f\left(t_i + \frac{3t_{step}}{8}, y_i + \frac{3k_1}{32} + \frac{9k_2}{32} \right) \\
k_4 &= t_{step} \times f\left(t_{i+1} + \frac{12t_{step}}{13}, y_i + \frac{1932k_1}{2197} + \frac{7200k_2}{2197} + \frac{7296k_3}{2197} \right) \\
k_5 &= t_{step} \times f\left(t_{i+1} + t_{step}, y_i + \frac{439k_1}{216} - 8k_2 + \frac{3680k_3}{513} - \frac{854k_4}{4104} \right) \\
k_6 &= t_{step} \times f\left(t_{i+1} + \frac{t_{step}}{2}, y_i - \frac{8k_1}{27} + 2k_2 - \frac{3544k_3}{2565} + \frac{1859k_4}{4104} - \frac{11k_5}{40} \right)
\end{aligned}
\tag{4.14}
$$

It is clear that the fifth order equations are much more complex than the fourth. This is one of the problems with numerical integration, as the order of the method increases, to reduce long term errors, so the complexity increases causing a much slower speed of orbit propagation.

4.3.3 : Multi-Step Methods

Historically, multi-step numerical integration was used almost exclusively prior to digital computers since it requires less evaluation at each step point, relying more on the accumulated data from the previous mesh points. With digital computers however single-step methods began to gain favour due to their conceptual simplicity, ease of implementation (no need for an initialisation procedure), and ease with which the step size could be changed. Conversely, multi-step methods are problematic to implement numerically in a digital computer due to their need for an initialisation routine whenever the step size is changed and at the start of the integration. The advantages of multi-step procedures is still speed and a correctly implemented procedure will be much faster than the equivalent single-step technique. For this reason it was decided to use a multi-step method in the orbit propagator.

Multi-step methods can be divided into *explicit* and *implicit* solutions. To apply an implicit method a first estimate is required and this is found from a suitable explicit

solution. The use of both multi-step types in this way is called the *Predictor-Corrector* (PC) method. Although this requires the evaluation of two functions for each element being integrated (one from the explicit predictor and one from the implicit corrector) at each step in the integration process, this can be used advantageously to monitor the acceptability of the current step size via the difference between predictor and corrector outputs, and if necessary, to calculate a more appropriate value - this will be expanded on in the next section.

A PC method in the form of a fifth order Adams-Bashford predictor, Adams-Moulton corrector was selected and will be detailed. In a test using equations (4.8) this technique was found to be around 30% faster than the fifth order RK method when constant step size was used.

The fifth order *Adams-Bashford* explicit method is:

$$y_{i+1}^{p} = y_i + \frac{t_{step}}{720}\left[1901f_i - 2774f_{i-1} + 2616f_{i-2} - 1274f_{i-3} + 251f_{i-4}\right]$$

$$\begin{aligned} f_i &= f\left(y_i, t_i\right) \\ f_{i-1} &= f\left(y_{i-1}, t_{i-1}\right) \\ f_{i-2} &= f\left(y_{i-2}, t_{i-2}\right) \\ f_{i-3} &= f\left(y_{i-3}, t_{i-3}\right) \\ f_{i-4} &= f\left(y_{i-4}, t_{i-4}\right) \end{aligned} \qquad (4.15)$$

where the superscript 'p' stands for predictor. The fifth order *Adams-Moulton* implicit method, which utilises the predictor value of y_{i+1} is,

$$y_{i+1}^{p} = y_i + \frac{t_{step}}{720}\left[251y_{i+1}^{p} + 646f_i - 264f_{i-1} + 106f_{i-2} - 19f_{i-3}\right] \qquad (4.16)$$

Comparison between equations (4.13), (4.14) and (4.15), (4.16) shows that the 5^{th} order RK routine requires five evaluations of f(y, t) at each step, whereas only one new value

is required in the 5^{th} order PC. It is this computational reduction which makes multi-step methods less time consuming in operation than single-step methods.

4.3.4 : Active Step Size Control

One of the problems with numerical integration is selecting the correct step size. This is a trade-off between truncation errors (in the case of 5^{th} order methods the local truncation error is proportional to t_{step}^{6}) and propagation speed requirements.

To address this for best performance, it is important to monitor and control the step size during integration. In the case of single-step methods such as the Runge-Kutta procedure the next higher order RK method (i.e. 6^{th} order if the integration is 5^{th} order) is used to estimate the local truncation error. Defining the actual error and the error tolerance as ε and ε_{max} respectively then,

$$\begin{aligned} \varepsilon &= \left| y_{i+1}^{c} - y_{i+1}^{p} \right| \\ \varepsilon_{max} &> \varepsilon \end{aligned} \tag{4.17}$$

where the lower order method gives the $y_{i+1}{}^{p}$ value and the higher order, the $y_{i+1}{}^{c}$ value. If this equation is not satisfied then the step is changed to,

$$t_{step} = t_{step} \left(\frac{\varepsilon t_{step}}{2\left| y_{i+1}^{c} - y_{i+1}^{p} \right|} \right)^{\frac{1}{4}}$$

which is quoted from Pocha [29].

In the case of multi-step methods the procedure is slightly different. Since we already have two estimates for the next mesh point from the predictor and corrector outputs, extra complexity is not needed and we can calculate the approximate local error directly from these. Again this estimate is given by (4.17), in this case 'p' stands for predictor and 'c', corrector. Calculating,

$$\sigma = \frac{\left| y^{c}_{i+1} - y^{p}_{i+1} \right|}{10 t_{step}} \tag{4.18}$$

The inequality to be satisfied to retain the current step value, from Pocha [29] is

$$\frac{\varepsilon}{10} < \sigma < \varepsilon \tag{4.19}$$

If this is not satisfied then the step is changed to,

$$t_{init} = t_{init} \left(\frac{\varepsilon}{2\sigma} \right)^{1/4} \tag{4.20}$$

Each time a step change occurs the slower Runge-Kutta procedure is required for the following several steps to provide enough information to re-initialise the PC (in the case of the selected method four such steps are needed). Because of this, equations (4.19) to (4.20) can be modified for the specific task to minimise the number of step size changes, in practice (for a given error tolerance) this means more time is spent using a slightly larger that absolutely required step interval to avoid having to use the RK more frequently.

It is worth noting that the step control algorithms can increase the step size as well as decrease it, again this affects propagation speed.

4.4 : Perturbation Acceleration Models

4.4.1 : Fundamentals

To accurately model any satellite orbit is it important to include effects due to the dominant perturbation sources. Without this an orbit propagator will generate a static orbit which will soon cease to be representative of the actual motion followed. In the specific case of GEO satellites an accurate position must be known to enabled the satellite to be controlled within what are usually fairly tight limits.

The perturbation acceleration components present in equations (4.8) are the summation of several, independent effects. For Earth satellites in general the main perturbation sources to consider are,

- The non-spherical nature of the Earth.
- Solar gravity effects.
- Solar pressure effects.
- Lunar gravity effects.
- Aerodynamic drag.
- Satellite manoeuvres.

In this section the first four will be modelled in detail. The fifth, aerodynamic drag, is not a significant factor at GEO altitudes. The sixth effect, satellite manoeuvres, is the only man-made source and will be dealt with in other chapters.

4.4.2 : The Non-Spherical Earth

The Earth is not the point gravitational source assumed in Newtonian orbit theory, instead both its shape and mass distribution lead to non-inverse square law effects on an orbiting satellite. An accurate model of the Earth can be obtained through the use of a series of spherical harmonics which effectively represent a gravitational body as a series of mass centres, some more dominant than others - the most dominant term being that of a perfectly uniform, sphere.

In terms of the gravitational potential of The Earth this can be written as,

$$\begin{aligned} V_E(r,\lambda,\phi) &= -\mu \sum_{n=0}^{\infty}\left(\frac{R_e{}^n}{r^{n+1}}\right)\sum_{m=0}^{n}\left(C_{nm}\mathrm{Cos}(m\lambda)+S_{nm}\mathrm{Sin}(m\lambda)\right)P_{nm}(\mathrm{Sin}(\phi)) \\ &= -\mu \sum_{n=0}^{\infty}\left(\frac{R_e{}^n}{r^{n+1}}\right)\sum_{m=0}^{n} J_{nm}\mathrm{Cos}(m(\lambda-\lambda_{nm}))P_{nm}(\mathrm{Sin}(\phi)) \end{aligned} \tag{4.21}$$

where $P_{nm}(\ )$ are the associated Legendre polynomials given below.

$$\begin{aligned} P_n(x) &= \frac{1}{2^n n!}\frac{d^n}{dx^n}\left[(x^2-1)^n\right] \qquad -1 \le x \le 1 \\ P_n{}^m(x) &= (1-x^2)^{m/2}\frac{d^m}{dx^m}\left[P_n(x)\right] \qquad -1 \le x \le 1\ ;\ m \le n \end{aligned} \tag{4.22}$$

The various types of harmonics resulting from (4.22) are illustrated in figure 4.3

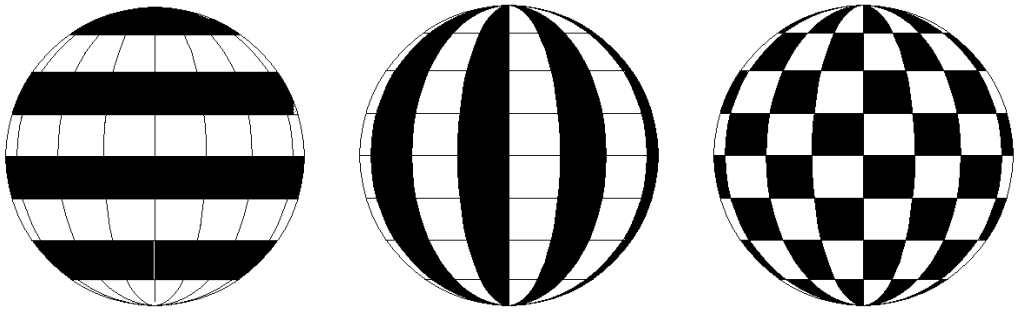

ZONAL P_{n0} SECTORIAL P_{nn} $(n \neq 0)$ TESSERAL P_{nm} $(n \neq m \neq 0)$

Figure 4.3 : Various Types of Harmonic Coefficients. White -Elevation Above; Black -Elevation Below Mean Spherical Surface

Consider now the components of (4.21). The n=0 term is the inverse square law component and if the origin of the co-ordinate system is the centre of gravity of the Earth then J_{10} and J_{11} equal zero. Using this information equation (4.21) can be rewritten as,

$$V_E = -\frac{\mu}{r}\left[1+\sum_{n=2}^{\infty}\left(\frac{R_e}{r}\right)^n J_{n0}P_n(\mathrm{Sin}(\phi)) + \sum_{n=2}^{\infty}\sum_{m=1}^{n}\left(\frac{R_e}{r}\right)^n P_n{}^m(\mathrm{Sin}(\phi))J_{nm}\mathrm{Cos}(m(\lambda-\lambda_{nm}))\right] \tag{4.23}$$

The perturbation accelerations along radial, longitudinal, and latitudinal axes (defined in appendix A) can now be found from the perturbing potential as:

$$a_{x_2} = \frac{\partial V_E}{\partial r} \quad ; \quad a_{y_2} = \frac{1}{r\mathrm{Cos}(\phi)} \frac{\partial V_E}{\partial \lambda} \quad ; \quad a_{z_2} = \frac{1}{r} \frac{\partial V_E}{\partial \phi} \tag{4.24}$$

The higher order the harmonic, the smaller the effect it produces. Restricting the final equations up to the fourth order harmonics provides reasonable accuracy and these equations are listed below in full.

The perturbing acceleration radially outwards due to the non-spherical Earth is,

$$\begin{aligned}
a_{x_2} = {} & \frac{3\mu_E Re^2}{r^4}\left(\frac{1}{2}J_{20}\left(3\mathrm{Sin}^2(\phi)-1\right)+3J_{22}\mathrm{Cos}^2(\phi)\mathrm{Cos}\left(2\left(\lambda-\lambda_{22}\right)\right)\right) \\
& + \frac{2\mu_E Re^3}{r^5}\left(J_{30}\left(5\mathrm{Sin}^2(\phi)-3\right)\mathrm{Sin}(\phi)+3J_{31}\left(5\mathrm{Sin}^2(\phi)-1\right)\mathrm{Cos}(\phi)\mathrm{Cos}\left(\lambda-\lambda_{31}\right)\right) \\
& + \frac{60\mu_E Re^3}{r^5}\left(J_{32}\mathrm{Cos}^2(\phi)\mathrm{Sin}(\phi)\mathrm{Cos}\left(2\left(\lambda-\lambda_{32}\right)\right)+J_{33}\mathrm{Cos}^3(\phi)\mathrm{Cos}\left(2\left(\lambda-\lambda_{33}\right)\right)\right) \\
& + \frac{5\mu_E Re^4}{4r^6}\left(\frac{J_{40}}{2}\left(35\mathrm{Sin}^4(\phi)-30\mathrm{Sin}^2(\phi)+3\right)+5J_{41}\left(7\mathrm{Sin}^2(\phi)-3\right)\mathrm{Sin}(2\phi)\mathrm{Cos}\left(\lambda-\lambda_{41}\right)\right) \\
& + \frac{75\mu_E Re^4}{2r^6}J_{42}\left(7\mathrm{Sin}^2(\phi)-1\right)\mathrm{Cos}^2(\phi)\mathrm{Cos}\left(2\left(\lambda-\lambda_{42}\right)\right) \\
& + \frac{525\mu_E Re^4}{r^6}\left(J_{43}\mathrm{Cos}^3(\phi)\mathrm{Sin}(\phi)\mathrm{Cos}\left(3\left(\lambda-\lambda_{43}\right)\right)+J_{44}\mathrm{Cos}^4(\phi)\mathrm{Cos}\left(4\left(\lambda-\lambda_{44}\right)\right)\right)
\end{aligned} \tag{4.25}$$

The perturbation acceleration longitudinally is,

$$
\begin{aligned}
a_{y_2} &= \frac{3\mu_E R_e^2}{r^4}\left(2J_{22}\,\mathrm{Cos}(\phi)\mathrm{Sin}\left(2\left(\lambda-\lambda_{22}\right)\right)+\frac{15\mathrm{Re}}{r}J_{33}\,\mathrm{Cos}^2(\phi)\mathrm{Sin}\left(3\left(\lambda-\lambda_{33}\right)\right)\right)\\
&+\frac{3\mu_E R_e^3}{r^5}\left(\frac{J31}{2}\left(5\mathrm{Sin}^2(\phi)-1\right)\mathrm{Sin}\left(\lambda-\lambda_{31}\right)+5J_{32}\,\mathrm{Sin}(2\phi)\mathrm{Sin}\left(2\left(\lambda-\lambda_{32}\right)\right)\right)\\
&+\frac{5\mu_E R_e^4}{r^6}\left(\frac{J_{41}}{2}\left(7\mathrm{Sin}^2(\phi)-3\right)\mathrm{Sin}(\phi)\mathrm{Sin}\left(\lambda-\lambda_{41}\right)+63J_{43}\,\mathrm{Cos}^2(\phi)\mathrm{Sin}(\phi)\mathrm{Sin}\left(3\left(\lambda-\lambda_{43}\right)\right)\right)\\
&+\frac{15\mu_E R_e^4}{r^6}\left(J_{42}\left(7\mathrm{Sin}^2(\phi)-1\right)\mathrm{Cos}(\phi)\mathrm{Sin}\left(2\left(\lambda-\lambda_{42}\right)\right)+28J_{44}\,\mathrm{Cos}^3(\phi)\mathrm{Sin}\left(4\left(\lambda-\lambda_{44}\right)\right)\right)
\end{aligned}
\tag{4.26}
$$

Finally, the perturbing acceleration in the latitudinal direction is,

$$
\begin{aligned}
az_2 &= \frac{3\mu_E R_e^2}{r^4}\left(-\frac{J_{20}}{2}\mathrm{Sin}(2\phi)+J_{22}\,\mathrm{Sin}(2\phi)\mathrm{Cos}\left(2\left(\lambda-\lambda_{22}\right)\right)\right)\\
&+\frac{3\mu_E R_e^3}{2r^5}\left(J_{31}\left(15\mathrm{Sin}^2(\phi)-11\right)\mathrm{Sin}(\phi)\mathrm{Cos}\left(\lambda-\lambda_{31}\right)-J_{30}\left(5\mathrm{Sin}^2(\phi)-1\right)\mathrm{Cos}(\phi)\right)\\
&+\frac{15\mu_E R_e^3}{r^5}\left(J_{32}\left(3\mathrm{Sin}^2(\phi)-1\right)\mathrm{Cos}(\phi)\mathrm{Cos}(2(\lambda-\lambda_{32}))+3J_{33}\,\mathrm{Cos}^2(\phi)\mathrm{Sin}(\phi)\mathrm{Cos}(3(\lambda-\lambda_{33}))\right)\\
&+\frac{5\mu_E R_e^4}{4r^6}\left(J_{42}\left(7\mathrm{Sin}^2(\phi)-4\right)\mathrm{Sin}(2\phi)\mathrm{Cos}(2(\lambda-\lambda_{42}))-J_{40}\left(7\mathrm{Sin}^2(\phi)-3\right)\mathrm{Sin}(2\phi)\right)\\
&+\frac{105\mu_E R_e^4}{r^6}\left(J_{43}\left(4\mathrm{Sin}^2(\phi)-1\right)\mathrm{Cos}^2(\phi)\mathrm{Cos}\left(3\left(\lambda-\lambda_{43}\right)\right)+4J_{44}\,\mathrm{Cos}^3(\phi)\mathrm{Sin}(\phi)\mathrm{Cos}\left(4\left(\lambda-\lambda_{44}\right)\right)\right)\\
&+\frac{5\mu_E R_e^4}{2r^6}J_{41}\left(28\mathrm{Sin}^4(\phi)-27\mathrm{Sin}^2(\phi)+3\right)\mathrm{Cos}\left(\lambda-\lambda_{41}\right)
\end{aligned}
\tag{4.27}
$$

Table 4.2 lists the values for the constants J_{nm} and λ_{nm} as used in the propagation program (Zee [36]).

n	m	J_{nm}	λ_{nm}
2	0	1082.6283×10^{-6}	
2	2	-1.8083×10^{-6}	-14.8949°
3	0	-2.5418×10^{-6}	
3	1	-2.1791×10^{-6}	7.0669°
3	2	-3.8480×10^{-7}	-17.0348°
3	3	-2.2132×10^{-7}	21.3183°
4	0	-1.6086×10^{-6}	
4	1	-6.7614×10^{-7}	220.7042°
4	2	-1.6853×10^{-7}	31.3316°
4	3	-5.9015×10^{-8}	-4.3093°
4	4	-7.3147×10^{-9}	29.5502°

Table 4.2: Earth Spherical Harmonic Constants to Fourth Order

Implementation of the Equations

To utilise equations (4.25) to (4.27) two things are required at each step in the propagation.

1. The polar variables $[r,\lambda,\phi]$ need to be calculated from the equinoctial elements. This is accomplished using the transformations given in appendix A.
2. The perturbation acceleration components need to be transformed into the orbital axis set as defined in appendix A.

The second of these uses a combination of equations (A.3) and (A.15), which are repeated below.

$$\begin{bmatrix} X \\ Y \\ Z \end{bmatrix} = A \begin{bmatrix} x_1 \\ y_1 \\ z_1 \end{bmatrix} \quad ; \quad \begin{bmatrix} X \\ Y \\ Z \end{bmatrix} = B \begin{bmatrix} x_2 \\ y_2 \\ z_2 \end{bmatrix}$$

giving the transformation matrix equation,

$$\begin{bmatrix} x_1 \\ y_1 \\ z_1 \end{bmatrix} = A^T B \begin{bmatrix} x_2 \\ y_2 \\ z_2 \end{bmatrix} \tag{4.28}$$

where A and B are the orthogonal matrices,

$$\begin{aligned} A &= \begin{bmatrix} \mathrm{Cos(L)} + \mathrm{Q1.c1} & -\mathrm{Sin(L)} + \mathrm{Q1.c2} & 2\mathrm{Q1}/\mathrm{q} \\ \mathrm{Sin(L)} - \mathrm{Q2.c1} & \mathrm{Cos(L)} - \mathrm{Q2.c2} & -2\mathrm{Q2}/\mathrm{q} \\ \mathrm{c1} & \mathrm{c2} & (2-\mathrm{q})/\mathrm{q} \end{bmatrix} \\ B &= \begin{bmatrix} \mathrm{Cos}(\alpha)\mathrm{Cos}(\phi) & -\mathrm{Sin}(\alpha) & -\mathrm{Cos}(\alpha)\mathrm{Sin}(\phi) \\ \mathrm{Sin}(\alpha)\mathrm{Cos}(\phi) & \mathrm{Cos}(\alpha) & -\mathrm{Sin}(\alpha)\mathrm{Sin}(\phi) \\ \mathrm{Sin}(\phi) & 0 & \mathrm{Cos}(\phi) \end{bmatrix} \end{aligned} \tag{4.29}$$

and the variables q, c1, c2 are,

$$\begin{aligned} \mathrm{q} &= 1 + \mathrm{Q1}^2 + \mathrm{Q2}^2 \\ \mathrm{c1} &= 2\left(\mathrm{Q2Sin(L)} - \mathrm{Q1Cos(L)}\right)/\mathrm{q} \\ \mathrm{c2} &= 2\left(\mathrm{Q2Cos(L)} + \mathrm{Q1Sin(L)}\right)/\mathrm{q} \end{aligned}$$

Multiplying out (4.29), noting that axis x_1 is identical to axis x_2 gives the overall transformation matrix as,

$$A^T B = \begin{bmatrix} 1 & 0 & 0 \\ 0 & \mathrm{Cos}(\alpha - \mathrm{L}) - \mathrm{c2.c4} & -\left(\mathrm{Sin}(\alpha - \mathrm{L}) + \mathrm{c2.c3}\right)\mathrm{Sin}(\phi) + \mathrm{c2Cos}(\phi) \\ 0 & -2\mathrm{c4}/\mathrm{q} & -\left(2/\mathrm{q}\right)\left(\mathrm{Cos}(\phi) - \mathrm{c3.Sin}(\phi)\right) - \mathrm{Cos}(\phi) \end{bmatrix} \tag{4.30}$$

where the variables c3, c4 are,

$$\begin{aligned} \mathrm{c3} &= \mathrm{Q1Cos}(\alpha) - \mathrm{Q2Sin}(\alpha) \\ \mathrm{c4} &= \mathrm{Q1Sin}(\alpha) + \mathrm{Q2Cos}(\alpha) \end{aligned}$$

At each step in the integration the equinoctial variables are known and so the above equations are used to compute the Earth harmonic perturbing accelerations in orbital axes.

4.4.3 : Solar Gravity Perturbations

The solar gravity perturbations can be modelled as a third body effect in inertial geocentric axes using equation (4.31) which is quoted from Agrawal [37].

$$\underline{a_S} = \frac{\mu_s r}{r_s^3}\left[3\left(\underline{i_r}.\underline{i_s}\right)\underline{i_s} - \underline{i_r}\right] \tag{4.31}$$

The corresponding vector directions are illustrated in figure 4.4.

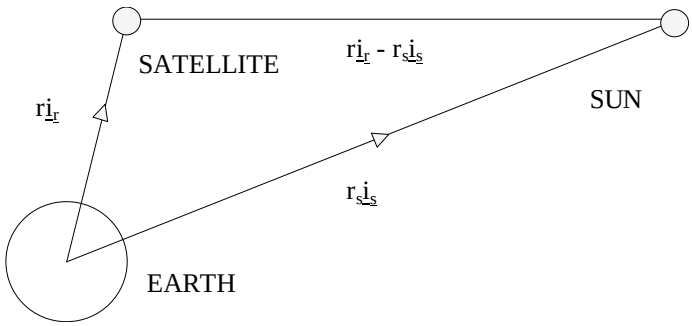

Figure 4.4 : Solar Gravity Geometry

Before using (4.27) the position vectors of the Earth and Sun are required. The first of these is found via equation (A.4) from appendix A and the second, via a series of empirical approximations, quoted below from Meeus [40].

The geometric mean longitude and mean anomaly of the Sun can be found at any epoch approximately as,

$$\begin{aligned} l_S &= 280^o.46645 + 36000^o.76983\mathrm{Tu} + 0^o.0003032\mathrm{Tu}^2 \\ M_S &= 357^o.52910 + 35999^o.05030\mathrm{Tu} - 0^o.0001559\mathrm{Tu}^2 - 0^o.00000048\mathrm{Tu}^3 \end{aligned} \tag{4.32}$$

The equation of centre for Sun is then,

$$\begin{aligned} C = &\left(1^o.9146 - 0^o.004817\mathrm{Tu} - 0^o.000014\mathrm{Tu}^2\right)\mathrm{Sin}\left(M_S\right) \\ &+\left(0^o.019993 - 0^o.000101\mathrm{Tu}\right)\mathrm{Sin}\left(2M_S\right) \\ &+0^o.00029\mathrm{Sin}\left(3M_S\right) \end{aligned} \tag{4.33}$$

The eccentricity of the Earth orbit and the obliquity of the ecliptic (the angle between equator and ecliptic) are,

$$\begin{aligned} e_S &= 0^o.016708617 - 0^o.000042037Tu - 0.0000001236Tu^2 \\ \varepsilon &= 23^o.439291 - 0^o.013004Tu - 1^o.639\times10^{-7}Tu^2 + 5^o.03\times10^{-7}Tu^3 \end{aligned} \tag{4.34}$$

In the above five equations the variable 'Tu' is the number of Julian centuries from the year 2000.0 epoch. It is calculated from the Julian date (JD) as follows.

$$Tu = \frac{JD - 2451545.0}{36525} \tag{4.35}$$

and for dates after 1900,

$$JD = 367Y - \left\langle \frac{7\left(Y + \left\langle \frac{M+9}{12} \right\rangle\right)}{4} \right\rangle + \left\langle \frac{275M}{9} \right\rangle + D + 1721013.5 + \frac{UT}{24}$$

where, Y = year; M = calendar month; D = calendar day; UT = universal time and '$\langle\ \rangle$' means 'the integer part of'.

Equations (4.32) to (4.35) can now be used to find the right ascension and declination of the solar orbit from,

$$\begin{aligned} Tan(\alpha_S) &= \frac{Cos(\varepsilon)Sin(l_S + C)}{Cos(l_S + C)} \\ Sin(\phi_S) &= Sin(\varepsilon)Sin(l_S + C) \end{aligned} \tag{4.36}$$

The ambiguity in the sign of α_s is removed by noting that α_s is in the same quadrant as the Sun's true longitude, (l_S+C). There is no ambiguity in ϕ_S since, -90°< ϕ_S <90°. To complete the polar co-ordinates of The Sun the radial distance r_S is,

$$r_S = \frac{a_S\left(1 - e_S{}^2\right)}{1 + e_S \mathrm{Cos}(M_S + C)} \tag{4.37}$$

The inertial geocentric co-ordinates, as needed for equation (4.31) are now,

$$\underline{i_s} = r_S \begin{bmatrix} \mathrm{Cos}(\phi_S)\mathrm{Cos}(\alpha_S) \\ \mathrm{Cos}(\phi_S)\mathrm{Sin}(\alpha_S) \\ \mathrm{Sin}(\phi_S) \end{bmatrix} \tag{4.38}$$

Comparison of the position of the Sun as calculated using the above method with values from the Astronomical Almanac for 1993 yielded errors of the order ±5 arcseconds.

The transform to orbital axes from geocentric inertial axes is performed using the same method as described for the non-spherical Earth perturbations in section 4.4.2.

4.4.4: Solar Radiation Perturbations

Solar radiation pressure is often ignored as a significant perturbation force, however as satellites become physically larger (due in part to larger power requirements necessitating larger solar panels) the surface area to mass ratio increases and solar radiation quickly ceases to be negligible, particularly for GEO satellites where satellite position must be tightly controlled.

The simplistic model detailed here can be found in Pocha [29] and is based on the following assumptions.

- The satellite area to mass ratio and surface reflectance are constant.
- The satellite is not eclipsed by any object at any point in its orbit.
- There is no interaction with any other perturbation source.

Referring to figure 4.4 the solar radiation perturbation acceleration vector can be written as,

$$\underline{a_{sp}} = a_{sp} \frac{\left(r\underline{i_r} - r_s \underline{i_s}\right)}{\left|r\underline{i_r} - r_s \underline{i_s}\right|} \tag{4.39}$$

where the magnitude a_{sp} is a function of the area to mass ratio of the satellite and its surface reflectance.

$$a_{sp} \approx G\left(\frac{A}{M}\right)\left(\frac{1+R}{2}\right) \tag{4.40}$$

where,

G is the solar radiation pressure constant acting on a perfectly reflecting flat surface = $9.1\times10^{-6}N/m^2$.

R is the surface reflectance (between 0 and 1, a value of 0.6 is average used).

A/M is the satellite area to mass ratio.

Calculating the actual perturbation acceleration in orbital axes is now done identically to the procedure followed for solar gravity.

4.4.5 : Lunar Gravity Perturbations

As in the case of solar gravity the effects of the Moon will be treated as a third body acting on the satellite. Although the mass of the Moon is much lower than that of the Sun the reduced distance between perturbing body and satellite makes the Lunar perturbation about equal to the Solar. Re-writing equation (4.31), replacing the Solar variables by the equivalent Lunar ones,

$$\underline{a_l} = \frac{\mu_l r}{r_l^3}\left[3\left(\underline{i_r}.\underline{i_l}\right)\underline{i_l} - .\underline{i_r}\right] \tag{4.41}$$

The relationships between the vectors used in this equation are illustrated in figure 4.5.

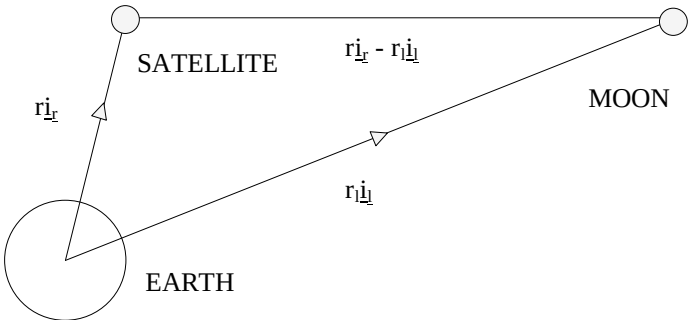

Figure 4.5 : Lunar Gravity Perturbations

Again the biggest problem is calculating the Moon's position at a given point in time. The following are empirical relationships quoted from Meeus [40] to allow this calculation to be made.

Ecliptic longitude of the Moon:

$$\begin{aligned}\lambda_l = {} & 218^o.32 + 481267^o.883Tu \\ & + 6^o.29Sin(134^o.9 + 477198^o.85Tu) + 1^o.27Sin(259^o.2 - 413335^o.38Tu) \\ & + 0^o.66Sin(235^o.7 + 890534^o.23Tu) + 0^o.21Sin(269^o.9 + 954397^o.70Tu) \\ & - 0^o.19Sin(357^o.5 + 35999^o.05Tu) - 0^o.11Sin(186^o.6 + 966404^o.05Tu)\end{aligned} \quad (4.42)$$

Ecliptic latitude of the Moon,

$$\begin{aligned}\phi_l = {} & 5^o.13Sin(93^o.3 + 483202^o03Tu) + 0^o.28Sin(228^o.2 + 960400^o.87Tu) \\ & - 0^o.28Sin(318^o.3 + 6003^o.18Tu) - 0^o.17Sin(217^o.6 - 407332^o.20Tu)\end{aligned} \quad (4.43)$$

Horizontal parallax of Moon,

$$\begin{aligned}h_p = {} & 0^o.9508 \\ & + 0^o.0518Cos(134^o.9 + 477198^o.85Tu) + 0^o.0095Cos(259^o.2 - 413335^o.38Tu) \\ & + 0^o.0078Cos(235^o.7 + 890534^o.23Tu) + 0^o.0028Cos(269^o.9 + 954397^o.70Tu)\end{aligned} \quad (4.44)$$

Radial Distance from centre of Earth,

$$r_l = \frac{6378137}{\mathrm{Sin}\left(h_p\right)} \tag{4.45}$$

The positional vector in geocentric co-ordinates of the Moon can now be calculated as,

$$\underline{r_l} = r_l \begin{bmatrix} \mathrm{Cos}(\phi_l)\mathrm{Cos}(\lambda_l) \\ +0.9175\mathrm{Cos}(\phi_l)\mathrm{Sin}(\lambda_l) - 0.3978\mathrm{Sin}(\phi_l) \\ +0.3978\mathrm{Cos}(\phi_l)\mathrm{Sin}(\lambda_l) + 0.9175\mathrm{Sin}(\phi_l) \end{bmatrix} \tag{4.46}$$

where the accuracy of the variables [λ_l, ϕ_l, r_l] are [0°.3, 0°.2, 0.2 of an Earth radii] respectively. As in the transform to orbital axes performed using the transformation equations given in appendix A.

4.5 : Software Implementation

The operation of the propagation program is summarised in figure 4.6. This diagram is a simplification of the actual program and does not include the error checking routines - which are used to predict and avert program crashes, the axis conversion routines - which is a separate program, and the fine details of the integration loop. A listing of the actual propagator along with the implemented perturbation forces code is included in appendix B.

The diagram includes several internal program variables. Their use is explained below.

element (where element = 1 to 6)

The variable 'element' is used to determine which of the six equinoctial elements is currently being integrated. The assignment is as follows; the variables [L, a, P2, P1, Q1, Q2] are mapped to element = [1, 2, 3, 4, 5, 6] in that order.

te[1 to 6]

The temporary array te[element] is used to store the values of the 'true' equinoctial elements at the beginning of the n^{th} step. During integration the te[ ] variables are used in place of the 'true' variables to allow the latter to be updated to the $(n+1)^{th}$ values as they are calculated without causing a step mis-match.

step

The interval in seconds between successive integration steps.

new_step[1 to 6]

If the difference between the predictor and corrector values exceed the error tolerance a new value for the next time step is calculated. Since this value is specific to the equinoctial variable being integrated the actual step size is not changed until all six elements are calculated, the minimum of these is then used for the following step.

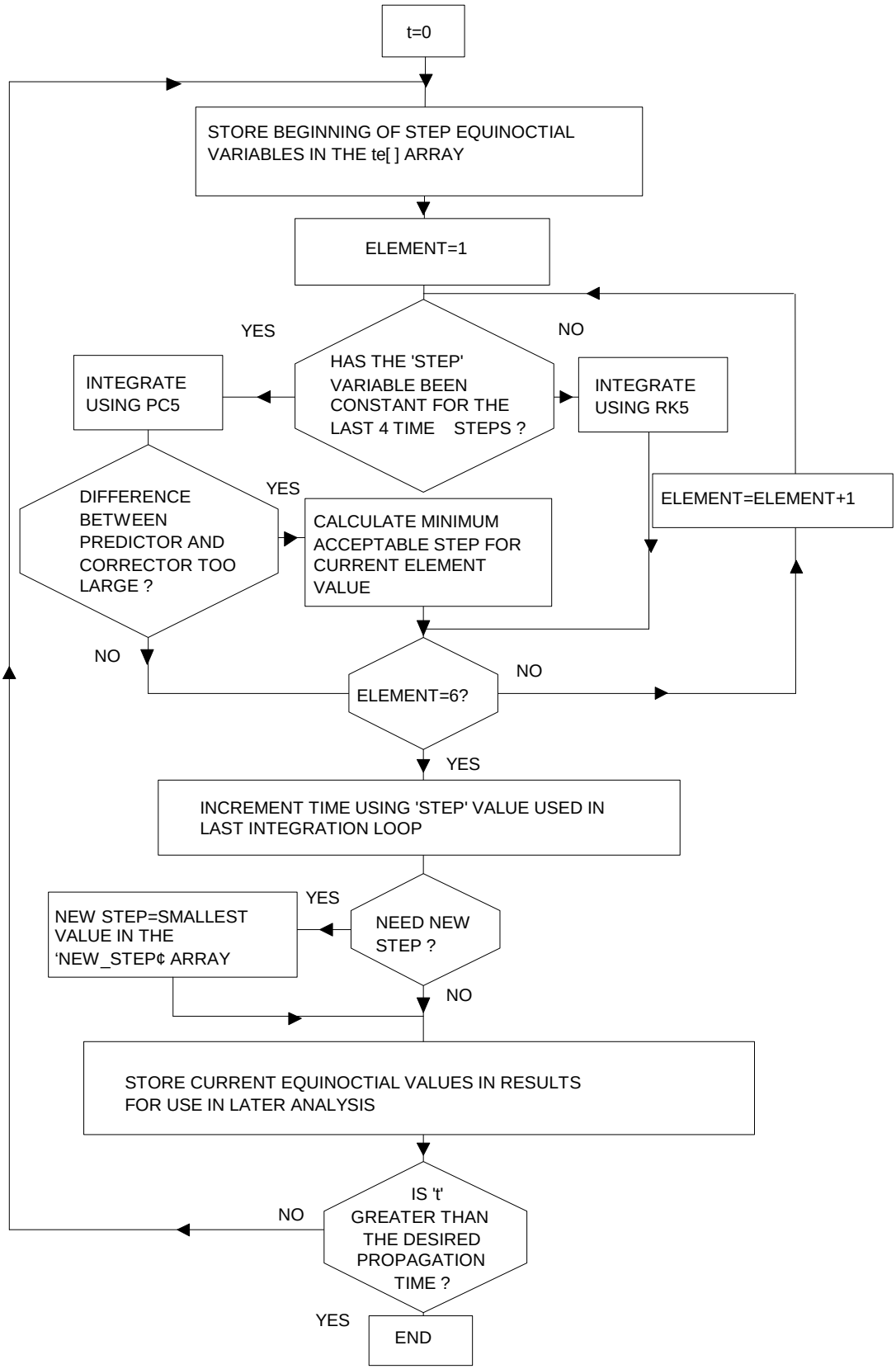

Figure 4.6: Orbit Propagation Flow Chart

To use the basic orbit propagator without enabling the autonomous station keeping option, which optimises certain initial conditions, user inputs are required for the initial orbit and the simulation conditions. These inputs are entered via the launch program (see chapter 1) which stores the values for future use and as a permanent record in an ASCII text file. An example of this file, which illustrates all the inputs required, is listed below *in the format in which it is stored*.

```
============================================================
GLOBAL SIMULATION OPTIONS
============================================================
 1          Number of satellites
 RUN1       Prefix to filenames of result files
 1995             Year
 1          Month
 1          Day
0           Universal Time
1                   Earth Harmonics      (1=enabled ; 0=disabled)
1           Solar Gravity                (1=enabled ; 0=disabled)
 1          Solar Radiation              (1=enabled ; 0=disabled)
1           Lunar Gravity                (1=enabled ; 0=disabled)
 6048000    Propagation time (secs)
300         Step interval (secs)
14400       Record Interval (secs)
============================================================
SATELLITE SPECIFIC OPTIONS
============================================================
SAT #1
==========================================
2.08366565416478    True Longitude (rad), (f+Somega+Bomega)
42166172            Semi-major axis (m)
-0.000451261        P1
-0.000265359        P2
0.000000000         Q1
0.000000000         Q2
500                 Satellite mass
25                  Satellite surface area
0.6                 Satellite surface reflectivity
==========================================
```

Although this file can be edited manually, and the propagation program run independently of the launch program, it is more useful not to do this. Using the launch program, other options can be enabled such as generating results in different axis sets (classical, polar, inertial, and relative are supported) which is not a function of the propagator and examining the results, both in text and graphically formats.

As an example of the entry method in the launch program the following two diagrams illustrate two data entry window, the first in figure 4.7 is the main data entry window for the propagator and the second, in figure 4.8 is the entry window for the [P1, P2]

elements, since these form the x and y components of the eccentricity vector in the eccentricity plane there is a visual element to this window.

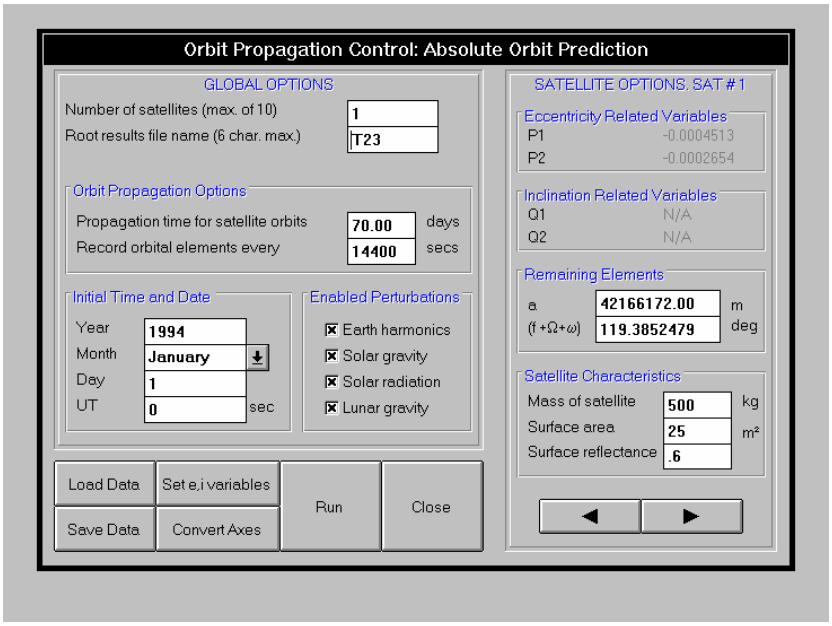

Figure 4.7 : Main Data Entry Window

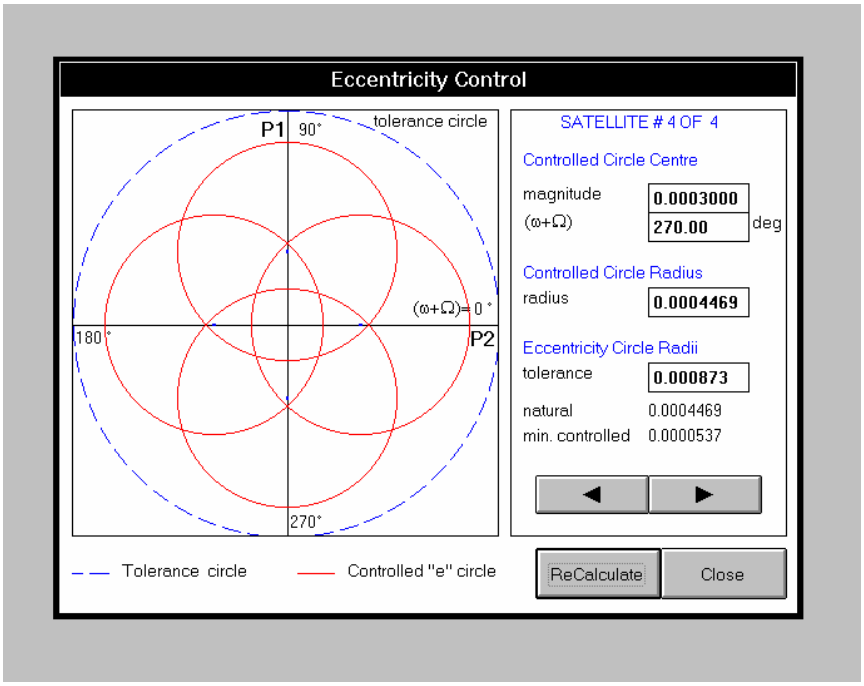

Figure 4.8 : Eccentricity Control Window

5 : STATION KEEPING

5.1 : Introduction

Over time a GEO satellite will drift both in longitude and latitude under the influence of the perturbations discussed in chapter 4. The aim of station keeping is to maintain a satellite within specified limits about some nominal position by the application of corrective burns at specific times. This chapter details a series of procedures that can be followed to ensure this and these procedures in turn have been incorporating into the orbit propagation program to allow autonomous station keeping control.

The control method detailed comprises two tangential (EW) corrective burns and one normal (NS) burn. It is worth noting that other control strategies can be used which in certain situations are preferable, however they are invariably more complicated and would pose problems to automate. For the purpose of developing a reasonable propagation model to examine colocation the method selected is used widely in practice and can be automated reasonably easily.

The remainder of this introduction will cover key points in station keeping, beginning with the definition and regulations concerning the GEO window.

5.1.1 : Corrective Manoeuvres

The orbit corrections required to maintain a satellite within a GEO window can be divided into two categories; those relating to the inplane orbital elements [L, a, P1, P2] and those relating to the motion of the orbit normal [Q1, Q2]. The first category can be dealt with by either radial or tangential burns and since tangential burns are more efficient these are usually used (in fact most GEO satellites lack significant thrusting capability along the radial axis for this reason). Corrections of this sort are referred to as EW burns and will be dealt with in detail in section 5.2.

The second category of burns (which control the inclination of the orbit) are referred to as NS burns and do not take place at the same time as the EW burns, nor is the NS cycle

the same length as the EW cycle (usually the former is longer). This category of corrections will be dealt with in section 5.3.

In both EW and NS station keeping analysis simplified perturbation models are used to estimate the mean motion of the satellite and the corrections required to maintain it within the GEO window. In the case of EW calculations the non-spherical nature of the Earth dominates the mean motion and for NS calculations, the combined effect of the Solar and Lunar gravity. The resulting velocity increments will be applied impulsively.

5.1.2 : Mean Orbital Elements

The station keeping burns will be calculated from the mean motion of the satellite it is thus necessary to extract this from the actual motion by means of some mathematical technique. In this case multiple linear regression can be used to calculate a curve fit for the mean motion between station keeping burns and thus the mean elements just prior to a burn. Details of the method for two and three functions is given in appendix B.1 for the elements of interest.

5.1.3 : Chapter Summary

GEO station keeping is complicated and it is not the intention of this chapter to detail the entire subject from first principles since this information can be found readily from existing literature. Instead the analysis is weighted towards applying the basic theory to the problem of creating an autonomous station keeping module for the orbit propagation program. To do this some basic theory is needed for clarification, and where appropriate this is included, however for a fuller treatment of the subject the reader is directed to references Michielsen et al [28], Pocha [29], Soop [31] and Eckstein [25].

EW and NS station keeping control will now be covered in turn.

5.2 : EW Station Keeping

5.2.1 : Overview

To formulate a suitable EW strategy control of both the mean longitude and the daily longitude libration caused by eccentricity must be performed. As stated in the introduction to this chapter the first of these is due to the non-spherical nature of the Earth. Specifically, the equatorial bulge raises the ideal GEO altitude and the elliptical cross section of the equator causes a slight EW acceleration. These effects can be represented reasonably accurately by the J_{20} and J_{22} harmonics respectively as done later in the text. The mean eccentricity evolution is a result of Solar pressure effects and will be dealt with separately.

This however is not the entire story since all the perturbations affect all the orbital elements to some degree. In the case of eccentricity, EH, SG and LG effects cause short term librations about the mean motion and in the case of semi-major axis, SG, SP and LG do the same. This can be seen from the graphs in appendix B which represent the evolution of the equinoctial elements as affected by each perturbation source individually. What this means in practice is that it is not acceptable merely to apply burns which will change the orbital elements so that they equal the desired mean values for the start of the next cycle. To illustrate this more clearly figure 5.1 shows a fictional element which has a constant mean value with a sinusoid superimposed on it. If the initial value of the element is set to equal the desired mean (represented by the circle on the diagram) this does not result in the desired mean motion being followed.

To ensure the correct mean values of the orbital elements after a station keeping correction the mean values before the correction are used to calculate the size of the required burn which is to be applied to the satellite.

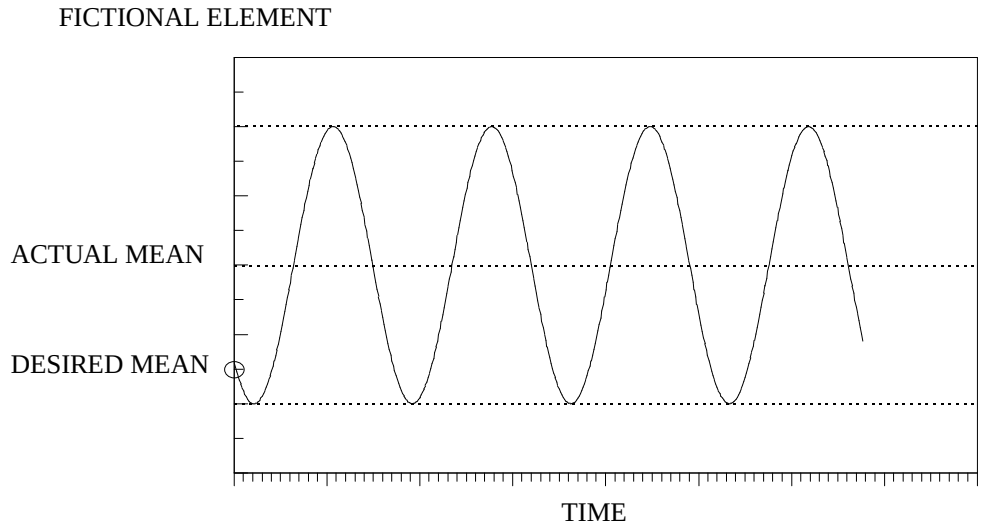

Figure 5.1 : Error in Mean Motion due to Incorrect Calculation

For initialisation at the start of a propagation period the procedure is slightly different. In this case the desired mean values are calculated from the simplified analysis and the orbit is propagated until the end of the current cycle using these as initial values. During this period actual values of the elements are recorded allowing a regression curve fit to be used to find the mean motion. Using this the corrections required at the start of the propagation to ensure the correct mean motion can be found. Finally the propagation proper begins using the corrected element values.

Calculations of the corrections used to control the mean longitude and the eccentricity are covered individually in the next two sections.

5.2.2 : Longitude Control

Two situations must be dealt with in producing a reasonable longitudinal control method.

- Initialisation of the satellite at the beginning of the propagation. For this it will be assumed we have control over all the elements relating to the orbit.
- The corrections applied at the end of each EW cycle. In this case we have a potentially erroneous longitude position (due to both simplification and manoeuvre errors) which cannot be instantaneously corrected.

To analyse these however we first need to examine the effects of the dominant Earth harmonic terms J_{20} and J_{22} on the mean Greenwich longitude.

The Equatorial Bulge (J_{20} Effect)

In near GEO orbits the equatorial bulge of the Earth, represented approximately by the J_{20} harmonic, effectively changes the ideal GEO altitude by changing the orbital period of a satellite at a given altitude. The differential Lagrange equation for mean longitude (see previous chapter) can be used to show this change is approximately equal to,

$$\Delta\dot{\lambda} = \Delta n = -\frac{3J_{20}R_e^{\,2}n}{a^2} \tag{5.1}$$

To correct for this effect the semi-major axis of the satellite must be increased by an amount,

$$\Delta a = -\frac{2a}{3n}\Delta n \tag{5.2}$$

The values of 'a' and 'n' on the R.H.S. of the equation can be approximated to the unperturbed ideal GEO values. Combining (5.1) and (5.2) the correction to 'a' needed to negate the equatorial bulge in terms of J_{20} is,

$$\Delta a_B = \frac{2J_{20}R_e^{\,2}}{a} \tag{5.3}$$

where the subscript 'B' means the correction is due to the equatorial bulge. Substituting numbers into (5.3) gives the offset required as approximately +2085 m. This is independent of longitudinal position and needs only be corrected for once, unlike the 'Δa' requirement due to the J_{22} effect.

Earth Triaxiality (J_{22} Effect)

The cross-section of the Earth at the equator is approximately elliptical. This causes a slight tangential perturbation acceleration on a GEO satellite the magnitude of which changes depending on the longitudinal position as shown in figure 5.2.

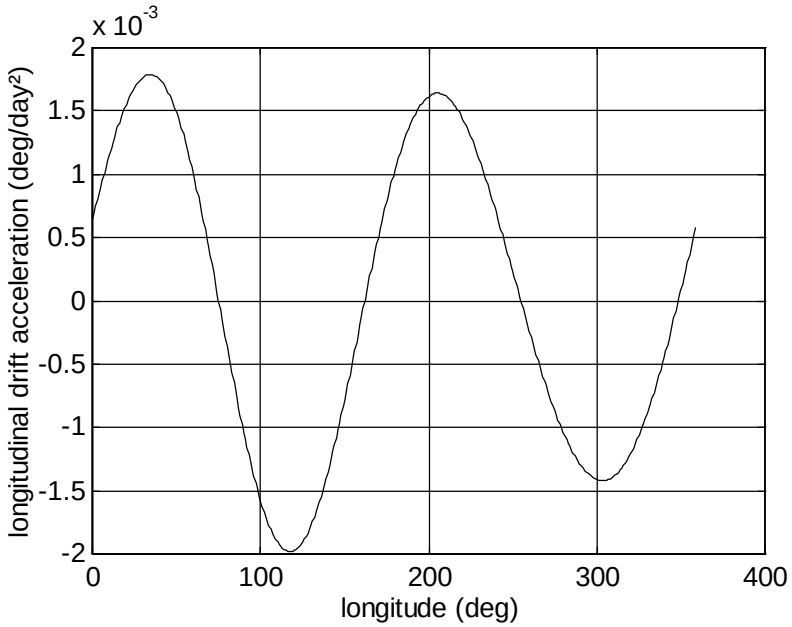

Figure 5.2 : Longitudinal Drift Acceleration Due to Triaxiality

Since the requirements of the EW cycle are such that the longitude change over one cycle is small (a typical deadband is ±0.1°) it is reasonable to approximate the longitudinal acceleration experienced during the cycle to a constant value. With this assumption the corresponding longitudinal motion can be found by integration as,

$$\begin{aligned} \ddot{\lambda} &= \ddot{\lambda}_0 \\ \dot{\lambda} &= \dot{\lambda}_0 + \ddot{\lambda}_0 t \\ \lambda &= \lambda_0 + \dot{\lambda}_0 t + \frac{\ddot{\lambda}_0}{2} t^2 \end{aligned} \tag{5.4}$$

where subscript '0' refers to values at t=0.

This clearly indicates parabolic motion. The optimum configuration therefore to maximise the length of the EW cycle is to arrange the parabola such that the turning

point on the curve occurs halfway through the cycle. For $(d^2\lambda/dt^2)>0$ this is illustrated in figure 5.3.

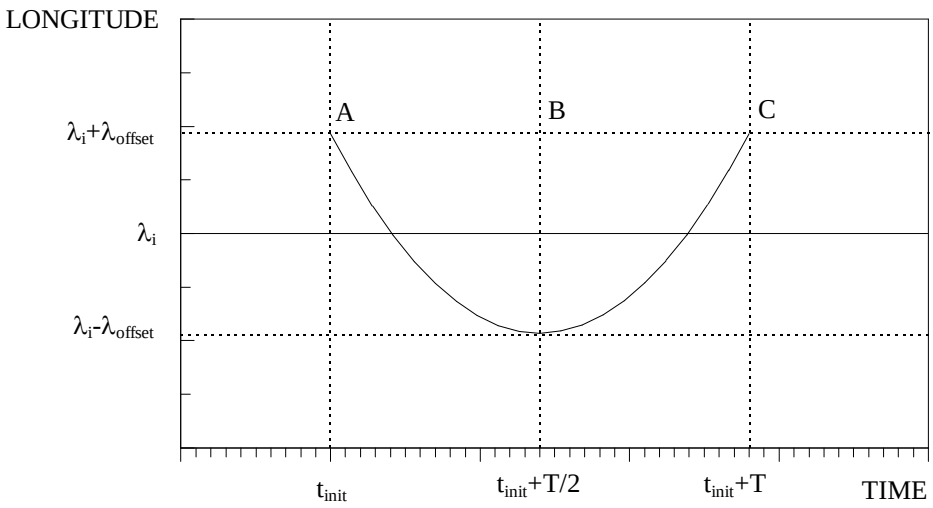

Figure 5.3 : Optimum Longitude Evolution From Triaxiality Considerations

If the parabola extends by an equal amount 'λ_{offset}' above and below the ideal longitude and this amount is set to equal half the allowable deadband then the entire deadband will be used over the course of a cycle and the cycle time, 'T', will be maximised. In practice however 'T' is usually chosen as the independent variable from which 'λ_{offset}' is calculated, this enables convenient EW cycle times to be chosen (usually a given number of weeks to avoid weekends).

Given that a new cycle starts at time $t=t_{init}$ the boundary conditions at point 'B' on figure 5.3 can be used to find the unknowns in equations (5.4) as,

$$\begin{aligned} \dot{\lambda}_0 &= -\ddot{\lambda}_0\left(t_{init} + T/2\right) \\ \lambda_0 &= \lambda_i - \lambda_{offset} + \frac{\ddot{\lambda}_0}{2}\left(t_{init} + T/2\right)^2 \end{aligned} \tag{5.5}$$

The boundary conditions at 'A' or 'C' can then be used to find 'λ_{offset}' as,

$$\lambda_{offset} = \ddot{\lambda}_0\, T^2/16 \tag{5.6}$$

The longitude drift rate at some time 't' is now,

$$\dot{\lambda} = -\ddot{\lambda}_0 / 2\left(T - 2\left[t - t_{init}\right]\right) \tag{5.7}$$

which can be combined with equation (5.2) to find the increment in semi-major axis needed at 't' to produce the desired mean motion, namely

$$\Delta a_T = \frac{a}{3n}\ddot{\lambda}_0\left(T - 2\left[t - t_{init}\right]\right) \tag{5.8}$$

where the subscript 'T' means the correction is due to triaxiality. Since this equation varies linearly with time so too does the actual semi-major axis, necessitating a correction in 'a' at the end of every cycle.

We are now in a position to analyse the EW manoeuvres required at the end of each EW cycle for Greenwich longitude control.

Greenwich Longitude Control Strategy

The 'ideal' parabolic mean motion shown in figure 5.3 does not quite occur due to limitations inherent in simplification and station keeping manoeuvre errors. The actual motion at best can be modelled as a non-symmetrical parabola, giving an 'imperfect' longitude and longitudinal drift rate at the end of the cycle. If corrective burns are calculated using the 'ideal' parabola and the orbit is propagated through multiple cycles the satellite soon exceeds the longitudinal deadband due to the gradual accumulation of errors. Such a system is therefore not acceptable for a propagation program which includes autonomous station keeping.

A stable solution is possible using the actual mean values of 'λ' and 'dλ/dt' at the end of a cycle to calculate a correction which ideally results in the correct mean values at the end of the next cycle.

Figure 5.4 shows three distinct paths that the mean longitude can follow after an EW correction. The first is the 'ideal' from figure 5.3; the second has the same cycle length but starts with incorrect values of 'λ' and 'dλ/dt'; and the third again starts from an incorrect position but this time the cycle period has had to been changed to prevent the mean longitude exceeding the longitude deadband.

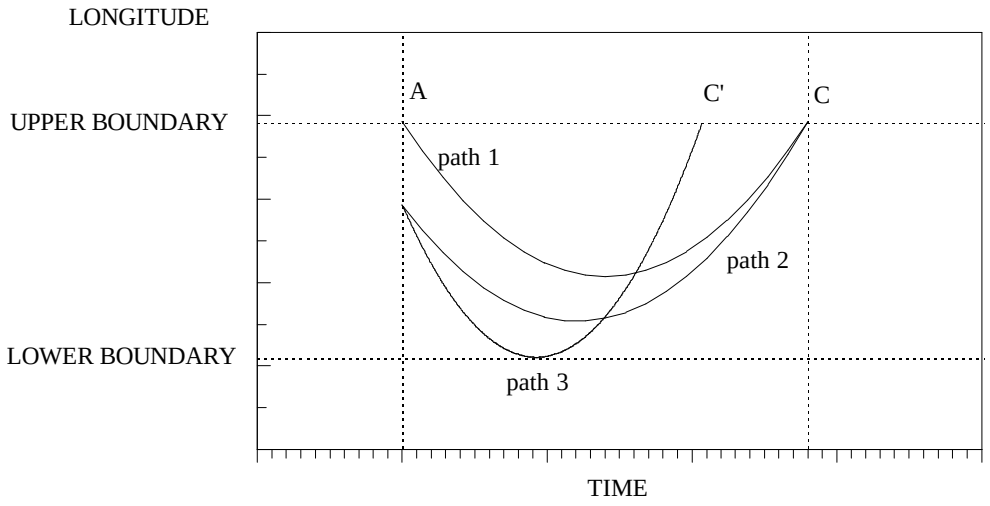

Figure 5.4 : Possible Paths Followed by Mean Longitude

Denoting the uncorrected motion by subscript '1' and the corrected motion by subscript '2', the mean motion of 'λ' can be approximated to,

$$\begin{aligned} \lambda &= \alpha_1 + \beta_1 t + \gamma_1 t^2 \\ \lambda &= \alpha_2 + \beta_2 t + \gamma_2 t^2 \end{aligned} \tag{5.9}$$

Since longitudinal acceleration is fixed by the position in the GEO ring both 'γ_1' and 'γ_2' are the same and by comparison with equation (5.4),

$$\gamma_1 = \gamma_2 = \frac{\ddot{\lambda}_0}{2} \tag{5.10}$$

A 'path 2' recovery can be found using the boundary conditions at points 'A' and 'C' in figure 5.4 which give two simultaneous equations in the unknowns 'α_2' and 'β_2'. Solving for these,

$$\begin{aligned}\alpha_2 &= \alpha - \frac{t_{init}}{T}\left(\lambda_i + \lambda_{offset} - \alpha_1 - \beta_1\left(t_{init} + T\right) - \gamma_1\left(t_{init} + T\right)^2\right)\\ \beta_2 &= \frac{\lambda_i + \lambda_{offset} - \alpha_1 - \beta_1 t_{init} - \gamma_1\left(t_{init} + T\right)^2}{T}\end{aligned} \tag{5.11}$$

This solution is only valid provided 'β_2' does not cause an excursion beyond the allowable deadband. In the limit, 'β_2' is such that the turning point on the parabola occurs at the edge of the deadband and in this case,

$$\beta_{2limit} = 2\gamma_1 t_{init} \pm 2\sqrt{\gamma_1^2 t_{init}^2 - \gamma_1\left(\lambda_i - \lambda_{offset} - \alpha_1 - t_{init}\beta_1\right)} \tag{5.12}$$

where the sign of the square root term is the opposite to that for '$d^2\lambda/dt^2$'. For a valid 'path 2' solution therefore the absolute value of 'β_2' calculated in equation (5.11) must be less than the absolute value of 'β_{2limit}'. If this inequality is not satisfied a 'path 3' solution is followed. In this case to affect the EW cycle period as little as possible 'β_2' is set to equal 'β_{limit}' and the new cycle length is calculated by rearranging equation (5.9) using 'β_{limit}' in place of 'β' as,

$$T = \left| -\left(\frac{\beta_{limit}}{\ddot{\lambda}_0}\right) \pm \sqrt{\left(\frac{\beta_{2limit}}{2\gamma_1}\right)^2 - \left(\frac{\alpha_1 + t_{init}\left(\beta_1 - \beta_{limit}\right) - \lambda_i - \lambda_{offset}}{\gamma_1}\right)} \right| \tag{5.13}$$

Ideally we do not want to change 'T' in this way and so it is usual to reserve a segment of the EW deadband for station keeping burn errors. In practice this means the 'usable' EW deadband is reduced but the 'path 2' recovery can then be followed in most cases. The remainder of the analysis will assume this will be done, allowing the equations for the 'path 2' motion to be used exclusively.

The size of the corrective burn can now be determined from 'β_2'. Differentiating equations (5.9) the difference between the actual and desired mean longitude drift rate is found as,

$$\Delta\dot{\lambda} = \frac{\lambda_i + \lambda_{offset} - \alpha_1 - \beta_1\left(t_{init} + T\right) - \gamma_1\left(t_{init} + T\right)^2}{T} \tag{5.14}$$

Since the aim of the burn is to change the semi-major axis of the orbit without effecting the eccentricity two equal tangential burns separated by 180° are required (actually procedures do exist to control the EW motion using just one burn, however these do not correct the orbit completely and require periodic two burn manoeuvres to prevent excessive error growth). The change in semi-major axis *for each burn* is thus,

$$\Delta a = -\frac{a}{3n}\left(\frac{\lambda_i + \lambda_{offset} - \alpha_1 - \beta_1\left(t_{init} + T\right) - \gamma_1\left(t_{init} + T\right)^2}{T}\right) \tag{5.15}$$

From the energy equation a relationship between an applied velocity increment and the resulting change in semi-major axis is derived as,

$$\begin{aligned} V^2 &= \mu\left(\frac{2}{r} - \frac{1}{a}\right) \\ 2V\Delta V &= \frac{\mu}{a^2}\Delta a \\ \Delta V &= \frac{V\Delta a}{2a} \end{aligned} \tag{5.16}$$

(using the approximation 'V=na'). Combining this with equation (5.15) gives the required velocity increment *per burn* as,

$$\begin{aligned} \Delta V &= -\frac{a}{6}\Delta\dot{\lambda} \\ \Delta V_t &= -\frac{a}{6T}\left(\lambda_i + \lambda_{offset} - \alpha_1 - \beta_1\left(t_{init} + T\right) - \gamma_1\left(t_{init} + T\right)^2\right) \end{aligned} \tag{5.17}$$

To apply this to the orbit propagation program the variables [α_1, β_1, γ_1] must be found numerically from the orbit prior to the manoeuvre using the technique discussed in the introduction.

Intermediate Orbit Correction

' Just about the time you think you can make ends meet somebody moves the ends '

Pansy Penner

There is one final problem relating to longitude control that needs to be addressed before the control strategy can be successfully implemented and this concerns the time between the two EW burns which so far has been ignored as a factor in the longitude evolution.

Again this region can be modelled as a parabolic motion in *mean* Greenwich longitude and the defining equations listed in equations (5.9) are thus increased by one to include the intermediate orbit. The new equations are listed in equations (5.18) below.

$$\begin{aligned} \lambda &= \alpha_1 + \beta_1 t + \gamma t^2 \\ \lambda &= \alpha_{inter} + \beta_{inter} t + \gamma t^2 \\ \lambda &= \alpha_2 + \beta_2 t + \gamma t^2 \end{aligned} \qquad (5.18)$$

where the subscript 'inter' refers to the intermediate orbit between EW burns.

To solve this modified form, additional boundary conditions are required at the beginning and end of the intermediate orbit and these are given in equations (5.19).

$$\begin{aligned} \text{First burn: } \Delta V &= \left(\Delta V_t + \Delta V_e\right) \\ \text{Second burn : } \Delta V &= \left(\Delta V_t - \Delta V_e\right) \end{aligned} \qquad (5.19)$$

In this equation 'ΔV_e' represents the velocity increment required for eccentricity control and its value and application will be discussed in the next section. Overall the result is an increase in the number of unknowns by three, making the solution more complex and

possibly confusing the basics of the correction mechanism which was described. It is for this reason it has not been mentioned earlier.

If this correction is now taken into account the subsequent equation for the magnitude of the triaxiality correction is given in equation (5.20).

$$\Delta V_t = -\frac{a\left(\lambda_i + \lambda_{offset} - \alpha_1 - \beta_1\left(t_{init} + T\right) - \gamma\left(t_{init} + T\right)^2 + \frac{\gamma T^2}{8} + \frac{129246\Delta V_e}{a}\right)}{6\left(T - 21541\right)} \qquad (5.20)$$

The size of the triaxiality correction burns is thus partially dependant on the size of the eccentricity control burns. The latter will now be discussed in detail.

5.2.3 : Eccentricity Control

Eccentricity causes a daily periodic libration of ±2e radians in and so may require control to prevent EW deadband violations. Over the course of a year the eccentricity vector describes a rough circle on the eccentricity plane (an example of which is shown in figure 5.5) with the direction of change of 'e' always being perpendicular to the Sun line. The circular motion is the result of solar pressure perturbations, and the oscillations on this mean motion are the result of the remaining perturbation sources.

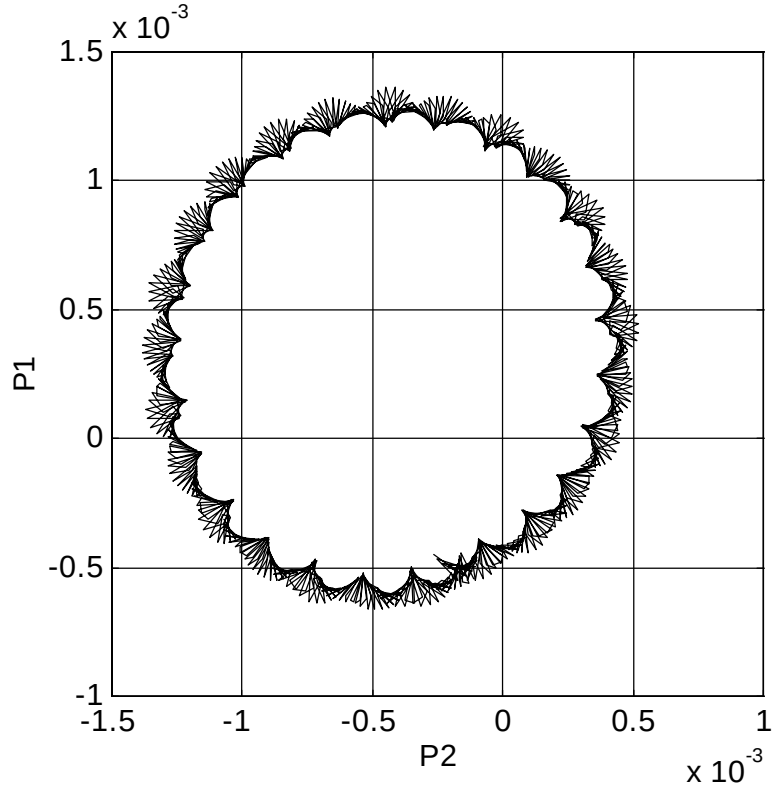

Figure 5.5 : Eccentricity Evolution Over Year (Results from Orbit Propagation)

Considering only solar pressure effects the evolution of 'P1' and 'P2' can be approximated by the following equations obtained by combining the Lagrange equations for 'P1' and 'P2' with the perturbation acceleration equations for solar pressure and integrating the results (a more complete derivation is presented in appendix B)

$$\begin{aligned} P1 &= e_n \mathrm{Sin}\left(n_s t + L_{s0}\right) + P1_0 - e_n \mathrm{Sin}\left(L_{s0}\right) \\ P2 &= e_n \mathrm{Cos}\left(n_s t + L_{s0}\right) + P2_0 - e_n \mathrm{Cos}\left(L_{s0}\right) \end{aligned} \tag{5.21}$$

where the subscript '0' refers to values at t = 0; 'e_n' is the natural radius of the eccentricity circle and,

$$\begin{aligned} e_n &= \frac{3a_{SP}}{2nan_s} \\ a_{SP} &= 9.1 \times 10^{-6}\left(\frac{A}{M}\right)\left(\frac{1+R}{2}\right) \end{aligned} \tag{5.22}$$

The centre of the natural eccentricity circle can be set by orbit initialisation however the radius can only be changed by altering the physical characteristics of the satellite. For satellites with large surface area to mass ratios the resulting evolution of 'e' must be controlled. To illustrate this in the case of figure 5.5 an area to mass ratio of 0.05 was used, resulting in a value of $e_n=9\times10^{-4}$. To obtain the lowest value of the maximum eccentricity over the course of a year the centre of the eccentricity circle should be set at zero in figure 5.5, however even if this is done the resulting daily libration is ±0.102° which is greater than the EW deadband allocated for many satellites.

The eccentricity control strategy will maintain the eccentricity vector within a circle with a radius less than the natural circle radius. During the course of a single EW cycle the mean eccentricity vector will follow an arc of the natural 'e' circle which intersects the controlled 'e' circle at the start 'A' and end 'B' points as shown in figure 5.6.

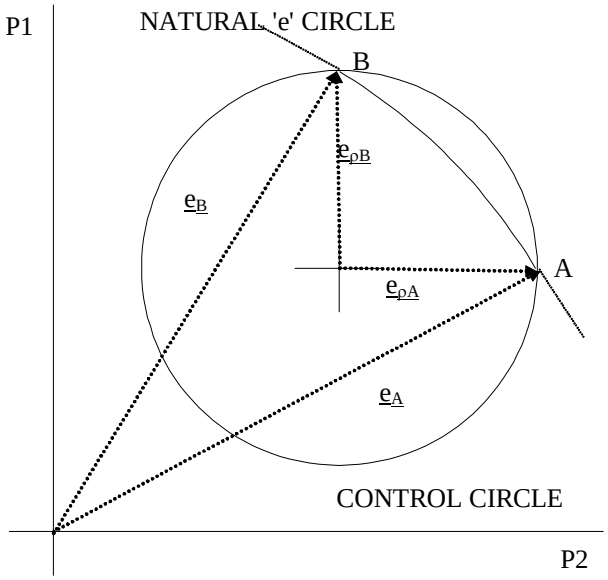

Figure 5.6 : Eccentricity Evolution Within Control Circle

At the start of the cycle (point A) the relative eccentricity vector, '$\underline{e}_{\rho A}$' (measured from the centre of the control circle) points behind the Sun line by some angle 'β'. In this case the perturbations will cause the eccentricity vector to follow the path indicated until at 'B' the natural and control circles again intersect. At this point a station keeping

manoeuvre must be applied. To maximise the arc length (and hence the EW cycle) between 'A' and 'B' the angle 'β' is selected such that the relative eccentricity vector at B, '$\underline{e}_{\rho B}$' is ahead of the Sun by this amount, thus making the motion symmetrical as shown in the diagram.

The minimum radius of the control circle for a set cycle length occurs when 'A' and 'B' are diametrically opposite on the control circle, this configuration however requires the largest corrective 'ΔV'. An alternative is for the line 'AB' to be a non-diameter chord of the tolerance circle which increases the number of manoeuvres required over a given period but decreases their size and thus reduces the absolute errors due to each burn. In the limit continual corrections can be applied although this method is not currently in use.

For optimum use of ground station time and minimum fuel consumption we will now develop a control strategy that can be applied at the same time as the longitude control corrections. The longitude correction specified two burns, 180° apart in sidereal angle with no constraints on the position/time of the first burn. This latter variable will be determined by the 'e' control strategy.

Ideal Eccentricity Control Strategy

Figure 5.7 illustrates the geometry of the eccentricity plane motion during a single EW station keeping cycle. Note that the relative eccentricity vectors, $\underline{e}_{\rho A}$ and $\underline{e}_{\rho B}$ originate at the centre of the controlled eccentricity circle and that this centre can lie anywhere on the eccentricity plane.

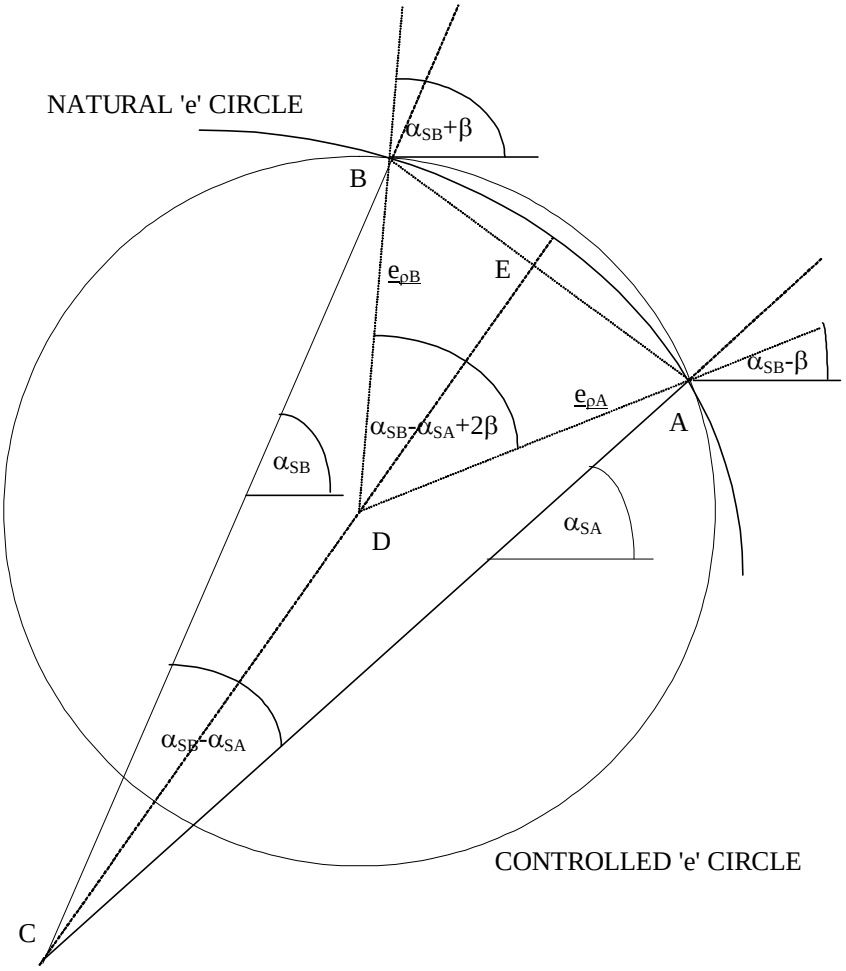

Figure 5.7 : Correction Strategy Geometry

During the EW cycle period, 'T' (= t_B-t_A) the relative eccentricity vector moves through arc lengths on the natural and controlled eccentricity equal to,

$$\begin{matrix} e_n\left(\alpha_{SB}-\alpha_{SA}\right) \\ e_c\left(\alpha_{SB}-\alpha_{SA}+2\beta\right) \end{matrix} \tag{5.23}$$

respectively. Consider now the right angle triangles DAE and CAE from figure 5.7. from these it can be shown that,

$$e_n \mathrm{Sin}\left(\frac{\alpha_{SB}-\alpha_{SA}}{2}\right) = e_c \mathrm{Sin}\left(\frac{\alpha_{SB}-\alpha_{SA}+2\beta}{2}\right) \tag{5.24}$$

Assuming that the Earth's rotation about the Sun is uniform, (α_{SB}-α_{SA}) = n_sT and equation (5.24) can be solved for 'β' as

$$\begin{aligned} \beta &= \mathrm{Sin}^{-1}\left[\frac{e_n}{e_c}\mathrm{Sin}\left(\frac{n_sT}{2}\right)\right] - \left(\frac{n_sT}{2}\right) + 2\pi m \\ \text{or} \quad \beta &= \pi - \mathrm{Sin}^{-1}\left[\frac{e_n}{e_c}\mathrm{Sin}\left(\frac{n_sT}{2}\right)\right] + \left(\frac{n_sT}{2}\right) + 2\pi m \end{aligned} \tag{5.25}$$

where 'm' is some integer value. To determine which value of 'β' to use the following inequality must be satisfied.

$$0 \le \beta \le \left(\frac{\pi - n_sT}{2}\right)$$

The lower limit corresponds to e_n=e_c (i.e. no control required) and the upper limit to the case where the chord of the arc AB along the natural eccentricity circle is equal to the diameter of the control 'e' circle.

At the end of each cycle a correction must be applied to rotate the relative eccentricity vector through an angle of -2β. Considering only eccentricity corrections this requires at least two tangential burns to leave the semi-major axis unaffected.

For the triaxiality corrections two burns were applied which were separated by 180° in sidereal angle in the same direction relative to the direction of orbital motion of the satellite about the Earth (i.e. if the first burn was applied Eastwards then so too was the second burn). For eccentricity corrections two burns separated by 180° in sidereal angle can again be applied, however in this case the burns will be in the opposite sense to each other (i.e. if the first burn was applied Eastwards then the second burn would be applied Westwards). This solution has two advantages, firstly both triaxiality and eccentricity corrections can be applied simultaneously (thus reducing ground station workload), and secondly the resulting total velocity increment required for EW station keeping is reduced. The reasons for the second of these is explained below.

Defining the velocity increment required *per burn* to correct for triaxiality as 'ΔV_T' and that required for eccentricity control *per burn* as 'ΔV_e' then the total requirements if the corrections are carried out separately are,

$$\begin{aligned}\Delta V &= \left|\Delta V_T\right| + \left|\Delta V_T\right| + \left|\Delta V_e\right| + \left|-\Delta V_e\right| \\ &= 2\left|\Delta V_T\right| + 2\left|\Delta V_e\right|\end{aligned}$$

Combining the manoeuvres however produces,

$$\begin{aligned}\Delta V &= \left|\Delta V_T + \Delta V_e\right| + \left|\Delta V_T - \Delta V_e\right| \\ &= 2\left|\Delta V_T\right| \quad \text{if} \quad \Delta V_T > \Delta V_e \\ &= 2\left|\Delta V_e\right| \quad \text{if} \quad \Delta V_e > \Delta V_T\end{aligned}$$

i.e. either triaxiality or eccentricity corrections, depending on which is bigger, is obtained 'for free'.

The linearised effect of the two eccentricity burns on the eccentricity vector is quoted from reference Soop [31] as,

$$\begin{aligned}\Delta e &= \frac{2}{V}\left(\Delta V_{e1} - \Delta V_{e2}\right)\begin{pmatrix}\mathrm{Cos}(s_1)\\ \mathrm{Sin}(s_1)\end{pmatrix} \\ &= \frac{4}{V}\Delta V_e\begin{pmatrix}\mathrm{Cos}(s_1)\\ \mathrm{Sin}(s_1)\end{pmatrix}\end{aligned} \tag{5.26}$$

where 'V' is the mean orbital velocity at GEO. The ideal relative eccentricity before and after the corrective burns can be found from figure 5.7 as,

$$\begin{aligned}\underline{e}_{\rho\text{before}} &= e_c\begin{pmatrix}\mathrm{Cos}(\alpha_s + \beta)\\ \mathrm{Sin}(\alpha_s + \beta)\end{pmatrix} \\ \underline{e}_{\rho\text{after}} &= e_c\begin{pmatrix}\mathrm{Cos}(\alpha_s - \beta)\\ \mathrm{Sin}(\alpha_s - \beta)\end{pmatrix}\end{aligned} \tag{5.27}$$

where 'α_S' is the value of the right ascension of the Sun at the time of the first burn (it will be assumed this value changes negligibly between the first and second burns). Combining (5.27) and (5.26),

$$\frac{4\Delta V_e}{V}\begin{pmatrix}\mathrm{Cos}(s_1)\\ \mathrm{Sin}(s_1)\end{pmatrix} = e_c\begin{pmatrix}\mathrm{Cos}(\alpha_s-\beta)-\mathrm{Cos}(\alpha_s+\beta)\\ \mathrm{Sin}(\alpha_s-\beta)-\mathrm{Sin}(\alpha_s+\beta)\end{pmatrix}$$

$$\begin{pmatrix}\mathrm{Cos}(s_1)\\ \mathrm{Sin}(s_1)\end{pmatrix} = \frac{Ve_c\mathrm{Sin}(\beta)}{2\Delta V_e}\begin{pmatrix}\mathrm{Cos}(\alpha_s-\pi/2)\\ \mathrm{Sin}(\alpha_s-\pi/2)\end{pmatrix} \tag{5.28}$$

from which the velocity increment and sidereal angle at which the first burn should be applied can be calculated as,

$$\Delta V_e = \frac{Ve_c\mathrm{Sin}(\beta)}{2}$$

$$s_1 = \mathrm{Tan}^{-1}\left(\frac{\mathrm{Sin}(\alpha_S-\pi/2)}{\mathrm{Cos}(\alpha_S-\pi/2)}\right) = \alpha_S-\pi/2 \tag{5.29}$$

It is worth noting that the times at which the burns are thus applied are 06:00 hrs and 18:00 hrs local satellite time.

Actual Eccentricity Control Strategy

Unfortunately due to mathematical simplifications and station keeping burn errors the relative eccentricity vector at the end of a cycle is not precisely that which is desired. To allow for this the analysis can be modified so that regardless of the position immediately prior to a burn the 'ideal' values after the burn are aimed for. Such an system has been implemented in the orbit propagation program and will be shown to be stable over the course of multiple EW cycles.

The relationship between the actual eccentricity vector at the end of a cycle (components [$P2_{end}$, $P1_{end}$]) and the relative eccentricity vector $\underline{e}_\rho$ can be seen in figure 5.8.

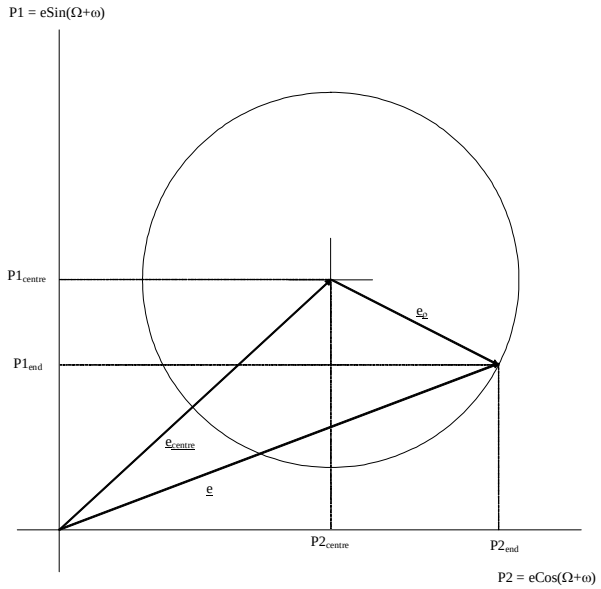

Figure 5.8 : Relationship Between Relative and True Eccentricity

From the diagram the relative eccentricity vector can be written as,

$$\underline{e}_{\rho before} = \begin{pmatrix} P2_{end} - P2_{centre} \\ P1_{end} - P1_{centre} \end{pmatrix} \tag{5.30}$$

and equation (5.28) can be rewritten using this in place of the 'ideal' expression in equation (5.27).

$$\frac{4\Delta V_e}{V}\begin{pmatrix} Cos(s_1) \\ Sin(s_1) \end{pmatrix} = e_c\begin{pmatrix} Cos(\alpha_s - \beta) \\ Sin(\alpha_s - \beta) \end{pmatrix} - \begin{pmatrix} P2_{end} - P2_{centre} \\ P1_{end} - P1_{centre} \end{pmatrix} \tag{5.31}$$

thus the actual values of 's_1' and 'ΔV_e' are,

$$\begin{aligned} \Delta V_e &= \frac{V}{4}\sqrt{\left(e_c Cos(\alpha_s - \beta) - P2_{end} + P2_{centre}\right)^2 + \left(e_c Sin(\alpha_s - \beta) - P1_{end} + P1_{centre}\right)^2} \\ s_1 &= Tan^{-1}\left(\frac{e_c Sin(\alpha_s - \beta) - P1_{end} + P1_{centre}}{e_c Cos(\alpha_s - \beta) - P2_{end} + P2_{centre}}\right) \end{aligned} \tag{5.32}$$

Defining the first burn (at s_1) as positive the ambiguity in the arctangent function is resolved by considering the signs of $Sin(s_1)$ and $Cos(s_1)$.

The eccentricity control corrective strategy is now complete.

5.2.4 : Software Implementation of EW Station Keeping

In this section the application of the analysis in sections 5.2.2 and 5.2.3 to the orbit propagation program to provide autonomous EW station keeping will be considered. Included are schematic flow diagrams that illustrate the key steps that the propagation program follows for initialisation and cycle end corrections. In addition, actual simulation results are presented to illustrate the difference between the evolution of the mean orbital elements and the actual elements, and to demonstrate the stability of the EW strategy as implemented.

Firstly however, a problem which has yet to be considered is that of initialisation at the start of the propagation period. At this point the values of all the equinoctial elements are selectable and the propagation begins in an 'ideal' position. Since we are not correcting an already known orbit the procedure followed is slightly different from the end-of-cycle correction problem and will now be dealt with.

Propagation Initialisation Procedure

Initialisation for EW station keeping involves calculating the actual starting values of the equinoctial variables, [L,l,a,P1,P2] based on the ideal longitude position (i.e. the mean longitude averaged over the EW cycle length), the difference between the current EW cycle start time and propagation start time, and the Julian date at which the propagation begins. The second of these is required to provide a means by which the NS and EW burn times do not coincide (the propagation always starts immediately after a NS correction, which will usually be part-way through an EW cycle).

The initialisation procedure followed is illustrated in figure 5.9.

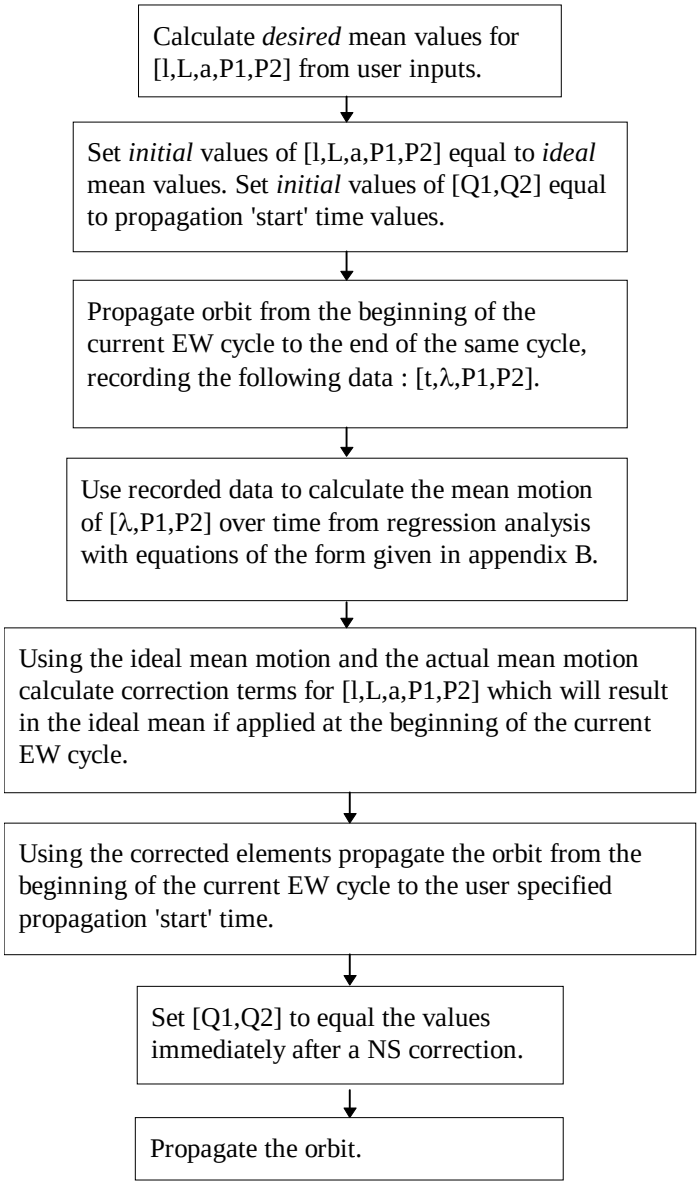

Figure 5.9 : Initialisation Procedure

During the procedure the [Q1,Q2] values prior to the propagation 'start' time are not strictly those which would occur during this period, however for EW cycle initialisation we are only interested in the evolution of [λ,P1,P2] which are relatively unaffected by changes in [Q1, Q2] provided the latter are small. Add to this the fact that [Q1, Q2] do not vary much over a typically short EW cycle (about 2 weeks) the approximation used in step 2 seems reasonable.

Two steps in figure 5.9 require further explanation, steps 1 and 5. These will now be expanded on in turn.

Calculation of Ideal Orbital Elements at EW Cycle Start (Initialisation Step 1)

Combining equation (5.6) with (5.4) the ideal mean Greenwich longitude at the beginning of the current EW cycle is,

$$\lambda = \lambda_i + \frac{\ddot{\lambda}_0}{16} T^2 \tag{5.33}$$

The effect of orbit inclination on longitude proportional to $i^2/4$ and thus is small near GEO, allowing the mean longitude corresponding to (5.33) to be calculated as,

$$l = \lambda + G \tag{5.34}$$

From which the true longitude can be found via the eccentric longitude using the technique given in chapter 4.

The ideal mean semi-major axis is found approximately as,

$$a = a_G + \frac{2J_{20}R_e{}^2}{a_G} + \frac{a_G}{3n}\ddot{\lambda}_0 T \tag{5.35}$$

by applying the corrections given in equations (5.3) and (5.8) to the unperturbed ideal value of 'a', (i.e. 'a_G') with t_{init}=0 to correspond to the start of the cycle.

The last two elements to be found are [P1,P2]. Using the notation in figure 5.8 these can be written as,

$$\underline{e} = \begin{pmatrix} P2 \\ P1 \end{pmatrix} = \begin{pmatrix} P2_{centre} \\ P1_{centre} \end{pmatrix} + e_c \begin{pmatrix} \mathrm{Cos}(\alpha_{sEWstart} - \beta) \\ \mathrm{Sin}(\alpha_{sEWstart} - \beta) \end{pmatrix} \tag{5.36}$$

where, '$\alpha_{sEWstart}$' is the right ascension of the Sun at the start of the current cycle, [$P1_{centre}$, $P2_{centre}$, e_c] are user selected, and 'β' is found from equation (5.25).

Calculation of Correction Terms (Initialisation Step 5)

Consider first the corrections that need to be applied as a result of the difference between the actual and ideal Greenwich longitude evolution. Representing the uncorrected response by subscript '1' and the ideal by '2' the mean Greenwich longitude can be written approximately as,

$$\begin{aligned} \lambda_1 &= \alpha_1 + \beta_1 t + \gamma t^2 \\ \lambda_2 &= \alpha_2 + \beta_2 t + \gamma t^2 \end{aligned} \tag{5.37}$$

where 't' is measured from the start of the current EW cycle. Using these equations the difference between the ideal and the actual starting value of 'λ' is,

$$\Delta\lambda = \alpha_2 - \alpha_1$$

In step 2 of figure 5.9 the initial value of 'λ' was set to equal the ideal mean value (i.e. $\lambda_{2EWstart}$) and thus the corrected starting value should be,

$$\begin{aligned} \lambda_{EWstart} &= \lambda_{ideal} + \Delta\lambda \\ &= \lambda_{2EWstart} + \Delta\lambda \\ &= 2\alpha_2 - \alpha_1 \end{aligned} \tag{5.38}$$

To establish the corrected value of semi-major axis we must consider '$d\lambda/dt$'. The difference between the uncorrected and corrected values of this can be found from the differential form of equations (5.37), resulting in the following expression at the beginning of the cycle.

$$\Delta\dot{\lambda} = \beta_2 - \beta_1$$

The corrected value can be found using arguments similar to those used to derive (5.38) resulting in,

$$\begin{aligned}\dot{\lambda}_{\text{EWstart}} &= \dot{\lambda}_{\text{ideal}} + \Delta\dot{\lambda} \\ &= \dot{\lambda}_{\text{2EWstart}} + \Delta\dot{\lambda} \\ &= 2\beta_2 - \beta_1\end{aligned} \tag{5.39}$$

Hence the correction required to semi-major axis can be found as,

$$\begin{aligned}\Delta\text{a} &= -\frac{2}{3}\frac{\text{a}}{\text{n}}\Delta\dot{\lambda} \\ &= -\frac{2}{3}\frac{\text{a}}{\text{n}}\left(\beta_2 - \beta_1\right)\end{aligned} \tag{5.40}$$

where ideal GEO values of 'a' and 'n' can be used on the R.H.S. of the equation with minimal error. The corrected starting value of 'a' is now,

$$\text{a}_{\text{EWstart}} = \text{a}_{\text{ideal}} + \Delta\text{a} \tag{5.41}$$

To use equations (5.38) to (5.41) the ideal motion variables [α_2,β_2,γ] are needed along with the regression values [α_1,β_1]. The latter are calculated using the method detailed in appendix B and since the former are ideal values they can be easily found using equations (5.4) to (5.7) and,

$$\begin{aligned}\alpha_2 &= \lambda_{\text{i}} + \ddot{\lambda}_0\,\text{T}^2/16 \\ \beta_2 &= -\ddot{\lambda}_0\,\text{T}/2 \\ \gamma &= \ddot{\lambda}_0/2\end{aligned} \tag{5.42}$$

completing the initialisation process.

Propagation Cycle End Procedure

A summary of software implementation of the EW cycle end procedure is illustrated in figure 5.10.

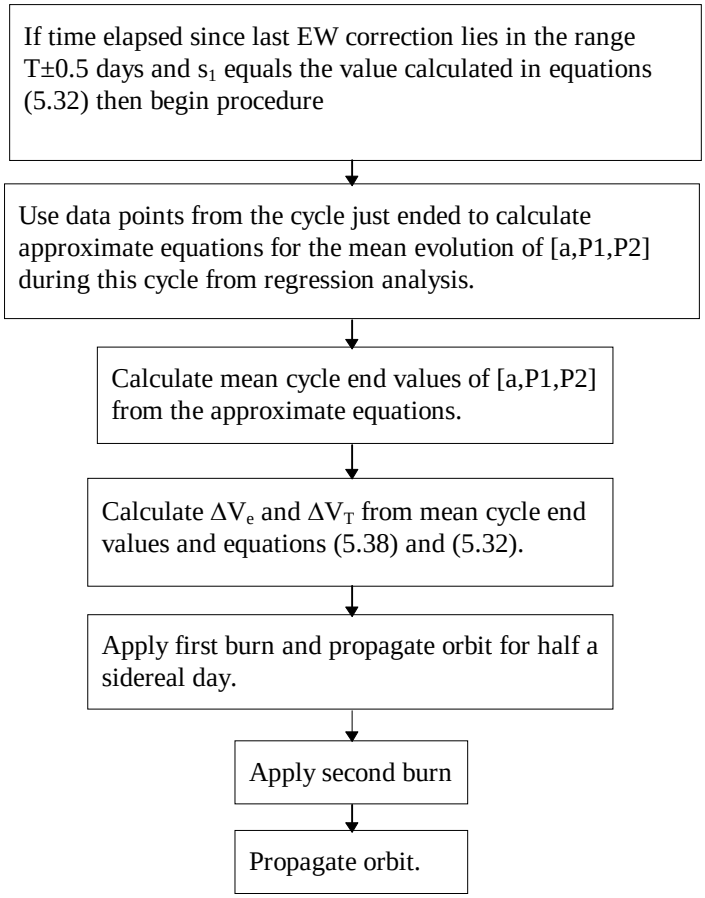

Figure 5.10 : Cycle End Procedure

The analytical theory has been discussed extensively in sections 5.2.2 and 5.2.3 and is not repeated here. A pure implementation problem however is the calculation of 's_1' from the eccentricity control analysis, since the values of '$P1_{end}$' and ' $P2_{end}$' change with time 's_1' cannot be calculated precisely except by simulation. This is dealt with in the propagation program in the following way. If the time elapsed since the last EW correction lies in the range (T±0.5) days then the actual value of 's_1' is compared with that calculated from equation (5.32) to establish whether the EW correction should be applied before the end of the next step. If this is the case the integration step interval is changed so that the next value of 's_1' will correspond to the equation (5.32) value. At this

point the first EW correction is applied. This solution is approximate since during the last step interval before the correction '$P1_{end}$' and ' $P2_{end}$' change, however since the step is small (<600 seconds commonly) and [P1,P2] vary slowly the effect is negligible.

Simulation Results, Evolution of Greenwich Longitude with Station Keeping

Figure 5.11 illustrates the evolution of Greenwich longitude with the described autonomous EW station keeping strategy enabled over a period of 600 days. The cycle length is 14 days and the satellite is positioned at a nominal longitude of 19° West.

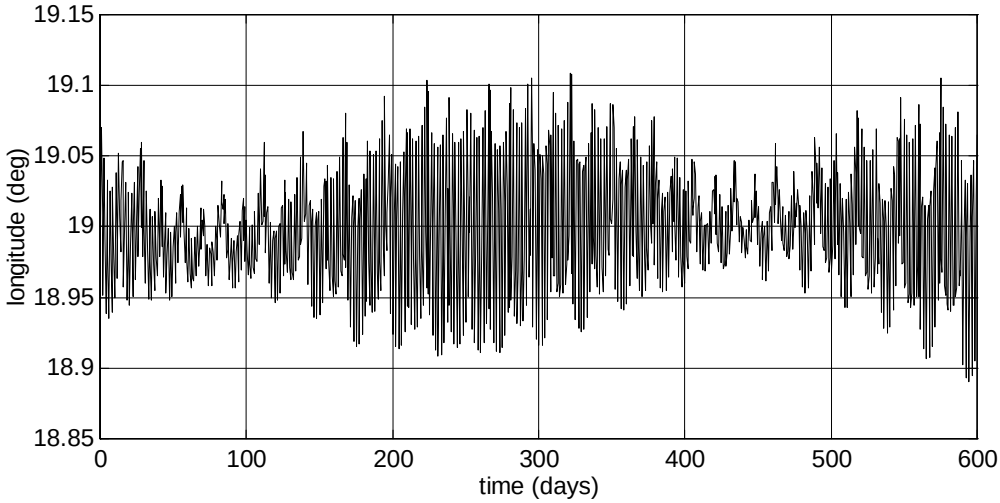

Figure 5.11 : Longitude Evolution Over 600 Days

The diagram indicates that for the propagation period of one year the control strategy provides stable control of Greenwich longitude. Both the parabolic motion and the librations due to eccentricity can be seen, the latter creating a sinusoidal envelope, with a period of one year.

The daily effect of eccentricity is more clearly seen on figure 5.12 which is identical to 5.11 except the time axis is reduced to 70 days, i.e. 5 complete EW cycles.

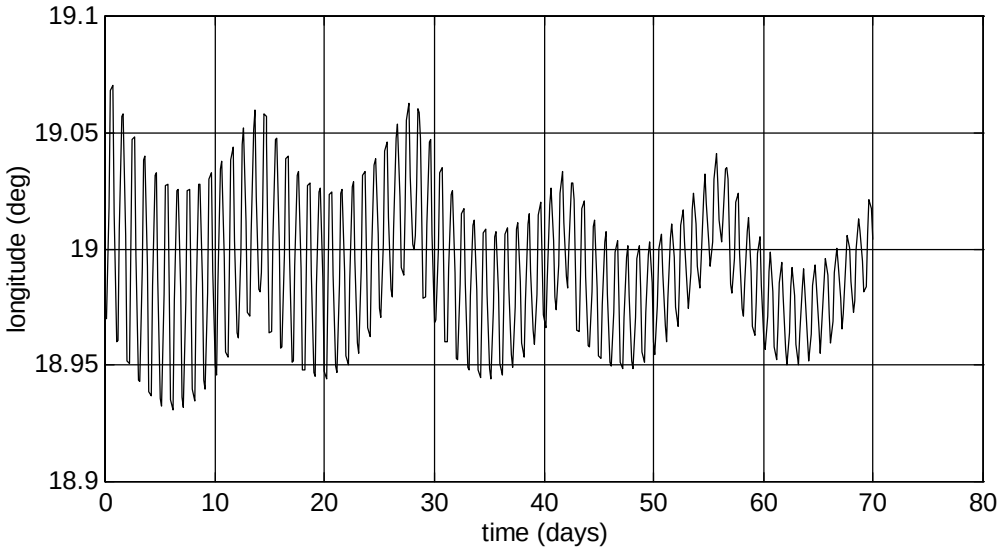

Figure 5.12 : Longitude Evolution Over 70 Days

The mean value of Greenwich longitude at the end of each cycle is used in the burn computations. This value is found by the propagation program from the 'best fit' parabola which is calculated from multiple linear regression using data stored during the previous cycle. These 'best fit' parabolas corresponding to the figure 5.12 motion are illustrated on figure 5.13.

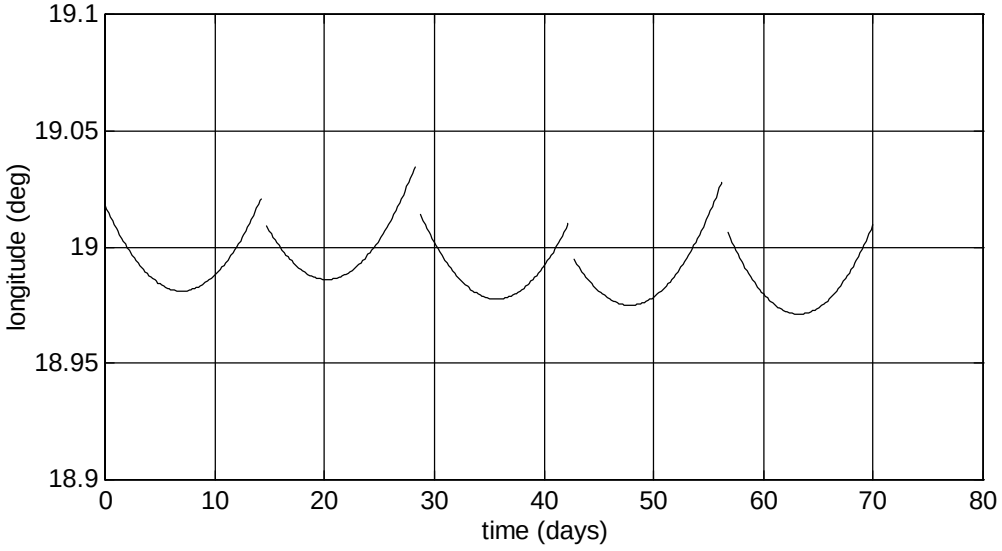

Figure 5.13 : Estimated Mean Longitude Evolution Over 70 Days

The intermediate orbit between EW burns is not modelled by the software and so is not shown in figure 5.13. The fact that the parabolas for successive cycles do not intersect at the end points illustrates the drift effect due to eccentricity in the intermediate orbit.

Simulation Results, Evolution of Eccentricity with Station Keeping

Figure 5.14 illustrates the simulated motion of the eccentricity vector over the course of 370 days. The satellite physical characteristics are identical to those used to produce figure 5.5 (i.e. a theoretical natural eccentricity circle radius of 9.0×10^{-4} , centred at [-0.0003, 0] on the eccentricity plane). For figure 5.14 the program was requested to control the eccentricity radius to half this value with the same centre.

Both the mean circular motion due to solar pressure and the second order effects due to the remaining perturbation sources are clearly visible on the diagram. As in the case of Greenwich longitude the motion appears stable.

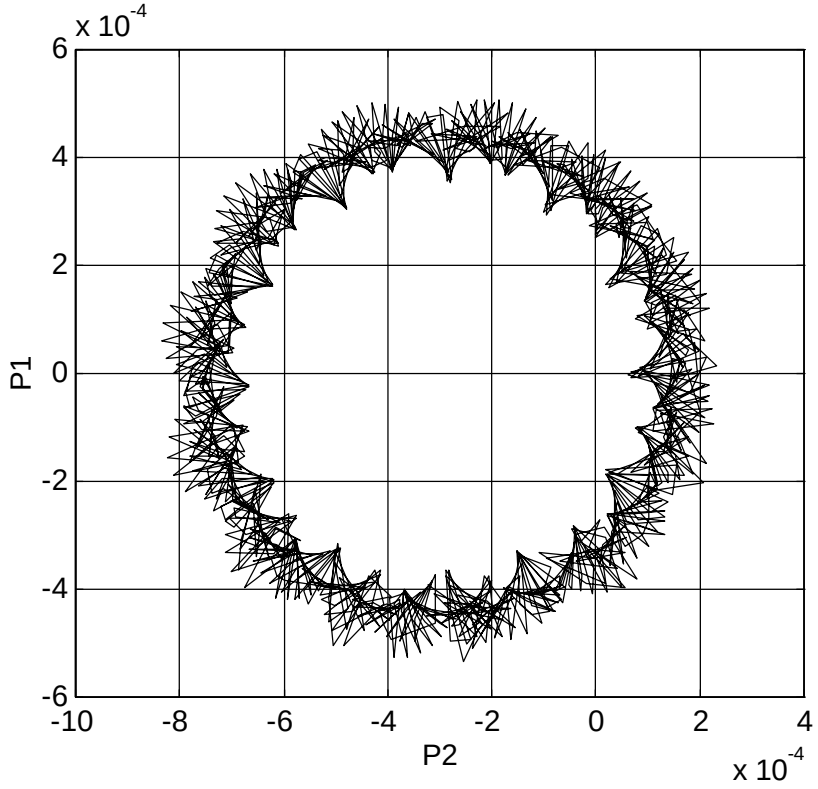

Figure 5.14 : Eccentricity Vector Evolution Over 1 Year

The mean motion which was used for eccentricity control calculations corresponding to figure 5.14 is shown in figure 5.15 along with the theoretical control circle.

It is difficult to distinguish between the mean motion and the control circle on figure 5.15, demonstrating how closely the mean motion is followed.

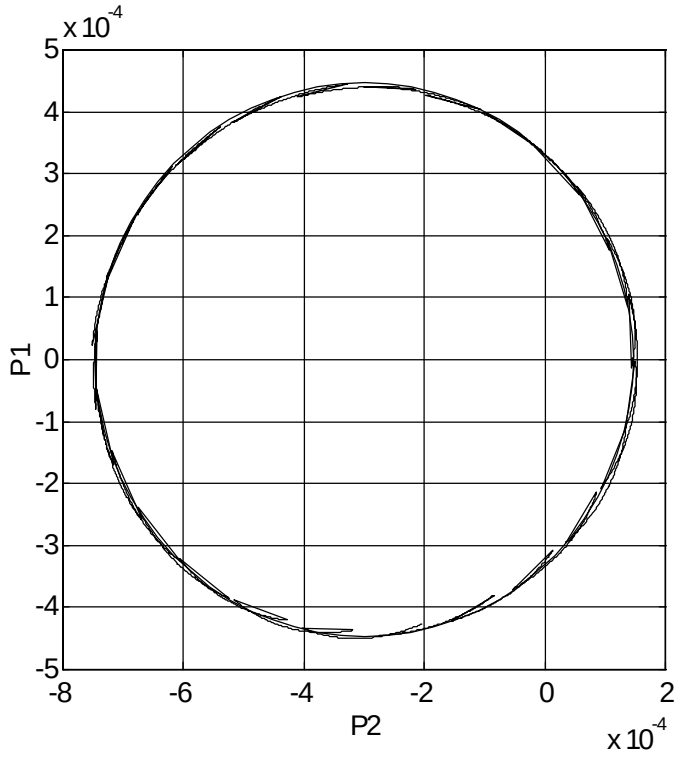

Figure 5.15 : Mean Eccentricity Vector Evolution Over 1 Year

Note that in figure 5.15 the 'straight-line' segments which move the satellite clockwise on the eccentricity circle occur at cycle-end/cycle-beginning. The simulated eccentricity plane motion does not follow these paths, since the eccentricity is instantaneously changed from the cycle-end value to the cycle-beginning one. The same effect is present in figure 5.14 also, however on that diagram it is much more difficult to see due to the presence of short term perturbations on the mean eccentricity motion.

5.3 : NS Station Keeping

5.3.1 : Overview

Lunar and Solar perturbation combine to increase the inclination of an initially zero inclination orbit producing a daily libration in latitude, the magnitude of which is ±i. If the perturbations cause the inclination to exceed the allowable latitude deadband of '$\pm i_{max}$' (commonly, between about ±0.05° to several degrees in magnitude) during the mission lifetime then periodic NS station keeping manoeuvres are required. It is this subject that will be dealt with here.

The equinoctial orbit elements of interest for NS station keeping are [Q1,Q2], corresponding to the classical elements [i,Ω]. Their evolution can be controlled by careful selection of their initial values and by the application of periodic velocity increments along the orbit normal, i.e. NS, direction. Various optimisation techniques can be followed to realise this control, Soop [31] details three and these are listed below.

1. Minimise the fuel required to keep the inclination below 'i_{max}' for a given mission lifetime.
2. Maximise the lifetime during which $i < i_{max}$ for a given amount of fuel.
3. Minimise the maximum inclination during a given lifetime with a given amount of fuel.

For the first option it may be possible to avoid manoeuvres altogether if the latitude deadband is sufficiently large or the mission lifetime short. The second option is most common in practice, usually with the added restraint that the lifetime exceeds some specified minimum. The third option requires more frequent manoeuvres than the other two and it is a modified form of this that has been used in the propagation program. The modifications and the reason for selection follows.

For colocated satellites using inclination separation (probably with eccentricity separation) it is desirable to separate the [Q1,Q2] values of each individual satellite by as large an amount as possible to minimise the risk of close approaches in the advent of station keeping manoeuvre errors. The drift in inclination over the NS cycle will

determine the largest value of this separation without the inclination exceeding 'i_{max}' at the end of the cycle, thus it is this that must be controlled.

Two restrictions will be placed on the control method. The first is operational in nature and states that as for EW station keeping, the NS cycle length will be chosen to be an integer number of weeks. The second restriction is along similar lines and states that the NS cycles will all be of identical lengths and this is included to simplify the software implementation of the control strategy. In practice NS corrections are not usually separated by uniform time periods (as an example in the case of ASTRA satellite cluster at 19°E the NS cycle varies between four and five weeks Wauthier et al [18]). Although the inclusion of these restrictions will lead to a slightly non-optimal solution the additional fuel usage should be small and is not directly of relevance to the research - provided each simulation uses the same cycle length the results should still be useful in evaluating the relative performance of each colocation scheme.

Since inclination changes much slower that the in-plane elements dealt with in EW station keeping, the NS correction will be limited to setting [Q1,Q2] back to the initial, user defined values. The absence of a large, short term perturbation effect on the mean motion of [Q1,Q2] makes the evaluation of mean motion unnecessary for the calculation of the corrective burns.

Inclination Plane Representation

The unit vector perpendicular to the orbit plane, pointing in the same direction as the angular momentum vector, is known as the three dimensional (3D) inclination vector and is written in geocentric axes as,

$$\underline{i}_{3D} = \begin{bmatrix} \mathrm{Sin(i)Sin(\Omega)} \\ -\mathrm{Sin(i)Cos(\Omega)} \\ \mathrm{Cos(i)} \end{bmatrix} = \frac{1}{1+Q1^2+Q2^2} \begin{bmatrix} 2Q1 \\ -2Q2 \\ 1-Q1^2-Q2^2 \end{bmatrix} \tag{5.43}$$

A more useful concept is the 2D inclination vector (here-after referred to as just, the inclination vector), which is used to represent the inclination evolution graphically on

the inclination plane. Different authors prefer different definitions for this, however all forms define a vector who's components related to the elements [i, Ω]. Since this work uses the equinoctial elements predominantly the inclination vector here will have components $[Q2, Q1]^T$. The 'Q2' variable is selected as the 'x' component so that the angle the inclination vector makes with the positive 'x' axis is the right ascension of the ascending node. As defined the inclination plane is illustrated in figure 5.16.

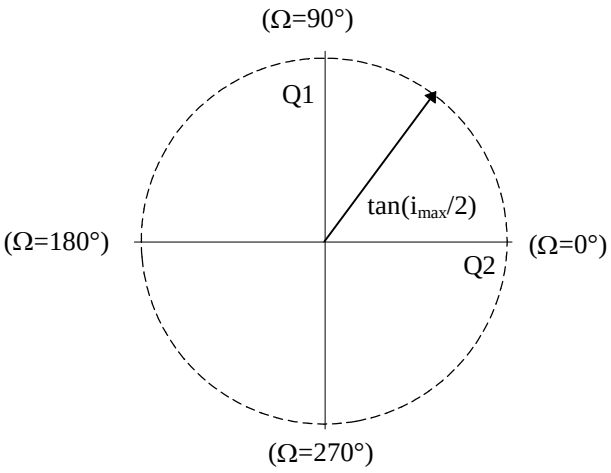

Figure 5.16 : The Inclination Plane

In the diagram the circle represents the limit imposed by the latitude deadband and has a radius of $Tan(i_{max}/2)$.

5.3.2 : Uncontrolled Inclination Evolution

Although all four of the major perturbation sources contribute to the out of plane acceleration which results in changes in the 'Q1' and 'Q2' elements, only three are significant; Earth oblateness, Solar gravity, Lunar gravity. It is important to understand their effects if they are to be controlled successfully, and so each will be described briefly. More detailed descriptions can be found in references Pocha [29], Soop [31], Agrawal [37], Cook [24] and Buglia [38].

Oblateness

Oblateness effects cause a rotation in the line of nodes, leaving the inclination virtually unchanged. In terms of the right ascension of the ascending node, the drift rate averaged over a single orbit is approximately (Agrawal [37]),

$$\dot{\Omega} = \frac{-3\mu J_2 R_e^{\,2}}{2hr^3}\mathrm{Cos}(i)$$

which is equal to about -4.9°/year for low orbit inclinations.

Solar Gravity

Over the course of one year the geocentric 'Z' co-ordinate of the Solar position varies from a maximum at mid-summer and mid-winter (when the Sun lies exclusively in the ZY plane) to a minimum when the Sun passes through the Vernal and Autumnal equinoxes (when the Sun lies along the 'X' axis). Since the geocentric 'Z' co-ordinate of the Sun determines the out of plane perturbation acceleration acting on a satellite this also therefore varies over the year, resulting in a twice-annual periodic force which changes the inclination vector. Figure 5.17 illustrates the effect on an equatorial orbit when the geometry of the Earth-Sun system produces maximum and minimum perturbation accelerations.

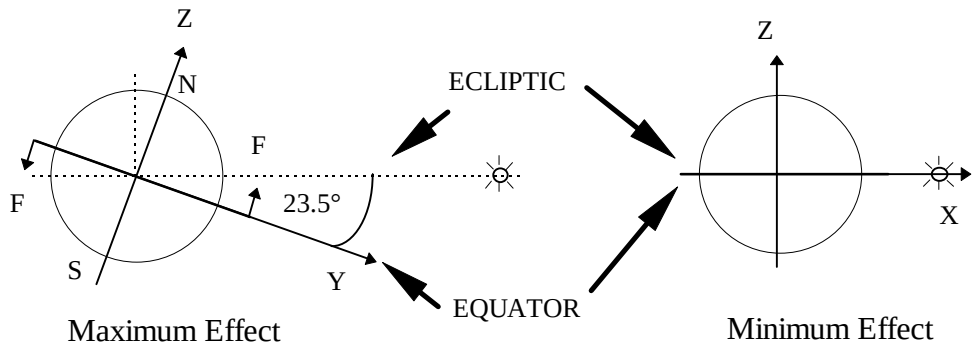

Figure 5.17 : Out of Plane Effect of Sun on GEO Orbit

The change in inclination vector as a result of this effect is always in a direction perpendicular to the sidereal angle of the Sun at a rate proportional to the out of plane

component of the Solar gravity. When the perturbation is a maximum the change is along the 'X' axis, from equation (5.43) therefore the Solar gravity must change the 'Q1' variable' much more than the 'Q2' variable.

As an example of the effect of the Sun figure 5.18 illustrates the inclination vector evolution from an initial value of zero under the influence of Solar gravity.

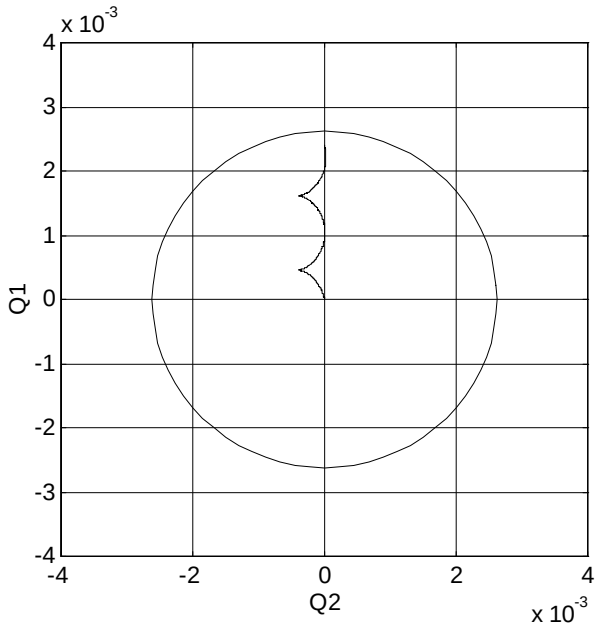

Figure 5.18 : Q1,Q2 Evolution due to Solar Effects Only

It should be remembered that the drift rate, and thus the 'speed' of motion across the inclination plane, is dependant on the right ascension of the ascending node of the orbit. Agrawal [37] derives the following relationship showing the inclination drift rate,

$$\frac{di}{dt} \approx \frac{3\mu_s r^2 \mathrm{Sin}(\Omega)\mathrm{Sin}(2i_s)}{8hr_s^3}$$

Applying this to the motion illustrated in figure 5.18, if the propagation were re-run using an initial non-zero value of 'Q2' then the sin(Ω) term in the equation would be smaller and the drift across the inclination plane, slower. Since the 'Q2' motion appears to be purely periodic however this would result in the inclination plane being traversed along a non-diameter chord of the maximum inclination tolerance circle, and thus less

absolute 'Q1' drift could be tolerated. The process will be complicated further by the presence of Lunar gravity which is discussed next, however this indicates some of the problems that need to be considered for optimisation.

Lunar Gravity

The Moon has a similar effect on a satellite as the Sun does, however there are differences due to the force of attraction, the period of rotation and the inclination of the Lunar orbit when compared with the Solar orbit. Of these three differences the most noteworthy is the last which will now be expanded on.

With respect to the ecliptic, the Moon's inclination is constant and equal to 5.14°. However relative to the equator the inclination changes with a period of 18.6 years under the influence of the effect of Solar gravity on the Moon. This in turn leads to an equatorial inclination variation of 23.45°±5.15°, and thus a varying perturbation effect on a satellite orbit. Depending on the point in this cycle, the inclination drift rate can vary between 0.4780°/year and 0.674°/year (Soop [31]). In the year 2005 the inclination drift due to Lunar gravity is a maximum and for this period figure 5.19 illustrates the inclination vector drift. As in figure 5.18 the initial vector magnitude is zero.

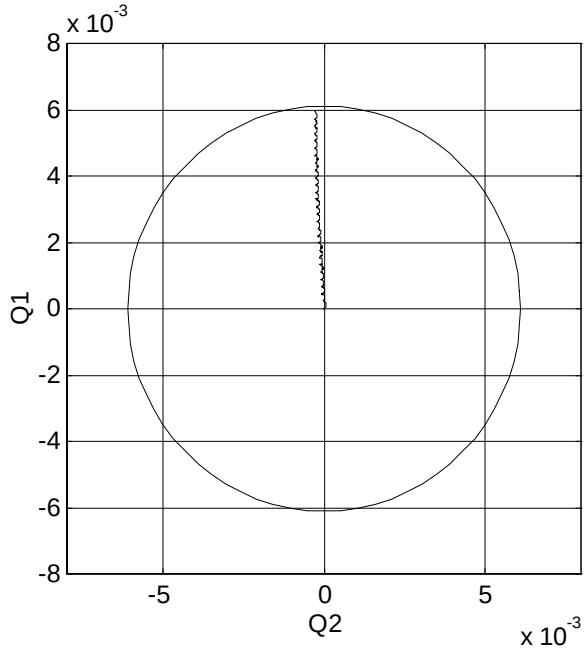

Figure 5.19 : Q1,Q2 Evolution due to Lunar Effects Only

Both the mean motion (again pre-dominantly along the 'Q1' axis) and the twice monthly periodic motion can be seen. By comparing the radii of the two circles in figures 5.18 and 5.19 the dominance of the Lunar gravity effect can be seen.

Combined Effect

The combined effect of the Sun, Moon, and Earth oblateness is approximately that found by superimposing the individual effects. This results in a perturbation with period of 18.6 years (due to the Moon), which has a strong underlying linear drift in the direction of 'Q1' and a much smaller drift in the direction of 'Q2'. Superimposed on this motion are two intermediate term periodic effects, the first is the twice annual oscillation caused by the Sun, and the second is the twice monthly oscillation caused by the Moon. Lastly the inclination vector undergoes a rotation by 4.9°/year due to Earth oblateness.

The graphs shown in figure 5.20 illustrate the overall effect on 'Q1' and 'Q2' for five different years; 1990, 1995, 2000, 2005 and 2010. Since this range covers more than one complete 18.6 year perturbation cycle, both the approximate maximum and the minimum yearly inclination vector drifts are visible on the plot.

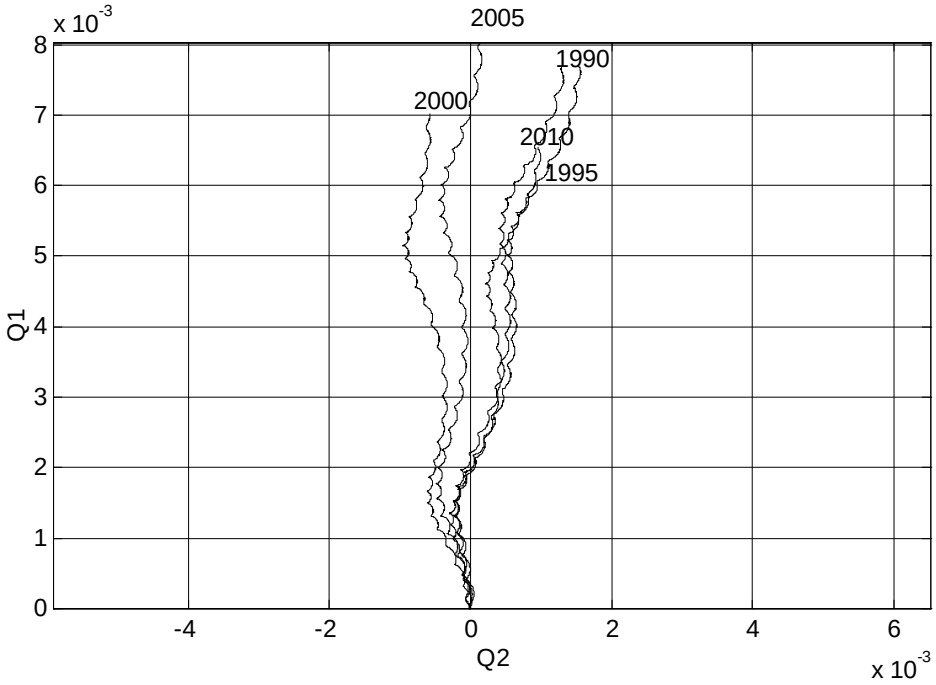

Figure 5.20 : Inclination Vector Drift During 1990-2010

Minimum drift occurs in 1995 and the maximum, in 2005. In terms of NS station keeping optimisation this complicates matters, since an optimal strategy for one year will not be quite so optimal for another year, and in practice this means optimal NS manoeuvres do not follow an 'orderly' pattern in either the burn magnitude or the interval between NS station keeping corrections.

5.3.3 : NS Manoeuvres, The Effect On The Inclination Vector

In developing an inclination control strategy two things are needed. The first is an understanding of the physical mechanism which makes such control necessary (covered above) and provides the basis for initial inclination vector and NS cycle length selection. The second requirement is the connection between the applied burn 'ΔV_{NS}' and the resulting change in the inclination vector components 'Q1' and 'Q2'. Starting with the angular momentum vector '$\underline{h}$' the mathematical treatment of the latter will now be dealt with.

The satellite angular momentum vector can be written as,

$$\underline{h} = \underline{r} \times \underline{v} \tag{5.44}$$

In geocentric co-ordinates the position and velocity, '$\underline{r}$' and '$\underline{v}$', are,

$$\begin{aligned} \underline{r} &= r\hat{\underline{r}} \\ \underline{v} &= \dot{r}\hat{\underline{r}} + r\dot{L}\hat{\underline{u}} \end{aligned} \tag{5.45}$$

where the unit vectors $[\,\hat{\underline{r}}, \hat{\underline{u}}, \hat{\underline{k}}\,]$ are defined in appendix A as equations (A.4) and represent the orbital axis directions in geocentric co-ordinates. Combining equations (5.44) and (5.45),

$$\underline{h} = \underline{r} \times \left(\dot{r}\hat{\underline{r}} + r\dot{L}\hat{\underline{u}} \right) = r\dot{L}\left(\hat{\underline{r}} \times \hat{\underline{u}} \right) = r\dot{L}\hat{\underline{k}} \tag{5.46}$$

or in terms of the equinoctial variables as,

$$\begin{aligned} \underline{h} &= h \begin{bmatrix} 2Q1/q \\ -2Q2/q \\ (2-q)/q \end{bmatrix} \\ \text{where } h &= r\dot{L} = \sqrt{a\mu\left(1 - P1^2 - P2^2\right)} \end{aligned} \tag{5.47}$$

Defining changes in 'Q1' and 'Q2' as 'ΔQ1' and 'ΔQ2' respectively, the corresponding change in angular momentum is then approximately given as,

$$\begin{aligned} \underline{\Delta h} &= h \begin{bmatrix} 2\Delta Q1 \\ -2\Delta Q2 \\ \Delta Q1^2 + 2Q1\Delta Q1 + 2Q2\Delta Q2 + \Delta Q2^2 \end{bmatrix} \\ \Delta h &\approx \pm 2h\sqrt{\Delta Q1^2 + \Delta Q2^2} \end{aligned} \tag{5.48}$$

Taylor series approximations were used to simplify equation (5.48), with only the first / most dominant terms being retained.

Returning now to equation (5.45) the change in velocity is the result of a velocity addition in the orbit normal direction. In geocentric axes the vector change in velocity is,

$$\begin{aligned}\underline{\Delta V}_{NS} &= \Delta V_{NS}\,\underline{\hat{k}} \\ &= \Delta V_{NS}\begin{bmatrix} 2Q1/q \\ -2Q2/q \\ (2-q)/q \end{bmatrix}\end{aligned} \tag{5.49}$$

Combining (5.49) with (5.44) the change in angular momentum in terms of the applied velocity is then,

$$\begin{aligned}\underline{\Delta h} &= r\Delta V_{NS}\left(\underline{\hat{r}}\times\underline{\hat{k}}\right) = -r\Delta V_{NS}\,\underline{\hat{u}} \\ &= -r\Delta V_{NS}\begin{bmatrix} -Sin(L)+2Q1(Q2Cos(L)+Q1Sin(L))/q \\ Cos(L)-2Q2(Q2Cos(L)+Q1Sin(L))/q \\ 2(Q2Cos(L)+Q1Sin(L))/q \end{bmatrix}\end{aligned} \tag{5.50}$$

and by equating (5.48) and (5.50) a relationship between the applied velocity and the resultant change in 'Q1' and 'Q2' is found as,

$$\begin{aligned}\Delta V_{NS} &\approx \pm\frac{2h}{r}\sqrt{\Delta Q1^2+\Delta Q2^2} \\ &\approx \pm 2V_e\sqrt{\Delta Q1^2+\Delta Q2^2}\end{aligned} \tag{5.51}$$

where the velocity of a satellite in an ideal geostationary orbit, $V_e \approx 3075$ m/s. Equating the first two components of the vectors given in (5.50) and (5.48), a specific value of 'L' can be found at which this velocity should be applied for a single burn solution. An approximate solution in given in equation (5.52), where only the most dominant terms have been retained.

$$\begin{aligned}\Delta V_{NS}Sin(L) &\approx -2V_e\Delta Q1 \\ -\Delta V_{NS}Cos(L) &\approx 2V_e\Delta Q2 \\ L &\approx Tan^{-1}\left(\frac{\Delta Q1}{\Delta Q2}\right)\end{aligned} \tag{5.52}$$

The quadrant ambiguity in equation (5.52) is resolved by the equations for Sin(L) and Cos(L), which in turn rely on the sign of 'ΔV_{NS}'. Since both negative and positive values are valid solution to (5.51) there exists two points per orbit as which the inclination

vector can be corrected, one requiring a North burn, and one requiring a South burn. In both cases the size of the burn is identical.

In operation, the propagation program always uses the positive burn although there is no specific reason for this, it is merely a convention which has been adopted.

5.3.4 : NS Station Keeping Control Strategy

Using equations (5.51) and (5.52) in conjunction with the knowledge of the perturbed motion of the inclination vector as discussed in section 5.3.2 selection of a suitable inclination control strategy can be made.

For single satellites the most common strategy is to set 'Ω' in the region of 270° with an inclination close to the tolerance value and then allow it to drift. Since this drift has been shown to be primarily in the direction of the positive 'Q1' axis the inclination first decreases until the Q1=0 line is crossed and then increases until it again reaches the tolerance limit (this time with 'Ω' in the region of 90°) at which point the NS station keeping manoeuvre is applied. Theoretically this maximises the interval between NS burns and is illustrated in figure 5.21 for an inclination tolerance of 0.1° over two NS cycles. Note that the 'Q2' motion is different for each cycle as a result of the geometry changes between the Sun, Moon and Earth during the propagation period which affect the perturbation forces acting on the satellite.

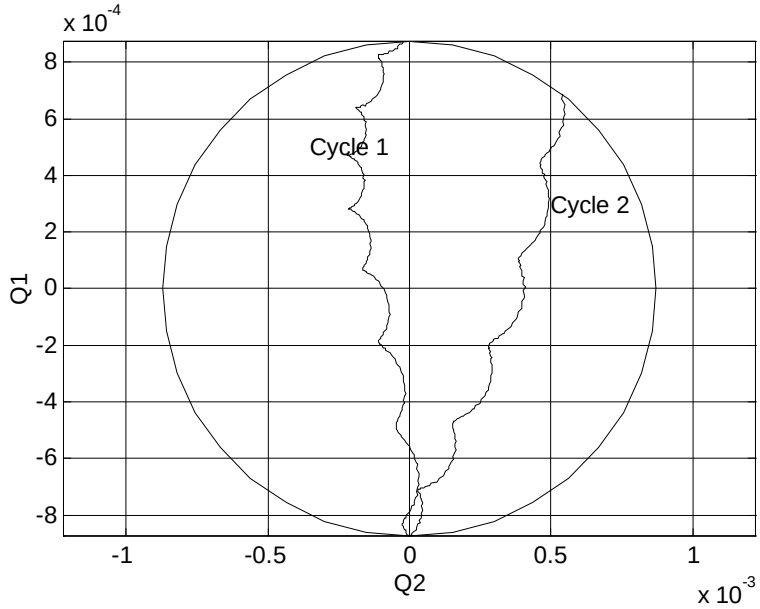

Figure 5.21 : Inclination Station Keeping

For cycle 1 the NS station keeping cycle length is about 103 days, and for cycle 2, about 72 days. The reduction is the result of a non-optimal path across the inclination tolerance circle for cycle 2. Approximating the motion as a chord of the tolerance circle, for cycle 1 the path followed is much closer to a diameter than for cycle 2, although neither cycles follow a true diameter.

This leads to an optimisation solution to maximise the interval between manoeuvres. If during the cycle the inclination vector passes through Q1=Q2=0 (i.e. the inclination passes through zero) then the starting position is referred to as an 'optimal node' and the interval between burns is a maximum. The value of this starting node can be found by propagating the orbit backwards from Q1=Q2=0, however this significantly lengthens the simulation run-time length as the procedure has to be performed for each cycle. A simpler approach using a simplified orbital model and including linearised effects of EW station keeping which attempts to optimise inclination control for the entire mission duration without the need for backwards integration is presented in Soop [27] and is used for mission support by ESA, however this too is beyond the complexity required here where inclination station keeping is not the primary concern.

Instead therefore a regular NS schedule will be followed, at the end of which the inclination vector will be set back to the initial values. This system reduces the user control of the inclination vector to the selection of the initial starting values of 'Q1' and 'Q2', and these will now be considered.

For single satellites or colocated satellites with no inclination separation it is preferable to start the cycle with Q2=0 for the reasons already given. In terms of 'Q1' a symmetrical approach about the 'Q2' axis is preferred, the initial value being selected so that the inclination at the beginning and end of the NS cycle are roughly equal. Where inclination separation is used it is preferable to separate the satellites such that the inclination path of a single satellite will never intersect the path of any other satellite (even if the two are not simultaneously at the same point), in some cases this will not be possible though. To perform the initial selection of 'Q1' and 'Q2' as outlined a design tool which here-after will be referred to as the, '*region of probable inclination vector motion*', was created. This is defined as a region of the inclination plane within which the inclination vector will remain, in the absence of control errors, during any one NS cycle (regardless of the position in the 18.6 year perturbation cycle). The geometry can be determined from the initial values of 'Q1', 'Q2' and the NS cycle length and is illustrated in figure 5.22.

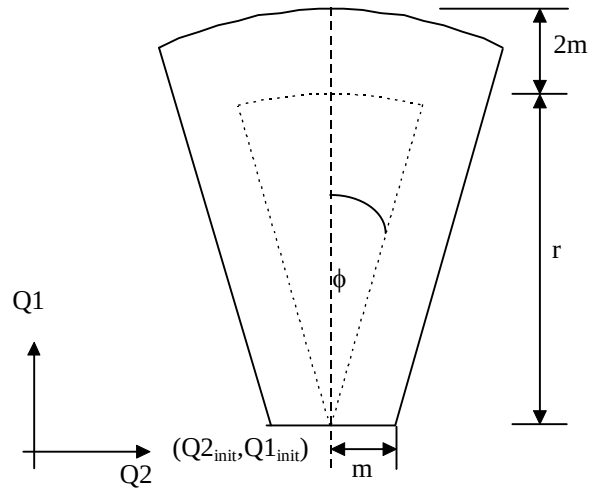

Figure 5.22 : Region of Probable Inclination Vector Motion

The sector of a circle shown using dotted lines in the diagram represents the region within which the inclination vector would remain if the drift rates of 'Q1' and 'Q2' were purely linear. To allow for the oscillatory motion that is superimposed on the linear (see figure 5.20) the amplitude of the largest oscillations, ±m is used to define the larger region bordered by solid lines. The variables [r, ϕ] are defined as,

$$\begin{aligned} r &= \tan\left(i_{max}/2\right) \\ \phi &= \pi/2 - \tan^{-1}\left(\left(dQ1/dQ2\right)_{max}\right) \end{aligned} \tag{5.53}$$

The values of $(dQ1/dQ2)_{max}$ and i_{max} are then found from the linear component in the 'Q1', 'Q2' data shown in figure 5.20 for the years producing maximums and the 'm' variable is found from the amplitude of the largest oscillation on the 'Q1', 'Q2' motion. Numerically these quantities were found to be,

$$\begin{aligned} m &= 0.000075 \\ \left(\frac{dQ1}{dQ2}\right)_{max} &= 2.07 \\ i_{max} &= 0^{o}.943 \times \left(\frac{T_{NS}}{365 \times 86400}\right) \times \frac{\pi}{180} = 5.22 \times 10^{-10} T_{NS} \end{aligned}$$

During the user input stage of using the developed software the region of probable inclination vector motion is displayed for each satellite simultaneously as an aid to cluster design. Figure 5.23 shows a screenshot of the input window on which this is done.

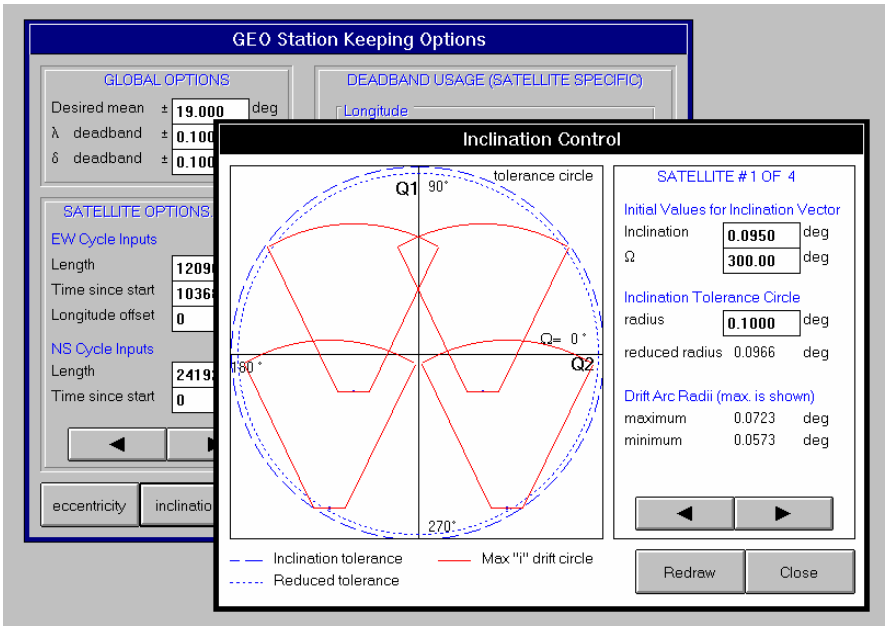

Figure 5.23 : User Input of Inclination Vector

Figure 5.23 shows a four satellite cluster with a NS cycle time of 28 days. The tolerance circle radius corresponds to an inclination of 0.1°. As noted earlier it is not always possible to position the regions with no overlap and this is evident in the diagram.

5.3.5 : Software Implementation of NS Station Keeping

As was done for EW control in section 5.2.4 this section is included to illustrate how the preceding theory has been incorporated into the propagation software to produce autonomous station keeping and to show the stability of the resulting motion.

To address the first point the key steps involved in the NS corrective cycle are shown in a flow chart and to address the second, simulation results over two 20 year periods, each with a different length of NS cycle, are shown graphically.

NS Cycle End Procedure

The length of the NS cycle in days is specified by the user, however the actual time of day when the NS correction is applied is computer controlled as a result of the limitations imposed by equation (5.52) which determines 'L'. Since 'Q1' and 'Q2' vary continuously so too do 'ΔQ1' and 'ΔQ2' and thus it is not possible to compute 'L' from

(5.52) analytically. To overcome this the software uses an iterative process to find the time at which to apply the correction, and then calculates the size of the correction from equation (5.51). The procedure is illustrated in more detail in figure 5.24.

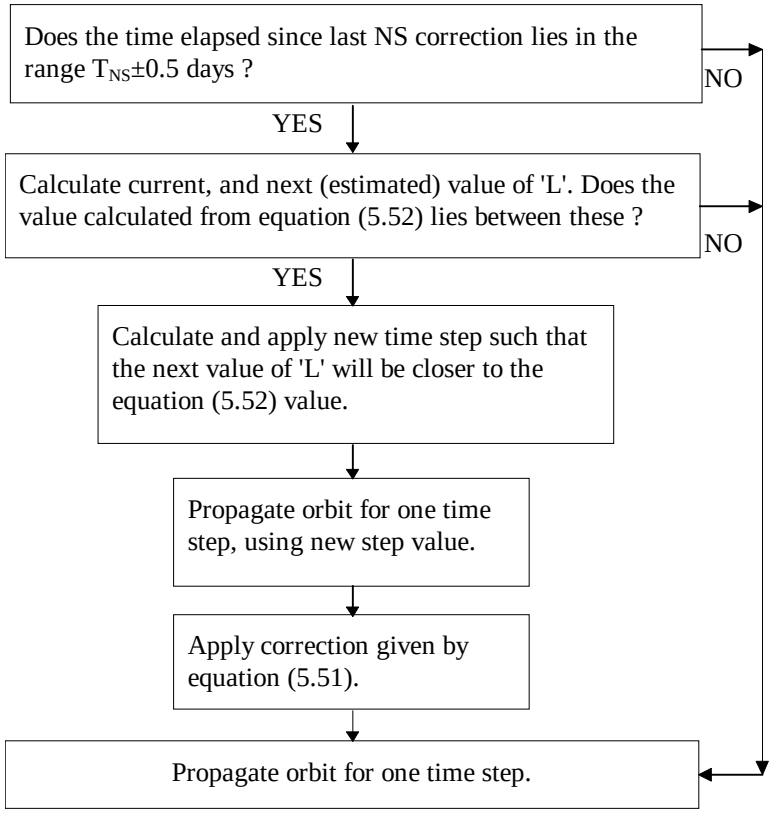

Figure 5.24 : NS Station Keeping Cycle End Procedure

In estimating the 'n+1th' value of 'L' from the 'nth' value the orbit was approximated to an ideal GEO and thus,

$$L_{n+1} \approx L_n + n_E \Delta t$$

where 'Δt' is the integration step size and 'n_E' is the angular velocity of the Earth about its own axis. Using this the new value of 'Δt' in step 3 can be calculated using the equation (5.52) value of true longitude, '$L_{5.52}$', in place of 'L_{n+1}' and rearranging, thus,

$$\Delta t = \left(\frac{L_{(5.52)} - L_n}{n_E} \right)$$

Since the orbital position at which the NS correction is applied is only approximately correct errors are expected in the post-burn values of 'Q1' and 'Q2', however both these elements vary slowly compared to a typical step interval of around 300 seconds and so the effect is minor. The proof of this is evident from figure 5.25 which is described next.

Simulation Results, Evolution of Inclination Vector With Station Keeping

With NS station keeping enabled two simulations were performed, the first using a NS cycle length of 28 days and the second, 56 days. In both the duration of the simulation was 20 years and the initial values of [Q2, Q1] were [0,-0.00035]. Data is shown for the years 1990, 1995, 2000, 2005, 2010 along with the regions of probable inclination vector motion, which are different for each simulation, in figure 5.25.

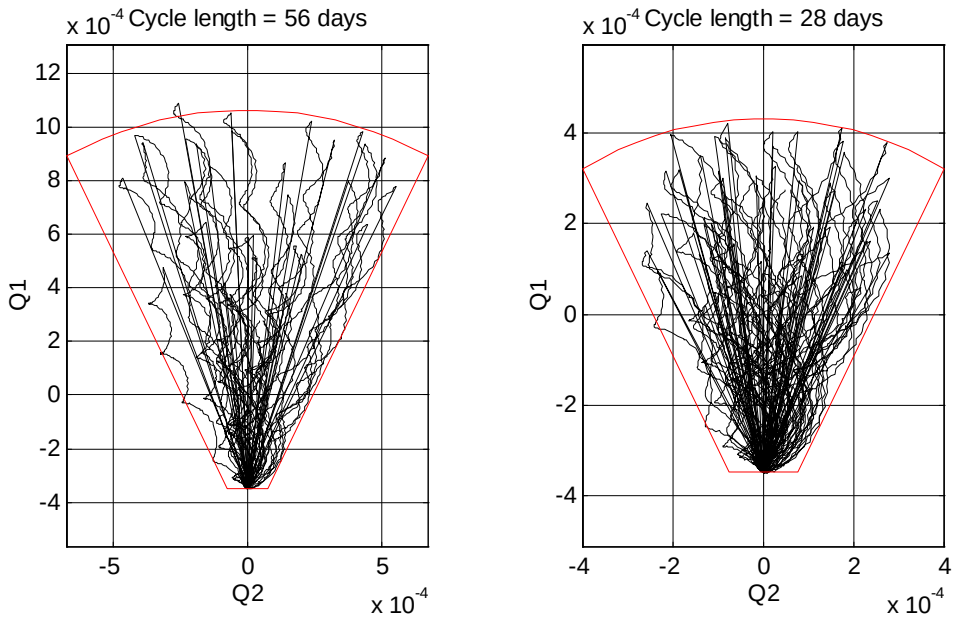

Figure 5.25 : Inclination Evolution Over 20 Years With NS Station Keeping

From the diagram note that the post-correction values deviate very little from the initial values of 'Q1' and 'Q2' - validating the approximations made in section 5.3.3 for NS manoeuvre time calculations.

5.4 : Station Keeping Error Analysis

5.4.1 : Overview

'If something can go wrong, it will go wrong'

Murphy's Law

Control of a GEO satellite is inexact. In practice neither the position or velocity is exactly known, and even if they were station keeping manoeuvres based on these would be applied inexactly due to imperfect thruster firing. To create a realistic model of GEO satellite control it is therefore necessary to include the effect of errors in the orbit propagation program. The topics that need to be addressed are,

- Quantification of errors (including the source of errors).
- Simulation of errors (i.e. how they are represented in orbit propagation).
- Error control methods.

Each of these topics will now be discussed individually, at the end of which simulated results for satellite control including the effects of errors will be presented.

5.4.2 : Quantification of Errors

The error sources affecting a satellite orbit can be divided into three groups, namely,

1. Tracking errors. These are due to imperfect knowledge of the satellite orbit. In practice their size will be determined by the characteristics of the controlling ground station(s). Bias and random components exist.
2. Burn execution errors. These are due to thruster firing inaccuracies and take the form of both directional and magnitude errors. Again bias and random components exist.
3. Mathematical modelling limitations. Station keeping correction manoeuvres are calculated from a model of the orbital motion not the actual motion. Discrepancies between these leads to errors in satellite control.

It has been assumed that the bias errors in 1 and 2 can be eliminated during the station acquisition phase of the mission and are not therefore modelled. The remaining errors will now be quantified.

Tracking Errors

The tracking errors used are based on measurements of the range 'ρ', the azimuth 'α' and the elevation 'ζ' of a satellite as measured from a single ground station. The geometry of this is illustrated in figure 5.26.

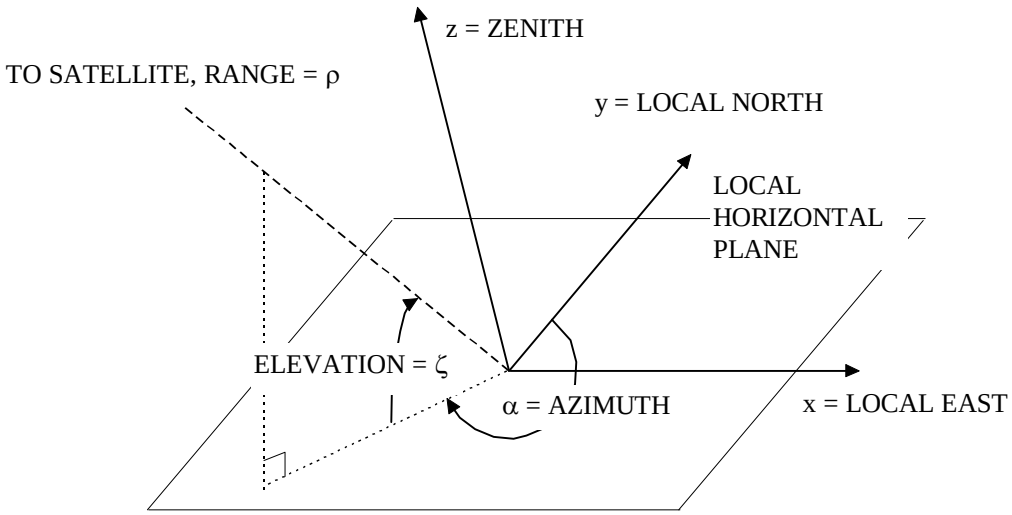

Figure 5.26 : Ground Station Topocentric Co-ordinates

The overall tracking errors are normally distributed with values quoted from Soop [31] of,

$$\Delta\rho \approx \pm 10 \text{ m}$$
$$\Delta\alpha \approx \pm 0^{o}.01$$
$$\Delta\varepsilon \approx \pm 0^{o}.01$$

at the 3σ level. Transforming these to equinoctial variable errors is complicated by the fact that both the longitude and latitude of the ground station in relation to the satellite affects the results. Since no specific satellite is to be simulated several relative

geometry's between satellite and ground station were considered and average equinoctial errors found. The resultant values, again at the 3σ level are,

$$\begin{aligned} \Delta L &\approx \pm 0.^{o}0075 \\ \Delta a &\approx \pm 500 \text{ m} \\ \Delta P1 &\approx \pm 0.000045 \\ \Delta P2 &\approx \pm 0.000045 \\ \Delta Q1 &\approx \pm 0.000034 \\ \Delta Q2 &\approx \pm 0.000034 \end{aligned} \tag{5.54}$$

These too are normally distributed and have mean values of zero. It is worth noting that changes in geometry between satellite and ground station have most effect on 'L' and 'a' and the 3σ errors for these can vary considerably from those listed in equation (5.54). An upper error limit exists however and this is based on the tracking requirements, basically the errors at the beginning of a station keeping cycle should not be large enough to cause a violation of the longitudinal deadband at the end of the cycle. With this restriction tracking requirements based on station keeping cycle length can be used to dismiss unsatisfactory ground station locations. Also note that since the station keeping procedure uses mean element values calculated via a least squares method the resulting errors in the mean elements at 3σ will be lower than the 'instantaneous' errors of equations (5.54). Knowledge of the accuracy of the mean elements is not required for software implementation and is not included here. A more comprehensive description of satellite tracking can be found in Soop [31] and Pocha [29].

Manoeuvre Execution Errors

Both the magnitude and the direction of the station keeping manoeuvre burns are modelled and both are assumed to be normally distributed with zero mean. Equation (5.55) lists a range of values for these, the lower are quoted from Eckstein et al [14] which refers to the TV-SAT-2 satellite and the higher are thought to be maximum acceptable values.

The directional errors are represented as the percentage of the applied burn which is cross-coupled into undesired axis directions (for example in the case of a NS burn the

undesired resulting velocity components along radial and orbit tangential/EW directions) and the magnitude error is a percentage of the desired nominal velocity increment. At the 3σ level the error ranges are given as,

$$\begin{aligned} \text{Magnitude error} &\approx \pm 2\% \text{ to } \pm 5\% \\ \text{Cross-coupling error} &\approx \pm 0.87\% \text{ to } \pm 2\% \end{aligned} \tag{5.55}$$

A third manoeuvre error exists in the time of execution of the correction. Since this can be controlled (theoretically) by careful planning it will be assumed to be negligible.

Mathematical Modelling Limitations

The graphs shown in figures 5.11 to 5.15 for EW station keeping, and figure 5.25 for NS station keeping illustrate the controlled motion of a GEO satellite with no error sources except those due to mathematical model limitations. Since this motion is clearly stable and within the prescribed window tolerances (see particularly figure 5.11 for the longitude evolution and figure 5.25 for inclination) the mathematical model limitations appear negligible.

5.4.3 : Simulation of Errors

As defined all the errors listed are normally distributed with zero mean. In simulating the errors the normal distribution has been truncated at the 3σ level which corresponds to the 99.87% confidence level.

To formulate mathematically relationships to allow absolute errors to be calculated two new sets of variables are introduced. The first set is 'ε_j' where 'j' is a subscript distinguishing one element from another. Each element of this set is a random variables having a normal distribution, and thus every time a specific element is used it will have a different value. With the 3σ truncation point the maximum value of an individual 'ε_j' element is ±3. The second set of variables are constants calculated from equations (5.54) and (5.55) and will be referred to as error coefficients. In representing these the symbol 'c' will be used, again with some distinguishing subscript.

The mathematical formulation of errors using these variables is detailed below.

Tracking Errors

Equations (5.54) list the 3σ errors for each of the equinoctial orbital elements. Every time the station keeping procedure of the propagation program is called these are used together with the actual propagation values to calculate approximate variables which include error components that are intended to represent tracking errors. The actual values of the equinoctial variables thus used to compute the station keeping manoeuvres and the associated error coefficients are,

$$\begin{aligned} L &= L_{actual} + c_L \varepsilon_L & c_L &= 0.000044 \\ a &= a_{actual} + c_a \varepsilon_a & c_a &= 133 \\ P1 &= P1_{actual} + c_{P1} \varepsilon_{P1} & c_{P1} &= 0.000015 \\ P2 &= P2_{actual} + c_{P2} \varepsilon_{P2} & c_{P2} &= 0.000015 \\ Q1 &= Q1_{actual} + c_{Q1} \varepsilon_{Q1} & c_{Q1} &= 0.000011 \\ Q2 &= Q2_{actual} + c_{Q2} \varepsilon_{Q2} & c_{Q2} &= 0.000011 \end{aligned} \tag{5.56}$$

The coefficient values were calculated from (5.54) by dividing by 3, to obtain 1σ values. In addition the coefficient for true longitude has been converted from degrees to radians.

Manoeuvre Errors

The actual applied velocity increments for NS and EW station keeping can be written in orbital axes (see appendix A.1.4) as,

$$\begin{aligned} \underline{\Delta V_{NS}} &= \left(1 + c_b \varepsilon_b\right) \Delta V_{NSideal} \begin{bmatrix} c_d \varepsilon_1 \\ c_d \varepsilon_2 \\ \sqrt{1 - \left(c_d \varepsilon_1\right)^2 - \left(c_d \varepsilon_2\right)^2} \end{bmatrix} \\ \underline{\Delta V_{EW}} &= \left(1 + c_b \varepsilon_b\right) \Delta V_{EWideal} \begin{bmatrix} c_d \varepsilon_1 \\ \sqrt{1 - \left(c_d \varepsilon_1\right)^2 - \left(c_d \varepsilon_3\right)^2} \\ c_d \varepsilon_3 \end{bmatrix} \end{aligned} \tag{5.57}$$

Where the directional cross-coupling coefficient is 'c_d' and the burn magnitude error coefficient is 'c_b'. Note that since these two vectors are not calculated at the same time

the 'ε_j' variables will differ for each. Using equations (5.55) the error coefficients are found as,

$$\begin{aligned} c_d &= 0.0029 \text{ to } 0.0067 \\ c_b &= 0.0067 \text{ to } 0.0167 \end{aligned} \tag{5.58}$$

Implementation of Errors

To illustrate more clearly how equations (5.56) to (5.58) are used to simulate tracking and manoeuvre errors figure 5.27 is included which shows the key steps in the process.

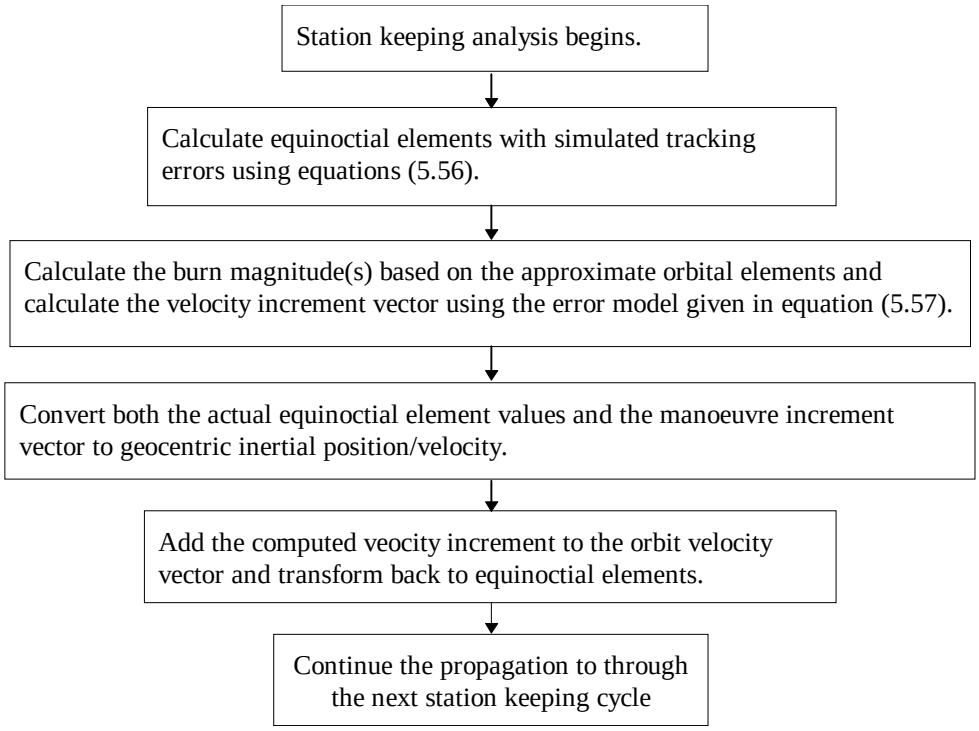

Figure 5.27 : NS Station Keeping Cycle End Procedure

5.4.4 : Error Control Methods

Four techniques can be employed to perform error correction/control and are summarised as,

1. GEO window reductions, in which segments of the longitude deadband are reserved to accommodate possible station keeping control errors which would otherwise lead to longitudinal violations occurring.
2. Satellite cluster design, in which the initial orbital elements of individual colocated satellites are selected to minimise close approaches.

3. Adaptive station keeping, in which each station keeping burn is computed based on the satellite position (including tracking errors) immediately prior to the manoeuvre such that an 'ideal' target orbit at the end of the next station keeping cycle is aimed for.
4. NS and EW burn phasing, in which the interval between NS and EW corrections are selected to reduce the effect of cross-coupling thruster errors.

All the methods are used in the satellite simulations presented in later chapters and the specifics of each will now be detailed. Since the first and second methods are intrinsically linked they are covered under a single heading.

GEO Window Reductions

For single GEO satellites this is often the only error control strategy required. By quantifying the probable errors to some suitable confidence level reductions to the GEO window can be made, effectively reducing the usable deadbands but providing provision for errors upto the desired limit.

Reductions to the latitude deadband (defined by inclination tolerance in section 5.3) are primarily due to imperfect knowledge of the [Q1, Q2] variables. Since inclination vector drift is mainly a function of the relative positions of the Sun and Moon and is only weakly related to the initial values of these variables then the reduction to the inclination tolerance can be approximately found directly from the tracking errors. The reduced inclination tolerance can be found from the differences between the radii of the overall window inclination tolerance circle ($\tan(i_{tol}/2)$) and the reduced tolerance circle ($\tan(i_{redtol}/2)$) which is '$\Delta Q1$' less than this (equation (5.54) lists identical inaccuracies for both 'Q1' and 'Q2'). Thus,

$$i_{redtol} = 2\mathrm{Tan}^{-1}\left(\mathrm{Tan}\left(i_{tol}/2\right) - \Delta Q1\right) \qquad (5.59)$$

As an example of the application of the reduction to a simulated cluster, the inclination plane spacing shown in figure 5.23 should be re-done so that the regions of probable

motion on the inclination plane all lie within the reduced tolerance circle given by equation (5.59). Unfortunately doing this results in a further overlap of the probable motion regions which could be compensated for by a reduction to the NS cycle length, however this will not be done since avoidance of close approaches within the GEO window are to be dealt with by a collision avoidance/recovery procedure detailed in a later chapter of this document.

Longitudinal deadband reductions are more complex due to the increased variables affecting the motion, specifically [L,a,P1,P2]. To add further complications reduction calculated for one side of the longitudinal window can be different from those calculated for the other. Figure 5.28 shows an example of a longitude deadband for one satellite and how this is segmented into usable and reserved segments. In this case the Earth triaxiality effect causes a longitudinal drift acceleration Eastwards (and hence the EW manoeuvres take place at the Western limit of the window).

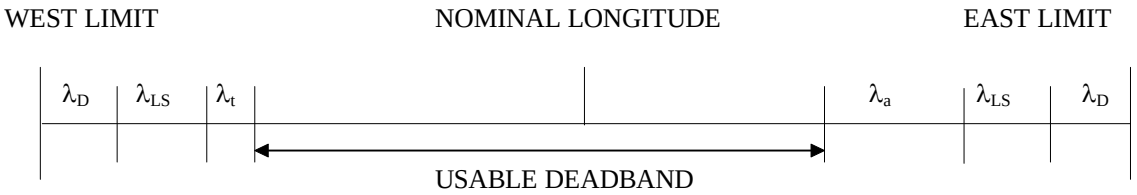

Figure 5.28 : Longitudinal Deadband Reductions

The reductions named in figure 5.28 are defined in table 5.1.

REDUCTION	EFFECTED LIMIT	DESCRIPTION
λ_D	Both	Orbit determination error for 'λ' using section 5.4.2 data this is approximately 0.°0075.
λ_{LS}	Both	Second order Luni-Solar perturbations, approximately 0.°007 (Hubert et al [2]).
λ_a	East	Errors in 'a' at the start of the cycle change the position of the turn around point on the longitude parabola halfway through the cycle. This is allowed for by reserving a segment of the deadband at the Eastern limit. The size of this is proportional to the EW cycle length. For a two week period this is approximately, 0.°02 based on knowledge of the mean value of 'a' to ±70 at 1σ (Pocha [29]).
λ_t	West	Errors in time of execution of an EW burn lead to errors in longitude at the beginning of the cycle which is allowed for by a reduction in the Western limit of the deadband. This has been assumed to be negligible.

Table 5.1 : Longitude Deadband Reductions

The usable deadband remaining after the reductions must accommodate both the daily eccentricity libration and the nominal triaxiality parabola. Sometimes the eccentricity allowance is included as a further reduction to the window deadband (see Hubert et al [2], Pocha [29] and Mirota et al [4] - the last includes computational procedures for quantifying the allowances), in this case the required reductions will again be asymmetric since the eccentricity vector magnitude will change during the cycle.

Both the longitude and latitude reductions discussed above can be applied to individual satellites, however this becomes progressively more unworkable as satellites are added to the window and the usable deadbands become so small that cycle lengths of one week or less for EW station keeping become necessary. Additionally since in normal operation the reserved areas of the deadband will not be used (over 60% of the time errors will not exceed the 1σ level) the window is not being used in an optimum way.

For these reasons deadband restrictions for the colocated satellites of primary concern here will be applied to the GEO window as a single entity and not to individual satellites within that window. Close approaches between satellites within the window will be discussed later.

The final reductions applied to the window will be those calculated from equation (5.59) for latitude restrictions, and those shown in figure 5.28 and quantified in table 5.1 for longitude restrictions. Ensuring the reductions are applied is done at the cluster design stage and not during the orbit propagation phase of the simulation. The tasks to be done are summarised as,

- Positioning the region of probable motion of the inclination vector on the inclination plane such that it lies within the reduced limits specified by equation (5.59) which is based on the overall latitude tolerance.
- Positioning the eccentricity control circles for individual satellites on the eccentricity plane so that these do not exceed the reduced eccentricity tolerance calculated from the longitude restrictions of table 5.1 and the expected motion due to triaxiality.
- Ensuring any longitude offset between satellites does not cause longitude deadband violations by failing to observe other effects.

Adaptive Station Keeping

Errors in station keeping lead to a non-ideal orbital path between manoeuvres. In correcting this it is not possible to calculate the size and times of the required manoeuvres in advance. Instead a more adaptive approach is needed which 'looks at' the orbital elements during the cycle, decides on the best time to initiate the manoeuvre and then attempts to apply a burn which will change the orbital elements to 'target' values. Since the burn applied will be non-ideal due to tracking and thrust errors the process is repeated for every cycle of the mission lifetime.

An ideal station keeping manoeuvre would change all the orbital elements to the target values instantly. Although this is theoretically possible for the variables

[a,P1,P2,Q1,Q2] (although coupling between them means a single burn is not sufficient to correct all simultaneously) the Greenwich longitude cannot be changed in this way. In this case the target value aimed at is at the *end* of the next station keeping cycle and the Greenwich longitude is slowly corrected (theoretically) throughout the upcoming cycle until this point is reached.

In sections 5.2 and 5.3 analytical equations based on the actual values of the orbital elements immediately prior to the corrective burn, using a set of suitable target elements for the orbit immediately after the burn (or in the case of Greenwich longitude at the end of the next cycle) were derived for both EW and NS station keeping (respectively, equations (5.32) and (5.38) for EW and equations (5.51) and (5.52) for NS). In this way the analytical relationships required to provide an autonomous adaptive scheme have already been generated.

Replacing the actual orbital element values prior to a correction by values including simulated tracking errors from equations (5.56), and using equations (5.57) to simulate thruster errors completes the description of how adaptive station keeping has be included in the station keeping element of the propagation software.

NS and EW burn phasing

In magnitude terms the size of the NS burn is usually much larger than the EW (a four week NS station keeping burn is around 5 m/s where-as a two week EW burn is only about 0.05 m/s - i.e. two orders of magnitude difference). The absolute size of the burns can be reduced by shortening the respective cycle lengths, however the magnitude discrepancies between EW and NS burns still persists.

In practical terms this means the *absolute* burn error which is cross-coupled into the undesired orbital axis directions is usually much larger following a NS burn, for example using equations (5.57) and (5.58) at the 1σ level the resulting velocity magnitude in the EW direction could be 0.015 m/s which is significant. To overcome this it is usual to phase the NS and EW burns so that the EW correction can 'counteract'

the EW cross-coupling error from the NS burn. Following any thruster manoeuvre, time is required to accumulate sufficient statistical data to perform an accurate orbit determination (and hence evaluate the effect of the manoeuvre) and for this reason it is usual to leave around two days between the NS and the first EW burns.

5.4.5 : Software Implementation and Overall Results

Software Implementation

Figure 5.29 summarises the complete station keeping procedure as implemented in the software with emphasis on the simulated errors as discussed. For clarity the diagram represents an example case in which the EW cycle is 14 days, the NS is 28 days, and the phasing between NS and EW corrections is 2 days. The propagation intervals between corrections are given as approximate values in days since the exact time of day for an optimal manoeuvre it not known in advance.

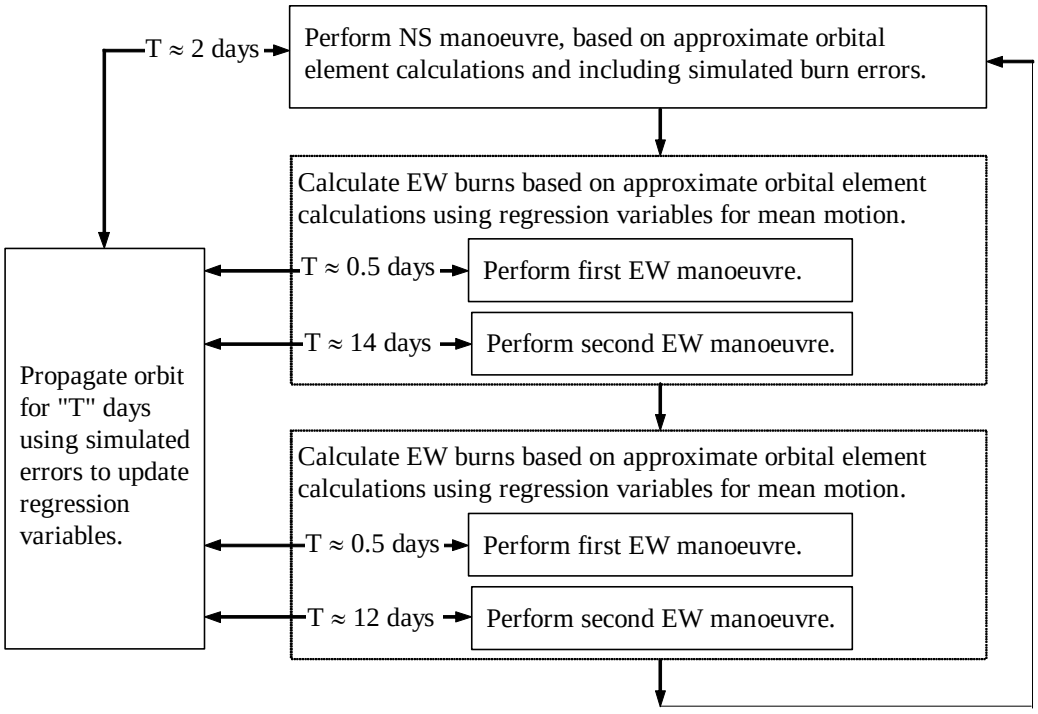

Figure 5.29 : Complete Station Keeping Procedure

Propagation Results With Simulated Station Keeping Errors

In practical situations the station keeping manoeuvre errors will be responsible for the majority of 'visible' station keeping control errors, specifically the longitude cross-coupling effect of the NS burn into radial and longitudinal directions is the biggest single source (Hubert et al [2]).

Since the aim of the propagation program is to provide a realistic simulation of the controlled orbit of a GEO satellite it is worth demonstrating that the errors affect the orbit as expected and that the control scheme given in sections 5.2 and 5.3 provides a stable and acceptable control method.

To this end a series of propagations were performed with the following control conditions imposed on the satellite.

1. Nominal longitude of 19° East with longitude and latitude deadbands of ±0°.1.
2. Eccentricity centre of zero, control circle radius of 0.00015 (theoretical minimum of 0.00004 corresponding to a surface area to mass ratio of 0.014).
3. Initial right ascension of ascending node of 270° with inclination magnitude of 0°.05 (corresponding to Q1 = 0.000436; Q2 = 0).
4. EW and NS cycle lengths of 14 and 28 days respectively, with a two day period for orbit determination between NS and EW manoeuvres.

In each case the impact of the included errors on the controlled orbit was examined. To represent the in-plane elements the Greenwich longitude was monitored since this element is the most sensitive to imperfect station keeping control and must be maintained within the longitudinal deadband. To represent the out-of-plane elements the two 2D inclination vector (components $[Q2,Q1]^T$) was monitored to examine possible latitude violations.

As expected manoeuvre errors were responsible for the largest deviations and of the two manoeuvre errors simulated the most important to Greenwich longitude deviations was the magnitude of the directional error coefficient. In terms of the impact on the latitude deadband the simulated errors produced a much smaller effect (due to the fact that unlike Greenwich longitude to first order an initial error in [Q1,Q2] position does not increase over time).

To illustrate the differences between orbit propagations with and without error modelling the following graphs show the longitude and inclination response of an 'ideal' case with no simulated errors and an actual case in which the tracking errors listed in equations (5.54) have been used along with the upper limits of thruster firing errors (i.e. 5% magnitude and 2% directional cross-coupling) from equations (5.55).

Considering the longitude motion first, the 'ideal' evolution is shown in figure 5.30.

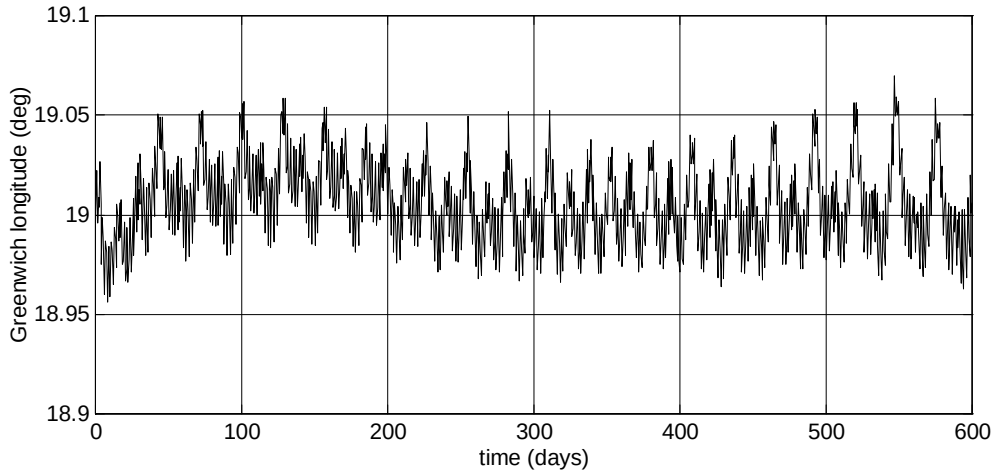

Figure 5.30 : Longitude Evolution; No Station Keeping Errors

There appears to be an underlying periodic motion in figure 5.30 which was not clear from figure 5.11 (a similar plot given in section 5.2). It is thought that this is a function of the approximations made in deriving the EW control procedure for the intermediate orbit between EW burns. Since the eccentricity burn component is larger for the propagation represented by figure 5.30 (the radius of the eccentricity control circle is

smaller) the motion during the intermediate orbit is more important and equation (5.38) becomes less applicable.

Due to the small amplitude of the oscillation removal of the effect by implementing a more complex the EW control scheme has not been done.

The same propagation including errors produces the response shown in figure 5.31.

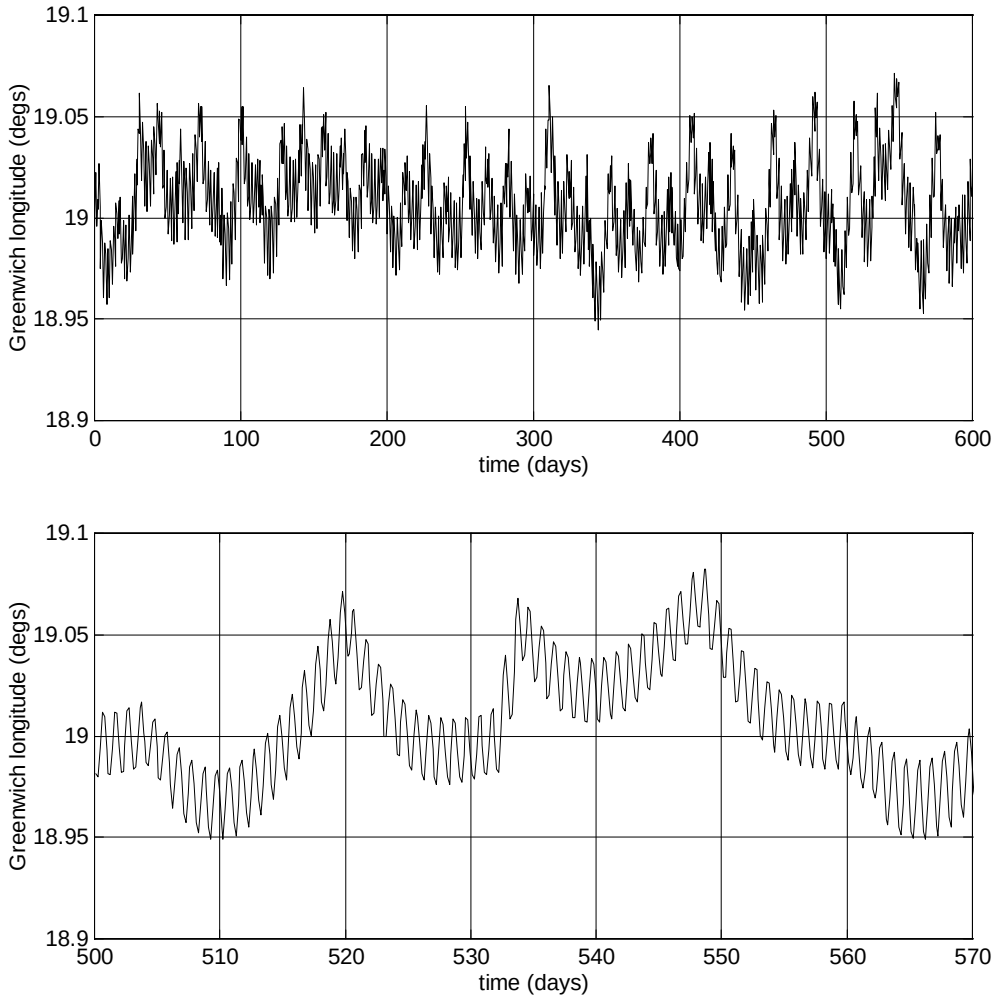

Figure 5.31 : Longitude Evolution; With Station Keeping Errors

From the first graph in figure 5.31 it is clear that the longitude evolution appears much more random than in figure 5.30, however the station keeping control software still maintains the longitude close to the nominal 19° value. Also of note is the amplitude of

the longitude envelope which is greater in figure 5.31 (although still controlled within tight control limits).

The second graph of figure 5.31 is an enlargement of the first and shows the motion between 500 and 570 days. At some point during the 532 day a NS manoeuvre is performed which causes a significant undesirable effect on the longitude motion. The EW manoeuvre starting during day 534 which is two days later effectively corrects this error, illustrating the effectiveness of NS-EW manoeuvre phasing.

The graphs for inclination vector evolution are shown in figure 5.32, along with the circle on the inclination plane representing 0.°1 inclination.

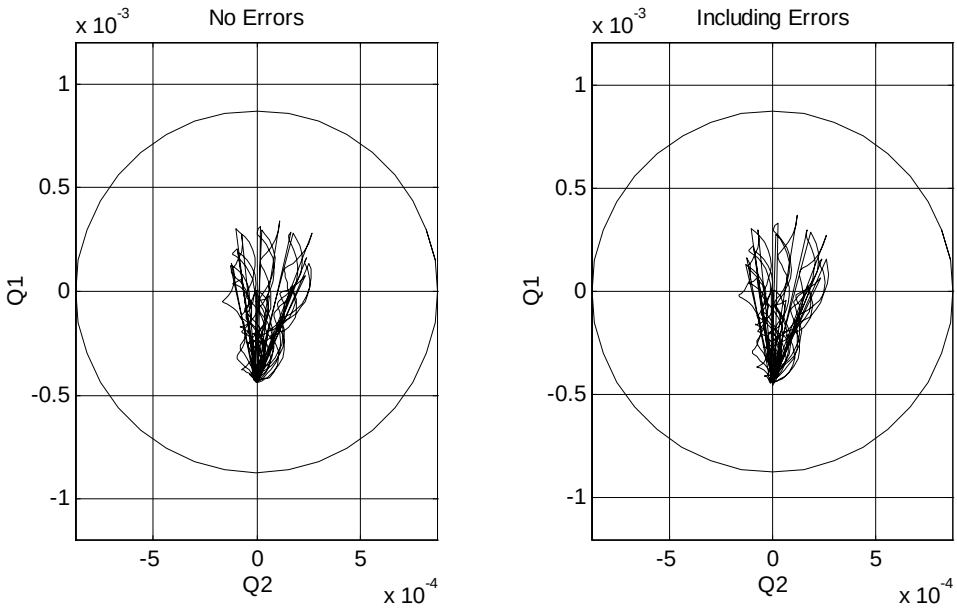

Figure 5.32 : Inclination Evolution; With and Without Station Keeping Errors

Again the differences are noticeable but small when compared to the tolerance circles. Cross-coupling effects from the EW manoeuvres are not noticeable, indicating that they are very small (as expected) and thus do not require correction.

6 : CLUSTER SIMULATION & RELATIVE MOTION

6.1 : Overview

There are too many combinations of possible colocation strategies to cover them all in detail in this document and it is the aim of this chapter to reduce the number under consideration using a knowledge of the mathematically derived advantages and disadvantages of each as gained from previous research (see chapter 3) and from more practical considerations such as additional costs and implementation problems.

In section 6.2 different cluster control options are discussed (e.g. SST), along with a description of the selected scheme (which is thought to be original).

Hill's equations of relative motion were introduced in chapter 2 to allow better visualisation of orbital element separation strategies and will be used to formulate a cluster geometry recovery strategy in the next chapter. The accuracy of these first order approximations is thus of interest and can now be evaluated using the simulation software described in chapters 4 and 5. This is detailed in section 6.3.

As for cluster control options, there are too many orbital element separation strategies to analyse them all here. In section 6.4 the number which are to be considered further are reduced to two and the reasons for 'dropping' the remainder are given.

From sections 6.2 and 6.4 two colocation configurations remain, each using the same cluster control algorithms but with a different orbital element separation method. Section 6.5 details the evolution of a four satellite cluster for each of these, including satellite approach frequency histograms and examples of the actual relative motion in comparison with the Hill's solution approximation. In chapter 7 similar plots will be used to illustrate the 'improvement' when the geometry recovery manoeuvre is included in the simulation software.

6.2 : Cluster Simulation and Control Options

6.2.1 : Synchronous Vs. Asynchronous Station Keeping

This subject has already been partially discussed in section 2.4, and a summary of the key points is repeated below.

- When used in isolation nominal separations between satellites do increase, however as the number of satellites increase the methods becomes ineffective since only a relatively small volume of the available GEO window is used.
- Used in conjunctions with orbital element separation the papers reviewed in section (3.2.2) agree that asynchronous manoeuvres tend to degrade the performance of orbital element separation strategies. Harting et al [8] presents an example using MLS with $\Delta\lambda=0.°05$. Introducing a one week manoeuvre offset the mean separation drops from about 20 km to 10 km.
- There is no fuel penalty in using a pure manoeuvre offset separation strategy.
- Asynchronous manoeuvres lead to lower peak ground station workload.
- Asynchronous manoeuvres lead to a variable cluster geometry, which presents complications for both SST systems and recovery manoeuvre calculations.

To these five points a sixth can be added which is related to the station keeping control algorithms derived in chapter 5. In section 5.2 the optimal right ascension, 's_1' (from which the time for the burn can be found) at which to perform the first of two EW corrections for an individual satellite was shown to be a function of the absolute values of the eccentricity vector components, $[P2, P1]^T$. If the 'e' vectors of each colocated satellite are separated, which they will be even if the E_3 and E_4 are nominally zero since the difference in other elements will cause slightly different perturbation accelerations and thus different eccentricity vector evolution, the optimal times for the manoeuvres for individual satellites will differ. Synchronous manoeuvres will thus produce non-optimal EW station keeping (even in the absence of control errors) since the time of the manoeuvres will only be 'ideal' for, at most, one satellite.

Considering all six points the author still believes asynchronous manoeuvres are best avoided for station keeping of large clusters of four plus satellites due to their inefficient use of the window in isolation and their degrading effect on orbital element separation strategies (although the ASTRA cluster at 19°.0 E successfully uses an intermediate scheme, controlling six satellites in three pairs).

Since synchronous manoeuvres have now been selected, the question of how to calculate the time to apply the EW correction for synchronous manoeuvres now needs addressing. Obviously a compromise case which produces minimum deviations from optimum manoeuvre time for all the satellites would be preferable and to do this a *reference orbit* is proposed which does not correspond directly to any satellite in the cluster but can be though of as representing the entire cluster for manoeuvre time calculations. The concept of a single reference orbit for colocation will be expanded on in section 6.2.4.

6.2.2 : Ground Based Tracking Vs Satellite to Satellite Tracking

SST has been proposed in several papers (e.g. Walker [1] and Murdoch et al [3]) as a means of obtaining data on the relative motion between colocated satellites. Since the absolute errors in the relative variables are smaller for SST than the absolute errors in the actual satellite variables measured by ground based tracking systems, co-variance analysis based on tracking measurements spread over time converges on an accurate solution more quickly for SST leading to 'faster' knowledge of the relative motion between satellites (although the absolute position is still determined by ground based tracking). In determining an erroneous relative orbit therefore SST appears to be greatly superior, however the difference diminishing with the development of improved ground based tracking systems (e.g. for DBSS an improvement in the quantity of tracking data can be realised by using the television signal as a range measurement, as discussed by DeAgostini et al [20] and used for tracking the ASTRA cluster Wauthier et al [19]).

An interesting extension of SST is the 'master-slave' colocation concept as discussed in Blumer [13] (reviewed in section 3.2.3). Specifically, a 'master' satellite is designated

which uses SST to evaluate the relative position of the remaining 'slave' satellites of the cluster and if geometry corrections are necessary they are calculated to re-establish the slave orbits with respect to the master from this data. If the hardware requirements of the master differ from those of a slave satellite then a back-up master appears to be required to avoid a single point failure system (adding to the cost). Extending the master-slave idea, control of the cluster could be reduced to control of the master satellite if the master is configured to autonomously control the remaining slave(s). From the point of view of the controlling ground station therefore the cluster is treated as a single satellite. Obviously this has problems when multi-agency control of the cluster occurs.

So far only the features and benefits of inter-satellite tracking have been discussed. In practical terms, the use of SST necessitates additional hardware on each colocated satellite, which incurs the following penalties.

1. Cost. Both the additional hardware and the validation costs must be considered. The latter could remove the savings possible in buying 'off-the-shelf' satellites.
2. Weight. The increased mass (from both the physical 'box' and the increased satellite power requirements leading to larger solar arrays) could affect the available fuel load, thus shortening the operational lifespan.
3. The view field of the selected sensors will have implications for the usable cluster geometries (individual satellites must remain within the viewable field of other satellites).

Considering all the factors discussed SST systems do not seem likely in practice for GEO DBSS applications and so are not considered further.

The tracking system used in the simulations discussed later will be a model of a ground based tracking system only, the specific limitations of which have already been quantified in section 5.4.

6.2.3 : Selected Control Strategy

To summarise the conclusions of sections 6.2.1 and 6.2.2 it was decided to use synchronous station keeping manoeuvres for each satellite in the cluster along with ground based tracking using the 'worst case' error model quantified in section 5.4. As already noted in section 6.2.1 a problem exists with synchronous station keeping in the timing of the EW manoeuvres, the optimum time for which will be different for each satellite. To overcome this a reference orbit has been defined which will now be defined.

Consider a single satellite positioned centrally in the GEO window, the nominal longitude is the longitudinal centre of the window and the eccentricity and inclination plane configurations are shown in figure 6.1 (simulation program screenshots).

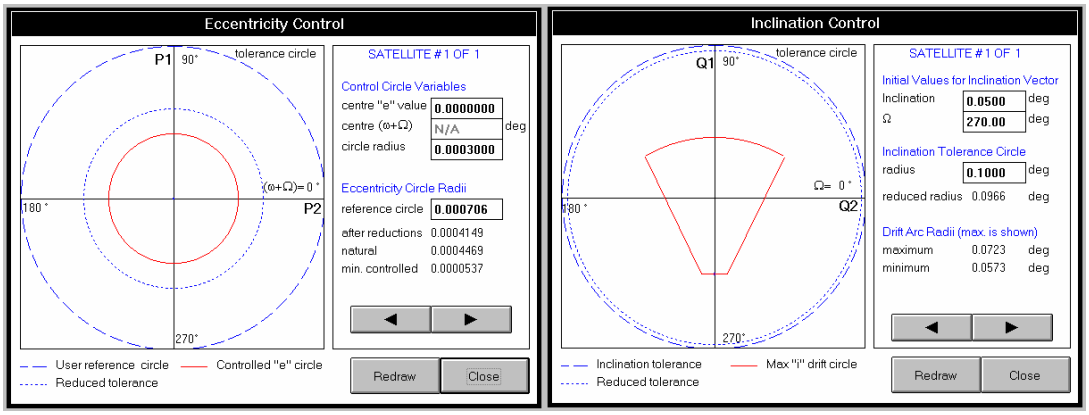

Figure 6.1 : Reference Orbit Eccentricity and Inclination Plane Configurations

For each cluster that is simulated the reference orbit is propagated for the entire propagation period with no manoeuvre or tracking errors, thus generating an 'ideal' single satellite propagation. The times at which the optimal EW station keeping manoeuvres occur for this case are recorded to a data file.

The actual cluster is then propagated (including simulated errors) and the EW burn times which were recorded for the reference orbit are used for the actual satellite EW station keeping burn times. The use of a centrally located 'phantom' satellite in this way

is thought to minimise the overall time differences between the ideal and the actual EW burn times for individual 'real' satellites.

The reference satellite will also be used as the origin of the relative axis frame [R,L,K]. Positions given in this frame are thus the summation of the actual nominal separation along that axis and the deviation from the ideal. This is the main reason why simulated control errors are not included in the 'phantom' satellite propagation.

To calculate the actual relative motion from the equinoctial orbit propagation files the procedure shown in figure 6.2 is followed.

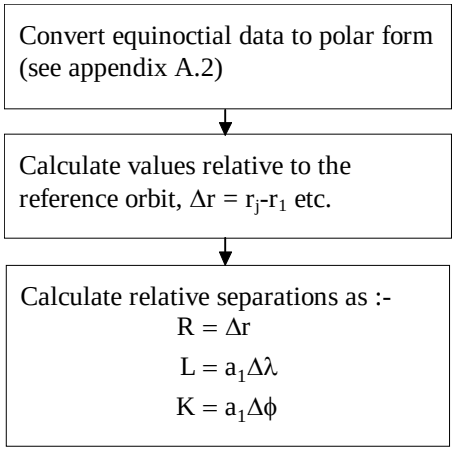

Figure 6.2 : Calculation of Relative Motion From Propagation Data

In figure 6.2 subscript '1' refers to the reference orbit value and 'j' refers to an actual satellite (j>1).

6.3 : Accuracy of First Order Relative Motion Equations

6.3.1 : Evaluation Procedure

In the next chapter Hill's first order equations of relative motion will be used to derive an analytical solution to the cluster geometry recovery problem. To use this solution effectively the inter-satellite separation distance at which the first corrective manoeuvre commences and the total time for the nominal geometry recovery (which are both user selectable) need to be determined. Since Hill's equations are approximations safety

margins must be used to allow for the gradual deviation of the approximate relative motion from the real relative motion and to allow for the instantaneous errors which result from the omission of second order and above terms from Hill's first order solution.

Two things need to be established. Firstly a maximum value for the amplitude of the relative motion deviation which is caused by the terms above first order (this will help determine the minimum inter-satellite separation distance at which a correction based on Hill's equations should be applied). Secondly, the time period during which the deviation of the first order relative motion from the actual relative motion remains within some prescribed limit (this will help determine the maximum time period between the beginning and end of the geometry recovery).

To perform the evaluation the approximate relative motion is calculated using equations (C.7) and (C.8) from appendix C and the actual relative motion is calculated using the procedure illustrated in figure 6.2.

6.3.2 : Comparison Test Cases

Two cases for the relative motion between two satellites (one of which will be a 'phantom' satellite as defined previously) will be presented. In both the nominal relative equinoctial variables [$\Delta\lambda$, Δa, $\Delta P1$, $\Delta P2$, $\Delta Q1$, $\Delta Q2$] are identical and are the maximum possible whilst still remaining inside a 19.°0E ±0.°1 GEO window. To achieve this the phantom satellite position on the eccentricity and inclination planes has been moved from that shown in figure 6.1. Note that this is the only time it is done. It is required here to illustrate the inaccuracies in Hill's equations for a 'worst case' scenario. The positions of the two satellites on the eccentricity and inclination planes is shown in figure 6.3.

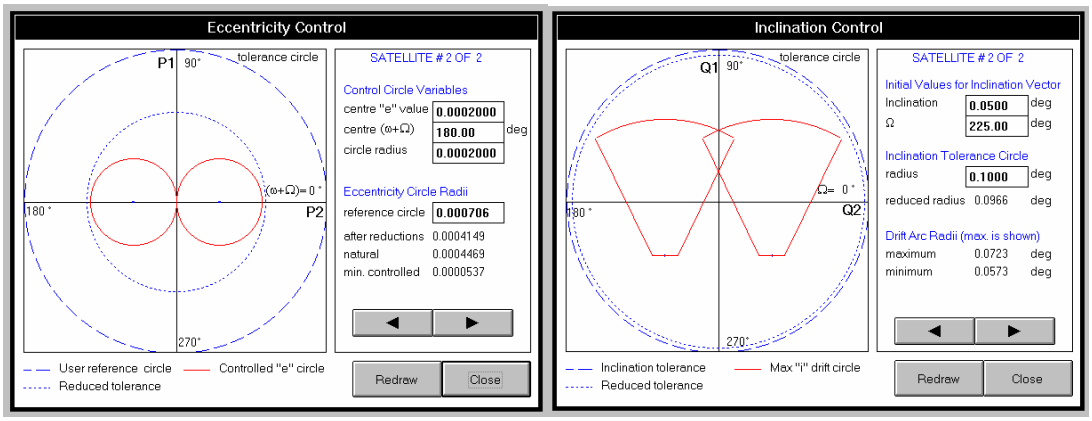

Figure 6.3 : Eccentricity and Inclination Plane Geometry For Test Cases

The relative equinoctial variables and the associated 'E_i' (i=1 to 6) variables are listed in table 6.1. In terms of the colocation geometries described in chapter 2 the strategy is a combination of MLS and EIS parallel. Each satellite has identical (A/M) ratios.

The propagation time period for the comparison is seven days. Use of Hill's equations for longer periods should not be required for cluster geometry correction calculations and so the accuracy after this period is not of primary importance.

RELATIVE EQUINOCTIAL VARIABLES				ASSOCIATED E_i VARIABLES			
$\Delta\lambda$	=	- 0.075	deg	E_1	=	- 55192.8	m
Δa	=	0.00	m	E_2	=	0.0	m
$\Delta P1$	=	0.0000000		E_3	=	16865.7	m
$\Delta P2$	=	- 0.0004000		E_4	=	0.0	m
$\Delta Q1$	=	0.0000000		E_5	=	0.0	m
$\Delta Q2$	=	- 0.0006171		E_6	=	- 52039.0	m

Table 6.1 : Relative Equinoctial Variables and Associated 'E_i' Values

It is worth noting that 'E_2' is zero. Since this is calculated from the difference in semi-major axis of the two satellites, and this in turn is nominally zero (to preserve an orbital rotation rate equal to the Earth's) 'E_2' will always be selected to equal zero.

The first test case is a simple orbit propagation, however during the second a NS station keeping manoeuvre occurs and is followed two days later by an EW burn pair. For both cases 'actual' relative motion is calculated using the absolute orbit propagator for two satellites to generate data which is then converted to the polar set [r,λ,ϕ]. Subtracting the first satellite polar values from the second and multiplying the angular variables by the semi-major axis of the first gives 'actual' relative positions in the [R,L,K] axis set.

The two first order Hill's equations predictions also differ, although only in the value of 't_0' which changes because the two cases are at different points in their respective EW cycles which leads to slightly different Greenwich longitudes and hence true longitudes.

The results and implications of the test cases are considered individually below.

Case 1 : No Station Keeping Manoeuvres in Propagation Interval

In figure 6.4 the relative motion graphs indicate that in magnitude terms Hill's equations provide a reasonable approximation to the actual relative motion over the propagation period shown. Examining the deviation graph below these, all three axis deviations show sinusoidal differences and the 'L' axis deviation also shows an underlying linear drift component which is potentially more dangerous.

Dealing first with the sinusoidal oscillations, these are thought to be a result of the second order and above terms which are missing from Hill's first order solution. In amplitude they are approximately equal at about 100 m.

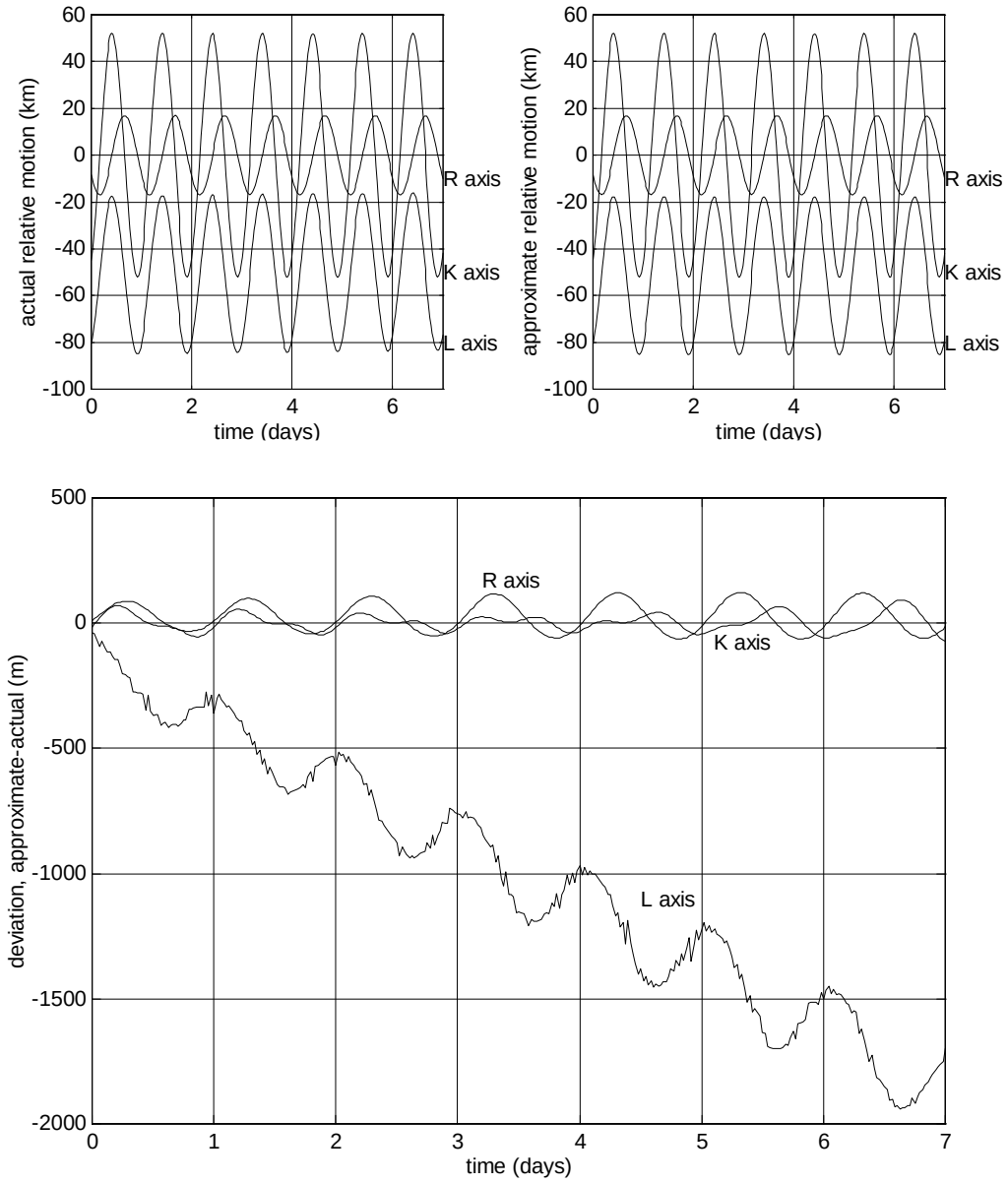

Figure 6.4 : Actual Relative Motion and Hill's Solution Deviations for Case One

The under lying linear drift in the 'L' axis deviation is more complex. In terms of equations (C.7) this could be explained by a non-zero 'E_2' variable which in turn would mean a non-zero value of 'Δa', however in the initial conditions no semi-major axis offset was introduced. To determine why 'E_2' is apparently non-zero the EW station keeping control strategy has to be considered.

In chapter 5 the Earth's triaxiality was shown to produce a constant longitudinal drift acceleration at a given Greenwich longitude (illustrated in figure 5.3). The resulting longitude evolution of a GEO satellite was thus shown to be parabolic and to optimise the EW cycle this parabola was 'selected' to be symmetrical about the nominal Greenwich longitude by introducing a suitable semi-major axis offset at the beginning of each EW cycle (see figure 5.5). Relating this to the test case presented here, the MLS component of the separation strategy means the longitudinal drift acceleration is slightly different for each satellite, and so the 'optimised' semi-major axes at the beginning of the EW cycle also differ, causing a non-zero 'E_2' value. For this test the difference in semi-major axes during the propagation period is shown in figure 6.5.

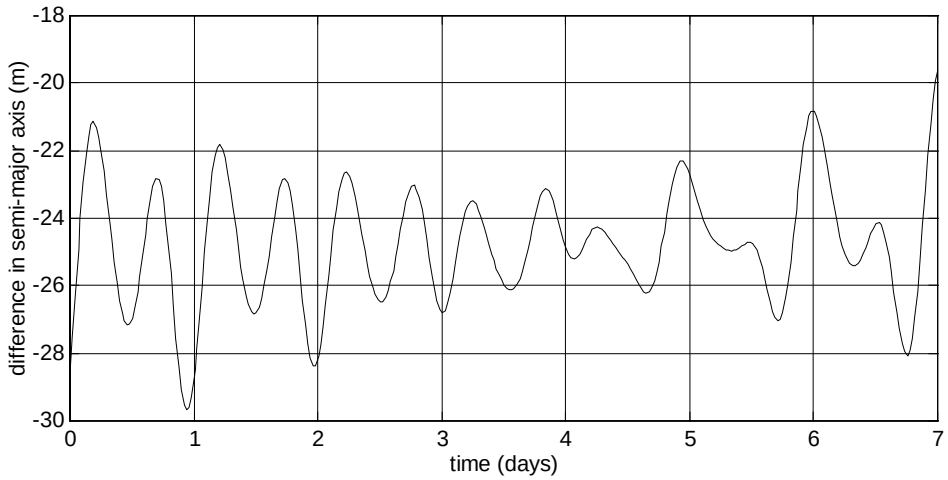

Figure 6.5 : Semi-major Axis Difference Between Satellites During Propagation

From figure 6.5 the mean difference in 'a' is approximately constant and equal to about -26 m (which accounts for the gradient of the 'L' axis deviation graph in figure 6.4), which means the non-zero 'E_2' is maintained throughout the cycle. Generally, the sign and magnitude of 'Δa' will vary as a function of the EW cycle length, the control strategy employed, and the nominal Greenwich longitude. The last of these is often not selectable, being controlled by ITU regulations, and its effects are worth considering in more detail.

Around 19° East the gradient of figure 5.3 is positive and since the optimised semi-major axis offset is proportional to longitude drift acceleration the satellite at the larger longitude (measured Eastwards) will have the larger semi-major axis. In terms of equations (C.7) this means that 'E_1' and 'E_2' will have opposite signs, resulting in the 'L' axis separation *diminishing* over time, which is potentially very dangerous. If the GEO window had been at a longitude position at which the gradient of figure 5.3 was negative the signs of 'E_1' and 'E_2' would be the same and the satellites would naturally drift apart during the EW cycle.

Examining figure 6.4 again, the drift rate is unlikely to cause serious problems during a 14 EW cycle at the start of which the nominal 'L' axis separation is about -50 km however for significantly longer EW periods the effect may be important. Reducing the size of 'E_1' is also unlikely to cause problems since the difference in longitudinal drift acceleration and hence 'Δa' will also reduce meaning a smaller value of 'E_2',

Although the 'E_2' effect has been shown to be negligible in most situations, it is interesting to note that even in the absence of station keeping manoeuvres errors if MLS is used the nominal value of 'E_2' will always be non-zero. This aspect of MLS does not appear to be mentioned in the literature reviewed in chapter 2.

Case 2 : NS and EW Station Keeping Manoeuvres in Propagation Interval

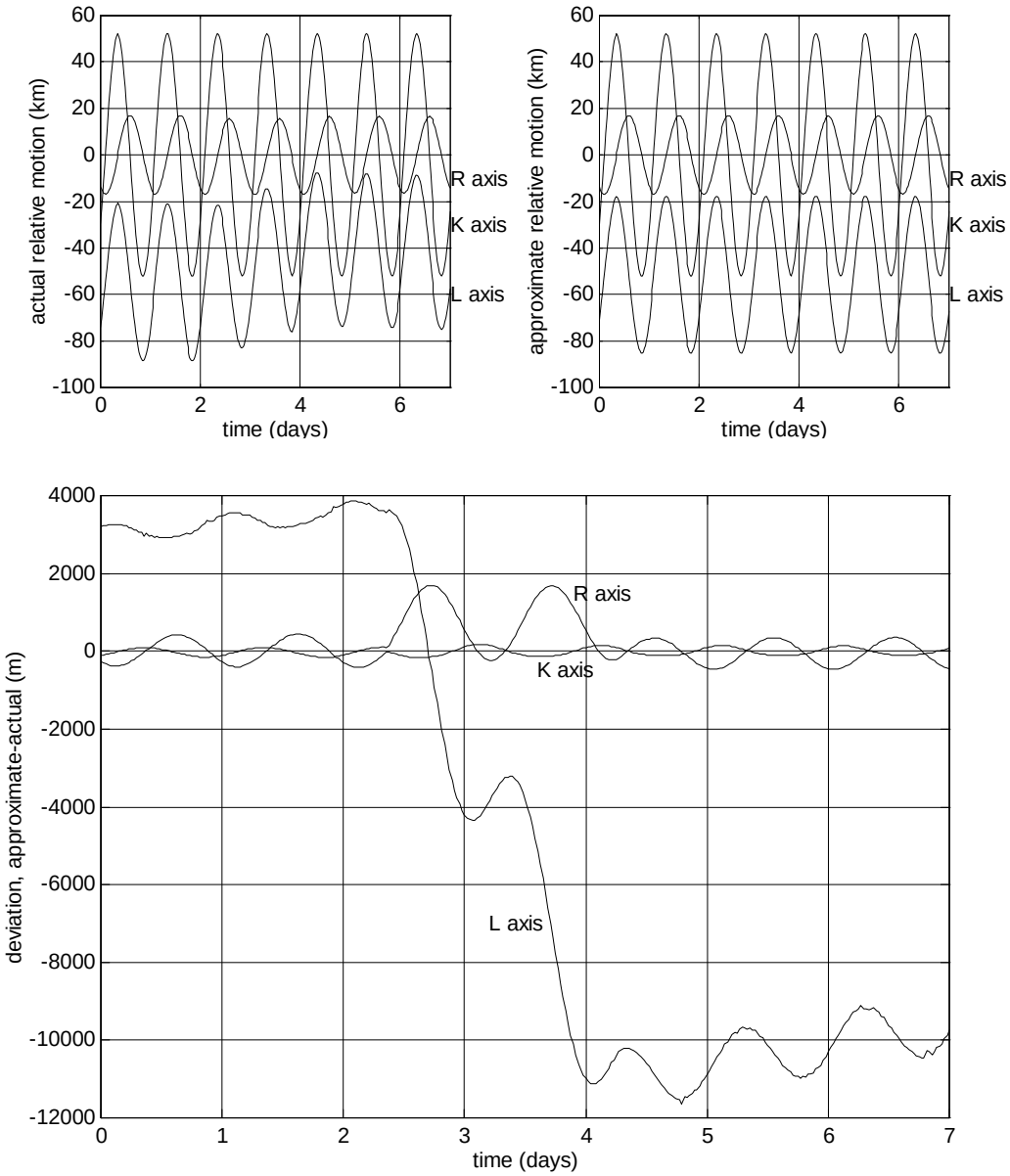

Figure 6.6 : Actual Relative Motion and Hill's Solution Deviations for Case Two

The NS station keeping manoeuvre occurs two days into the propagation shown in figure 6.6 and is followed on day four by the EW manoeuvres. Again the relative motion diagrams show little different in absolute terms, however the differences are evident in the deviation graph.

As for case 1 the sinusoidal deviation components are present along all three axes and the largest derivation occurs along the 'L' axis. The non-zero 'E_2' effect described previously is still present, however for this test the biggest influence on the deviation is the error in the application of the NS burn, which resulted in a significant EW cross-coupled component.

The 'speed' at which the 'L' axis separation changes following the NS manoeuvres indicates two things. Firstly, if close approaches are to occur then they are much more likely following a NS manoeuvre than an EW manoeuvre and secondly, the EW strategy derived in chapter 5 appears to be effective at correcting the relative motion following erroneous NS manoeuvres (the unwanted 'E_2' value following the EW burns is significantly reduced from the post NS burn value).

Considering now the accuracy of equations (C.7), if 2 km is defined as the maximum permissible deviation between first order predictions and the actual relative motion then in the two days following the NS manoeuvre the first order equations do not provide an acceptable approximation to the actual relative motion (the 'L' deviation changes by about 15 km in this period) and based on this evidence it is advisable not to use Hill's equations *across* the NS station keeping discontinuities. In contrast, for case 1, a 2 km permissible deviation means the motion is acceptable for approximately 7 days.

6.3.3 : Summary

To summaries the results of the two test cases presented in section 6.3.2, Hill's equations provide a good representation of the relative motion of two colocated satellites for a period of 7 days *provided* there is no manoeuvre (or other disturbance) during the propagation period and a 2 km deviation from actual motion is acceptable. This means that a cluster correction strategy based on Hill's equation should perform adequately provided the time period over which the equations are used is less than 7 days and the manoeuvre is applied when the satellites are separated by at least 2 km.

6.4 : Orbit Element Separation Strategies

6.4.1 : Selection of Retained Strategies

The orbital element separation strategies described in chapter 2 will now be grouped into three categories; ineffective, redundant, and useful methods. Of these only the last category of methods will be retained, and this category will be further reduced to just two methods for analysis in section 6.5.

Ineffective Strategies

The ineffective methods are the CONTROL and IS schemes. The first is obvious, identical control laws and initial positioning lead to similar orbit evolutions. In fact it is only the differences between the (A/M) ratios and the station keeping control errors (tracking and manoeuvre) which will cause different satellites in a CONTROL cluster to follow different orbital paths. The IS scheme is ineffective for two reasons. The main problem is that orbits separated only in inclination will still intersect twice every sidereal day (see figure 2.4). A secondary problem, which is only relevant for clusters larger than three, is that only a small region of the available GEO window is used. From an examination of Hill's equation (C.7) the 'K' axis motion is uncoupled from the 'R' and 'L' motions to first order, meaning that in IS only one dimension of the GEO window is being used.

Redundant Strategies

The redundant strategies are ES and EIS circular. For most cases the region of probable motion on the inclination plane (figure 5.23) will be much smaller than the allowable inclination tolerance circle and hence can be positioned on the inclination plane in a non-central position, as shown in figure 6.3, without violating the deadband. Since the evolution of inclination is approximately independent of the starting values of 'Q1' and 'Q2' there is no fuel penalty in doing this, and so an increase in mean separation between satellites is obtained 'free', making pure ES redundant. In certain cases where very tight inclination control is needed this may not be the case, however this is thought unlikely for GEO applications where the common latitude deadband is ±0.°1. Concerning the

second 'redundant' scheme, EIS circular is discarded since its main advantage lies in its usefulness for SST applications which are not going to be modelled in this document.

Useful Strategies

The remaining strategies may be described as 'useful' and include MLS and EIS parallel and perpendicular. Of these MLS and one of the EIS schemes will be retained the reasons for which are explained below.

Concerning MLS, it is accepted that it only uses the longitudinal dimension of the available window (nominally) and is thus non-optimal. However unlike IS, the nominal separation is constant and for small clusters large separations can be easily obtained. As an example two satellites separated by 0°.05 in longitude have a theoretical mean separation of over 36 km. Such a separation reduces the maximum value of the eccentricity control circle radius and as such incurs a fuel penalty *if* the resultant eccentricity correction 'ΔV' is larger than the triaxiality correction.

Moving on to the remaining EIS schemes, parallel and perpendicular both have advantages and disadvantages. As mentioned in chapter 2, in terms of mean separation between satellites EIS perpendicular is theoretically superior to EIS parallel, however in the presence of control error the situation is reversed. To illustrate why this is, consider the following EIS configurations.

PARALLEL	PERPENDICULAR
$\Delta P1 = 0.000300$	$\Delta P1 = 0.000300$
$\Delta P2 = 0$	$\Delta P2 = 0$
$\Delta Q1 = 0.000436$	$\Delta Q1 = 0$
$\Delta Q2 = 0$	$\Delta Q2 = 0.000436$

In both cases the eccentricity and inclination vectors are separated by equal amounts and the resulting overall nominal separation ($\rho = \sqrt{R^2 + L^2 + K^2}$) and the RK plane separation ($\rho_{RK} = \sqrt{R^2 + K^2}$) as calculated from Hill's equations, are shown in figure 6.7.

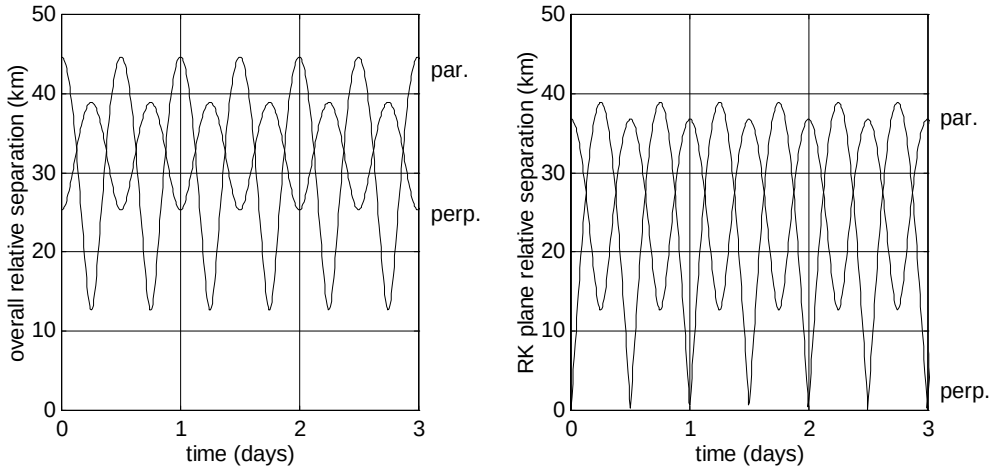

Figure 6.7 : Comparison of EIS Perpendicular and Parallel

To interpret figure 6.7 it is useful to re-state the orbital element formulation of Hill's equations (see appendix C for the derivation) namely,

$$\begin{aligned} R &= \Delta a - a_G \Delta P1 \mathrm{Sin}\left(n_G(t-t_0)\right) - a_G \Delta P2 \mathrm{Cos}\left(n_G(t-t_0)\right) \\ L &= a_G \Delta\lambda_0 - \frac{3\Delta a}{2} n_G(t-t_0) - 2a_G \Delta P1 \mathrm{Cos}\left(n_G(t-t_0)\right) + 2a_G \Delta P2 \mathrm{Sin}\left(n_G(t-t_0)\right) \\ K &= 2a_G \Delta Q2 \mathrm{Sin}\left(n_G(t-t_0)\right) - 2a_G \Delta Q1 \mathrm{Cos}\left(n_G(t-t_0)\right) \end{aligned} \qquad (6.1)$$

The ideal overall separation graphs of figure 6.7 show that, as expected, the 'ideal' mean separation distance is less for EIS parallel than for EIS perpendicular and further, that EIS perpendicular exhibits a smaller amplitude deviation from this mean (although the minimum separations for both are well above zero).

Examining the 'RK' plane motion, the 'R' and 'K' expressions of equations (6.1) have the same phase for EIS perpendicular, amplifying the 'RK' oscillatory motion and causing the nominal value of 'ρ_{RK}' to equal zero twice per orbit. In contrast for EIS parallel, the 'R' and 'K' motions are 90° out of phase which causes a small oscillation amplitude and no zero separation points. In an ideal situation this difference is unimportant, however if errors are considered this changes.

The 'R' and 'K' expressions of equations (6.1) are basically sinusoidal which means a small error in the relative variables [Δa, ΔP1, ΔP2, ΔQ1, ΔQ2] will produce a small error in the subsequent 'RK' response. The 'L' expression however has a linearly increasing term, '$(3/2)\Delta a n_G(t-t_0)$' which means a small error in 'Δa' can have significant long term effects on the value of 'L'. Applying this to the two EIS cases, as 'L' approaches zero due to a propagated 'Δa' error EIS parallel should still have a relatively large 'RK' separation, however EIS perpendicular will have a low value of 'RK' separation twice per orbit, which increases the probabilities of close approaches.

This increase in close approach risks for EIS perpendicular over EIS parallel has been confirmed via simulation by Rajasingh [9] and others.

It is worth noting that the 'L' axis approach problem is also experienced when using MLS strategies. In comparison to these, EIS perpendicular is superior (again see Rajasingh [9]).

Having considered to main disadvantage of EIS perpendicular the main problem with EIS parallel will now be detailed. For EIS parallel the relative ellipse is seen 'edge on' with reference to the Earth (see figure 2.5) which can lead to satellite eclipses or more likely, rf signal interference between satellites. For the perpendicular configuration the relative eclipse is 'face on' to the Earth (see figure 2.6) and so this problem does not occur.

Considering the problems with both parallel and perpendicular one solution is to select an intermediate compromise case, as was done for the ASTRA cluster. Instead of this EIS perpendicular will be selected for the following reason. The interference problem with EIS parallel cannot be avoided, however active control of the cluster geometry should make it possible to decrease the close approach frequencies for EIS perpendicular, making it the preferred strategy *when cluster geometry control is included*. From the point of view of minimising close approach frequencies EIS parallel is still the 'best' solution however.

6.4.2 : MLS and EIS Perpendicular Implementation Definitions

The orbital element separation strategies to be retained have now been reduced to two, namely MLS and EIS perpendicular. In this section the specific form of the two simulated clusters using these strategies (in terms of number and positioning of satellites) will be defined.

The specific MLS and EIS implementations which have been analysed have certain variables in common and these are listed in table 6.2.

VARIABLE	VALUE
Window location	19.0°E±0.°1 in both longitude and latitude
EW cycle length	14 days
NS cycle length	28 days (with a 2 day phasing between NS and EW manoeuvres)
Number of satellites in cluster	4
Area to mass ratio of all satellites	0.025 (m^2/kg)

Table 6.2 : Common Variables for Simulated Clusters

The relative orbital elements (relative to the 'phantom' satellite) for each cluster are listed in table 6.3.

MLS CLUSTER				
VARIABLE	**SAT 1**	**SAT 2**	**SAT 3**	**SAT 4**
Δa	0.00 m	0.00 m	0.00 m	0.00 m
$\Delta\lambda$	-0.°03	-0.°01	0.°01	0.°03
$\Delta P1$	0.000000	0.000000	0.000000	0.000000
$\Delta P2$	0.000000	0.000000	0.000000	0.000000
$\Delta Q1$	0.000000	0.000000	0.000000	0.000000
$\Delta Q2$	0.000000	0.000000	0.000000	0.000000

EIS PERPENDICULAR CLUSTER				
VARIABLE	**SAT 1**	**SAT 2**	**SAT 3**	**SAT 4**
Δa	0.00 m	0.00 m	0.00 m	0.00 m
$\Delta\lambda$	0.°00	0.°00	0.°00	0.°00
$\Delta P1$	0.000000	0.000100	0.000000	-0.000100
$\Delta P2$	0.000100	0.000000	-0.000100	0.000000
$\Delta Q1$	0.000480	0.000000	-0.000350	0.000000
$\Delta Q2$	0.000000	-0.000402	0.000000	0.000402

Table 6.3 : Relative Variables

Although table 6.3 lists the relative variables the 'physical' geometry of the clusters are not evident. To illustrate the absolute positions therefore figure 6.8 shows a representation of the EW deadband (not to scale) for the MLS strategy and figure 6.9 shows the eccentricity and inclination plane diagrams for the EIS perpendicular cluster.

The eccentricity and inclination plane diagrams for the MLS configuration are identical to figure 6.1 (zero separation means all the satellite representations are overlaid on these planes) and so there is no need to repeat the diagram here. Similarly, since the nominal longitudes for the EIS cluster are identical there is no need to show the EW deadband for this cluster either.

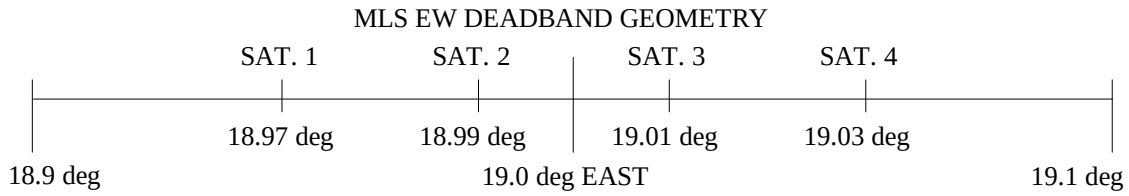

Figure 6.8 : EW Deadband Geometry for MLS Cluster

In figure 6.8 the 0.°07 region West of satellite 1 and East of satellite 4 is comprised of 0.°05 to allow for triaxiality and eccentricity libration during the EW cycle plus a safety margin of 0.°02 to allow for errors in 'Δa' as described in table 5.1. Similar considerations were used to select the eccentricity an inclination plane geometries for the EIS strategy.

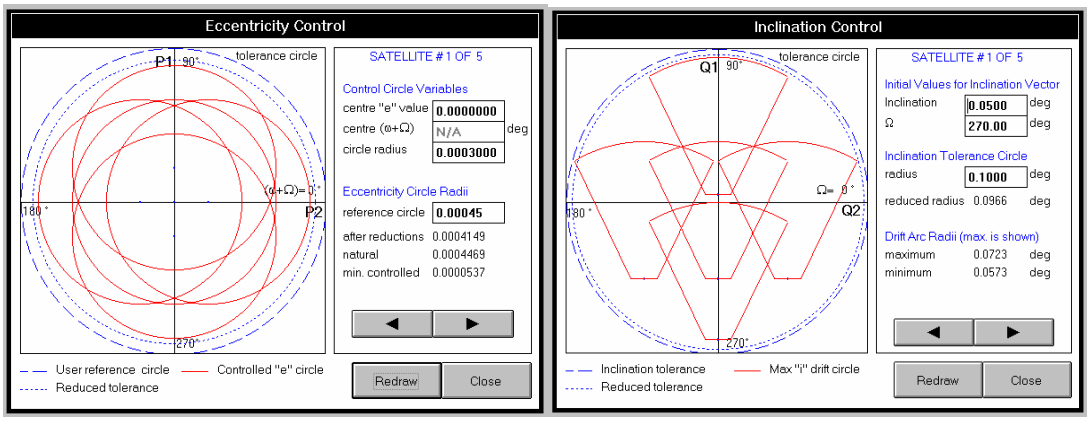

Figure 6.9 : Eccentricity and Inclination Plane Geometries for EIS Perpendicular

6.5 : Cluster Simulation Results With No Geometry Control

6.5.1 : Approach Frequency Analysis

For the two strategies detailed in the section 6.4 a series of cluster simulations have been propagated, and from these a frequency analysis of the minimum approach distances has been performed. Inter-satellite distance less than 50 km were recorded and categorised into 20 frequency bins, each of which is 2.5 km wide. Results were stored for each satellite pair in the cluster, the total number of pairs being given by the arithmetic progression,

$$\sum_{i=1}^{i=N-1} i = \frac{1}{2}(N-1)N \qquad (6.2)$$

where 'N' is the number of satellites in the cluster.

The motion of each individual satellite with reference to the phantom satellite is calculated using the procedure given in figure 6.2 and the minimum distances between satellite pairs are then calculated using the following equation,

$$\rho_{ij} = \sqrt{(R_i - R_j)^2 + (L_i - L_j)^2 + (K_i - K_j)^2} \qquad (6.3)$$

where 'i' and 'j' are integer values denoting individual satellites, obeying the conditions.

$$i \leq N \quad ; \quad j \leq (N-1) \quad ; \quad i \neq j$$

Perturbations with a daily oscillation are superimposed on the mean relative distances and so only the minimum daily approach distances are used for the frequency analysis. Each cluster was simulated for 25 years and the results were factored to generate histograms showing the expected frequency of minimum approaches for one year.

6.5.2 : MLS Cluster Results

There are three distinct classes of satellite pairs for the MLS configuration corresponding to the nominal longitude separations between individual satellites. These classes and the associated satellite pairs are summarised in table 6.4. The *equivalent range distance* is obtained by multiplying the angular separation by the nominal GEO altitude. The value is expected to be the mean close approach distance between satellites in a given class.

VARIABLE	CLASS 1	CLASS 2	CLASS 3
Nominal 'λ' separation	0.02°	0.04°	0.06°
Equivalent range distance	14.7 km	29.4 km	44.2 km
Satellite pairs in class	1&2, 2&3, 3&4	1&3, 2&4	1&4

Table 6.4 : MLS Cluster Satellite Pairs Description

Figure 6.10 illustrates the histograms associated with each class of satellite pairs as produced by Monte-Carlo simulation. For comparison purposes the total frequencies for the class 1 and class 2 pairs have been divided by two and three respectively. The resulting three histograms therefore represent the expected close approach frequency distributions between any satellite pair of a given class over a one year period.

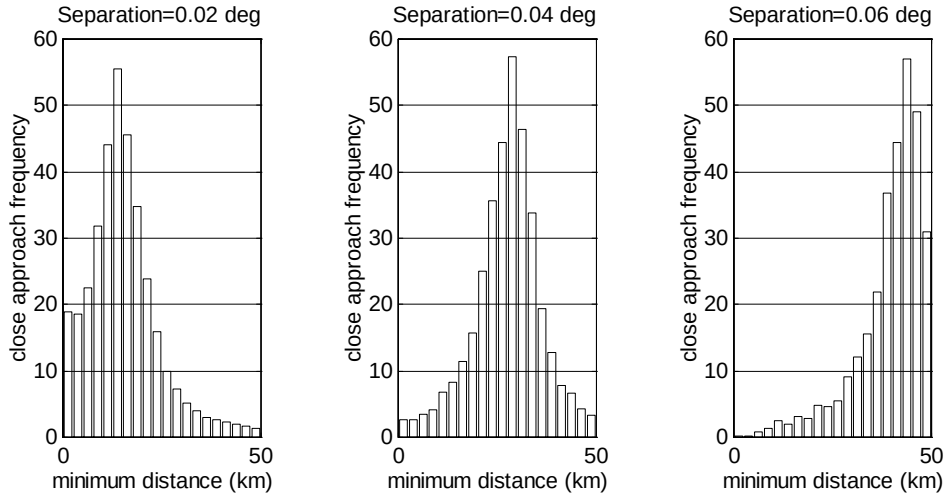

Figure 6.10 : MLS Close Approach Frequency Histograms

Considering all three histograms together firstly, the expected mean separation values given in table 6.4 appear to be adhered to fairly well with approach frequencies dropping off to both sides of these values.

Examining individual graphs, the class two distribution forms a good approximation to the normal distribution curve - which makes sense considering this is how the control errors were modelled during the propagation. On the class 3 histogram there is insufficient data to say the same, however the class 1 plot has an obvious positive skew. Considering three satellite pairs were used to generate this plot where-as only two and one generated the class 2 and 3 cases (i.e. there are 50% more results for the class 1 plot than the class 2 and 150% more than the class 3) more weighting should be given to the first plot than the other two.

In fact examining the approach frequencies of the first two plots below 5 km (i.e. the first two bars) there are slightly more approaches between 0.0 km and 2.5 km than 2.5 km and 5.0 km. This effect has been noted elsewhere, specifically Harting et al [20], and it is thought to result from large NS cross-coupling effects into the EW direction. The majority of the data points used to generate the histograms are extreme values points, however a large NS burn error could cause two satellites to pass each other before the motion is corrected at the end of the current EW cycle. In this case the data point is an

instantaneous distance at the time the satellites pass and not an extreme value point, which thus affects the distribution curves. If the satellites do pass in this way they will probably 're-pass' closely as a result of the next EW correction and so one control error can generate two minimum approach frequencies. It is this which probably causes the second, minor peak at very small separations on figure 6.10.

If minimum approaches below 5 km are now examined then for class 1 pairs there is the likelihood of 36 events; for class 2, 5 events and for class 3, 0.4 events per year. Obviously the class 1 and 2 event numbers are unacceptable, to correct the situation three things can be done,

1. Increase the nominal separation between satellites. The implications of this are a smaller 'e' control circle radius and thus an increased fuel consumption.
2. Decrease the magnitude of the control error by improving tracking accuracy and/or thruster magnitude and directional errors.
3. Include a cluster geometry recovery control scheme which monitors the approach distances and corrects the geometry if these are too low.

As with the first option the third incurs a fuel penalty, however this is not applied every station keeping cycle and thus (depending on the minimum threshold distance at which a geometry correction is applied) may be the lower of the two.

As noted earlier the form and implementation of the third option will be examined in the next chapter.

6.5.3 : EIS Perpendicular Cluster Results

Ideally for pure EIS perpendicular all four satellites in the cluster should follow the same relative ellipse, the phantom satellite being at the centre. This is not true in this case due to the positioning of the probable motion regions on the inclination plane (see figure 6.9 where the initial value of $\sqrt{Q1^2 + Q2^2}$ differs between satellites) to obtain maximum separation without violating the inclination deadband limit.

The result is that individual satellites in the EIS cluster follow different relative ellipses, *all of which* are in an EIS perpendicular configuration with respect to the phantom satellite *but not* with each other. The actual angle between the relative inclination and eccentricity vectors for a given satellite pair is therefore not 90°, however the cluster has been defined such that the maximum deviation from this value is at most ±5° and so no satellite pairs will eclipse each other from the point of view of an observer on the Earth. The advantage of this is that the cluster is still 'basically' EIS perpendicular, with 'slightly' larger relative ellipses between certain satellites which increases the average separations and should therefore increase the extreme value approach frequency mean.
Table 6.5 lists the relative ellipse semi-major and minor axis values and the angles between the relative eccentricity and inclination vectors for each satellite pair.

SATELLITE PAIR	**REL. ELLIPSE MAJOR-AXIS (km)**	**REL. ELLIPSE MINOR-AXIS (km)**	**ANGLE BETWEEN '$\underline{\Delta e}$' AND '$\underline{\Delta i}$' (deg)**
1 & 2	53.1	11.9	95
1 & 4	53.1	11.9	85
2 & 3	45.3	11.9	94
3 & 4	45.3	11.9	86
2 & 4	68.3	16.9	90
1 & 3	70.4	16.9	90

Table 6.5 : EIS Cluster Satellite Pairs Description

If Hill's equations were exact then the minimum distance between satellites would occur when the separation equalled the semi-minor axis of the appropriate relative ellipse. For the real system the daily minimum extreme value should therefore occur near this value and the frequency histograms will reflect this by having peak event frequency in the class intervals containing or near these separation values.

Figure 6.11 shows the histograms associated with the approach frequencies between each pair of satellites. As was done for the MLS cluster histograms, event frequencies have been scaled such that the graphs represent the expected minimum approach frequencies for a one year period.

Considering all the histograms together the peak frequency values occur in the expected class intervals. Also note that although the size of the relative ellipse semi-minor axes produces a lower nominal separation than those for the closest MLS cluster pairs (nominally 14.7 km apart) the frequency of approaches below 5 km is less for the EIS cluster (the maximum is 6 events per year for satellites 1 & 2). The explanation for this is that for MLS close approaches an erroneous 'L' axis motion must occur since 'R' and 'K' are already nominally zero, where-as for EIS close approaches both the 'R' and 'K' axes must be in error. As already noted a small 'E_2' variable in Hill's equations (C.7) can cause major long term deviations along the 'L' axis, making significant 'L' axis errors more likely and thus a more gradual 'drop off' in minimum approach distance frequencies below and above the nominal separation distance for the MLS satellite pairs than the EIS pairs.

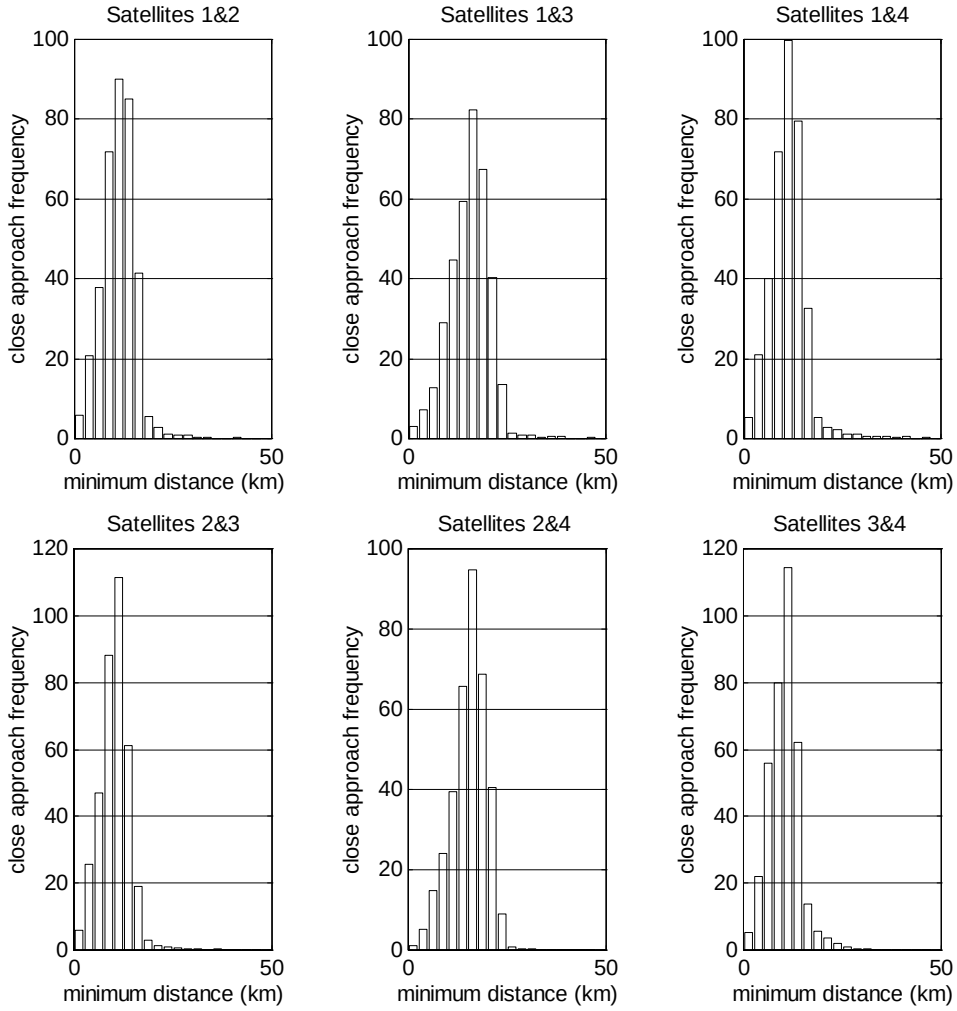

Figure 6.11 : EIS Close Approach Frequency Histograms

Examining individual satellite pairs now, the increased nominal semi-minor axes of the satellite pairs 1&3 and 2&4 which resulted from optimised inclination plane positioning has lead the peaks of the respective graphs to occur at higher minimum distances. Since the 'drop-off' pattern is approximately the same for all the histograms the event frequencies below 5 km are therefore lower for these two pairs, specifically between satellites 1&3, 3 events per year are predicted and between satellite 2&4, 2 events. Both of these predicted values are less than half that predicted for satellites 1&2 (6 events per year) which shows the advantages of using a 'slightly' imperfect EIS perpendicular scheme.

Even with the improvement in the sub 5 km approach frequencies that the EIS configuration affords the absolute number of events per year are still thought to be excessive. The options available to improve the situation are the same as those listed in the discussion on the MLS cluster. With reference to the improved tracking/control accuracy option it is worth re-iterating that the error model magnitudes used for both clusters is a 'worst case scenario' and could probably be significantly improved upon. The advantage of using the current error model values however is that a statistically significant number of close approach events are recorded for a relatively short cluster propagation period (in this case 25 years), thus accelerating the generation of statistically useful results.

7 : CLUSTER GEOMETRY RECOVERY

7.1 : Overview

As demonstrated in chapter 6 the 'test case' satellite clusters are unacceptable from the point of view of the frequency and absolute value of the minimum approach distances between satellite pairs. To improve the characteristics of the close approach histograms shown in figures 6.10 and 6.11 it is proposed that a geometry maintenance/recovery manoeuvre is implemented as required and this is the subject of this chapter.

The derivation of the proposed manoeuvre begins with Hill's equations (see appendix C) from which the times and values of the required corrective burns will be calculated. It is desirable to have a solution which only requires corrective manoeuvres along the EW and NS directions since only these directions are commonly used for GEO station keeping and the potential addition of significant thruster capability along the radial direction can thus be avoided. Due to cross-coupling between the 'R' and 'L' axis motion this is possible but only if a series of 'L' axis burns, separated in time, are applied.

A solution which allows for velocity increments to be applied along 'R', 'L' and 'K' axis has previously been derived in Hardacre [21] and is not included here.

The remainder of this chapter considers the cluster geometry correction strategy as outlined above in more detail. Firstly, the formulation and solution of the relative motion equations for a recovery is detailed. Optimisation to minimise the total velocity increment required is then discussed and an examination of the stability of the procedure in the presence of manoeuvre errors (the magnitudes of which are the same as those used for the cluster simulations detailed in chapter 6) is made. Finally, the integration of the geometry control system into the orbit propagation software and the results from this are dealt with.

7.2 : Solution of Relative Equations

7.2.1 : Hill's Equations Basics

Hill's equations giving the first order relative position and velocity in terms of the 'E_j' (j=1 to 6) variables are the basis of the proposed strategy and it is worth re-listing them here along with the inverse relationships (see appendix C.3 for derivations).

$$\begin{aligned}
R &= -\frac{2}{3}E_2 + E_3\mathrm{Cos}\left(n_G(t-t_0)\right) + E_4\mathrm{Sin}\left(n_G(t-t_0)\right)\\
L &= E_1 + E_2 n_G(t-t_0) - 2E_3\mathrm{Sin}\left(n_G(t-t_0)\right) + 2E_4\mathrm{Cos}\left(n_G(t-t_0)\right)\\
K &= E_5\mathrm{Cos}\left(n_G(t-t_0)\right) + E_6\mathrm{Sin}\left(n_G(t-t_0)\right)\\
\dot{R} &= -n_G E_3\mathrm{Sin}\left(n_G(t-t_0)\right) + n_G E_4\mathrm{Cos}\left(n_G(t-t_0)\right)\\
\dot{L} &= E_2 n_G - 2n_G E_3\mathrm{Cos}\left(n_G(t-t_0)\right) - 2n_G E_4\mathrm{Sin}\left(n_G(t-t_0)\right)\\
\dot{K} &= -n_G E_5\mathrm{Sin}\left(n_G(t-t_0)\right) + n_G E_6\mathrm{Cos}\left(n_G(t-t_0)\right)
\end{aligned} \tag{7.1}$$

$$\begin{aligned}
E_1 &= \left(3n_G t\dot{L} + 6{n_G}^2 tR + n_G L - 2\dot{R}\right)/n_G\\
E_2 &= -3\left(\dot{L} + 2n_G R\right)/n_G\\
E_3 &= -\left(\left[2\dot{L} + 3n_G R\right]\mathrm{Cos}\left(n_G(t-t_0)\right) + \dot{R}\mathrm{Sin}\left(n_G(t-t_0)\right)\right)/n_G\\
E_4 &= -\left(\left[2\dot{L} + 3n_G R\right]\mathrm{Sin}\left(n_G(t-t_0)\right) - \dot{R}\mathrm{Cos}\left(n_G(t-t_0)\right)\right)/n_G\\
E_5 &= \left(-\dot{K}\mathrm{Sin}\left(n_G(t-t_0)\right) + Kn_G\mathrm{Cos}\left(n_G(t-t_0)\right)\right)/n_G\\
E_6 &= \left(\dot{K}\mathrm{Cos}\left(n_G(t-t_0)\right) + Kn_G\mathrm{Sin}\left(n_G(t-t_0)\right)\right)/n_G
\end{aligned} \tag{7.2}$$

Examining equations (7.1) since the 'K' motion is uncoupled, the correction along this axis can be dealt with independently and will result in a one burn correction which can be applied twice per orbit. This 'K' axis recovery solution is detailed in section 7.2.2.

The 'R', 'L' motion nominally requires two manoeuvres separated in time with velocity increments being applied parallel to both these axes for each manoeuvre, however by restricting the recovery to use only 'L' and 'K' axis burns this minimum requirement changes to three manoeuvres. This 'RL' recovery solution is detailed in section 7.2.3.

7.2.2 : Single Burn Recovery for Uncoupled 'K' Axis

The ideal and erroneous 'K' motions can be represented using equations (7.1) with different values of the 'E_j' variables for each. Since both the K and $\dot{K}$ equations are purely sinusoidal with equal periods the ideal and erroneous 'K' motion must intersect twice per orbit, at some time 't_K'. At these points the motion can be corrected by the application of a single burn. Denoting the ideal motion by the subscript addition 'i', the equations to be solved are,

$$\begin{aligned} K &= E_5 \mathrm{Cos}\left(n_G\left(t_K - t_0\right)\right) + E_6 \mathrm{Sin}\left(n_G\left(t_K - t_0\right)\right) \\ K &= E_{5i} \mathrm{Cos}\left(n_G\left(t_K - t_0\right)\right) + E_{6i} \mathrm{Sin}\left(n_G\left(t_K - t_0\right)\right) \\ \dot{K} &= -n_G E_5 \mathrm{Sin}\left(n_G\left(t_K - t_0\right)\right) + n_G E_6 \mathrm{Cos}\left(n_G\left(t_K - t_0\right)\right) \\ \dot{K}_i &= -n_G E_{5i} \mathrm{Sin}\left(n_G\left(t_K - t_0\right)\right) + n_G E_{6i} \mathrm{Cos}\left(n_G\left(t_K - t_0\right)\right) \end{aligned} \tag{7.3}$$

where the correction occurs at the intersection point of the ideal and actual motions and hence 'K' has the same value in lines 2 and 3 of equations (7.3). Solving these equations for 't_K' and the required velocity increment '$\Delta\dot{K}$',

$$\begin{aligned} t_K &= t_0 - \frac{1}{n_G}\mathrm{Tan}^{-1}\left(\frac{E_5 - E_{5i}}{E_6 - E_{6i}}\right) + \left(\frac{2\pi}{n_G}\right)m \\ \text{or } t_K &= t_0 - \frac{1}{n_G}\mathrm{Tan}^{-1}\left(\frac{E_5 - E_{5i}}{E_6 - E_{6i}}\right) + \left(1 + \frac{2\pi}{n_G}\right)m \\ \Delta\dot{K} &= \pm n_G\sqrt{\left(E_5 - E_{5i}\right)^2 + \left(E_6 - E_{6i}\right)^2} \end{aligned} \tag{7.4}$$

where 'm' is a positive integer, selected such that 't_K' exceeds some minimum. The positive velocity increment is required for the first 't_K' solution and the negative, for the second.

7.2.3 : Three Burn Recovery for Coupled 'R' and 'L' Axes

Figure 7.1 represents the main features of the proposed three burn 'R', 'L' axes recovery. There are three correction points, occurring at times; t_A, t_B and t_C. In addition to the uncorrected and corrected relative orbits there are two *corrective* relative orbits which will be referred to by the subscripts 'c1' and 'c2' respectively.

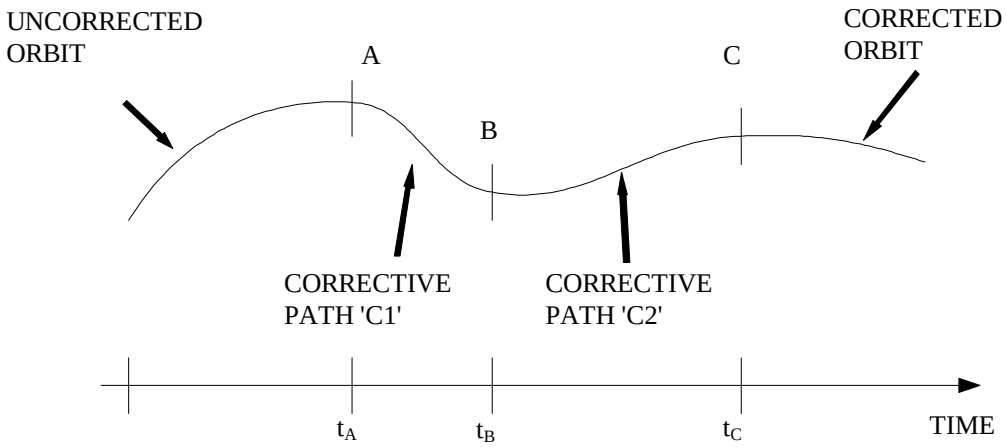

Figure 7.1 : Three Burn R, L Axes Recovery

Assuming that 't_A' and 't_C'; the actual relative position and velocity at 'A'; and the ideal relative position and velocity at 'C' are known then the motion between points 'A' and 'C' can be completely described by applying equations (7.1) at the three correction points. The resulting sixteen equations are listed as (7.5) to (7.7) where the following notational reductions have been made.

$$n = n_G$$

$$sA = \mathrm{Sin}\left(n_G\left(t_A - t_0\right)\right) \qquad sB = \mathrm{Sin}\left(n_G\left(t_B - t_0\right)\right) \qquad sC = \mathrm{Sin}\left(n_G\left(t_C - t_0\right)\right)$$

$$cA = \mathrm{Cos}\left(n_G\left(t_A - t_0\right)\right) \qquad cB = \mathrm{Cos}\left(n_G\left(t_B - t_0\right)\right) \qquad cC = \mathrm{Cos}\left(n_G\left(t_C - t_0\right)\right)$$

Equations at A

$$\begin{aligned} R_A &= -\frac{2}{3}E_2 + E_3 cA + E_4 sA \\ L_A &= E_1 + E_2 n(t_A - t_0) - 2E_3 sA + 2E_4 cA \\ \dot{R}_A &= -nE_3 sA + n_G E_4 cA \\ \dot{L}_A &= E_2 n - 2nE_3 cA - 2nE_4 sA \end{aligned} \tag{7.5}$$

Equations at B

$$\begin{aligned} R_B &= -\frac{2}{3}E_{2C1} + E_{3C1} cB + E_{4C1} sB \\ L_B &= E_{1C1} + E_{2C1} n(t_B - t_0) - 2E_{3C1} sB + 2E_{4C1} cB \\ \dot{R}_{B1} &= -nE_{3C1} sB + nE_{4C1} cB \\ \dot{L}_{B1} &= E_{2C1} n - 2nE_{3C1} cB - 2nE_{4C1} sB \\ R_B &= -\frac{2}{3}E_{2C2} + E_{3C2} cB + E_{4C2} sB \\ L_B &= E_{1C2} + E_{2C2} n(t_B - t_0) - 2E_{3C2} sB + 2E_{4C2} cB \\ \dot{R}_{B2} &= -nE_{3C2} sB + nE_{4C2} cB \\ \dot{L}_{B2} &= E_{2C2} n - 2nE_{3C2} cB - 2nE_{4C2} sB \end{aligned} \tag{7.6}$$

Equations at C

$$\begin{aligned} R_C &= -\frac{2}{3}E_{2C2} + E_{3C2} cC + E_{4C2} sC \\ L_C &= E_{1C2} + E_{2C2} n(t_C - t_0) - 2E_{3C2} sC + 2E_{4C2} cC \\ \dot{R}_C &= -nE_{3C2} sC + nE_{4C2} cC \\ \dot{L}_C &= E_{2C2} n_G - 2nE_{3C2} cC - 2nE_{4C2} sC \end{aligned} \tag{7.7}$$

where the unknowns are,

$$t_B, \dot{L}_A, R_B, \dot{R}_{B1}, \dot{R}_{B2}, L_B, \dot{L}_{B1}, \dot{L}_{B2}, \dot{L}_C,$$
$$E_{1c1}, E_{2c1}, E_{3c1}, E_{4c1}, E_{1c2}, E_{2c2}, E_{3c2}, E_{4c2}$$

and the subscripts '1' and '2' in '$\dot{R}_B$' and '$\dot{L}_B$' refer to the pre-burn and post-burn values of these variables and, '$\dot{L}_A$' is the post 'A' burn value of this variable. Ideally the 'R' axis velocity change at 'B' is zero and so $\dot{R}_{B1} = \dot{R}_{B2}$, however it is useful to retain the difference between these two variables for the following reason.

It is clear from equations (7.5) to (7.7) that the unknown 't_B' cannot be found explicitly. If this variable is temporarily regarded as an additional known the number of unknowns is

reduced to sixteen, and can be solved for analytically as functions of known quantities. Subtracting the resulting expressions for '$\dot{R}_{B1}$' and '$\dot{R}_{B2}$' then provides an equation which can be solved iteratively for 't_B' since $\dot{R}_{B1} - \dot{R}_{B2}$ should equal zero for a solution requiring no radial axis burns.

It is not necessary to derive expressions for all the unknowns listed. If expressions for the 'key variables; '$\dot{L}_A$', '$\dot{L}_{B2}$' and '$\dot{R}_{B1} - \dot{R}_{B2}$' are found then a combination of equations (7.1) and (7.2) at each burn point can be used to find the remaining unknowns.

Again notational reductions have been made to shorten the equation listings and these are given below.

$$\begin{aligned} cBA &= \mathrm{Cos}\left(n_G\left(t_A - t_B\right)\right) & cCB &= \mathrm{Cos}\left(n_G\left(t_C - t_B\right)\right) & cCA &= \mathrm{Cos}\left(n_G\left(t_C - t_A\right)\right) \\ sBA &= \mathrm{Sin}\left(n_G\left(t_A - t_B\right)\right) & sCB &= \mathrm{Sin}\left(n_G\left(t_C - t_B\right)\right) & sCA &= \mathrm{Sin}\left(n_G\left(t_C - t_A\right)\right) \end{aligned}$$

The derivation process followed to obtain the three 'key' variables in terms of known boundary conditions from equations (7.5) to (7.7) is documented in appendix C.4 and the resulting expressions are given below.

$$\begin{aligned} &2D \times \dot{L}a = \\ &-nR_A\left[4(3sCA - 3sBA - 4sCB) + 3n\left(4\left(t_C - t_A\right) - 3cBA\left(t_C - t_B\right) - 4cCB\left(t_B - t_A\right)\right)\right] \\ &-\dot{R}_A\left[4(1 - cCB + cCA - cBA) + 3nsBA\left(t_C - t_B\right)\right] - nR_C\left[4sCB - 3ncCB\left(t_C - t_B\right)\right] \\ &+\dot{R}_C\left[8(1 - cCB) - 3nsCB\left(t_C - t_B\right)\right] + 2n\left(L_A - L_C\right)(1 - cCB) \end{aligned} \tag{7.8}$$

$$\begin{aligned} &2D\dot{L}b = \\ &+nR_A(3 - 4cCB)\left[4sBA - 3cBAn\left(t_B - t_A\right)\right] + \dot{R}_A(3 - 4cCB)\left[8 - 8cBA - 3sBAn\left(t_B - t_A\right)\right] \\ &+nR_C\left[4(sCA + sCB(3 - 4cBA)) + 3cCBn\left(t_A + 3t_B - 4tC + 4cBA\left(t_C - t_B\right)\right)\right] \\ &-\dot{R}_C\left[4(sCBsBA + 7(1 - cCB)(1 - cBA)) - 3sCBn\left(t_B - t_A + 4(tC - tB)(1 - cBA)\right)\right] \\ &-n\left(L_A - L_A\right)(1 - cBA)(6 - 8cCB) \end{aligned} \tag{7.9}$$

$$
\begin{aligned}
&D \times \left(\dot{R}_{b1} - \dot{R}_{b2} \right) = \\
&-\dot{R}_A \left[4\left(sCB - sCA + sBA \right) + 3n(t_C - t_B + cCA\left(t_B - t_A \right) - cBA\left(t_C - t_A \right)) \right] \\
&+3n^2 R_A \left[sCA\left(t_B - t_A \right) - sBA\left(t_C - t_A \right) \right] \\
&+\dot{R}_C \left[4(sCB - sCA + sBA) + 3n\left(t_B - t_A + cCA\left(t_C - t_B \right) - cCB\left(t_C - t_A \right) \right) \right] \\
&+3n^2 R_C \left[sCA\left(t_C - t_B \right) - sCB\left(t_C - t_A \right) \right] + 2n\left(L_A - L_C \right)(sBA + sCB - sCA)
\end{aligned}
\tag{7.10}
$$

where the common element 'D' in these three equations is,

$$
D = 4(sCA - sCB - sBA) + 3n\left(t_C - t_A - cBA\left(t_C - t_B \right) - cCB\left(t_B - t_A \right) \right) \tag{7.11}
$$

The existence of a time 't_B' which causes equation (7.8) to equal zero, and thus a solution to exist, depends on the boundary conditions at 'A' and 'C' and will now be considered.

Equation (7.10) can be rewritten as,

$$
\begin{aligned}
&0 = D\left(\dot{R}_{B1} - \dot{R}_{B2} \right) = \left(G1^2 + G2^2 \right)^{1/2} Cos\left(n_G t_B - \tan^{-1}\left(G2/G1 \right) \right) - G3\left(n_G t_B \right) - G4 \\
&0 = g\left(t_B \right) - f\left(t_B \right)
\end{aligned}
\tag{7.12}
$$

where,

$$
\begin{aligned}
G1 &= 2\left(2\dot{R}_C - 2\dot{R}_A + n\left(L_A - L_C \right) \right)\left(sC - sA \right) - 3n(t_C - t_A)\left(\dot{R}_C cC - \dot{R}_A cA + n\left(R_C sC - R_A sA \right) \right) \\
G2 &= -2\left(2\dot{R}_C - 2\dot{R}_A + n\left(L_A - L_C \right) \right)\left(cC - cA \right) - 3n(t_C - t_A)\left(\dot{R}_C sC - \dot{R}_A sA - n\left(R_C cC - R_A cA \right) \right) \\
G3 &= -3\left(\left(\dot{R}_C - \dot{R}_A \right)(1 - cCA) - nsCA\left(R_C - R_A \right) \right) \\
G4 &= 3n\left(\dot{R}_A\left(t_C - cCAt_A \right) + \dot{R}_C\left(t_A - cCAt_C \right) \right) + sCA\left(4\left(\dot{R}_C - \dot{R}_A \right) + 2n\left(L_A - L_C \right) - 3n^2\left(R_C t_C - R_A t_A \right) \right)
\end{aligned}
$$

and,

$$g(tB) = \left(G1^2 + G2^2\right)^{1/2} \mathrm{Cos}\left(nt_B - \tan^{-1}(G2/G1)\right)$$
$$f(tB) = G3(nt_B) + G4$$

The intersection points of the functions g(tB) and f(tB) correspond to *possible* solution points. Substituting $t_B=t_A$ or $t_B=t_C$ cause equation (7.12) to equal zero however these values also cause 'D' to equal zero and so are not valid solutions. A third solution between 't_A' and 't_C' must therefore be sought. Figure 7.2 shows this graphically.

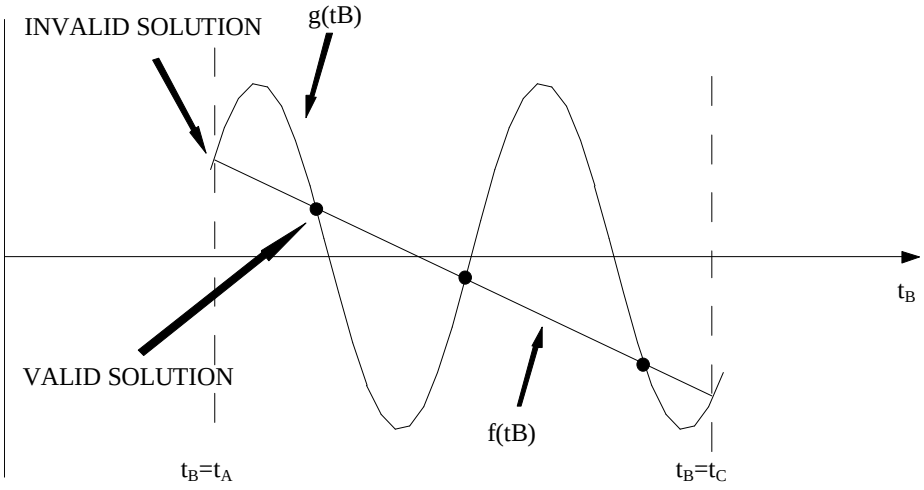

Figure 7.2 : Possible Solutions for 't_B'

From the diagram it is clear that at least two stationary points on the graph of the function $\left(g(t_B) - f(t_B)\right)$ must exist between $t_B=t_A$ and $t_B=t_C$ for a valid solution to exist. Differentiating equation (7.12) the stationary values (at times 't_{BSP}') are found to occur when,

$$t_{BSP} = \pm\frac{1}{n_G}\mathrm{Cos}^{-1}\left(G3\Big/\left(G1^2 + G2^2\right)^{1/2}\right) - \frac{1}{n_G}\mathrm{Tan}^{-1}(G1/G2) + \left(\frac{2\pi}{n_G}\right)m \qquad (7.13)$$

Since the period of the sinusoidal component is one sidereal day the minimum time interval between 't_A' and 't_C' for which a valid solution is *possible* is half a sidereal day. In most cases however this will not be the case.

The minimum time interval between 't_A' and 't_C' for which a valid solution is *guaranteed* can also be found. If 't_A' and 't_C' are separated by an integer number of sidereal days the 'G3' term in equation (7.12) equals zero and the equation is solvable analytically, resulting in the solutions for 't_B' given by equation (7.14) below.

$$t_B = t_A - \frac{2}{n}\mathrm{Tan}^{-1}\left[\frac{n(Rc - Ra)}{\dot{R}c - \dot{R}a}\right] + \left(\frac{2\pi}{n}\right)m \qquad (7.14)$$

The minimum time interval between 'A' and 'C' for a *guaranteed* valid 't_B' is thus one sidereal day *provided* the boundary conditions are not such that R_C-R_A=0. The implications of this and the importance of the 'R_C-R_A' to the recovery fuel requirement will be discussed later.

The remainder of this chapter will use the condition, t_C-t_A=*1 sidereal day* as the time interval between the beginning and end of the recovery procedure for two main reasons. Firstly, the recovery manoeuvres will be 'standardised', which is advantageous from a ground station operations point of view. Secondly, an interval of one sidereal day between 'A' and 'C' means that an opportunity to correct the uncoupled 'K' axis motion will always exist between 't_A' and 't_C' (see equation (7.4)) and thus the total recovery time interval is also one sidereal day.

The complete 'R' and 'L' axis recovery as proposed is summarised below in five steps.

1. Use equation (7.14) to find 't_B' based on the boundary conditions at 'A' and 'C'.
2. Substitute 't_B' in equations (7.8), (7.9) and (7.11) to find the ideal velocities along the 'L' axis *after* the 'A' and 'B' burns.

3. Use equations (7.2) with the values *after* the 'A' manoeuvre to calculate the variables defining corrective path 'c1'.
4. Use equations (7.2) with the values *after* the 'B' manoeuvre to calculate the variables defining corrective path 'c2'.
5. Calculate the 'L' axis velocity increments required at 'A', 'B' and 'C' using the now known values before and after each burn (at 'C' the post-burn value of '$\dot{L}_C$' is the ideal value).

7.3 : Application Method

7.3.1 : Method of Examination

Before integrating a cluster geometry control system into the main orbit propagation program certain issues still need to be addressed, the most important of which is when to initiate the correction cycle. Obviously the form of the erroneous relative motion will be the main influence, however the fuel requirement for the total recovery manoeuvre will also be a factor and this can be at least partially minimised by careful selection of 't_A'. The analytical solution derived in section 7.2 therefore needs to be examined in the context of how it can 'best' be applied.

To address this a software implementation of the proposed control system was written which, given an erroneous relative orbit, computes and applies the required manoeuvres. To 'test' the system in isolation from the orbit propagator (which simplifies debugging) a series of erroneous relative orbits were used as input data. To make this simulation as relevant as possible the relative orbits used for the inputs were computed from close approach data from the EIS cluster detailed in chapter 6. How this was done is summarised below.

The relative motion during the cycle following a station keeping manoeuvre can be modelled until the next manoeuvre by Hill's equations with reasonable accuracy (see section 6.3). Certain cycles produce close approaches and using regression analysis on the relative motion along the [R,L,K] axes as generated by the simulations of section 6.5 the

best fit values of the variables, 'E_j' (j=1 to 6) can be calculated, thus defining a set of pre-'A' burn values. The 'E_j' values for a series of orbits which produced significant deviations from the ideal motion were calculated in this way and it is these which were used as the input data to test the cluster geometry control system.

7.3.2 : Recovery Optimisation

As previously noted, for optimal control of the cluster geometry via corrective manoeuvres two things need to be considered:- the deviation of the relative motion from the ideal (which will determine if close approaches are likely) and the velocity requirement of the total correction.

The proposed control solution is to use two threshold distances. If the *first threshold* is violated then a recovery procedure will be deemed necessary and this will be initiated within either some maximum time interval following the violation or before the time at which the *second threshold* is violated. The available time interval between the first threshold violation and the first corrective burn of the recovery procedure will then be the smaller of these two time interval values.

The purpose of the system is to provide a time window during which the recovery can be initiated, thus allowing some flexibility in the selection of 't_A' which means the recovery procedure can be at least partially optimised to minimise the total fuel requirement.

Threshold Violation Criteria

The threshold distances can be defined in two ways. For the first method, if the relative motions of all the satellite pairs in a cluster is continuously monitored throughout the propagation a recovery procedure could begin when the inter-satellite distance between any pair falls below an inter-satellite threshold distance. Alternatively for the second method, if the relative orbit of each satellite is monitored with respect to the phantom satellite a recovery procedure could begin when the deviation of a single satellite from the known ideal exceeds some threshold value.

In selecting which method to use, consider the number of relative orbits which need to be monitored for each. The total number of satellite pairs in a cluster of 'N' satellites can be calculated from equation (6.2), which is repeated below.

$$\text{number of pairs} = \sum_{i=1}^{i=N-1} i = \frac{1}{2}(N-1)N$$

For a cluster of 4 satellites this means 6 relative orbits must be monitored for the first method where-as only 4 are monitored using the second, and so the computational overhead of the second is less. For larger clusters the saving is more pronounced, for example in a cluster of 8 satellites the first method must monitor 28 pairs where-as the second, only 8. For this reason the second method of defining a threshold has been selected.

Optimisation of Recovery Initiation Point

The overall deviation of the actual relative motion from the 'ideal' given by Hill's equations can be computed as,

$$\Delta\rho = \sqrt{(R - R_i)^2 + (L - L_i)^2 + (K - K_i)^2}$$

and figure 7.3 shows a typical profile of this over a period of 500 days using orbit propagation data for satellite 1 of the EIS cluster which was defined in section 6.4.2.

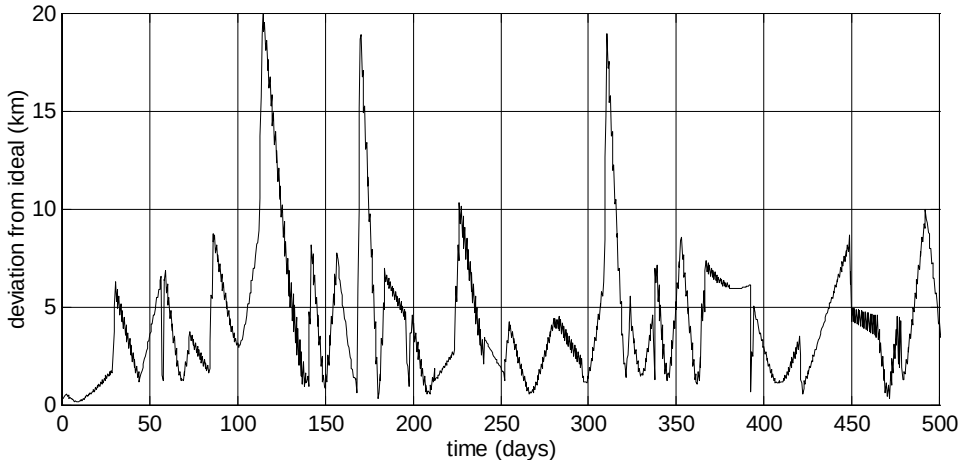

Figure 7.3 : Satellite 1 Relative Motion Deviation from the Ideal

To place the graph in context, the nominal semi-minor axis of the relative ellipse (and thus the nominal minimum daily approach distance) of this satellite with its closest neighbour is approximately 12 km, which must be considered in selecting a suitable value for the larger deviation threshold if close approaches are to be avoided.

Ideally a value less then 6 km should be used for the second threshold if the aim is to remove the risk of collisions altogether since in the worst case if two satellites each deviate by 6 km the semi-major axis of the relative ellipse could theoretically equal zero. This is not the only factor to be considered however. The value of the first deviation threshold will determine the number of recovery procedures which will be performed on average for a given propagation time period (the larger the value, the fewer recovery procedures) and since this value must be lower than the second threshold a cursory examination of figure 7.3 shows clearly that for a value less than 6 km a recovery procedure would be initiated during the majority of station keeping cycles (indicated by discontinuities on the graph) which is unappealing.

The proposed compromise solution which should reduce the frequency of recovery procedures by over 50% is to change the first threshold from less than 6 km (realistically this would have to be about 5 km since a time interval between the two thresholds is desirable for the reasons discussed earlier) to 7.5 km. The second threshold would then

have to be changed and based on the peak deviation gradient of figure 7.3, a value of 9 km should provide at least 6 hours between a first and second threshold violation.

This creates the possibility of the semi-minor axis of the relative ellipse becoming zero since there is a 6 km overlap region between the second deviation threshold of the satellite and that of its closest neighbour. It is unlikely however that both satellites will deviate into this region at the same time, and more unlikely still that if they do the recovery procedure will be initiated near the second threshold limit (if initiated near the first threshold the overlap is only 3 km) and so close approach probabilities should still be dramatically reduced.

Minimising Fuel Requirements

Having now selected suitable threshold distances the minimisation of the recovery fuel requirement (comprising the three burns for the coupled 'R' and 'L' motions plus the single 'K' burn) can be addressed. The 'K' burn will be constant and a function of the original and ideal 'E_j' variables only (see equations(7.4)), however the 'L' burns are functions of 't_A' and can be changed by the selection of this variable.

Consider an erroneous relative orbit which violates the first deviation threshold and for which the 'E_j' values are known. Using Hill's equations and the recovery burn equations derived in section 7.2 at any future time the deviation from the ideal and the total velocity requirement of the correction procedure *if it were then initiated* can be calculated. The data resulting from this can be used to predict when (or if) the second threshold is violated and the optimal time before this at which the recovery should be initiated from a fuel requirements point of view.

Figure 7.4 was constructed from such data and shows both the deviation from the ideal and the total velocity requirement as the relative orbit is propagated past the first threshold violation point. Since the recovery must be initiated between the two threshold violations only the corresponding time period is shown (about 0.7 days for this case) on the 'x' axis.

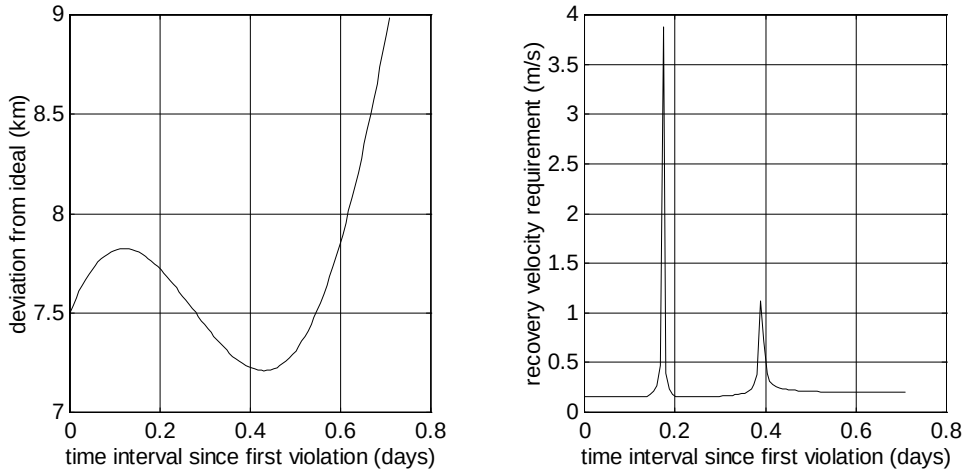

Figure 7.4 : Satellite Deviation and Recovery Velocity Between Violation Points

The peaks on the velocity graph correspond to values of 't_A' which cause the '(R_C-R_A)' term in equation (7.14) to equal zero. At these points the velocity requirement is infinite, however this is not clear from the graph since this is a plot of discrete points which are connected by straight lines. A clearer indication of the pattern of this graph can be seen by lengthening the time axis beyond the second threshold violation point and restricting the 'y' axis to a narrow band with the limits 0.1 and 0.5 m/s. This has been done and the resulting graph is shown in figure 7.5 along with the corresponding graph of '(R_C-R_A)'.

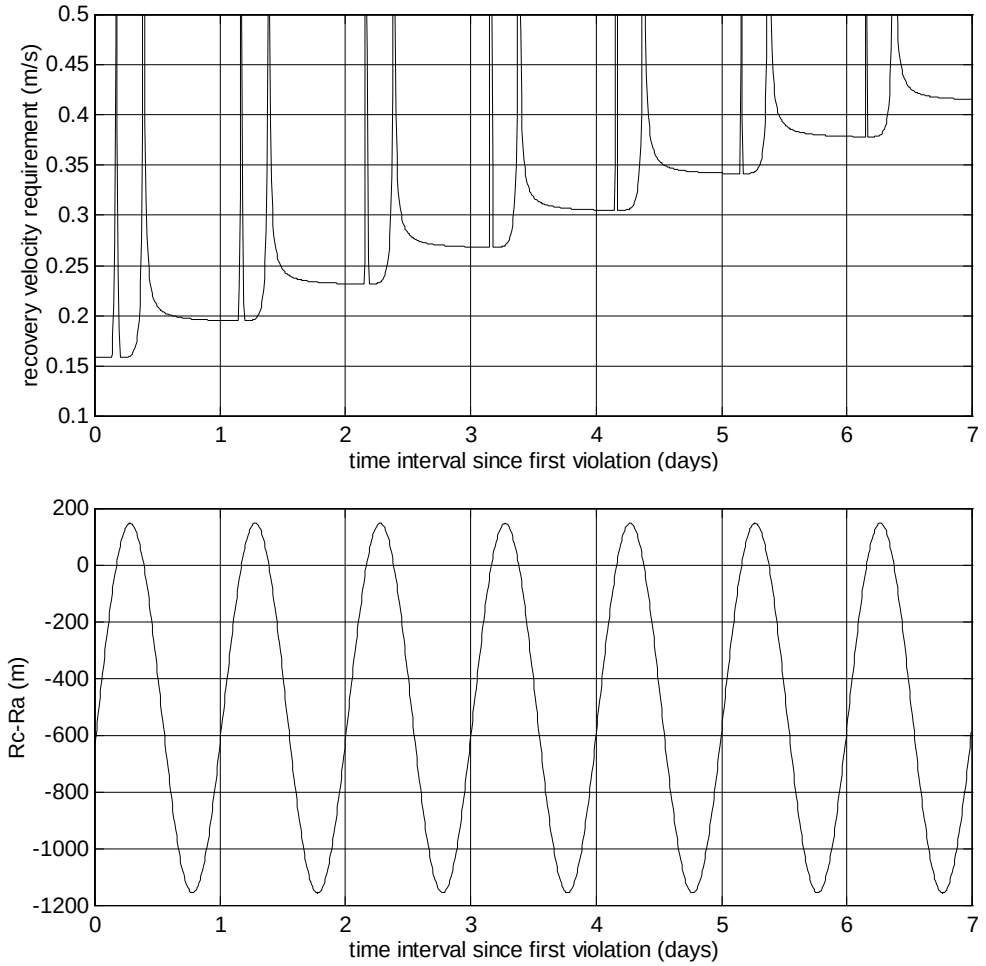

Figure 7.5 : Recovery Velocity Requirement Over 7 Day Period

For the top graph two singularities are seen to occur every sidereal day , and these can be seen to correspond to the times at which $(R_C\text{-}R_A)=0$ on the lower graph. Continuing the analysis, all the possible 'forms' of the upper graph can be deduced from an analytical equation for '$(R_C\text{-}R_A)$'. Subtracting the appropriate lines of equations (7.5) and (7.7), and simplifying the result by using the substitution '$t_C=t_A+2\pi/n$' gives the following expression,

$$\left(R_C - R_A\right) = -\frac{2}{3}\left(E_{2i} - E_2\right) + \sqrt{\left(E_{3i} - E_3\right)^2 + \left(E_{4i} - E_4\right)^2}\,\mathrm{Sin}\left[n\left(t_A - t_0\right) + \tan^{-1}\left(\frac{E_{3i} - E_3}{E_{4i} - E_4}\right)\right] \quad (7.15)$$

For this to equal zero the magnitude of the $(E_{2i}\text{-}E_2)$ term must be less than or equal to the envelope of the sinusoidal term. In the first case '$(R_C\text{-}R_A)$' will equal zero twice every

sidereal day and the velocity requirement profile will show two singularities at these points where-as in the second case only one singularity will occur every sidereal day. If the magnitude of the '$(E_{2i}-E_2)$' term is greater than the sinusoidal term then no singularities will occur and the recovery can be initiated at any point.

The likelihood of a velocity profile possessing singularities can be seen to be a function of the difference between the uncorrected and ideal 'E_j' values and due to the nature of the station keeping control errors producing the uncorrected motion this cannot be predicted. It is thought however that the variation of the differences is independent of the orbital element separation strategy used and thus equal occurrences of singularity and non-singularity cases should be present in both the MLS and EIS test clusters.

A final feature of the velocity profiles is the underlying gradient which is visible in figure 7.5 and results from the linear '$E_2n(t-t_0)$' term in the 'L' expression of Hill's equations. Basically, the larger the initial uncorrected 'E_2' value, the larger this gradient. Since all non-zero values of 'E_2' cause a cumulative deviation from the nominal relative motion the gradient will always be positive. If this was the only factor influencing the velocity graph profile the recovery should be initiated as soon as possible after the first threshold violation point. As it happens another effect must be considered, relating to the changing value of 't_A-t_B' as 't_A' increases.

A graph of 't_B-t_A' against the time since the first threshold violation, for the same test conditions as used to generate figure 7.5, is shown in figure 7.6.

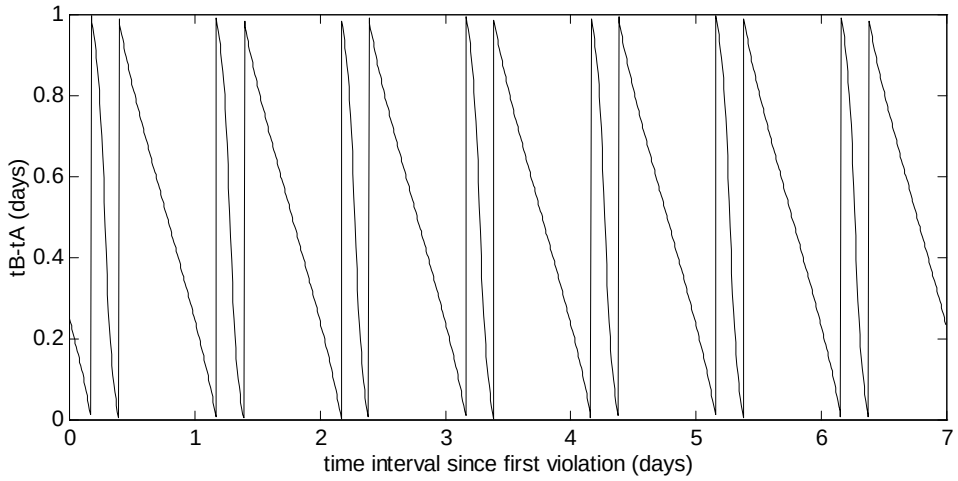

Figure 7.6 : 't_B' Solution Profile

The discontinuities on this diagram correspond to the singularity points on figure 7.5 which should be expected since $t_B=t_A$ and $t_B=t_C$ have already been shown to be invalid solutions.

As 't_A' increases (along the 'x' axis) the solution for 't_B' can be seen to obey the following cyclic pattern (which starts at a discontinuity on the graph),

1. $t_B=t_C$.
2. (t_B-t_A) decreases until $t_B=t_A$.
3. t_B 'jumps' to again equal t_C (causing a discontinuity).

Consider the implications of the second point to equations (7.8) and (7.9) which give the ideal post 'A' and 'B' values for '$\dot{L}$'. Over time the increased fuel requirement resulting from the progressively increasing 'L' axis deviation (the 'E_2' effect) is offset by the reducing 't_B-t_A' value. Even when no singularities occur on the velocity profile the 'E_2' effect and the 't_B-t_A' effect will cause discontinuities, between which the velocity requirement can diminish (dependant on the relative magnitudes of the two effects) and across which the velocity requirement will 'jump' to a larger value. Examining figure 7.5 between singularities the fuel requirement diminishes *for this case*.

In practical terms a trade-off between the two effects means that it is worthwhile examining the velocity profile between singularities when attempting to minimise fuel requirements of the recovery. Since all the velocity profiles have a period of one sidereal day this would seem to be a suitable value for selection as the maximum interval between the first violation point and the start of the recovery in the event of no second threshold violation.

7.3.3 : Summary of Application Method

The values of the two threshold distances and the maximum time between the violation of the first threshold and the first recovery burn are summarised in table 7.1 below.

CONSTANT	VALUE
First deviation threshold	7.5 km
Second deviation threshold	9.0 km
Maximum acceptable time interval (between first threshold and first recovery burn)	86164 sec

Table 7.1 : Summary of Recovery Constants

The software implementation of the recovery procedure *once the first threshold has been violated* is summarised in figure 7.7.

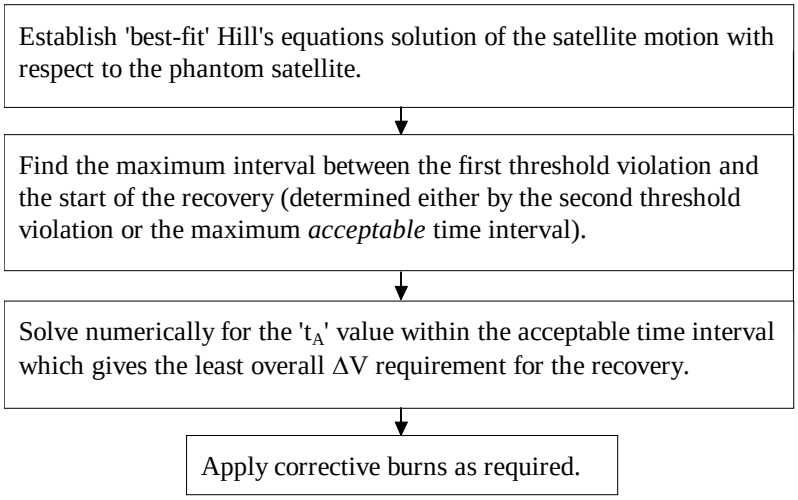

Figure 7.7 : Software Implementation of Recovery Procedure

7.4 : Validation of Procedure and Stability of Solution

The basics of the geometry control system have now been developed however two issues need to be addressed before it can be integrated into the orbit propagation and station keeping software. Firstly, the validity of both the derived equations and the proposed recovery procedure must be established and secondly the stability of the procedure when control errors are included must be examined.

The two issues are discussed in turn below.

7.4.1 : Validation of Proposed Recovery Procedure

The complexity of the derivation and implementation of the recovery procedure leads to a high probability of human error occurring at some point, and this in fact happened several times before a final solution was reached, and so it is important to establish that the procedure as described operates as expected in an ideal environment.

To do this a validation has been performed via software simulation of a relative orbit which is propagated using Hill's equation of relative motion. Using characteristic 'E_j' data which causes a threshold violation (obtained as described in section 7.3.1) the recovery procedure was simulated using the appropriate equations of section 7.2 and the optimisation process discussed in section 7.3 for a range of different ' E_j' inputs to provide a reasonable amount of certainty that the solution is correct.

It is impractical to show all the test cases here, however a single example is useful. In addition to helping to validate the procedure the case chosen can also be used to show typical numerical values for the correction velocity increments. A summary of the test selected is given in table 7.2.

SIMULATED RECOVERY TEST CONDITIONS				
t_0 (required when using equations (7.1))			= 57634.75	sec
Ideal Burn Times and Velocity Increments Required				
t_A = 4398637	sec	ΔL_A	= 0.028858	m/s
t_B = 4474352	sec	ΔL_B	= -0.026601	m/s
t_C = 4484800	sec	ΔL_C	= -0.001344	m/s
t_K = 4468935	sec	ΔK_K	= -0.071974	m/s
Initial and Ideal 'E_j' values (j=1 to 6)				
E1 = -5503.10	m	Ideal	= 0.00	m
E2 = 37.57	m	Ideal	= 0.00	m
E3 = -4725.57	m	Ideal	= -4216.42	m
E4 = -214.11	m	Ideal	= 0.00	m
E5 = -41240.84	m	Ideal	= -40308.95	m
E6 = 325.24	m	Ideal	= 0.00	m

Table 7.2 : Summary of Sample Recovery Test Conditions

Applying these conditions the subsequent recovery path (in terms of the deviation from the nominal) is shown in figure 7.8.

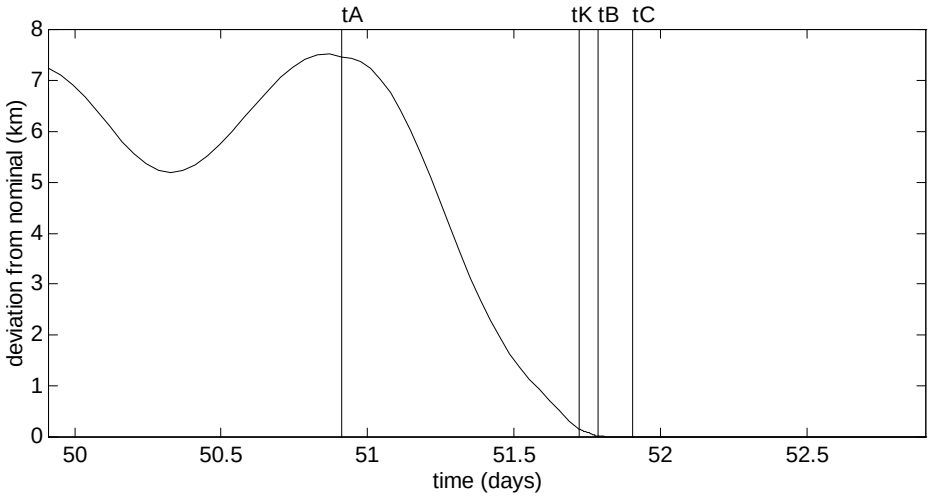

Figure 7.8 : Relative Motion Recovery Profile

The diagram clearly illustrates that for this test case the erroneous relative motion is effectively corrected between by 't_A' and 't_C' on the diagram. Outside of the correction

region the relative motion for one day pre-correction and one day post-correction is shown, the latter indicates the relative velocities are also correct at time 't_C'.

Based on this and similar tests the equations derived in section 7.2 are thought correct.

7.4.2 : Stability of Solution

In practice the recovery procedure suffers from the same control errors as the station keeping model in chapter 5 and as with any control system which processes a varied range of inputs there is the possibility that a certain combination will cause the system become unstable. It is important therefore to simulate the control system in operation under the influence of errors for a typical range of inputs to ensure that if instabilities do exists they are not within the expected input range.

The main error source is the burn magnitude error with a 'worst case' value of 5% at 3σ (quoted from section 5.4) and for simplicity this will be the only error which is added to the simulation from section 7.4.1. To justify the non-inclusion of cross-coupling errors consider the following. Using a 2% worst case cross-coupling (section 5.4) with a 5% magnitude error and the highest velocity increment which is applied during the recovery (in this case for the 'K' correction) the cross-coupling error results in a possible velocity component of 0.0015 m/s, which is negligible. A more comprehensive simulation including this error source is discussed in section 7.5. In this section we are more interested in the 'general' response of the recovery procedure.

By adding burn magnitude error terms to the 'ideal' recovery burn values used in the previous simulation and then propagating a recovery multiple times the stability of the system can now be assessed from an examination of the distribution of the relative position and velocity errors at 't_C' (i.e. the end of the recovery).

For the test case summarised in table 7.2 the recovery has been propagated 1000 times with the inclusion of these errors and histograms of the deviations, constructed. The results

are shown, to the 3σ level, in figure 7.9. There is no histogram for the 'K' error at 't_C' since this is a function of the tracking and manoeuvre time errors, which are being ignored.

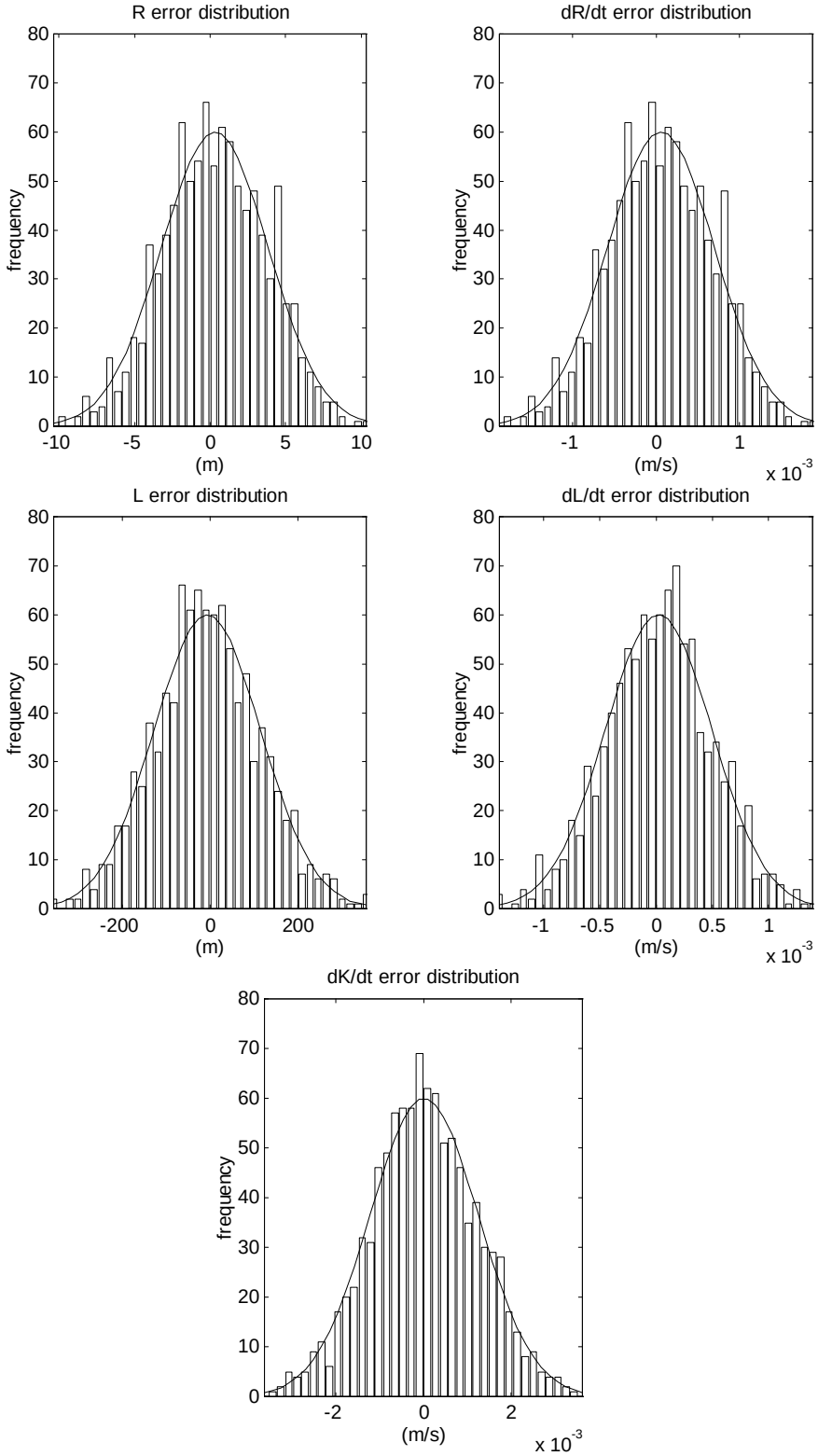

Figure 7.9 : Predicted Deviations from Nominal at End of Recovery

Examining the histograms which are shown in figure 7.9, the recovery appears to be stable for the input test conditions with the position and velocity errors at the end of the

procedure appearing to be normally distributed (the curves shown represent the 'best fit' normal distribution), which could be expected based on the way the input errors are modelled.

Looking at the positional error graphs, of note is the fact that the standard deviation of the 'L' error is much larger than that of the 'R'. The reason for this is the cumulative effect of a non-zero 'E_2' variable on the 'L' axis motion, which occurs in the presence of errors.

In magnitude terms the 3σ errors of both the 'R' and 'L' errors appear very low considering the corrective burn magnitudes (see table 7.2) are comparable to EW station keeping burn magnitudes and the latter have been shown to produce much larger errors at the same confidence level. The discrepancy is thought to be the result of a combination of the omitted error sources and the fact that the motion throughout the recovery simulation are calculated from a Hill's equations propagation of the relative orbit and not an absolute propagation. In an absolute propagation differences in perturbation accelerations would also influence deviations from the ideal at the end of the recovery procedure.

To summarise the results of this simulation, the histograms indicate the recovery procedure is 'resistant' to errors (the relative velocity errors are negligible and the positional errors have been explained) however a more comprehensive simulation would seem to be necessary to assess the usefulness in practice.

The subject of the recovery procedure response in a realistic environment requires the integration of the recovery procedure software into the orbit propagation and station keeping code and this is discussed in the next section.

7.5 : Cluster Simulation Results with Autonomous Geometry Control

7.5.1 : Implementation Issues

With minor modifications the recovery procedure validation software program of section 7.4 can be integrated into the absolute orbit propagation and station keeping software,

providing a realistic environment in which the proposed autonomous control solution can be tested.

The only non-trivial modification required is to evaluate the 'E_j' variables following a normal station keeping manoeuvre, and hence predict (within the limits of the accuracy of Hill's equations) if a threshold violation is expected to occur during the subsequent station keeping cycle. In section 7.4 sample 'E_j' values that were known to cause violations were used thus the problem was avoided. In operational situations these variables cannot be calculated until after each station keeping manoeuvre and this should be reflected in the 'complete' cluster simulation program.

To address the problem, multiple regression has been used to estimate the 'E_j' values from data obtained during a specific time interval following the completion of either NS or EW station keeping procedure. In the worst case scenario an erroneous NS manoeuvre can cause the relative orbit to deviate beyond the first threshold before the next EW manoeuvre can be applied to compensate for it. In this situation the recovery procedure should be automatically applied, however due to the two day phasing between NS and EW, which represents the tracking interval commonly used to evaluate an *absolute* orbit, the geometry control procedure must be initiated within one day following the NS manoeuvre and this requires the approximate 'E_j' values to be evaluated as quickly as possible.

In practical situations the almost equal perturbation accelerations which act on each satellite in a cluster and the simplicity of the relative motion compared to the absolute motion means the 'E_j' variables can be calculated to a reasonable level of accuracy using just 6 hours worth of data. Using this value in the software thus provides 18 hours in which the recovery procedure can be initiated.

7.5.2 : Single Satellite Deviation Results

Figure 7.3 was introduced in section 7.3 to illustrate the 'typical' relative motion deviations over time of an individual satellite in the EIS cluster using data output from the simulation

program in which only conventional station keeping control was enabled. It is possible to perform the same test with the recovery procedure enabled *using identical control errors* up to the time when the first recovery procedure correction is applied. This has been done restricting the time axis to 45 days for clarity and the results are shown in figure 7.10.

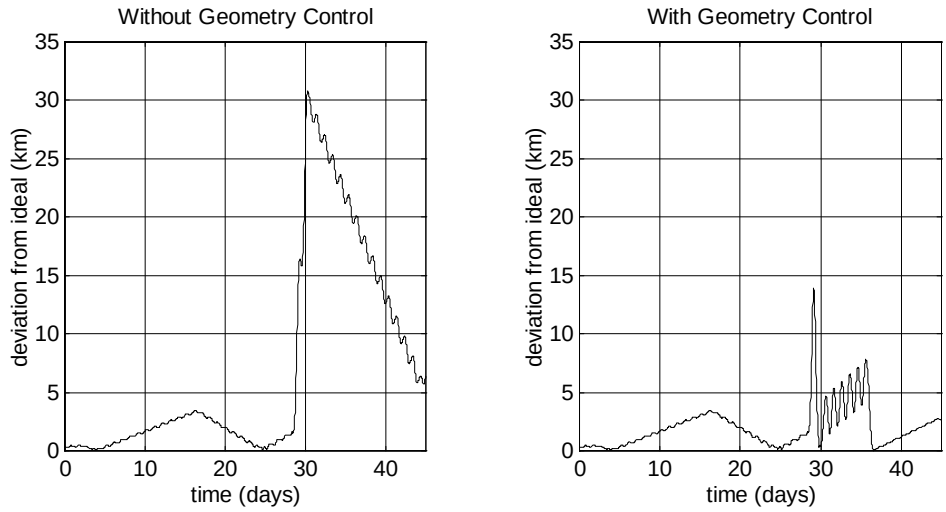

Figure 7.10 : Example of Deviation of EIS Satellite 1 from Ideal Relative Motion Without and With Geometry Control

For the case shown in figure 7.10 the first unacceptable deviation occurs following the NS manoeuvre which is applied around day 28. The size of this manoeuvre makes potential cross-coupling velocity components into the longitudinal and radial directions much larger, and hence more problematic than those following an EW manoeuvre. This is reflected in the 'rapid' deviation following day 28 which illustrates the need for quick evaluation of the 'E_j' values following a manoeuvre of this kind as has already been noted.

The improvement between the two test cases is significant with both the peak deviation and the time spent in violation of the second threshold being smaller for the case employing geometry control. Even with this control however the peak deviation occurring is larger than the semi-minor axis of the relative ellipse between this satellite and its closest neighbour (table 6.5 lists this as 12 km for EIS cluster satellites 1 and 2) and so potentially close approaches between at least one other satellite is possible. With the 3σ control error magnitudes used for the simulations occurrences of this kind are inevitable,

the important question is does the perceived improvement in figure 7.10 translate to a reduction in close approach event frequencies ? This can be examined by comparing the yearly average approach frequency histograms with the geometry control system enabled to the equivalent histograms that were presented in chapter 6 and this is detailed next.

7.5.3 : MLS Cluster Results

Close Approach Analysis

In section 6.5.2 a description of and the results from the MLS cluster test without active geometry control was given, culminating in the approach frequency histograms of figure 6.10. The same simulation was re-run with the geometry recovery procedure enabled and the resulting histograms for this test are shown in figure 7.11. Again satellite pairs have been categorised into one of three classes determined by the nominal longitudinal separation between them, The format of figure 7.11 is therefore identical to that of figure 6.10.

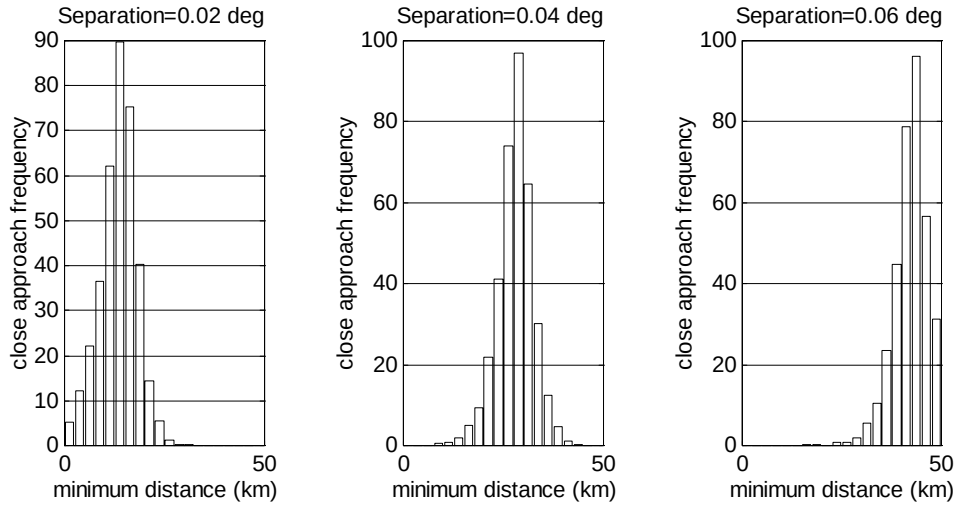

Figure 7.11 : MLS Close Approach Frequency Histograms

Comparing figures 7.11 and 6.10 the reduction in close approach frequencies within the smallest storage bin shown on the graphs is not clear and for clarity the actual values for both tests are given in table 7.3 in which tabulated values are the yearly average event frequencies of approaches below 2.5 km between satellites (i.e. the numerical values corresponding to the height of the first bar in figures 6.10 and 7.11). Satellite pairs can

be categorised into classes 1 to 3 which again are defined in terms of the possible nominal longitudinal separation between any two satellites of 0.°02, 0.°04 and 0.°06 respectively.

SATELLITE PAIR	NO GEOMETRY CONTROL APPROACHES BELOW 2.5 km	GEOMETRY CONTROL APPROACHES BELOW 2.5 km
class 1	18.0	5.2
class 2	2.6	0.0
class 3	0.2	0.0

Table 7.3 : Approach Frequencies Below 2.5 km for the MLS Cluster

Examining the histograms of the two diagrams the reduction in standard deviation for all three classes of satellite pairs due to the introduction of the recovery manoeuvre is dramatic, with the event frequencies all three histograms falling sharply away from the nominal daily minimum approach distance.

This is reflected is the sub-2.5km approaches listed in table 7.3 in which both class 2 and 3 approach frequencies in this region have been reduced to zero and it is worth noting that so too were the 2.5-5.0 km frequencies.

Even thought the class 1 satellite pairs approach frequencies in this region have been reduced by approximately 70% the expected value of 5.2 approaches below 2.5 km per year is still unacceptable. In practical terms the spacing between satellites cannot easily be increased if safety margins and eccentricity libration bands are to be retained at both sides of the longitudinal deadband, and so other methods must be sought to reduce the number of close approaches. The most effective solutions are thought to be either decreasing the NS cycle time (to produce lower individual NS burn requirements, and hence smaller average cross-coupling burn components into the 'RL' plane) or decreasing the 3σ burn magnitude errors.

Yearly Mean Fuel Requirements of the Recovery Procedure

The perceived effectiveness of the recovery procedure is based on the reductions in close approaches which are obtained through its use. To assess the feasibility of the procedure in practical terms however the fuel penalties incurred by individual satellites must be examined and for the test case presented in figure 7.11 the average velocity increments required every year are summarised in table 7.4 below.

SATELLITE	RECOVERY PROCEDURE FUEL USAGE PER YEAR (m/s)
1	3.2896
2	4.4602
3	3.9679
4	3.9933
TOTAL	15.711 m/s

Table 7.4 : Predicted Recovery Procedure Fuel Usage Per Year for MLS Cluster

To place the values of table 7.4 in context, the additional velocity increment required per satellite due to the inclusion of the recovery procedure is comparable to the magnitude of a typical single NS manoeuvre, which nevertheless represents a shortening of the satellite mission lifetime. The important point to note from the table however is that the recovery procedure is feasible from the velocity requirement point of view since it does not significantly reduce the operational lifetime of the satellites using it.

Examining the mean values in table 7.4, although they are similar in size (as could be expected) the deviations between individual satellites are significant, satellite 1 showing the largest variation from the overall cluster mean. The reasons for this are not currently known and could be worth further study.

7.5.4 : EIS Cluster Results

Close Approach Analysis

In section 6.5.3 a description and the results of the EIS cluster test without active geometry control was given, culminating in the approach frequency histograms of figure 6.11. As in

section 7.5.3 the same simulation was re-run with the geometry recovery procedure enabled and the resulting histograms for this test are shown in figure 7.12.

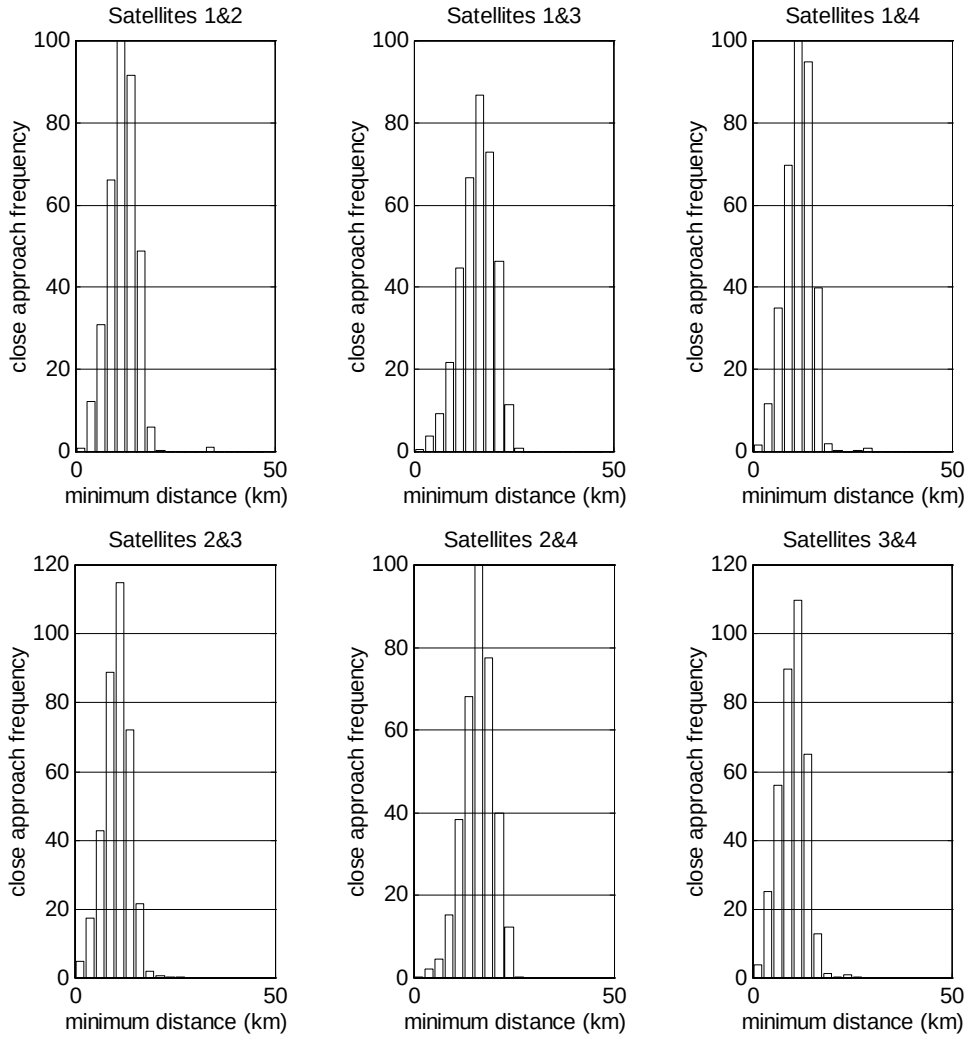

Figure 7.12 : EIS Close Approach Frequency Histograms

Comparing figures 7.12 and 6.11 the reduction in close approach frequencies within the smallest storage bin shown on the graphs is not clear and for clarity the actual values for both tests are listed in table 7.5. As in table 7.3, tabulated values are the yearly average event frequencies of approaches below 2.5 km between satellites.

SATELLITE PAIR	NO GEOMETRY CONTROL APPROACHES BELOW 2.5 km	GEOMETRY CONTROL APPROACHES BELOW 2.5 km
1 & 2	5.9	0.9
1 & 3	2.9	0.6
1 & 4	5.2	1.6
2 & 3	5.9	4.8
2 & 4	1.6	0.4
3 & 4	5.3	3.8

Table 7.5 : Approach Frequencies Below 2.5 km for the EIS Cluster

Comparing first the histograms in figures 6.11 and 7.12, the addition of the geometry recovery procedure has resulted in individual satellites adhering more closely to the nominal relative motion (which was the aim) and as a consequence of this the standard deviation of the approach frequency distributions on all the graphs has been reduced, producing a corresponding reduction in close approach events.

From table 7.5 actual numerical comparisons can be made. The satellite pairs 1&2, 1&3, 1&4 and 2&4 all show reductions in excess of 70% which is encouraging. The remaining pairs 2&3 and 3&4 show a smaller reduction of about 20% and 30% respectively. The reason for the differential is thought to be linked to the parameters of the relative ellipse between the two satellites in each pair.

Examining table 6.5 in which the EIS cluster is defined, the relative ellipses between the satellite pairs 2&3 and 3&4 have the smallest semi-major *and* semi-minor axes of all the pairs. The low semi-minor axis dictates the nominal daily minimum separation distance, however the semi-major axis will determine how long the satellites will remain close to this point. The addition of errors to the system thus means the 'dangerous' part of the relative orbit is longer for these two pairs and so the close approach frequencies are subsequently higher.

It is interesting to note that the effect is more noticeable in the event frequencies obtained from simulations which included the relative geometry control system. With

this enabled the relative orbit is periodically corrected in an attempt to obtain an unachievable nominal motion and on a longer time scale the adaptive station keeping control system performs a similar task. The actual relative motion can thus be considered as the sum of the ideal motion plus some oscillatory perturbation component, the amplitude of which can be controlled by reducing the values selected for the first and second threshold limits discussed in section 7.3.2. Maintaining these thresholds at some constant values and gradually reducing the semi-major and minor axes of the relative ellipse will thus cause the improvements gained by the inclusion of the recovery procedure to diminish and this is what is thought to be happening in the case of satellite pairs 2&3 and 3&4. Larger reductions are thought to be achievable by reducing the thresholds, however this will have an adverse effect on the mission lifetime due to the increased fuel demands (both from more frequency recovery manoeuvres and shorter time periods in which the recovery can be optimised).

Yearly Mean Fuel Requirements of the Recovery Procedure

As in the case of the MLS cluster it is important to assess the mean fuel requirements of the recovery manoeuvre over the mission lifetime for a single satellite and for the test case detailed the average velocity increments required every year are summarised in table 7.6 below.

SATELLITE	RECOVERY PROCEDURE FUEL USAGE PER YEAR (m/s)
1	4.0889
2	4.2928
3	4.4825
4	3.8630
TOTAL	16.7272

Table 7.6 : Predicted Recovery Procedure Fuel Usage Per Year for EIS Cluster

Again the fuel penalties found are comparable to the magnitude of a typical single NS manoeuvre. However it may be possible to reduce this penalty without a significant loss in close approach performance.

Considering only the recovery procedure, the fuel requirement can be diminished by increasing the value of the first threshold, although this will have adverse affects on the close approach frequencies. Another possible alternative is to not apply the 'K' axis correction. The nominal values of 'E_5' and 'E_6' are a factor of ten larger than 'E_3' and 'E_4' and it is reasonable to assume that the *percentage* deviation in 'E_5' and 'E_6' due to control errors will much smaller than the equivalent errors in 'E_3' and 'E_4' since the error sources affecting both are the same. With this assumption, close approaches *for the EIS cluster* are much more likely to occur as a result of erroneous 'RL' plane motion and thus not applying the 'K' axis correction should have only a small effect on the close approach frequencies. Examining the 'typical' recovery procedure burn values given in table 7.2 for an EIS recovery this would result in a fuel saving of 50%.

8 : DISCUSSIONS AND CONCLUSIONS

8.1 : Discussions

In chapters 4, 5, 6 and 7 methods by which the software developed during the research operates are detailed. These chapters contain assumptions and simplifications which therefore influence the validity and limitations of the software, and thus the research in general. Although most of the issues were addressed as they arose it is worth re-examining how each in turn affects the overall results, and how certain aspects can either be improved upon or extended by further research.

8.1.1 : Orbit Propagation

The sole requirement of the orbit propagator is to provide an accurate 'testing' environment for the control systems detailed in chapters 5 and 7. To assess this accuracy the validation procedure detailed in appendix B was performed and excluding the eccentricity comparison with the ESA propagator illustrated in figure B.24 the results are reasonable.

The cause of the eccentricity error is the approximation used in the solar radiation pressure model that a satellite is a flat plate of constant area and mass which never enters eclipse. In a 'real' cluster simulation test case the importance of these restrictions will be based on the nominal separation between the clustered satellites and the different configurations of individual satellites.

Addressing the first point, as discussed in chapter 7 the approximation that clustered satellites experience nearly identical perturbation accelerations becomes progressively less accurate as nominal separation values increase and thus model errors in solar pressure acceleration will be larger for more 'widely' spaced clusters. This is thought to be a minor effect however if a proposed cluster is expected to remain within a ±0.°1 window. A larger effect involving separation distances will be due to one satellite being in eclipse whilst a second is not. The difference in perturbation accelerations for this period could be significant and cannot be analysed currently by the propagator.

The second factor influencing the effect of solar pressure is the difference in configuration of individual satellites and this becomes more important as the area to mass ratio increases. For the test clusters of chapters 6 and 7 this should not be a problem with A/M = 0.025 m^2/kg however doubling the effect to A/M = 0.05 m^2/kg which could theoretically occur would magnify the errors inherent in the 'flat plate' model.

Considering the integration scheme used for the propagator, the multi-step procedure employed was complicated to implement and debug due to the need to switch to a single step method every time the step size changed. The method was initially selected for speed of propagation, however as computers become faster the importance of this is diminishing. As an example during the course of this research the speed of a typical IBM compatible PC (upon which all the software operates) has approximately doubled every year.

In operation the orbit propagation integration scheme is reasonably stable, nevertheless for propagations in excess of five years some simulations did diverge when station keeping control was included. The reasons for this are unclear, however repeating simulations starting close to the point at which the original diverged again yielded initially stable operation. This indicates the possibility of integrator instability in certain situations, possibly as a result of the integration step size control specifying too low a step value, or more likely as a result of truncation errors as the size of certain variables grows, most notable simulation time which starts at zero and increases throughout the propagation. Limiting the propagation time for individual simulations and constructing 'composite' long term propagations in which one starts at the point the last one ended was done in certain cases as a 'work around' solution.

8.1.2 : Autonomous Station Keeping

The station keeping schedule detailed in chapter 5 and used for the cluster simulation conditions of chapter 7 is only one of several that are commonly used. The two burn EW

solution can be replaced by three burns or even one burn (although the latter cannot correct both longitude and eccentricity exactly) and similar modifications can be applied to the NS cycle. Even considering the scheme that is used, characteristics of the cluster evolution will change as the lengths of the EW and NS cycles and the phasing between them changes.

Bearing these factors in mind, it should be remembered that the aim of the research was to examine the effectiveness of the internal cluster geometry control solution offered by the use of the relative motion equations as solved in chapter 7, *in a realistic simulation environment*, and the station keeping scheme used provides this. Analysis of the response of the control algorithms to different test conditions could be the subject of further work now that the basic feasibility of the system has been shown.

The same arguments can be applied to the choice of using a 'worst case' scenario for the modelling of the manoeuvre control errors. Using smaller errors may be more realistic and in fact neither the uncontrolled nor controlled test clusters of chapter 6 and 7 are acceptable in terms of the close approach event probabilities, however the larger errors present a more demanding test for the autonomous geometry control system and produce statistically significant close approach data over reasonably short propagation periods (in the case of chapters 6 and 7, 25 years).

In operation the non-augmented station keeping control algorithms detailed in chapter 6 were usually found to be stable and under most conditions, maintained an individual satellite within the required window where it follows the expected motion. Improvements to the system are possible however, the 'wavy' longitudinal motion of figure 5.30 was described in chapter 5 as being probably a function of the EW station keeping control system and as such for autonomous station keeping purposes in general would be worth examining in detail to find (and if possible) remove to provide 'tighter' longitudinal control. In the context of relative motion, the oscillations imposed by the station keeping control system are not reflected in the motion of one satellite with respect to another, indicating they are approximately the same and thus cancel out. For

analysis of close approach events therefore this limitation of the station keeping control system is thought to have minimal effect.

8.1.3 : Cluster Simulation and Relative Motion Control

The test cases with and without the inclusion of the active geometry control system detailed in chapter 7 illustrate the response for very specific input conditions, and thus represent only a small sub-set of possible colocation implementations. Considering the variation in station keeping methods (as already discussed), orbital element separation schemes and relative geometry control parameters (first and second thresholds etc.) it was impractical to examine every combination and chapters 6 and 7 both attempt to justify the selections for the two test cases which were used.

Several issues relating to relative motion and how the recovery control procedure of chapter 7 maintains the internal cluster geometry are of note and are discussed in turn below.

Applicability of the Recovery Procedure

The simulation performed indicates the usefulness of the recovery procedure in terms of the reduction in the close approach event frequencies obtained with its inclusion in the cluster simulation. However the absolute number of approaches below five kilometres is still too high for actual applications.

For the two test cases the majority of the close approaches can be removed by reducing the error magnitudes of the station keeping thrusters from 5% at 3σ to 2% (which is obtainable in practice), and for a four satellite EIS cluster, doing this reduces the probabilities of close approaches to an acceptable level without the need for a geometry control system. If larger clusters are used however or for some other reason close separation between satellites in required, then a limit will still be reached at which a 'conventional' system will be unacceptable and it is in this situation that the geometry control procedure could be potentially useful.

Given a set of control error limitations chapter 7 demonstrates that 'tighter' control can be obtained over the relative position of individual satellites by the inclusion of the proposed procedure *even when this too suffers from the same control errors*. An extrapolation therefore is that given a reduction in control errors and a decrease in nominal satellite separation distances the same can still be said, indicating the potential of the system for future colocation occurrences involving large numbers of satellites.

Relative Motion During the Geometry Correction Interval

No attempt has been made to analyse the recovery paths during the correction cycle. It is possible that in the short term satellites could approach closer that the second threshold whilst still following the 'nominal' recovery path (and this probably causes a large percentage of the close approach events which where generated during the test cases in chapter 7). The fact that the simulations of chapter 7 are a significant 'improvement' on those from chapter 6 indicates that in the majority of cases in which the recovery procedure is employed this does not occur.

Based on this, a possible extension to chapter 7 could be to analyse the corrective path during the period in which 't_A' is being optimised (for fuel consumption) with the second threshold being re-defined as the maximum allowable deviation from the nominal relative motion for the entire propagation period, including the interval during which the recovery procedure is being applied. The 'improved' system would thus take into account both fuel requirements and maximum deviation distances.

The selection of the re-defined second threshold distance could become increasingly complex and a dynamic value may be required if situations arise in which it is impossible to avoid violating this limit. Obviously there is a trade-off between fuel usage and acceptable relative motion deviations which would require further study.

Comparison Between Test Case Results

Examining the results of the MLS and EIS clusters before and after the inclusion of the geometry recovery procedure it is interesting to note that without the additional control

the EIS perpendicular is, as expected, the more effective orbital element separation scheme, however with the additional control the MLS solution seems to be superior, both in the number of close approach frequencies and the recovery manoeuvre fuel requirement (the latter being attributable to a relatively large average 'K' correction value for the EIS cluster corrections).

This effect is undoubtedly a function of the mean nominal separation distances between satellites. In the case of the MLS cluster the lowest nominal daily separation is 15 km where-as for the EIS cluster this figure is 12 km. As discussed in the EIS cluster results section 7.5.4 the effectiveness of the recovery procedure is dependant on the values of the first and second threshold distances *in relation* to the nominal separation between satellites. If the nominal separation is decreased whilst maintaining the same thresholds, a point is eventually reached at which the recovery procedure offers no significant improvement to the overall number of close approach events. Applying this effect to the test clusters, the nominal separations between satellites is higher for the MLS case and thus the recovery procedure is more effective at reducing close approach events than in the EIS case *for the specific threshold values used* in the simulations of chapters 6 and 7. If the thresholds were altered the situation would change, however the reduction in thresholds would result in increased fuel consumption which is to be avoided.

From tables 7.3 and 7.6 within both the MLS and EIS clusters the satellite pairs whose nominal relative separations with respect to their closest neighbour are least (i.e. class 1 pairs in the MLS cluster and pairs 2&3 and 3&4 in the EIS cluster) show much less 'close approach improvement' with the addition of the geometry recovery procedure than the other pairs in each cluster. This could therefore supports the arguments in the previous paragraph.

The Cost of Cluster Geometry Maintenance

Increased fuel consumption, documented for the two test cases in tables 7.4 and 7.6, is incurred if the recovery procedure is to be used. For individual satellites in each cluster

the expected values per year were found to be approximately 3.9m/s for the MLS case and 4.2 m/s in the EIS case. Relating this to an individual recovery, quoting from table 7.2, the average (mode) requirement is about 0.15 m/s although for some cases the value can be as high as 0.5 m/s and this is reflected in the expected yearly figures.

Reductions in the figures given may be obtainable if the 'K' axis correction is omitted. The feasibility of this will probably be a function of the colocation orbital element separation strategy used and could be worth further investigation.

8.2 : Conclusions

A new software program for the simulation of the absolute orbital motion of a cluster of GEO satellites has been constructed with the following main features.

- Autonomous station keeping.
- Control system errors modelling capabilities.
- The ability to perform autonomous internal cluster geometry correction.

With this tool the close approach frequencies between any pair of satellites in one MLS and one EIS test cluster were examined with and without the geometry control procedure enabled and the effectiveness of the procedure was thus established.

It was found that in the trade-off between minimising the number of recovery procedures over the mission lifetime and reducing the close approach frequencies to an acceptable level the MLS test case benefited more than the EIS case from the inclusion of the procedure *with the recovery procedure variables that were selected*. This highlights the importance of optimising the recovery for the specific orbital element separation strategy which is to be used in any colocation occurrence.

It has been suggested that improvements in both tracking and manoeuvre burn accuracy are the preferred solutions to reducing close approach risks to acceptable levels for the four satellite clusters simulated in the chapters 6 and 7. This method however will have

limitations as the size of the cluster increases (and based on ITU longitudinal position allocation policy this is likely to occur in the future).

Further reductions in close approach characteristics can be obtained by reducing the station keeping cycle lengths of individual satellites, thus minimising the absolute burn errors at each manoeuvre point and shortening the propagation time for errors. In practice the increased fuel requirements of such a scheme are greater than those needed for the proposed geometry recovery procedure which is applied only as required and effectively 'supplements' the station keeping system.

Considering all three options (decreasing control errors, decreasing station keeping cycle lengths and using the recovery procedure) it is expected that tracking and control improvements, possibly followed at a later date by station keeping cycle reductions, will be used in practice to compensate for increases in cluster size before a geometry recovery procedure is considered seriously. However the recovery procedure does have significant benefits over the second option provided the threshold parameters are optimised for the orbital element separation scheme which is to be used.

9 : REFERENCES

[1] **J. G. Walker.**
The Geometry of Satellite Clusters.
Journal of the British Interplanetary Society. Vol. 35, pp 345-354, 1982.

[2] **S. Hubert, J. Swale.**
Stationkeeping of a Constellation of Geostationary Communications Satellites.
AIAA/AAS Astrodynamics conference (AIAA TP 84-2042), Seattle USA 1984.

[3] **J. Murdoch, G. Swinerd, M. Chabrol, J. Marie.**
Synchronised Attitude and Orbit Control of Satellites Operating in Clusters Final Report.
ESA Contract Report ESA CR (P) 2268, 1985.

[4] **A. Tanaka, H. Mineno, M. Miyashita.**
Station-Keeping Methods for Two Broadcasting Satellites in the Same Geostationary Position.
Proceedings of the Second International Symposium on Spacecraft Flight Dynamics (ESA SP-255), Darmstadt Germany, 1986.

[5] **S. Carlini, F. Graziani.**
An Eccentricity Control Strategy for Coordinated Station Keeping.
ESA Symposium on Spacecraft Flight Dynamics (ESA SP-326), Darmstadt Germany 1991.

[6] **G. Fusco, A. Buratti.**
Crowding of the Geostationary Orbit.
ESA Contract Report No. 5705/83/NL/PP (SC), 1984.

[7] **A. Harting, C. K. Rajasingh, M. C. Eckstein, A. F. Leibold, K. N. Srinivasamurthy.**
On the Collision Hazard of Colocated Geostationary Satellites.
Technical Report DFVLR-FB 88-02, 1988.

[8] **A. Harting, C. K. Rajasingh, M. C. Eckstein, A. F. Leibold, K. N. Srinivasamurthy.**
On the Collision Hazard of Colocated Geostationary Satellites.
AIAA 88-4239. AIAA/ AAS Astrodynamics conference, Minneapolis 1988.

[9] **C. K. Rajasingh.**
On the Collision Hazard of Colocated Geostationary Satellites at 19° West.
GSOC IB 89-01, 1989.

[10] **L. Maisonobe, C. Dejoie.**
Analysis of Separation Strategies for Colocated Satellites
Proceedings of the ESA Symposium on Flight Dynamics, Darmstadt 1991.

[11] **J. J. Pocha, J. Murdoch.**
The Orbit Dynamics of Satellite Clusters.
IAF paper No. 82-54. 33rd International Astronautical congress, Paris 1982.

[12] **J. Murdoch**.
Cooperative Orbit Control Strategies for Colocated Geostationary Satellites.
AIAA/AAS Astrodynamics conference (AAS 85-375), Vail USA 1985.

[13] **P. Blumer.**
A Future Concept of Coordinated Orbit Control of Colocated Geostationary Satellites.
AIAA/ AAS Astrodynamics Conference, Hilton Head Island, SC, 1992.

[14] **M. C. Eckstein, C. K. Rajasingh, P. Blumer.**
Colocation Strategy and Collision Avoidance for the Geostationary Satellites at 19 Degrees West.
CNES international Symposium on Space Dynamics, Toulouse (France), 1989.

[15] **F. Dufor.**
One Year of Co-location at 19 degrees West with TDF1 and TDF2 Spacecrafts.
ESA Symposium on Spacecraft Flight Dynamics (ESA SP-326), Darmstadt Germany 1991.

[16] **A. Pietrass, M. Eckstein, O. Montenbruck.**
Software for Station Keeping of Co-located Geostationary Satellites.
Proceedings of the IV European Space Conference (ESA SP-242), Paris France 1991.

[17] **P. Francken, P. Wauthier.**
Numerical Simulation of Multiple Satellite Co-location.
Flight Dynamics Symposium, St. Petersburg-Moscow 1994.

[18] **P. Wauthier, P. Francken, H. Laroche.**
On the Co-location of the Three ASTRA Satellites.
Flight Dynamics Symposium, Moscow, 1994.

[19] **P. Wauthier, P. Francken.**
The ASTRA co-location strategy for three to six satellites.
Pre-publication paper from personal communication with Société Européenne des Satellites 1994.

[20] **A. De Agostini, F. Palutan, E. Detoma, S. Leschiutta.**
Telecommunications-Satellite Orbit Determination via Television-Signal Range Measurements.
ESA Journal, Vol. 7, pp 247-256, 1983.

[21] **S. Hardacre.**
Collision Avoidance for Colocated Geostationary Satellites.
MSc. Thesis, Cranfield Institute of Technology England, 1992.

[22] **H. A. Kellner, G. Lecerf.**
Basic Outline of Numerical Orbit Integration for a Synchronous Satellite.
ESRO Scientific Memorandum SM-73 (ESOC), 1968.

[23] **R. M. Green.**
Spherical Astronomy.
Cambridge University Press, 1985.

[24] **G. E. Cook.**
Luni-solar Perturbations of the Orbit of an Earth Satellite.
Royal Aircraft Establishment, Farnborough, RAE TN G.W. 582, 1961.

[25] **M. C. Eckstein.**
Station Keeping Strategy Test, design and Optimization by Computer Simulation.
Space Dynamics for Geostationary Satellites Conference, Toulouse 1985.

[26] **M. C. Eckstein.**
Geostationary Orbit Control Considering Deterministic Cross Coupling Effects.
41st Congress of the International Astronautical Federation, IAF-90-326, Dresden 1990.

[27] **E. M. Soop.**
Geostationary Orbit Inclination Strategy.
ESA Journal, Vol. 9, pp 65-74, 1985.

[28] **H. F. Michielsen, E. D. Webb.**
Station Keeping of Stationary Satellites Made Simple.
Lockheed.

[29] **J. J. Pocha.**
Mission Design for Geostationary Satellites.
Space Technology Library, 1987.

[30] **W. L. Morgan & G. D. Gordon**
Communications Satellite Handbook
John Wiley & Sons, ISBN 0-471-31603-2, 1989.

[31] **E. M. Soop.**
Introduction to Geostationary Orbits.
ESA SP-1053, 1983.

[32] **A. E. Roy.**
The Foundations of Astrodynamics.
Macmillan Publishing, 1965.

[33] **R. R. Bate, D. D. Mueller, J. E. White.**
Fundamentals of Astrodynamics.
Dover Publications Inc., ISBN 0-486-60061-0, 1971.

[34] **R. H. Battin.**
An Introduction to the Mathematics and Methods of Astrodynamics.
AIAA Education Series, ISBN 0-930403-25-8, 1987.

[35] **J. R. Wertz, W. J. Larson (editors)**
Space Mission Analysis and Design 2nd Edition.
Kluwer Academic Publishers, ISBN 0-7923-1998-2 1994.

[36] **C. Zee.**
Theory of Geostationary Satellites.
Kluwer Academic Publishers, ISBN 90-277-2636-1, 1989.

[37] **B. N. Agrawal.**
Design of Geosynchronous Spacecraft.
Prentice-Hall, ISBN 0-13-200114-4 025, 1986.

[38] **J. J. Buglia.**
Compilation of Methods in Orbital Mechanics and Solar Geometry.
NASA publication 1204, 1988.

[39] **P. Duffett-Smith.**
Practical Astronomy with Your Calculator.
Cambridge University Press, ISBN 0-521-35699-7, 3rd Edition 1988.

[40] **J. Meeus.**
Astronomical Algorithms.
Willmann-Bell Inc. ISBN 0-943396-35-2, 1991.

APPENDIX A : TOPICS IN APPLIED MATHEMATICS

This section includes mathematical relationships and derivations which, although directly relevant, would only serve to confuse the main text. A breakdown of the appendix follows.

- A.1 : Axis and variable set definitions. Definitions of the various astrodynamical variable sets and axes referred to in the main text.
- A.2 : Axis and variable set transformations. Transformation equations for the axes and variable sets defined in A.1.
- A.3 : Curve fitting. General description of the technique used and specific cases of the implementation.

A.1 : Axis and Variable Set Definitions

Different axes and variable sets are useful for different problems (in this document several are used in chapter 4 alone) and it is important to define these. Since the inclusion in the main text would detract from the narrative, the subject is dealt with here and referred to as needed.

The following variable / axis sets are defined:

- Equinoctial variables.
- Rectangular geocentric inertial axes.
- Spherical polar axes.
- Rectangular orbital axes.
- Rectangular radial, longitudinal and latitudinal axes.

All the axis frames have their origin at the geocentric centre of the Earth.

A.1.1 : Equinoctial Variables

The equinoctial variables are defined in terms of the classical orbital elements as,

$$\begin{aligned} P1 &= e\mathrm{Sin}(\Omega+\omega) \\ P2 &= e\mathrm{Cos}(\Omega+\omega) \\ Q1 &= \tan(i/2)\mathrm{Sin}(\Omega) \\ Q2 &= \tan(i/2)\mathrm{Cos}(\Omega) \\ a &= a \\ L &= (\Omega+\omega)+f \\ l &= (\Omega+\omega)+M \end{aligned} \qquad \text{(A.1)}$$

Their use removes the singularity problems present in the classical elements at low inclinations and eccentricities. Since only six elements are needed to fully define a three dimensional position the user has a choice between using either the sixth or seventh element given in equation (A.1). For numerical orbit propagation the mean longitude is easier to deal with, however for conceptual visualisation the true longitude is preferable

(being based on an angle relevant to the actual orbit). Because of this both elements are referred to in the main text and so both are defined here.

A.1.2 : Rectangular Geocentric Inertial Axes

The vector directions defining the rectangular geocentric inertial axes, here after referred to as just the *inertial axes*, are as follows.

- The X axis points in the direction of the Vernal Equinox.
- The Z axis points northwards.
- The Y axis lies in the equatorial plane, completing the right handed axis set.

The precession and nutation of the Earth means this frame is not truly inertial, however the discrepancy is of the order of 10^{-5} radians which can be tolerated for all but high precision calculations.

The inertial axes are used throughout the main text as an intermediate step in changing between different variable sets, for example equinoctial to polar.

A.1.3 : Spherical Polar Variables

The three spherical polar variables are defined below.

- r is the radial position of the satellite.
- α is the right ascension of satellite (= λ+G).
- ϕ is the declination (and sub-satellite latitude) of the satellite.

These variables are illustrated, with reference to the inertial axes, in figure A.1.

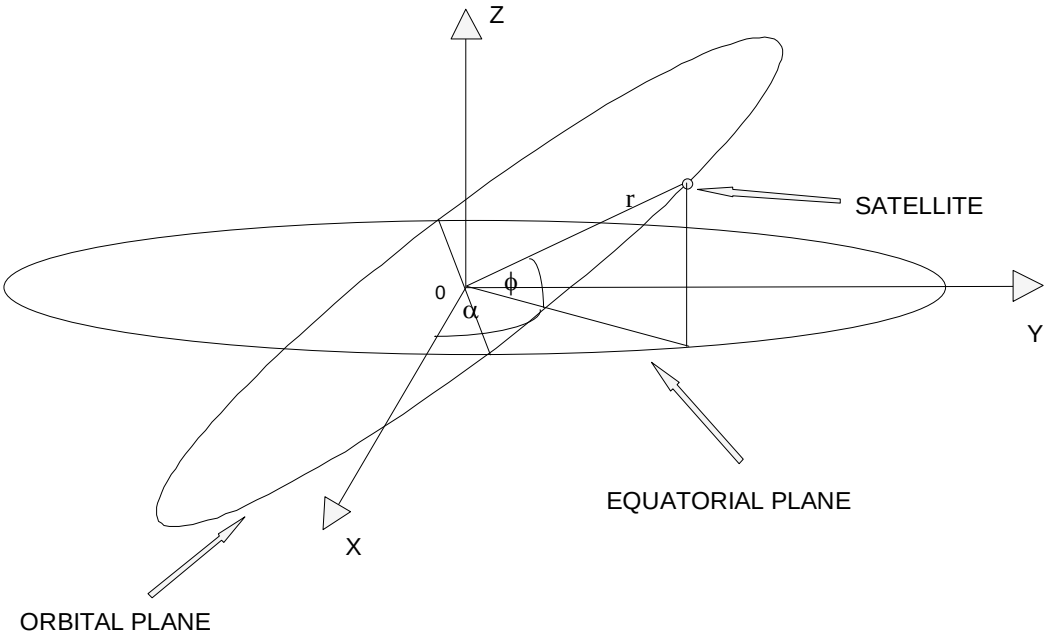

Figure A.1: Spherical Polar Variables

Spherical polar variables are used in chapter 4 in reference to the positions of the Sun and Moon for perturbation acceleration calculations.

A.1.4 : Rectangular Orbital Axes

The vector directions defining the rectangular orbital axes are given below and illustrated in figure A.2.

- The x_1 axis points radially outwards to the centre of the satellite.
- The y_1 axis lies in the orbit plane, pointing in the prograde direction.
- The z_1 axis is perpendicular to the orbit, completing the right handed triad.

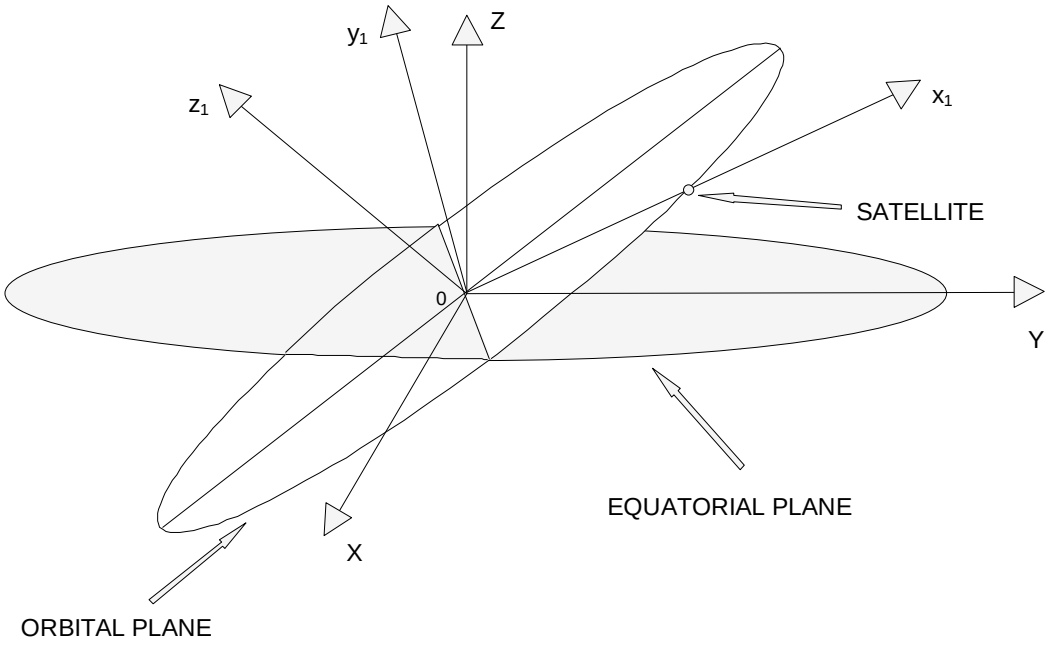

Figure A.2: Orbital Axes

The orbital axes are used for the integration part of the orbit propagation and thus perturbation acceleration components calculated in other reference frames must be converted to orbital axes before summation and integration.

A.1.5 : Rectangular Radial/Longitudinal/Latitudinal Axes

The axis definitions are given below and illustrated in figure A.3.

- x_2 is the radial vector.
- y_2 points in the east direction at the subsatellite point (longitudinally).
- z_2 points in the north direction at the subsatellite point (latitudinal). Note this is not along the Z axis unless the satellite latitude is zero.

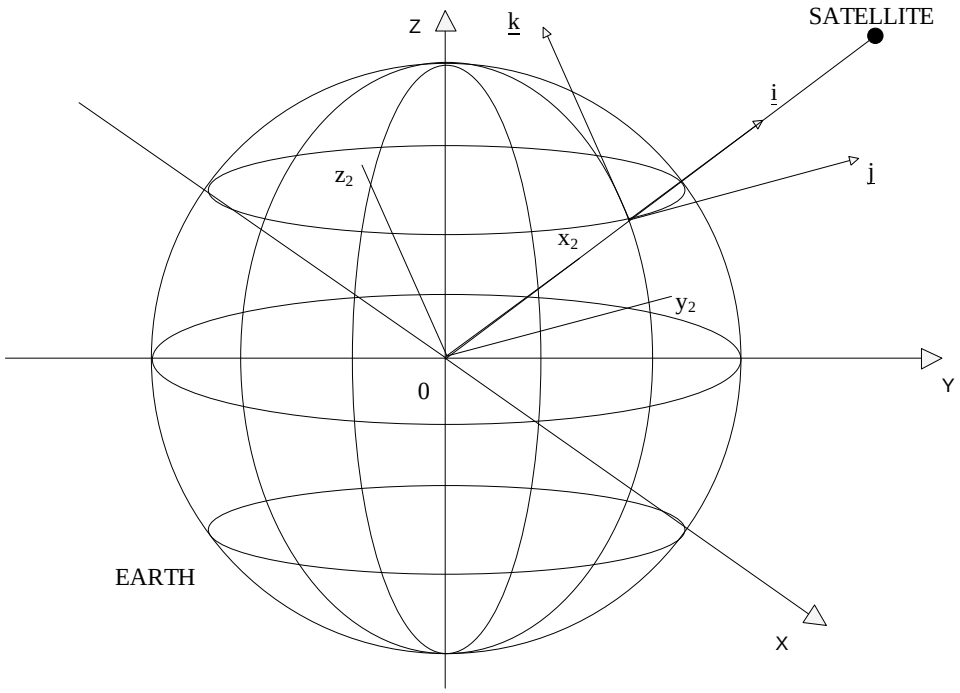

Figure A.3: Radial/Longitudinal/Latitudinal Axes Directions

In the figure [i, j, k] are unit vectors parallel to the axes [x_2, y_2, z_2], they are drawn at the subsatellite point to clarify the axis directions with respect to the Earth.

The Earth harmonics perturbations are calculated in this frame prior to conversion to orbital axes.

A.2 : Axis and Variable Set Transformations

The following transformations are documented.

- Equinoctial to classical elements (equations (A.1) gives the inverse relations).
- Inertial position to orbital axes and vice-versa.
- Equinoctial variables to inertial position and velocity and vice-versa.
- Inertial position to radial/longitudinal/latitudinal axes and vice-versa.
- Polar variables to inertial position.
- Equinoctial variables to polar variables.

A.2.1 : Equinoctial to Classical Elements

The inverse relationships to equations (A.1) can be derived as:

$$
\begin{aligned}
e &= \sqrt{P1^2 + P2^2} \\
i &= 2\mathrm{Tan}^{-1}\sqrt{Q1^2 + Q2^2} \\
\Omega &= 2\mathrm{Tan}^{-1}\left(Q1 / Q2\right) \quad \text{if } Q2 \geq 0 \;;\; 2\mathrm{Tan}^{-1}\left(Q1 / Q2\right) + \pi \text{ if } Q2 < 0 \\
\omega &= \mathrm{Tan}^{-1}\left(P1 / P2\right) - \Omega \text{ if } P2 \geq 0 \;;\; \mathrm{Tan}^{-1}\left(P1 / P2\right) - \Omega + \pi \text{ if } P2 < 0 \\
f &= L - \left(\Omega + \omega\right) \\
a &= a
\end{aligned}
\qquad \text{(A.2)}
$$

note that the semi-major axis is common to both element sets.

A.2.2 : Inertial Position to Orbital Axes and Vice-Versa

The following set of Euler rotations transforms the inertial axes to the orbital axes shown in figure A.2.

1. Rotation of 'Ω' about the Z axis.
2. Rotation of 'i' about the rotated X axis.
3. Rotation of '(ω+f)' along the orbital plane about the rotated Z axis.

The matrix equation relating the two frames is derived in classical elements as :

$$\begin{bmatrix} x_1 \\ y_1 \\ z_1 \end{bmatrix} = A^T \begin{bmatrix} X \\ Y \\ Z \end{bmatrix} \quad \text{or} \quad \begin{bmatrix} X \\ Y \\ Z \end{bmatrix} = A \begin{bmatrix} x_1 \\ y_1 \\ z_1 \end{bmatrix} \tag{A.3}$$

where A is the orthogonal matrix :

$$A = \begin{bmatrix} \text{Cos}(\Omega)\text{Cos}(\omega + f) - \text{Cos}(i)\text{Sin}(\Omega)\text{Sin}(\omega + f) & -\text{Cos}(\Omega)\text{Sin}(\omega + f) - \text{Cos}(i)\text{Sin}(\Omega)\text{Cos}(\omega + f) & \text{Sin}(i)\text{Sin}(\Omega) \\ \text{Sin}(\Omega)\text{Cos}(\omega + f) + \text{Cos}(i)\text{Cos}(\Omega)\text{Sin}(\omega + f) & -\text{Sin}(\Omega)\text{Sin}(\omega + f) + \text{Cos}(i)\text{Cos}(\Omega)\text{Cos}(\omega + f) & -\text{Sin}(i)\text{Cos}(\Omega) \\ \text{Sin}(i)\text{Sin}(\omega + f) & \text{Sin}(i)\text{Cos}(\omega + f) & \text{Cos}(i) \end{bmatrix}$$

which can be rewritten in equinoctial variables using equations (A.1) as :

$$A = \begin{bmatrix} \text{Cos}(L) + 2Q1(Q2\text{Sin}(L) - Q1\text{Cos}(L))/q & -\text{Sin}(L) + 2Q1(Q2\text{Cos}(L) + Q1\text{Sin}(L))/q & 2Q1/q \\ \text{Sin}(L) - 2Q2(Q2\text{Sin}(L) - Q1\text{Cos}(L))/q & \text{Cos}(L) - 2Q2(Q2\text{Cos}(L) + Q1\text{Sin}(L))/q & -2Q2/q \\ 2(Q2\text{Sin}(L) - Q1\text{Cos}(L))/q & 2(Q2\text{Cos}(L) + Q1\text{Sin}(L))/q & (2-q)/q \end{bmatrix}$$

and : $$q = 1 + Q1^2 + Q2^2$$

Completing the information required to perform the transformation.

A.2.3 : Equinoctial to Inertial and Vice-Versa

The columns of matrix ‘A’ used in equation (A.3) are unit vectors parallel to the axes $[x_1, y_1, z_1]$ respectively. Naming these,

$$\hat{\underline{r}} = \begin{bmatrix} \text{Cos}(L) + 2Q1(Q2\text{Sin}(L) - Q1\text{Cos}(L))/q \\ \text{Sin}(L) - 2Q2(Q2\text{Sin}(L) - Q1\text{Cos}(L))/q \\ 2(Q2\text{Sin}(L) - Q1\text{Cos}(L))/q \end{bmatrix}$$

$$\hat{\underline{u}} = \begin{bmatrix} -\text{Sin}(L) + 2Q1(Q2\text{Cos}(L) + Q1\text{Sin}(L))/q \\ \text{Cos}(L) - 2Q2(Q2\text{Cos}(L) + Q1\text{Sin}(L))/q \\ 2(Q2\text{Cos}(L) + Q1\text{Sin}(L))/q \end{bmatrix} \tag{A.4}$$

$$\hat{\underline{k}} = \begin{bmatrix} 2Q1/q \\ -2Q2/q \\ (2-q)/q \end{bmatrix}$$

the satellite position is thus :

$$\underline{r} = r\hat{\underline{r}} \tag{A.5}$$

since the direction 'x_1' is identical to the radial direction. Differentiating equation (A.5) and ignoring perturbations (i.e. assuming [a, P1, P2, Q1, Q2] are constant) the velocity vector is:

$$\dot{\underline{r}} = \dot{r}\hat{\underline{r}} + r\dot{L}\hat{\underline{u}} \tag{A.6}$$

The variables required to compute equations (A.5) and (A.6) are given below.

$$\begin{aligned} r &= \left(h^2 / \mu\right) / \left(1 + P1\mathrm{Sin}(L) + P2\mathrm{Cos}(L)\right) \\ \dot{r} &= -\left(\mu / h\right)\left(P1\mathrm{Cos}(L) - P2\mathrm{Sin}(L)\right) \\ r\dot{L} &= \left(\mu / h\right)\left(1 + P1\mathrm{Sin}(L) + P2\mathrm{Cos}(L)\right) \end{aligned} \tag{A.7}$$

where,

$$\dot{L} = \frac{h}{r^2} \quad \text{and} \quad h = \sqrt{\mu a\left(1 - P1^2 - P2^2\right)}$$

The inverse relationships are more complex and require the computation of the eccentricity, angular momentum and node vectors (a vector pointing in the direction of the ascending node and passing through the origin) as an intermediary step. In inertial axes these are found as,

$$\begin{aligned} \underline{e} &= \begin{bmatrix} e_x \\ e_y \\ e_z \end{bmatrix} = \frac{1}{\mu}\left[\left(v^2 - \frac{\mu}{r}\right)\underline{r} - \left(\underline{r}.\underline{v}\right)\underline{v}\right] \\ \underline{h} &= \begin{bmatrix} h_x \\ h_y \\ h_z \end{bmatrix} = \underline{r} \times \underline{v} \\ \underline{n} &= \begin{bmatrix} -h_y \\ h_x \\ 0 \end{bmatrix} \end{aligned} \tag{A.8}$$

The angular momentum vector can also be written in terms of the orbit normal vector as,

$$\underline{h} = h\hat{\underline{k}} = h\begin{bmatrix} 2Q1/q \\ -2Q2/q \\ (2-q)/q \end{bmatrix} \tag{A.9}$$

Equating components between equation (A.8) and (A.9) representations of '$\underline{h}$',

$$Q1 = \frac{h_x q}{2h} \quad ; \quad Q2 = -\frac{h_y q}{2h} \quad \text{where} \quad q = \frac{2h}{h + h_z} \tag{A.10}$$

With f=0 the unit vector '$\hat{\underline{r}}$' from equation (A.4) is identical to the direction of the eccentricity vector. In this case L=(Ω+ω) and multiplying through by 'e',

$$\underline{e} = \begin{bmatrix} P2 + 2Q1(Q2P1 - Q1P2)/q \\ P1 - 2Q2(Q2P1 - Q1P2)/q \\ 2(Q2P1 - Q1P2)/q \end{bmatrix} \tag{A.11}$$

Again by equating components, this time for '$\underline{e}$', the variables 'P1' and 'P2' are found as,

$$P1 = \frac{q\left[\left(1 + Q2^2 - Q1^2\right)e_y - 2Q1Q2e_x\right]}{\left[1 - \left(Q1^2 + Q2^2\right)^2\right]} \quad ; \quad P2 = \frac{q\left[\left(1 + Q1^2 - Q2^2\right)e_x - 2Q1Q2e_y\right]}{\left[1 - \left(Q1^2 + Q2^2\right)^2\right]} \tag{A.12}$$

The semi-major axis is now found as,

$$a = \frac{h^2}{\mu\left(1 - P1^2 - P2^2\right)} \tag{A.13}$$

For the sixth element, the true longitude will be chosen and if the mean longitude is required then this can be calculated using the technique given in chapter 4. The angle between the node vector and the position vector is (ω+f) hence,

$$\begin{aligned} \underline{r}.\underline{n} &= rnCos(\omega + f) \\ (\omega + f) &= Cos^{-1}\left(\frac{-r_x.h_y + r_y.h_x}{rn}\right) \end{aligned} \tag{A.14}$$

which exists only if $(Q1^2+Q2^2) \neq 0$ (i.e. non-zero inclination). Thus under these conditions the true longitude is,

$$\begin{aligned} L &= f + \omega + \Omega \\ L &= Cos^{-1}\left(\frac{-r_x.h_y + r_y.h_x}{rn}\right) + Tan^{-1}\left(\frac{Q1}{Q2}\right) \end{aligned} \tag{A.15}$$

where the inverse tangent ambiguity is removed by considering the signs of 'Q1' and 'Q2' and the inverse cosine ambiguity, by considering the 'X' and 'Y' components of the position vector given in equation (A.5).

If $(Q1^2+Q2^2) = 0$ (i.e. zero inclination) then the true longitude can be found directly from the dot product between the 'X' axis and the position vector.

$$\begin{aligned} \begin{bmatrix} r_x \\ r_y \\ r_z \end{bmatrix} \cdot \begin{bmatrix} 1 \\ 0 \\ 0 \end{bmatrix} &= rCos(L) \\ L &= Cos^{-1}(r_x/r) \end{aligned} \tag{A.16}$$

Again the sign ambiguity is resolved by considering the 'X' and 'Y' axis components of the position vector.

A.2.4 : Inertial to Radial/Longitudinal/Latitudinal and Vice-Versa

The radial / longitudinal / latitudinal axes are obtained from the inertial axes via Euler rotations in the polar angles in the order:

1. Rotation of α about the Z axis.
2. Rotation of ϕ about the rotated Y axis.

The matrix equation relating the two frames is then derived as:

$$\begin{bmatrix} x_2 \\ y_2 \\ z_2 \end{bmatrix} = B^T \begin{bmatrix} X \\ Y \\ Z \end{bmatrix} \quad \text{or} \quad \begin{bmatrix} X \\ Y \\ Z \end{bmatrix} = B \begin{bmatrix} x_2 \\ y_2 \\ z_2 \end{bmatrix} \tag{A.17}$$

where B is the orthogonal matrix:

$$B = \begin{bmatrix} \text{Cos}(\alpha)\text{Cos}(\phi) & -\text{Sin}(\alpha) & -\text{Cos}(\alpha)\text{Sin}(\phi) \\ \text{Sin}(\alpha)\text{Cos}(\phi) & \text{Cos}(\alpha) & -\text{Sin}(\alpha)\text{Sin}(\phi) \\ \text{Sin}(\phi) & 0 & \text{Cos}(\phi) \end{bmatrix} \tag{A.18}$$

A.2.5 : Polar Variables to Inertial Position

Since the 'x_2' axis is identical to the radial vector the inertial position can be written in polar elements using the first column of matrix 'B' as written in equation (A.18). Thus,

$$\underline{r} = r \begin{bmatrix} \text{Cos}(\phi)\text{Cos}(\alpha) \\ \text{Cos}(\phi)\text{Sin}(\alpha) \\ \text{Sin}(\phi) \end{bmatrix} \tag{A.19}$$

where, $\alpha = \lambda + G$

The right ascension of the Greenwich meridian, 'G' is calculated empirically from the Julian date 'JD' as,

$$\text{JD} = 100^o.4606184 + 36000^o.77005\text{Tu} + 0^o.000387933\text{Tu}^2 - 0^o.000000258\text{Tu}^3 \tag{A.20}$$

'Tu' is the number of Julian centuries from the year 2000.0 epoch and,

$$\begin{aligned} \text{Tu} &= (\text{JD} - 2451545.0)/36525 \\ \text{G} &= 100^o.4606184 + 36000^o.77005\text{Tu} + 0^o.000387933\text{Tu}^2 - 0.000000258\text{Tu}^3 + n_E\text{UT} \end{aligned} \tag{A.21}$$

where 'UT' is universal time in seconds and 'n_E' is the mean rotation rate of the Earth.

A.2.6 : Equinoctial Variables to Polar Variables

To calculate α and ϕ (and thus λ) equate the inertial position vector written in equinoctial and polar variables as equations (A.5) and (A.19) respectively,

$$\begin{bmatrix} X \\ Y \\ Z \end{bmatrix} = r \begin{bmatrix} \mathrm{Cos}(\phi)\mathrm{Cos}(\alpha) \\ \mathrm{Cos}(\phi)\mathrm{Sin}(\alpha) \\ \mathrm{Sin}(\phi) \end{bmatrix} = r \begin{bmatrix} \mathrm{Cos}(L) + 2Q1(Q2\mathrm{Sin}(L) - Q1\mathrm{Cos}(L)) / q \\ \mathrm{Sin}(L) - 2Q2(Q2\mathrm{Sin}(L) - Q1\mathrm{Cos}(L)) / q \\ 2(Q2\mathrm{Sin}(L) - Q1\mathrm{Cos}(L)) / q \end{bmatrix} \tag{A.22}$$

Solving this for the polar angular variables,

$$\alpha = \lambda + G = \mathrm{Tan}^{-1}\left(\frac{\mathrm{Sin}(L) - 2Q2\left(Q2\mathrm{Sin}(L) - Q1\mathrm{Cos}(L)\right) / q}{\mathrm{Cos}(L) + 2Q1\left(Q2\mathrm{Sin}(L) - Q1\mathrm{Cos}(L)\right) / q} \right) \qquad \text{if } X \geq 0$$

$$\alpha = \lambda + G = \mathrm{Tan}^{-1}\left(\frac{\mathrm{Sin}(L) - 2Q2\left(Q2\mathrm{Sin}(L) - Q1\mathrm{Cos}(L)\right) / q}{\mathrm{Cos}(L) + 2Q1\left(Q2\mathrm{Sin}(L) - Q1\mathrm{Cos}(L)\right) / q} \right) + \pi \quad \text{if } X < 0 \tag{A.23}$$

$$\phi = \mathrm{Sin}^{-1}\left(2\left(Q2\mathrm{Sin}(L) - Q1\mathrm{Cos}(L)\right) / q\right)$$

and to complete transformation, the first line of equation (A.7) can be used to calculate the radial distance, 'r'.

A.3 : Curve Fitting

A.3.1 : Multiple Linear Regression Theory

The problem of determining the underlying mean motion of a given variable with respect to time from the actual motion (which includes short term perturbation effects) can be dealt with via the technique of multiple linear regression. Applying this to the mean motion of the equinoctial elements, satisfactory results can be obtained using a linear combination of two, three or four functions (the choice depends on the specific element). If the variable in question is 'y' then the mean motion can be described as,

$$\begin{aligned} y &= \alpha f_0(t) + \beta f_1(t) \\ y &= \alpha f_0(t) + \beta f_1(t) + \gamma f_2(t) \\ y &= \alpha f_0(t) + \beta f_1(t) + \gamma f_2(t) + \mu f_3(t) \end{aligned} \qquad \text{(A.24)}$$

where $[f_0, f_1, f_2, f_3]$ are known functions of time and the coefficients $[\alpha, \beta, \gamma, \mu]$ are to be determined.

Given that the actual value of 'y' is known at a set of discrete points in the time domain, then the coefficients $[\alpha, \beta, \gamma, \mu]$ can be found using a least squares technique. The solutions for the three cases are given in tables A.1 to A.3. Note that as the order of the method increases so too does the complexity. For computer simulations using these equations it is advisable to use the lowest order method which adequately describes the actual response if either computational speed or variable storage space is an issue.

TWO FUNCTION SOLUTION	
$M = \sum f_0^{\,2}$ $P = \sum f_0 f_1$ $R = \sum f_1^{\,2}$ $U = \sum y f_0$ $V = \sum y f_1$	$D = MR - P^2$ $\alpha = (UR - VP)/D$ $\beta = (-UP + VM)/D$

Table A.1 : Least Squares Data Fit With Two Functions

THREE FUNCTION SOLUTION	
$M = \sum f_0^{\,2}$ $P = \sum f_0 f_1$ $Q = \sum f_0 f_2$ $R = \sum f_1^{\,2}$ $S = \sum f_1 f_2$ $T = \sum f_2^{\,2}$ $U = \sum yf_0$ $V = \sum yf_1$ $W = \sum yf_2$	$D = MRT + 2PQS - MS^2 - RQ^2 - TP^2$ $\alpha = \left(U\left(RT - S^2\right) + V(QS - PT) + W(PS - QR)\right)\Big/D$ $\beta = \left(U(SQ - PT) + V\left(MT - Q^2\right) + W(PQ - MS)\right)\Big/D$ $\gamma = \left(U(PS - RQ) + V(PQ - MS) + W\left(MR - P^2\right)\right)\Big/D$

Table A.2 : Least Squares Data Fit With Three Functions

FOUR FUNCTION SOLUTION

$D = -Q^2J^2-2PTJH+K^2MR-P^2K^2-2KRQH+2SQJH-2KMSJ+TMJ^2+MS^2L+RQ^2L+2PKQJ+P^2TL-2PSQL$
$+TRH^2-MRTL-S^2H^2+2PKSH$

$\alpha = (UK^2R-HKRW+HRTX-QRKX+QRWL-URTL-2UKSJ+UTJ^2+US^2L+PJKW+PSKX-PJTX$
$-PVK^2+PVTL-PSWL+QKJV-QSVL+QSJX-QWJ^2-HTJV-HS^2X+HKSV+HSJW)/D$

$\beta = -(-PQKX-PUTL+PHTX+PQWL+PUK^2-PHKW+QSUL-QKJU+Q^2JX+MJKW+MSKX-QWJH$
$-MJTX-MVK^2-HKSU+2QKHV-H^2TV-QSHX+MVTL+HTJU-MSWL+H^2SW-Q^2VL)/D$

$\gamma = (P^2WL-P^2KX-2PWJH-PSUL+PSHX-PQVL+PKHV+PKJU+PQJX+MRKX-KMJV-KRHU$
$-QJ^2U+QJHV-RQHX-MRWL+MSVL-SH^2V+SHJU-MSJX+RQUL+WMJ^2+WRH^2)/D$

$\mu = -(KRQU-TMJV-P^2TX-PKQV-SQJU-KMRW-MS^2X-TRHU+MRTX-SQHV-RQ^2X+S^2HU$
$+P^2KW+Q^2JV-PQJW+KMSV+PTHV-PSHW+MSJW+RQHW-PKSU+2PSQX+PTJU)/D$

$M = \sum f_0^{\,2}$ $\quad T = \sum f_2^{\,2}$ $\quad U = \sum yf_0$

$P = \sum f_0 f_1$ $\quad H = \sum f_3 f_0$ $\quad V = \sum yf_1$

$Q = \sum f_0 f_2$ $\quad J = \sum f_3 f_1$ $\quad W = \sum yf_2$

$R = \sum f_1^{\,2}$ $\quad K = \sum f_3 f_2$ $\quad X = \sum yf_3$

$S = \sum f_1 f_2$ $\quad L = \sum f_3^{\,2}$

Table A.3 : Least Squares Data Fit With Four Functions

A.3.2 : Specific Cases

The calculations of burn magnitudes and times for EW station keeping as discussed in chapter 5 require the mean values of the elements [a, λ, P1, P2]. The linear regression functions used for each element by the station keeping module of the simulation software for this purpose are given below, along with the justification for their selection.

Semi-major Axis

From the validation graphs for semi-major axis in appendix B it can be seen that the mean motion is mainly a function of the Earth harmonics perturbations and varies approximately linearly with time (the remaining perturbation sources produce periodic motion which is superimposed on this). The regression equation selected is thus linear.

$$\begin{aligned} y_i &= a_{mean} \approx \alpha_a + \beta_a t \\ f_0 &= 1 \\ f_1 &= t \end{aligned} \qquad \text{(A.25)}$$

Greenwich Longitude

The approximate evolution of Greenwich longitude has been shown to be parabolic in chapter 5, leading to the following three function regression equation.

$$\begin{aligned} y_i &= \lambda_{mean} \approx \alpha_\lambda + \beta_\lambda t + \gamma_\lambda t^2 \\ f_0 &= 1 \\ f_1 &= t \\ f_2 &= t^2 \end{aligned} \qquad \text{(A.26)}$$

This is suitable when data points for an entire EW cycle are available, however following a NS burn with errors (section 5.4 of the main text) cross-coupling effects lead to a change in the in-plane orbital elements, and thus Greenwich longitude. In this situation only the data points following the NS burn are available for regression analysis and since usual practice is to perform the next EW correction around 2 days after the NS (to reduce the effect of the cross-coupling error) there are insufficient periods of the

perturbed longitude motion *including* eccentricity libration to make a parabolic least squares fit practical. In this case a fourth order solution has been used which includes modelling of the eccentricity libration effect. The regression equation is,

$$y_i = \left(\lambda_{mean} - \frac{\ddot{\lambda}}{2} t^2 \right) \approx \alpha_\lambda + \beta_\lambda t + \gamma_\lambda \mathrm{Sin}(n_E t) + \mu_\lambda \mathrm{Cos}(n_E t)$$

$$\begin{aligned} f_0 &= 1 \\ f_1 &= t \\ f_2 &= \mathrm{Sin}(n_E t) \\ f_3 &= \mathrm{Cos}(n_E t) \end{aligned} \qquad \text{(A.27)}$$

It should be noted that the eccentricity libration period is the same as the satellite orbital period and so will not be precisely equal to 'n_E' and that the magnitude of the eccentricity will change over time, making [γ, μ] non-constant. Additionally, to remove the need for a much more complicated five function method, the longitudinal drift acceleration is assumed constant in equation (A.27) and is calculated from the longitude value of the centre of the GEO window (see figure 5.3).

With these assumptions equation (A.27) produces better results than (A.26) when applied over a small time interval (such as between NS and EW station keeping corrections) where the eccentricity problems are minor. Over longer periods (A.26) is better.

Station keeping calculations based on the regression variables calculated using the four function method do not use the values of [γ, μ] since only the underlying mean motion of longitude is needed (i.e. the parabolic constants). Because of this [γ, μ] do not need to be calculated explicitly by the software program, and for efficiency therefore they are not.

P1 and P2

From the orbit propagation validation graphs for 'P1' and 'P2' in appendix B it can be seen that the uncontrolled mean motion of these elements is a result of the solar pressure

perturbation and can be approximated by a sinusoid with a period of one year, added to which is a constant offset term. The regression equations are thus a linear combination of three functions, defined below.

$$\begin{aligned} P1_{mean} &\approx \alpha_{P1} + \beta_{P1}\mathrm{Sin}(n_s t) + \gamma_{P1}\mathrm{Cos}(n_s t) \\ P2_{mean} &\approx \alpha_{P2} + \beta_{P2}\mathrm{Sin}(n_s t) + \gamma_{P2}\mathrm{Cos}(n_s t) \end{aligned} \qquad (A.28)$$

$$\begin{aligned} f_0 &= 1 \\ f_1 &= \mathrm{Sin}(n_s t) \\ f_2 &= \mathrm{Cos}(n_s t) \end{aligned}$$

Note that the values of the coefficients [α, β, γ] are different for 'P1' and 'P2'.

A.3.3 : Use of Regression Analysis in Propagation Software

At each step in the orbit propagation the actual values of [t, a, λ, P1, P2] are used to update the relevant summation terms listed in tables A.1 to A.3, dependant on form of the regression equation used to represent the individual element. At the end of the EW cycle these summations are used to calculate the regression coefficients [α, β, γ] for each element, which are then used to calculate the mean values of the elements prior to the station keeping correction.

Having obtained the pre-burn mean values the EW corrections can be calculated and applied, at which point the summation terms are re-initialised and the cycle begins again. This re-initialisation also takes place following a NS manoeuvre.

APPENDIX B : ORBIT PROPAGATOR VALIDATION

This section includes technical information about the operation and validation of the orbit propagator element of the software written during the course of the research. The breakdown of the appendix is as follows.

- B.1: Overview of validation procedure. Details of the reasoning behind the validation procedure as followed.
- B.2: Theoretical validation. Comparative tests with simplified analytical models are used to confirm that specific elements of the propagator produce reasonable results.
- B.3: Comparison with second propagator. Using the same starting conditions, orbit propagation data generated by an ESA propagation program is compared with equivalent results generated using the propagator evolved for this research.

B.1 : Overview of Validation Procedure

As noted in the main text software validation is vital and in this appendix the subject is addressed in two ways. Firstly the orbit propagator results are compared with simplified analytical solutions derived from the perturbation equations given in chapter 4 to show that these have been implemented correctly. Secondly output from the propagator is compared with similar output from an ESA orbit propagator. This comparison is intended to show the accuracy of the method used here when compared with a system that has been proven in practice.

No attempt has been made to quantify the error accumulation of the results over prolonged time periods based on an assessment of the limitations inherent in the simplifications made in chapter 4 when modelling the space environment.

Validation Test Descriptions

In chapter 4 a set of six differential equations, repeated here as equations (B.1), were formulated which when integrated would result in a description of a satellite orbit.

$$
\begin{aligned}
\frac{dl}{dt} &= n - \frac{r}{h}\left\{\begin{aligned}&\left[\frac{a}{a+b}\left(\frac{p}{r}\right)\left(P1\mathrm{Sin}(L)+P2\mathrm{Cos}(L)\right)+\left(\frac{2b}{a}\right)\right]a_{x_1}\\ &+\left[\frac{a}{a+b}\left(1+\frac{p}{r}\right)\left(P1\mathrm{Cos}(L)-P2\mathrm{Sin}(L)\right)\right]a_{y_1}\\ &+\left[Q1\mathrm{Cos}(L)-Q2\mathrm{Sin}(L)\right]a_{z_1}\end{aligned}\right\}\\
\frac{da}{dt} &= \frac{2a^2}{h}\left\{\left[P2\mathrm{Sin}(L)-P1\mathrm{Cos}(L)\right]a_{x_1}+\left[\frac{p}{r}\right]a_{y_1}\right\}\\
\frac{dP1}{dt} &= \frac{r}{h}\left\{-\left[\frac{p}{r}\mathrm{Cos}(L)\right]a_{x_1}+\left[P1+\left(1+\frac{p}{r}\right)\mathrm{Sin}(L)\right]a_{y_1}-\left[P2\left(Q1\mathrm{Cos}(L)-Q2\mathrm{Sin}(L)\right)\right]a_{z_1}\right\}\\
\frac{dP2}{dt} &= \frac{r}{h}\left\{\left[\frac{p}{r}\mathrm{Sin}(L)\right]a_{x_1}+\left[P2+\left(1+\frac{p}{r}\right)\mathrm{Cos}(L)\right]a_{y_1}+\left[P1\left(Q1\mathrm{Cos}(L)-Q2\mathrm{Sin}(L)\right)\right]a_{z_1}\right\}\\
\frac{dQ1}{dt} &= \frac{r}{2h}\left(1+Q1^2+Q2^2\right)\mathrm{Sin}(L)a_{z_1}\\
\frac{dQ2}{dt} &= \frac{r}{2h}\left(1+Q1^2+Q2^2\right)\mathrm{Cos}(L)a_{z_1}
\end{aligned}
\qquad \text{(B.1)}
$$

Without simplification these cannot be solved analytically and so a numerical integration scheme was detailed, requiring a computer orbit propagation program to be written which thus providing a special perturbation solution. This will be referred to as the 'simulation solution'.

The second solution was derived by making approximations to (B.1) to enable them to be integrated analytically, thus providing a general perturbation solution. This will be referred to as the 'analytical solution'.

The theoretical validation procedure detailed in section B.2 involved comparing these two solutions through a number of tests and accessing the source of the differences between them when these seemed unreasonably large. Three possibilities for the differences existed,

1. Limitations of the integration method used by the software (the method is inexact since it is a discrete approximation to a continuous process).
2. Software programming errors (the most common reason for differences).
3. Simplifications/errors in the derivation of the analytical solutions.

Mainly by trial and error individual errors were traced to individual sources. In most cases this was the second of the three options, however sometimes the analytical solution was found to be too simplistic/erroneous and it had to be improved upon. In no cases was the first option found to be the cause.

Where the source of the error was the propagator source code this had to be re-written. In instances were the change was minor and affected only a small segment of the code (e.g. an inverse tangent quadrant resolution incorrectly calculated) the 'failed' test was re-run with the modification and the validation process continued. However, when the change could conceivably affect the numerical integration process as a whole (e.g. at one stage the propagator integrated 'L' as the sixth orbital element until is was found that using 'l' was more accurate) the entire validation process was re-started with the

modified code. The test results presented here represent the final 'run through' of the process.

The theoretical tests performed can be divided into two parts. In the first, the perturbation forces were not active thus allowing the basic operation of the numerical integrator to be checked. For these tests exact analytical solutions to the orbital motion are possible. Specifically, with the exception of time and true longitude the evolution of which can be computed analytically, the orbital elements should all remain constant.

In the second part of the theoretical validation, four tests were performed and in each a single perturbation source was 'active' and the resulting orbit, compared with the analytical solution to the equinoctial form of the Lagrange equations (B.1). This procedure was used to verify correct implementation of the perturbations due to Earth harmonics, Solar gravity, Solar radiation and Lunar gravity effects. Since the implementation of each set of perturbation equations do not directly interact is it unnecessary to perform a third set of tests in which all the perturbation sources are active.

Table B.1 summarises the initial values of the equinoctial elements, for each theoretical test performed. Test names which prefix all the associated result files are also given.

TEST	**EQUINOCTIAL VARIABLES**					
NAME	**a**	**L**	**P1**	**P2**	**Q1**	**Q2**
IDEAL1	42164171.71	0^o	0	0	0	0
IDEAL2	42164171.71	0^o	-0.000873	0	-0.000873	0
EH	42164171.71	0^o	0	0	0	0
SG	42164171.71	0^o	-0.000873	0	-0.000873	0
LG	42164171.71	0^o	-0.000873	0	-0.000873	0
SP	42164171.71	0^o	0	0	-0.000873	0

Table B.1: Summary of Validation Tests Initial Conditions

All six tests start at the same epoch: January 1st 1994; 00:00.00 hrs GMT.

The initial conditions for the comparison with the second orbit propagator will be given in section B.3.

Comments on Test Results

Along with the graphical results for each test are comments on the probable source of the deviations which still exist between the 'actual' and 'expected' results. Generally, these are intended to explain the differences that are visible in the graphs.

For the theoretical validation in section B.2 the existence of the deviations is a consequence of simplifying the Lagrange equations so that they can be integrated, commonly by assuming that elements on the right hand side of the equations are constants for the purpose of integration when in fact this is not the case (although for elements which vary slowly or periodically with small amplitude the simplified equation is still reasonably accurate). The deviations in themselves are not important, what is important is that they can be explained adequately in terms of the limitations of the analytical solution (and thus show that significant programming errors are not responsible).

For the comparisons with the second propagator the differences in results are thought to be a result of model simplification, mainly in the solar radiation model.

B.2 : Theoretical Validation

B.2.1 : Test 1: Ideal GEO (Test Name : *IDEAL1*)

Summary

The initial orbit is the ideal geostationary orbit, which was propagated for 14 days with results recorded every 15 minutes.

Expected Results

The equinoctial variables [, P1, P2, Q1, Q2] are expected to remain constant and the true longitude 'L' is expected to increase linearly from the initial value with a rate of change identical to the mean rotation rate of the Earth.

Analytical Solution

The true longitude 'L' should vary linearly from 0° to 360° with a period of one sidereal day. The exact analytical equation for zero eccentricity and inclination is :

$$L = L_0 + \sqrt{\frac{\mu}{a^3}}t$$

Comparisons between Simulated and Analytical Results

As expected the equinoctial variables [, P1, P2, Q1, Q2] remained constant and thus graphical representations of the deviations from ideal results are not included for these elements. The difference between the propagated and the 'ideal' solution for 'L' is plotted in figure B.1 .

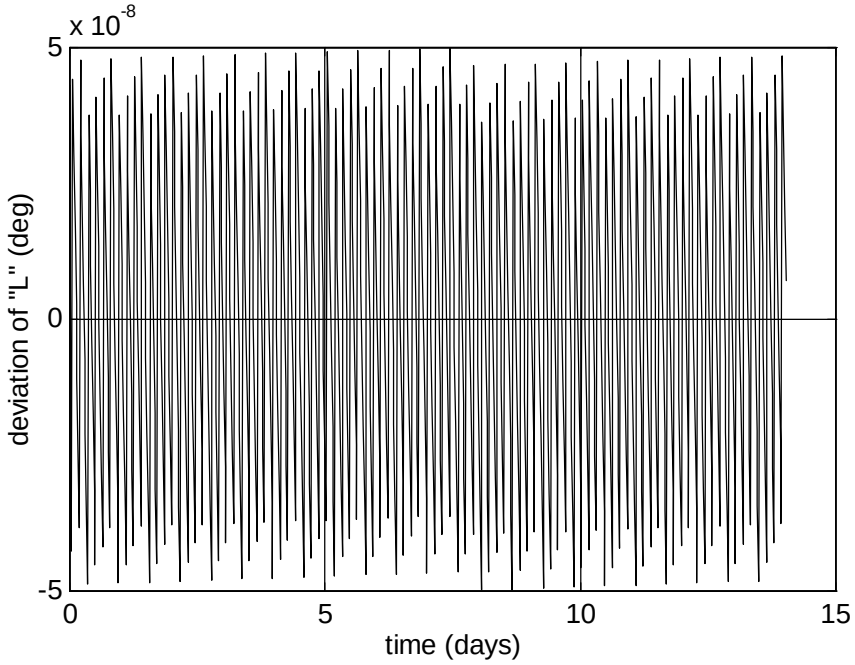

Figure B.1: Deviation From Ideal True Longitude for Test 1

The error signal varies between $\pm 5 \times 10^{-8}$ degrees, which is as expected since the true longitude is only recorded to seven decimal places in the output files. There is no obvious underlying linear gradient on the graph and so program output appears acceptable for this test.

Since the analytical solution is exact for this test this result can be considered in terms of what this means to an actual orbit. For a GEO window with a ±0.°1 longitude deadband the error recorded here represents one tenth of one millionth of a percent.

B.2.2 : Test 2: Near GEO (Test Name : *IDEAL2*)

Summary

The input orbit is geosynchronous, having a small inclination and eccentricity. The orbit was propagated for 14 days and results were recorded every 15 minutes.

Expected Results

As in the case of test 1 the variables [, P1, P2, Q1, Q2] should remain constant. Unlike test 1 however 'L' should vary non-linearly, describing a daily periodic motion about some mean GEO position.

Analytical Solution

Assuming the mean longitude 'l' is known the eccentric longitude ‘K’ is calculated iteratively from equation (B.2).

$$l = K + P1\cos(K) - P2\sin(K) \tag{B.2}$$

The true longitude is then found from:

$$\begin{aligned} \sin(L) &= \frac{a}{r}\left[\left(1 - \frac{a}{a+b}P2^2\right)\sin(K) + \frac{a}{a+b}P1P2\cos(K) - P1\right] \\ \cos(L) &= \frac{a}{r}\left[\left(1 - \frac{a}{a+b}P1^2\right)\cos(K) + \frac{a}{a+b}P1P2\sin(K) - P2\right] \end{aligned} \tag{B.3}$$

where:

$$\frac{a}{a+b} = \frac{1}{1+\sqrt{1-P1^2-P2^2}}$$

Since the mean longitude can be written as:

$$l = nt + l_0$$

the problem of predicting 'L' is now reduced to calculating the initial value 'l_0', which is done using equations (B.3) and (B.2) in the reverse order knowing that 'L_0' is zero.

Comparisons between Simulated and Analytical Results

As expected the equinoctial variables [, P1, P2, Q1, Q2] remained constant and thus deviation graphs are not included for these elements. The deviation of 'L' from the analytical solution is shown on figure B.2.

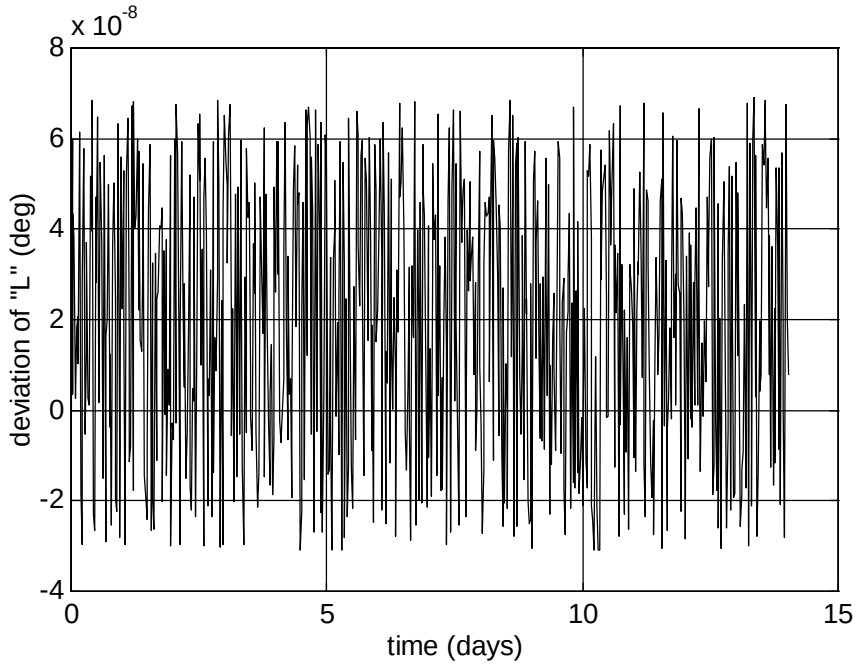

Figure B.2: Deviation From Ideal True Longitude for Test 2

As in the case of test 1 the deviation illustrated can be attributed to round-off error in the recording of results and is an insignificant part of a typical GEO station keeping window.

B.2.3 : Test 3: Earth Harmonics (Test Name : *EH*)

Summary

The aim of this test is to validate the implementation of the Earth harmonics perturbation acceleration equations. Combining equation (B.1) with the Earth harmonic perturbation equations from chapter 4 analytical solutions to the equinoctial variables are calculated. These are not expected to form perfect matches with the simulated data, however programming errors will show up as unexplainable deviations.

The orbit was propagated for 14 days, which is sufficient to show all the major effects.

Expected results

Two effects should be visible on true longitude; the first is a result of the J_{20} harmonic which effectively increases the ideal GEO altitude by about 2 km, and the second is a result of the J_{22} term which introduces a longitudinal drift acceleration. The first of these has the larger impact on true longitude, producing a constant rate longitudinal drift, superimposed on this will be a parabolic variation due to the second effect (if the overall longitude change over the course of the simulation is small enough to regard the drift acceleration as a constant). The J_{22} term will also effect the semi-major axis, causing this to change approximately linearly with time, the sign of this change is dependant on the starting longitudinal position. The remaining equinoctial elements are expected to oscillate daily about some mean values, physically this has no significance and is the result of fitting elliptical orbital elements to a real orbit.

Analytical Solution

For low inclination and eccentricity the radial/longitudinal/latitudinal axis set and the orbital axis set are approximately the same. Additionally, as a first estimate, assuming [P1, P2, Q1, Q2] are constant the following approximations can be made, based on the initial conditions.

$$\phi = 0$$
$$L = nt$$
$$\lambda = L - (G_0 + nt) = -G_0$$
$$r = a = a_0$$

The Earth harmonic perturbation accelerations can now be approximated to :

$$a_{x_1} = \frac{\mu R_e^2}{a_0^4}\left(\begin{array}{l} -\frac{3}{2}J_{20} + 9J_{22}\cos(2(G_0+\lambda_{22})) \\ +\left(\frac{Re}{a_0}\right)\left(-6J_{31}\cos(G_0+\lambda_{31}) + 60J_{33}\cos(3(G_0+\lambda_{33}))\right) \\ +\left(\frac{Re}{a_0}\right)^2\left(\frac{15}{8}J_{22} - \frac{75}{2}J_{42}\cos(2(G_0+\lambda_{42})) + 525J_{44}\cos(4(G_0+\lambda_{44}))\right) \end{array}\right) \quad \text{(B.4)}$$

$$a_{y_1} = \frac{\mu R_e^2}{a_0^4}\left(\begin{array}{l} -6J_{22}\sin(2(G_0+\lambda_{22})) \\ +\left(\frac{Re}{a_0}\right)\left(-45J_{33}\sin(3(G_0+\lambda_{33})) + \frac{3}{2}J_{31}\sin(G_0+\lambda_{31})\right) \\ +\left(\frac{Re}{a_0}\right)^2\left(15J_{42}\sin(2(G_0+\lambda_{42})) - 420J_{44}\sin(4(G_0+\lambda_{44}))\right) \end{array}\right) \quad \text{(B.5)}$$

$$a_{z_1} = \frac{\mu R_e^3}{a_0^5}\left(\begin{array}{l} -\frac{3}{2}J_{30} - 15J_{32}\cos(2(G_0+\lambda_{32})) \\ +\left(\frac{Re}{a_0}\right)\left(-105J_{43}\cos(3(G_0+\lambda_{43})) + \frac{15}{2}J_{41}\cos(G_0+\lambda_{41})\right) \end{array}\right) \quad \text{(B.6)}$$

Applying the same simplifications to equations (B.1),

$$
\begin{aligned}
\frac{dl}{dt} &= n_0 - 2\sqrt{\frac{a_0}{\mu}}a_{x_1} \\
\frac{da}{dt} &= \frac{2}{n_0}a_{y_1} \\
\frac{dP1}{dt} &= \frac{1}{n_0 a_0}\left(-\mathrm{Cos}(nt)a_{x_1} + \mathrm{Sin}(nt)a_{y_1}\right) \\
\frac{dP2}{dt} &= \frac{1}{n_0 a_0}\left(\mathrm{Sin}(nt)a_{x_1} + \mathrm{Cos}(nt)a_{y_1}\right) \\
\frac{dQ1}{dt} &= \frac{1}{2n_0 a_0}\mathrm{Sin}(nt)a_{z_1} \\
\frac{dQ2}{dt} &= \frac{1}{2n_0 a_0}\mathrm{Cos}(nt)a_{z_1}
\end{aligned}
\qquad \text{(B.7)}
$$

Which can now be integrated to give,

$$
\begin{aligned}
l &= \left(n_0 - \sqrt{\frac{a_0}{\mu}}a_{x_1}\right)t + l_0 \\
a &= \left(\frac{2}{n_0}a_{y_1}\right)t + a_0 \\
P1 &= -\frac{1}{{n_0}^2 a_0}\left(\mathrm{Sin}(nt)a_{x_1} + 2\mathrm{Cos}(nt)a_{y_1} - 2a_{y_1}\right) \\
P2 &= -\frac{1}{{n_0}^2 a_0}\left(\mathrm{Cos}(nt)a_{x_1} - 2\mathrm{Sin}(nt)a_{y_1} - a_{x_1}\right) \\
Q1 &= -\frac{1}{2{n_0}^2 a_0}\left(\mathrm{Cos}(nt)a_{z_1} - a_{z_1}\right) \\
Q2 &= \frac{1}{2{n_0}^2 a_0}\mathrm{Sin}(nt)a_{z_1}
\end{aligned}
\qquad \text{(B.8)}
$$

For low eccentricity the mean longitude can be approximated to the true longitude and equations (B.8) can thus be used to verify the propagation program output.

Comparisons between Simulated and Analytical Results

The difference between the simulated data and analytical data are plotted against time in the following diagrams. Discussion of the deviations from the analytical values are included with the graphs for each element. To show more clearly the semi-major axis variations the graphs illustrating the change in 'a' over time have been plotted as 'a-a_G'.

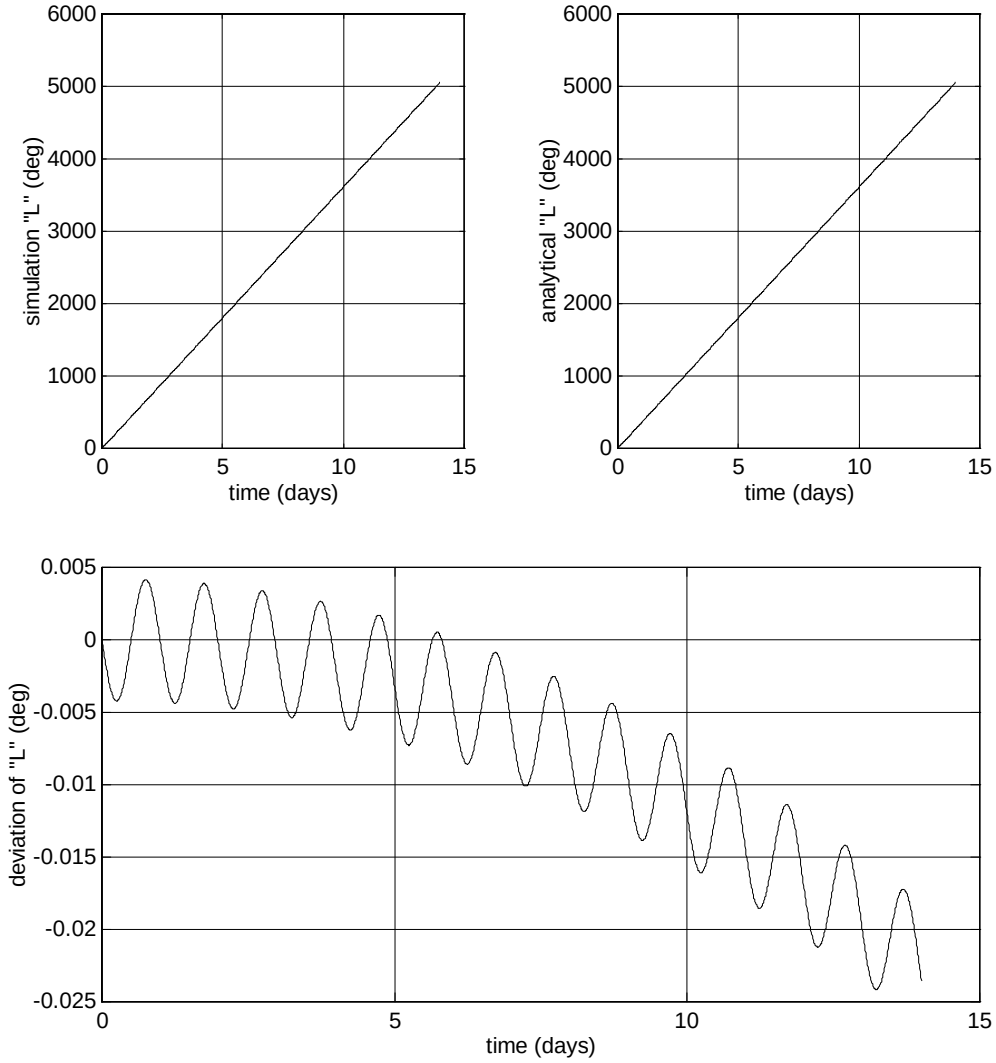

Figure B.3: True Longitude; Analytical, Simulated and Deviation for Test 3

From the first graph the mean value of dL/dt is 7.29262×10^{-5} r/s, which differs from unperturbed orbit theory by 5.023×10^{-9} r/s. The majority of this is caused by the difference in semi-major axis between the starting orbit (the unperturbed ideal value of 'a') and the perturbed ideal value (which as stated previously is about 2 km greater). The remaining 4×10^{-10} r/s difference is due to the longitudinal drift acceleration (chapter 5).

The parabolic shape of the deviation graph is due to the constant value of 'a' used for integration purposes in the analytical solution. The superimposed oscillatory motion is due to the mean eccentricity of the orbit, unaccounted for in the analytical solution.

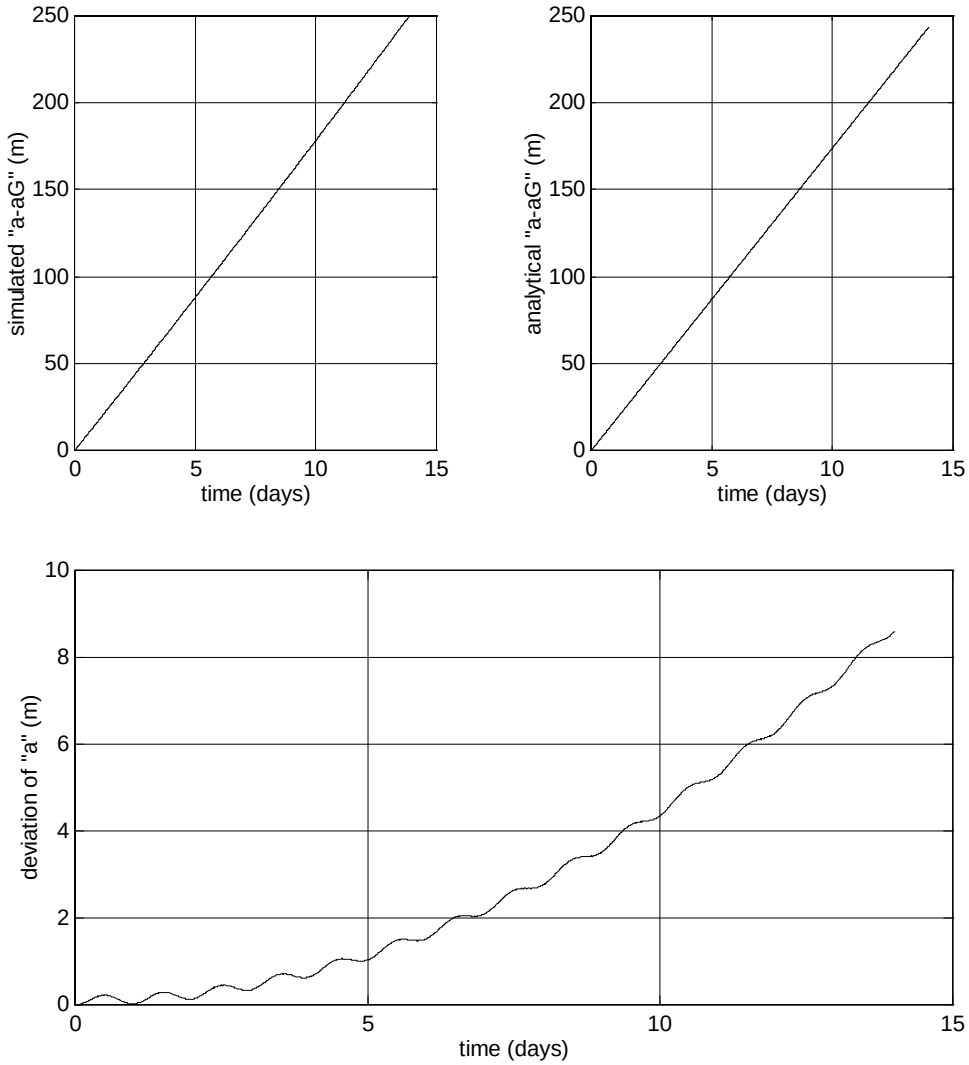

Figure B.4: Semi-major Axis; Simulated, Analytical and Deviation for Test 3

The parabolic deviation in semi-major axis is due to the assumption of a constant value of 'a' for integration purposes in the analytical solution. Replacing the 'a_0' terms in the perturbation equations by the actual value of 'a' at each time step would remove the effect, unfortunately this would also mean the differential equation could not be integrated analytically.

As in the case of true longitude, the superimposed oscillatory motion is the result of the mean eccentricity of the orbit.

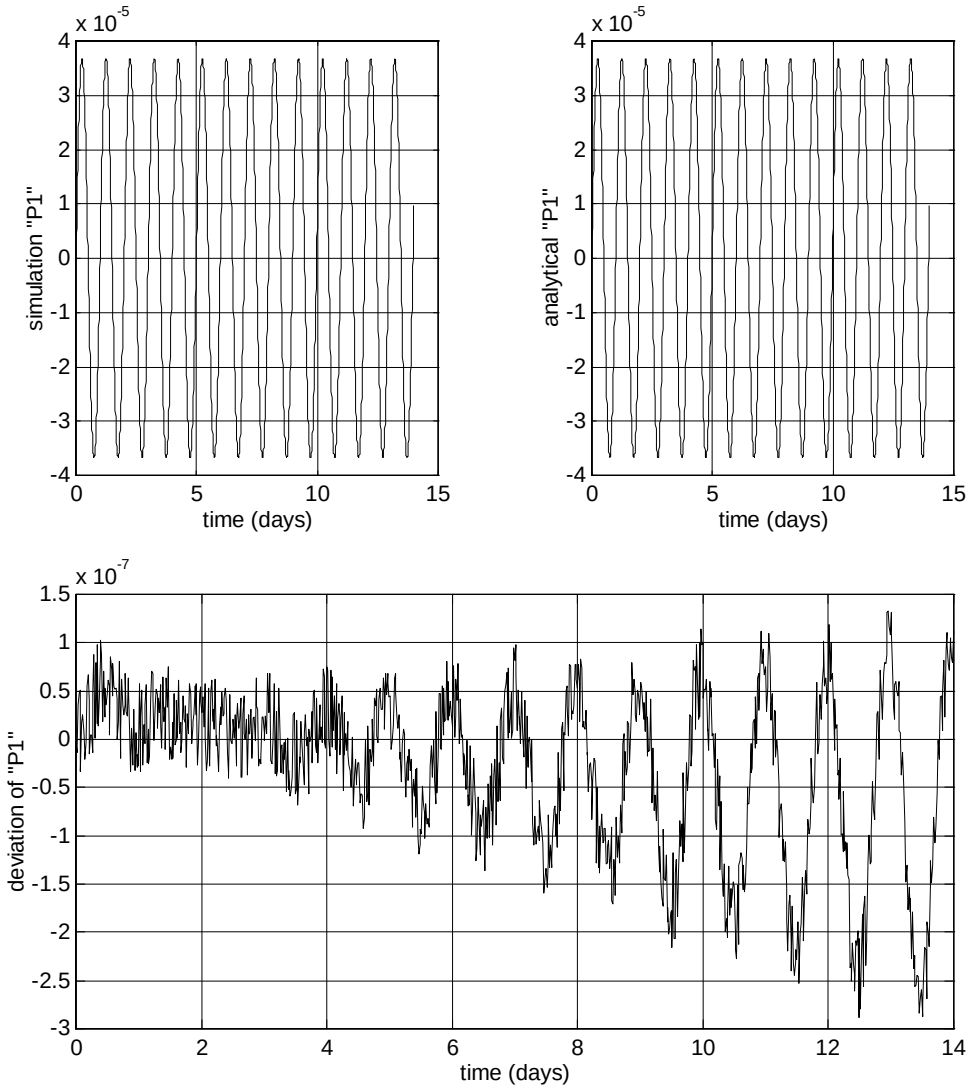

Figure B.5: P1; Simulated, Analytical and Deviation for Test 3

The motion of 'P1' oscillates with the expected period of one sidereal day. The deviation graph exhibits two main features; a linearly increasing envelope and a daily periodic function. It can be shown that both effects are a result of using the approximation $L=n_0t$ in equations (B.8) and the assumption of a constant longitude in equations (B.4) to (B.6). This was discovered by progressively simplifying the orbit propagator until its results matched those of the analytical solution. Another way of proving this would be to derive a more complex analytical solution, however this was thought to be more time consuming and of no additional advantage.

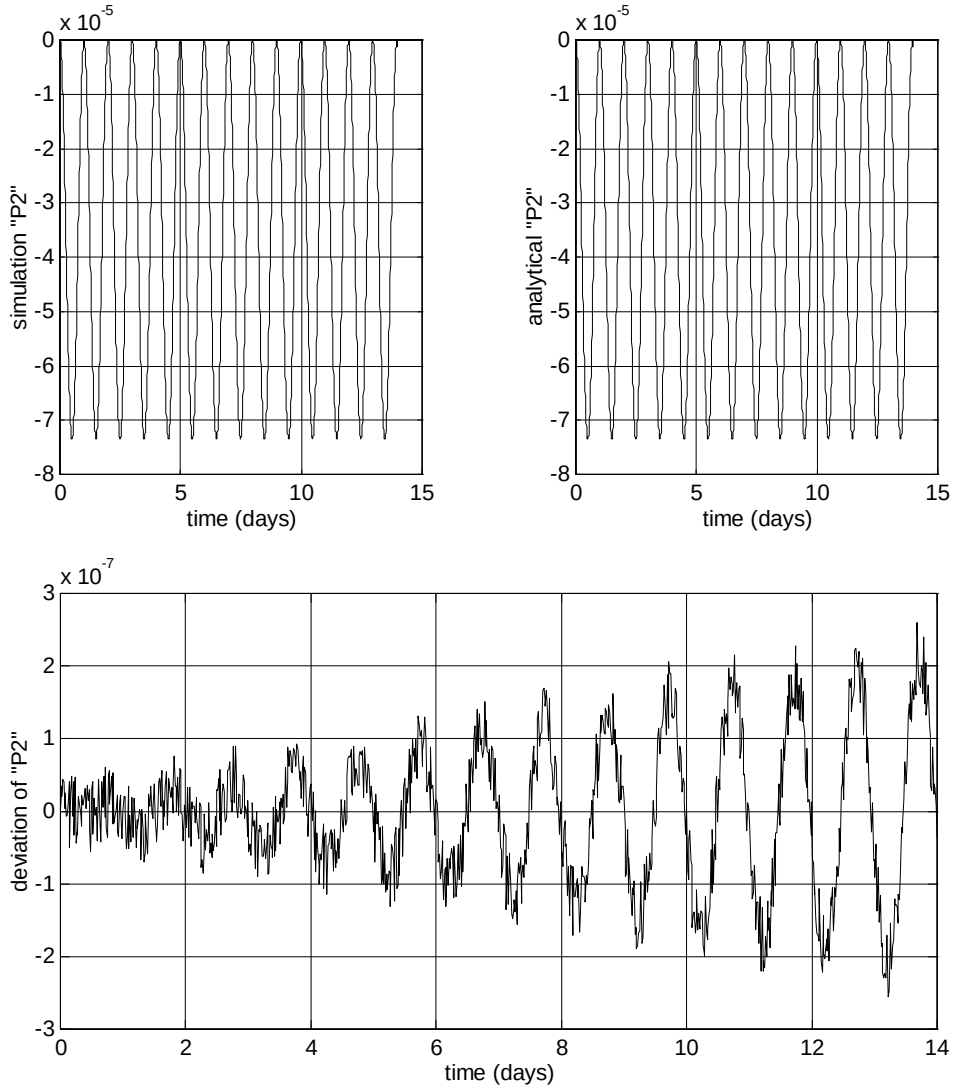

Figure B.6: P2; Simulated, Analytical and Deviation for Test 3

The form of the response is again as expected. The deviation graph is the result of the same effects as discussed for the 'P1' element.

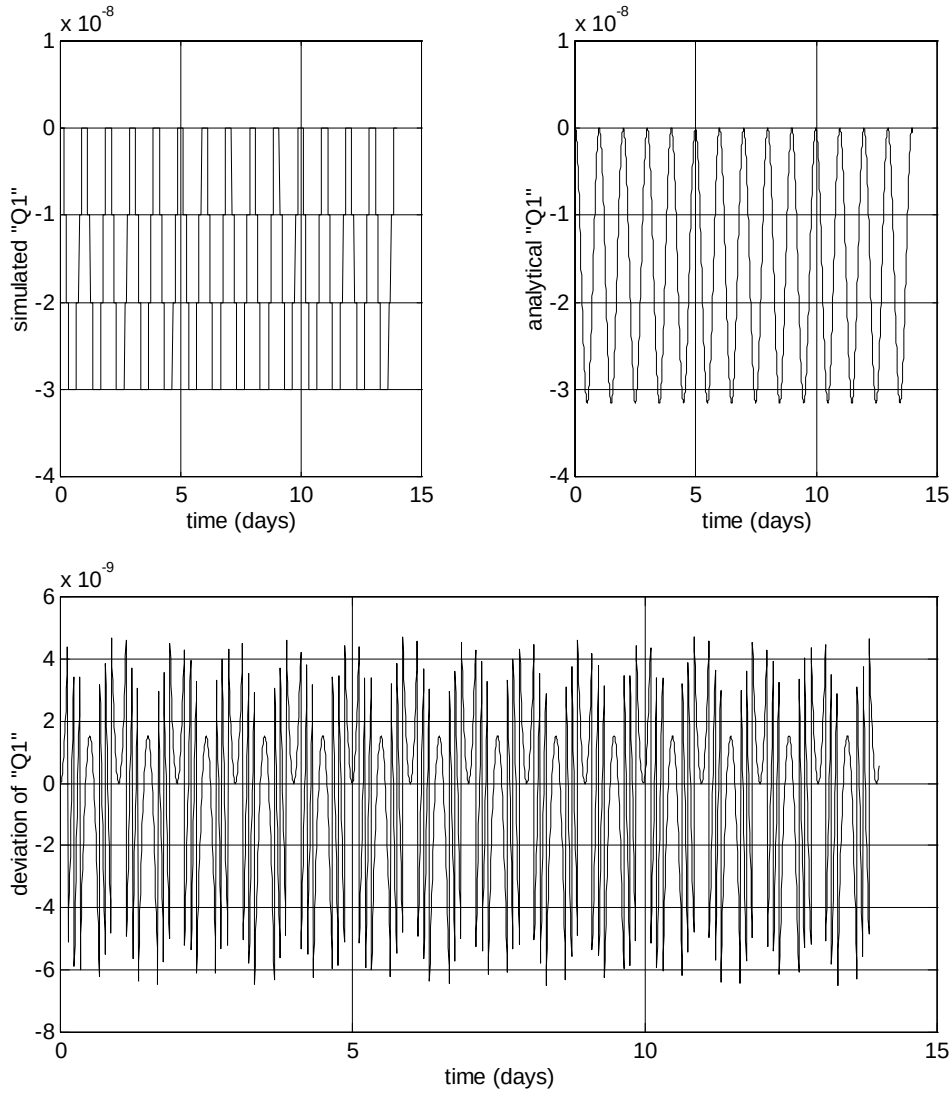

Figure B.7: Q1; Simulated, Analytical and Deviation for Test 3

The almost 'square wave' appearance of the simulated 'Q1' graph is the result of the number and spacing of the recorded data points combined with the linear fit method used to plot the graph. Disregarding this, correlation with the analytical data is very good considering the amplitude of the motion.

The deviation graph reflects the accuracy of the stored results, both 'Q1' and 'Q2' are recorded to 8 decimal places in the output file and so a $\pm 5 \times 10^{-9}$ truncation error is expected.

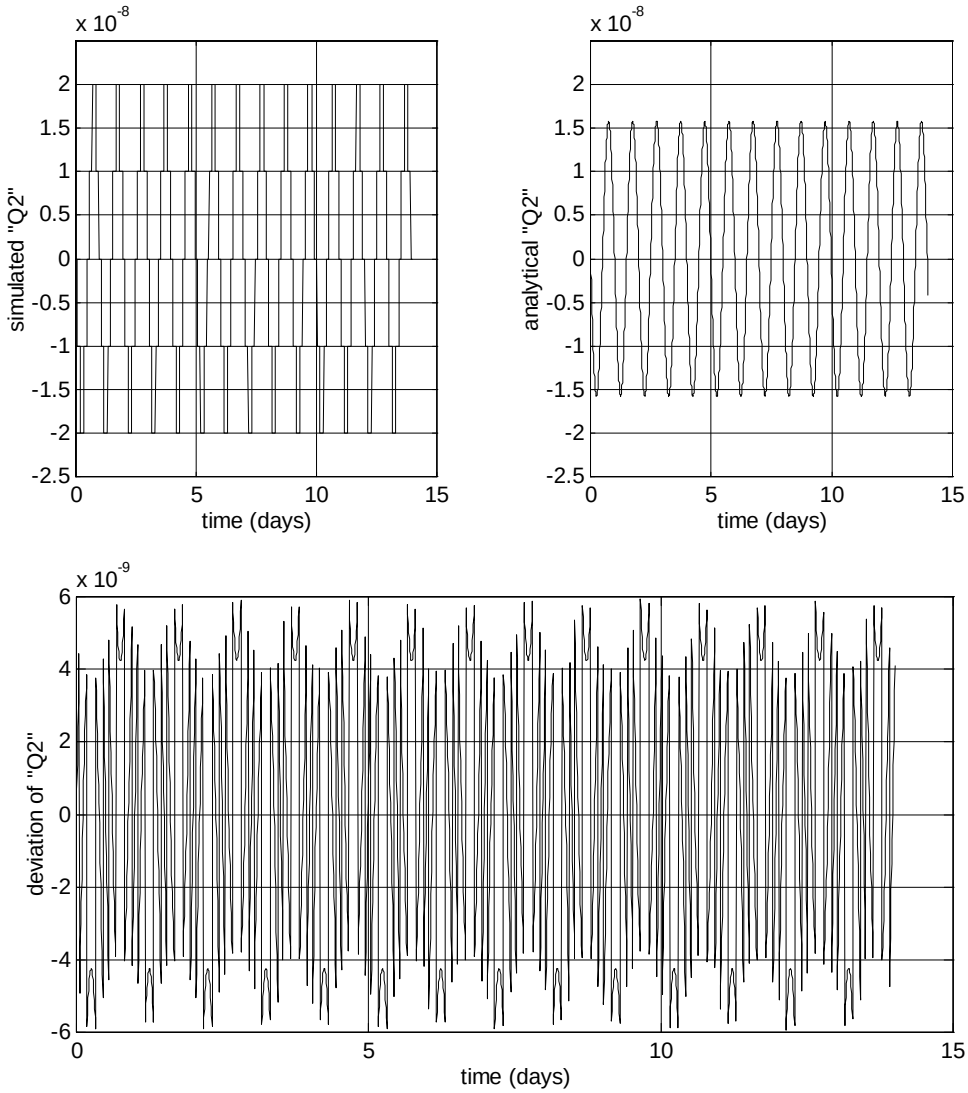

Figure B.8: Q2; Simulated, Analytical and Deviation for Test 3

Visually, the fit of analytical to simulated data is not as good as that shown in the graphs for 'Q1', however the deviation graph still shows the maximum differences are of approximately the same magnitude as the $\pm 5 \times 10^{-9}$ truncation error present in the simulated data. On this basis the results are acceptable.

B.2.4 : Test 4: Solar Gravity Test (Test Name : *SG*)

Summary

The aim of this test is to validate the implementation of the Solar gravity perturbation acceleration equations. Combining simplified forms (B.1) with the relevant perturbation equations from chapter 4 analytical solutions to the equinoctial variables are calculated. Again, perfect matches with the simulated data are not expected. Due to the long term nature of the solar gravity effects this test has been performed for a 1.5 year propagation period.

Expected Results

The most effected equinoctial elements are 'Q1' and 'Q2' (i.e. the inclination related variables). In the short term a daily periodic effect is expected; in the intermediate term, a semi-annual periodic effect Soop [31]; and in the long term the inclination should increase at a rate of about $0.269\times\mathrm{Sin}(\Omega)$ degs/year Agrawal [37]. The remaining equinoctial elements experience short term oscillations; 'a' librates with a period of half a sidereal day and 'P1' and 'P2' (i.e. the eccentricity related variables) with a period of one sidereal day. Additionally, an intermediate term sinusoidal variation exists in 'P1' and 'P2', causing plots of 'P1' and 'P2' against time to show the short term oscillation within a long term sinusoidal envelope.

Analytical Solution

The third body gravitational perturbation equation for the Sun is written below.

$$\underline{a_s} = \frac{\mu_s r}{r_s^3}\left[3\left(\underline{i_r}.\underline{i_s}\right)\underline{i_s} - .\underline{i_r}\right] \tag{B.9}$$

Where, for low inclination and eccentricity, in geocentric inertial axes :

$$\underline{i_r} = \begin{bmatrix} \mathrm{Cos}(L) \\ \mathrm{Sin}(L) \\ 0 \end{bmatrix} \quad ; \quad \underline{i_s} = \begin{bmatrix} \mathrm{Cos}(L_s) \\ \mathrm{Cos}(i_s)\mathrm{Sin}(L_s) \\ \mathrm{Sin}(i_s)\mathrm{Sin}(L_s) \end{bmatrix} \tag{B.10}$$

Combining these equations the acceleration vector in geocentric inertial co-ordinates is:

$$\underline{a_s} = \frac{\mu_s r}{r_s^3}\begin{bmatrix} 3\big(\mathrm{Cos}(L)\mathrm{Cos}(L_s)+\mathrm{Cos}(i_s)\mathrm{Sin}(L)\mathrm{Sin}(L_s)\big)\mathrm{Cos}(L_s)-\mathrm{Cos}(L) \\ 3\big(\mathrm{Cos}(L)\mathrm{Cos}(L_s)+\mathrm{Cos}(i_s)\mathrm{Sin}(L)\mathrm{Sin}(L_s)\big)\mathrm{Cos}(i_s)\mathrm{Sin}(L_s)-\mathrm{Sin}(L) \\ 3\big(\mathrm{Cos}(L)\mathrm{Cos}(L_s)+\mathrm{Cos}(i_s)\mathrm{Sin}(L)\mathrm{Sin}(L_s)\big)\mathrm{Sin}(i_s)\mathrm{Sin}(L_s) \end{bmatrix} = \begin{bmatrix} a_{sx} \\ a_{sy} \\ a_{sz} \end{bmatrix} \quad \text{(B.11)}$$

Converting to orbital axes using the matrix A^T from appendix A.2 (with Q1=Q2=0) gives the acceleration vector in orbital axes as,

$$\underline{a_s} = \begin{bmatrix} \mathrm{Cos}(L)a_{sx}+\mathrm{Sin}(L)a_{sy} \\ -\mathrm{Sin}(L)a_{sx}+\mathrm{Cos}(L)a_{sy} \\ a_{sz} \end{bmatrix} \quad \text{(B.12)}$$

Where the true longitudes 'L' and 'L_s' can be approximated by :

$$\begin{aligned} L &= n_0 t + L_0 = n_0 t \\ L_s &= n_{s0} t + L_{s0} \end{aligned} \quad \text{(B.13)}$$

Equations (B.12) and (B.13) can be combined with (B.1) to form differential expressions for the equinoctial elements, which in turn can be integrated. The procedure is fairly straightforward, but the algebra is tedious and will not be included here.

Using the simplifying expressions:

$$\begin{aligned} n_1 &= n_0 - n_s & c_1 &= -L_{s0} \\ n_2 &= 3n_0 - 2n_s & c_2 &= -2L_{s0} \\ n_3 &= n_0 - 2n_s & c_3 &= -2L_{s0} \end{aligned}$$

The final equations, retaining only the dominant terms for brevity are given below.

$$l = n_0 t - \frac{{n_{s0}}^2}{n_0}\left(t + \frac{3\left(\mathrm{Sin}\left(2\left(n_1 t + c1\right)\right) - \mathrm{Sin}\left(2c_1\right)\right)}{2n_1}\right)$$

$$a = \frac{3{n_{s0}}^2 a_0}{n_0}\left(\mathrm{Cos}(is)\left(\frac{\mathrm{Cos}\left(2\left(n_1 t + c1\right)\right) - \mathrm{Cos}\left(2c_1\right)}{2n_1}\right) + \mathrm{Sin}^2\left(\frac{i_s}{2}\right)\left(\frac{\left(\mathrm{Cos}(2n_0 t) - 1\right)}{n}\right)\right) + a_0$$

$$P1 = \frac{{n_{s0}}^2}{2n_0}\left(-\frac{\mathrm{Sin}\left(n_0 t\right)}{n_0} + \frac{3\left(\mathrm{Sin}\left(n_2 t + c_2\right) - \mathrm{Sin}\left(c_2\right)\right)}{2n_2} - \frac{9\left(\mathrm{Sin}(n_3 t + c_3) - \mathrm{Sin}(c_3)\right)}{2n_3}\right) \qquad \text{(B.14)}$$

$$P2 = \frac{{n_{s0}}^2}{2n_0}\left(-\frac{\mathrm{Cos}\left(n_0 t\right) - 1}{n_0} + \frac{3\left(\mathrm{Cos}\left(n_2 t + c_2\right) - \mathrm{Cos}\left(c_2\right)\right)}{n_2} + \frac{9\left(\mathrm{Cos}(n_3 t + c_3) - \mathrm{Cos}(c_3)\right)}{2n_3}\right)$$

$$Q1 = \frac{3{n_{s0}}^2}{16n_0}\mathrm{Sin}\left(i_s\right)\left(2\mathrm{Cos}\left(i_s\right)t - \frac{\mathrm{Sin}\left(2n_0 t\right)}{n_0} - \frac{\mathrm{Sin}\left(2\left(n_{s0} t + L_{s0}\right)\right) - \mathrm{Sin}(2L_{s0})}{n_{s0}} + \frac{\mathrm{Sin}\left(2\left(n_1 t + c_1\right)\right) - \mathrm{Sin}(2c_1)}{n_1}\right)$$

$$Q2 = -\frac{3{n_{s0}}^2}{16n_0}\mathrm{Sin}\left(i_s\right)\left(\frac{\mathrm{Cos}\left(2n_0 t\right) - 1}{n_0} + \frac{\mathrm{Cos}\left(2\left(n_{s0} t + L_{s0}\right)\right) - \mathrm{Cos}(2L_{s0})}{n_{s0}} - \frac{\mathrm{Cos}\left(2\left(n_1 t + c_1\right) - \mathrm{Cos}(2c_1)\right)}{n_1}\right)$$

Again, the mean longitude will be used as an approximation to the true longitude. The obliquity of the ecliptic, 'i_s' is approximated to 23.4° and the initial true longitude of the Sun is found using the empirical equation below (Duffet-Smith [39]).

$$L_{s0} = 0.985647D + 1.9151687\mathrm{Sin}\left(0.985647D - 3.365119\right) + 279.403303 \ \ \mathrm{deg}$$

Where 'D' is the number of days from 00:00 hrs GMT, 31/12/1989 (January 0.0 1990).

Comparisons between Simulated and Analytical Results

The difference between the simulated data and analytical data are plotted against time in the following diagrams. The length of the time axis differs between graphs to show the dominant periodic terms clearly. Discussion of the variations and deviations from the analytical values are included with the graphs for each element.

To show more clearly the magnitude of the semi-major axis variations the graphs illustrating the change in 'a' over time have been plotted as 'a-a_G' against time.

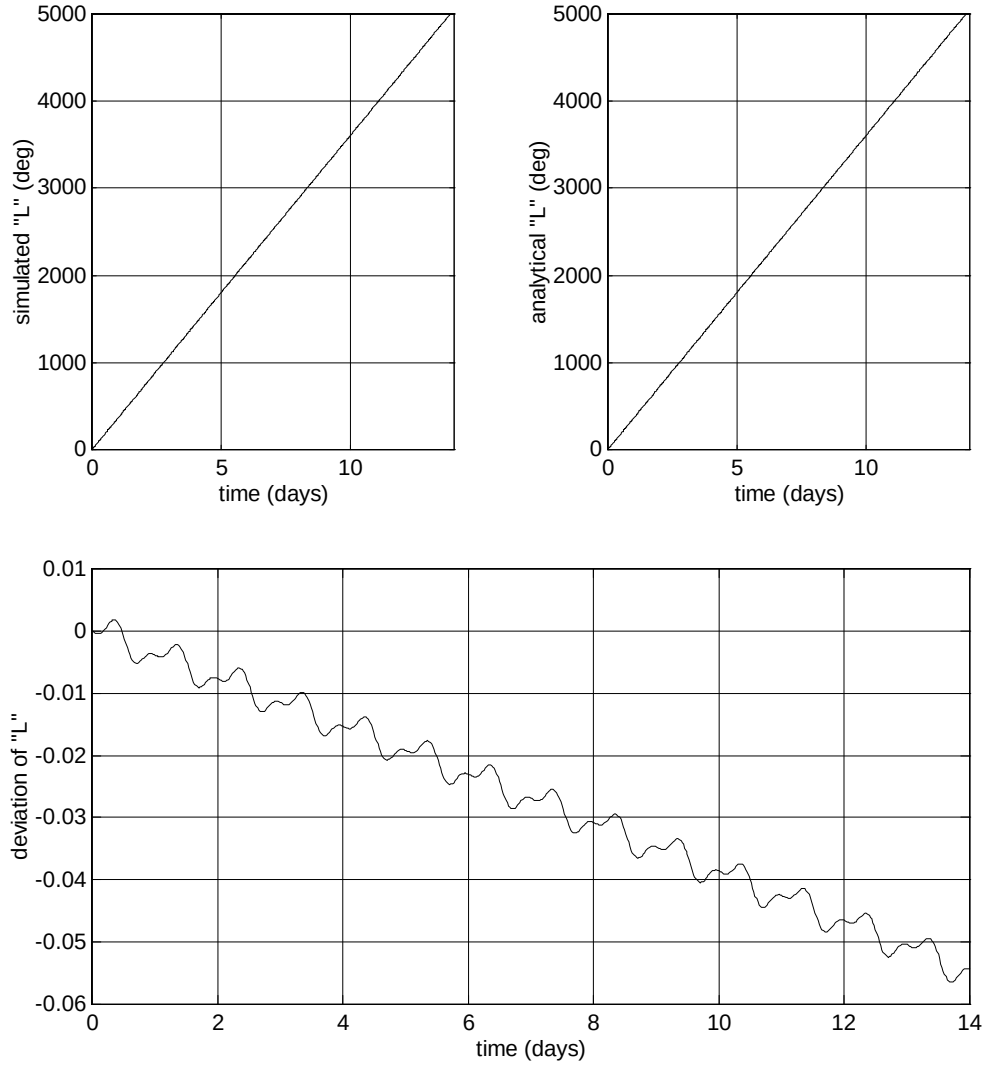

Figure B.9: True Longitude; Simulated, Analytical and Deviation for Test 4

To explain the deviation in 'L' the deviation in 'a' must be considered. The graph for the variation of semi-major axis (figure B.10) shows a mean offset in 'a' of about 400 m, the effect of this on the mean orbital rate 'n', accounts for the linear drift in true longitude, illustrated above. The smaller sinusoidal oscillations superimposed on the linear drift are caused by the eccentricity of the orbit and are the result of approximating the mean longitude to the true longitude, the former not being influenced by eccentricity.

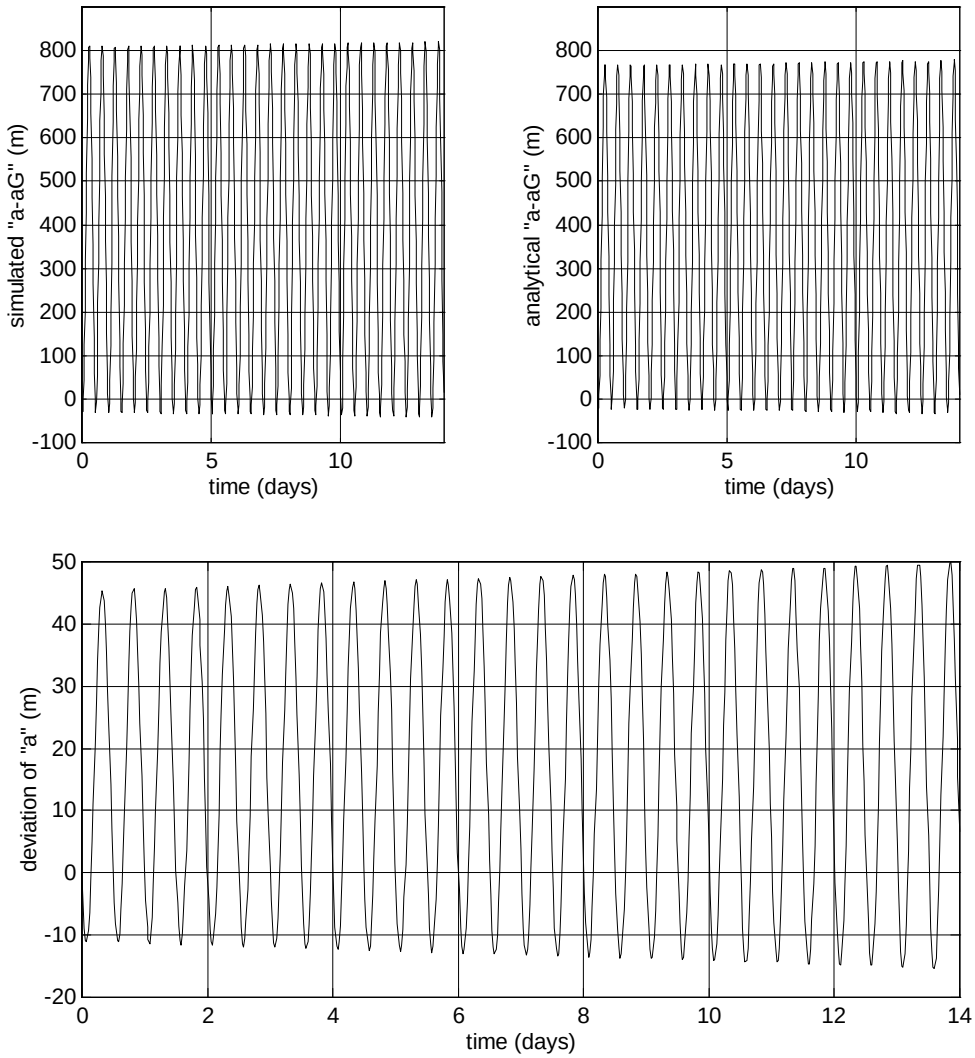

Figure B.10: Semi-major Axis; Simulated, Analytical and Deviation for Test 4

The deviation of semi-major axis is sinusoidal, and is caused mainly by the approximation that $r_s=a_s$ which precludes of the effects of the eccentricity of the Earth-Sun orbit. The approximately constant offset term is caused by the mean semi-major axis differing from the ideal (which was used in the formulation of the analytical equations) by about 400 m.

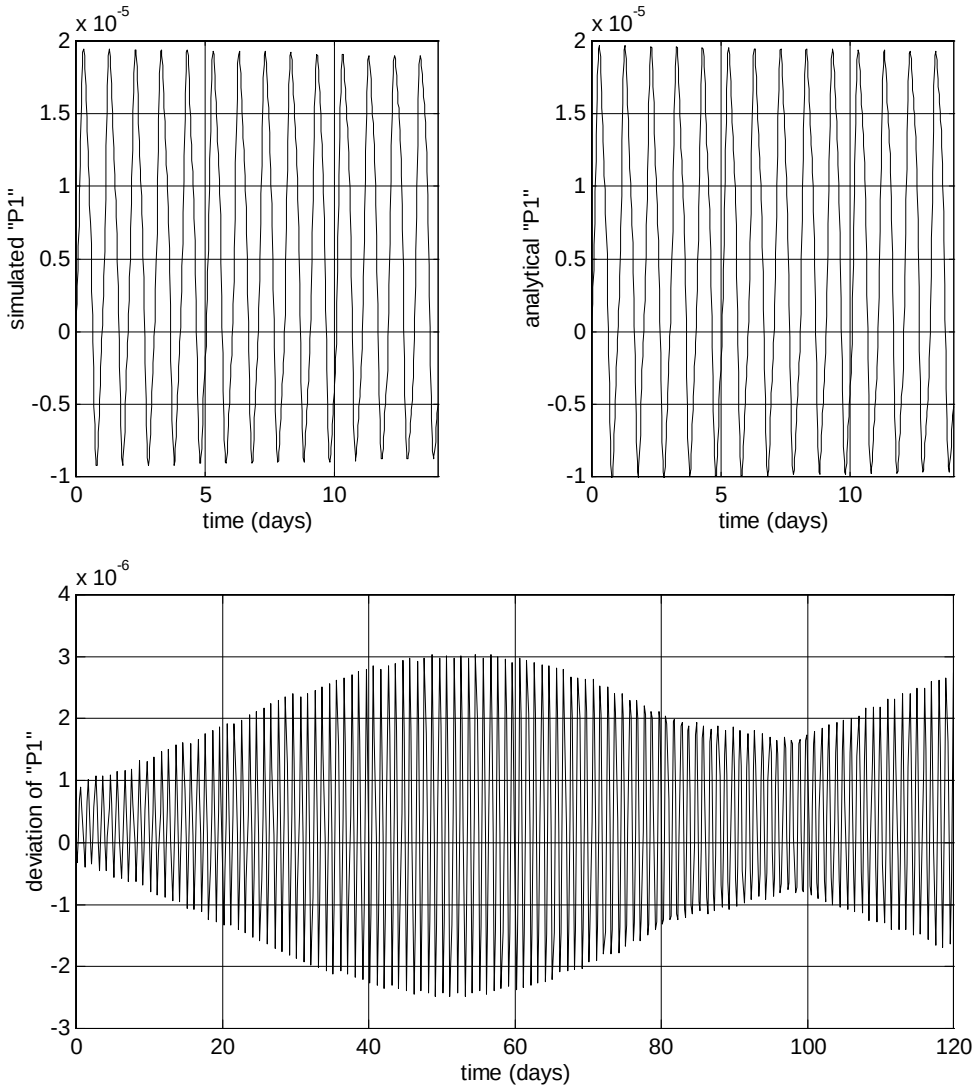

Figure B.11: P1; Simulated, Analytical and Deviation for Test 4

Both simulated and analytical 'P1' graphs show the expected daily libration, the long term envelope is not visible due to the length of the time axis (chosen for clarity of the more dominant short term motion). The deviation graph can be accounted for by the approximation that $r_s=a_s$ and by the omission of inclination terms from the 'P1' expression in equations (B.14). The evident sinusoidal envelope continues along the time axis beyond the extent of the time axis shown.

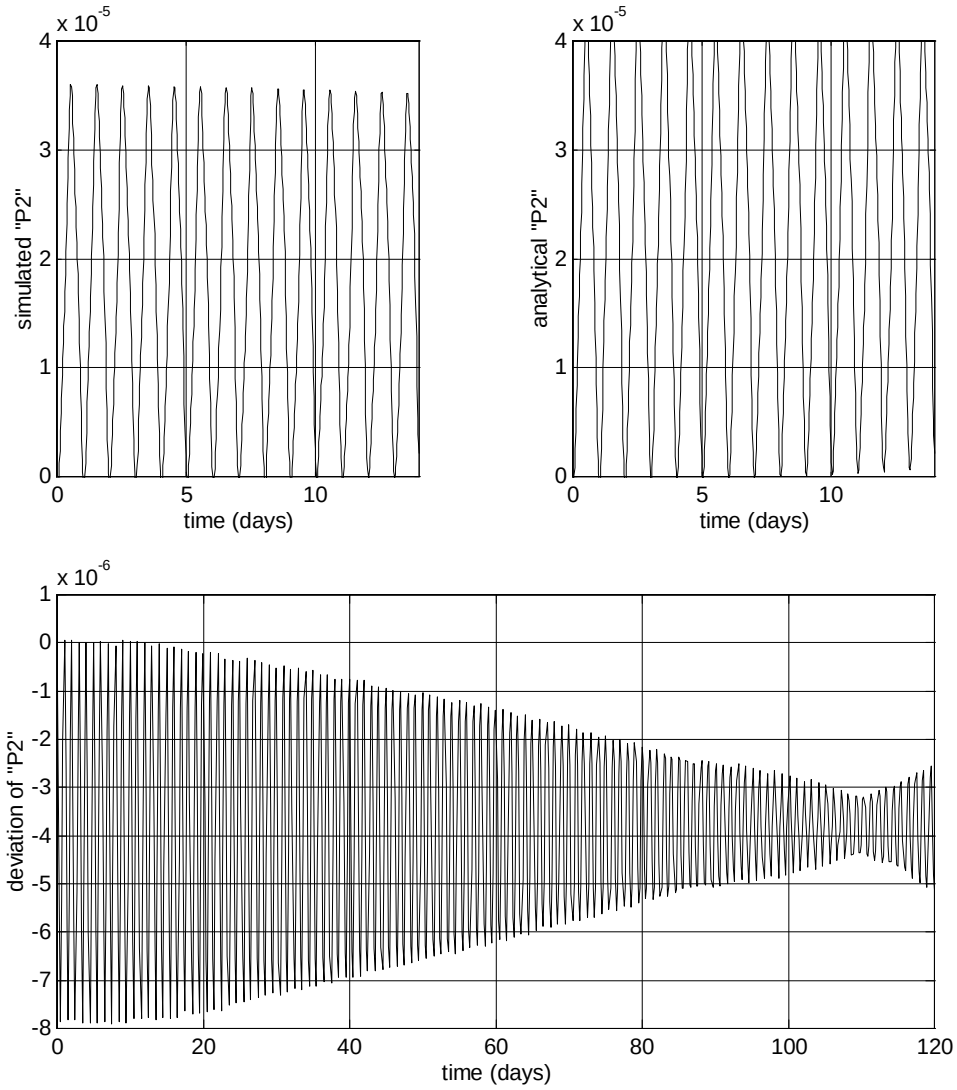

Figure B.12: P2, Simulated and Analytical for Test 4

The arguments applied to the previous graphs for 'P1' are equally valid for 'P2' with the addition that the mean value of 'P2' is significantly larger, in terms of the overall magnitude of the motion, than zero, which equation (B.14) uses for the mean value. Thus, the deviation response appears offset on the 'P2' axis (the same can be said for the 'P1' deviation graph although the effect is much smaller).

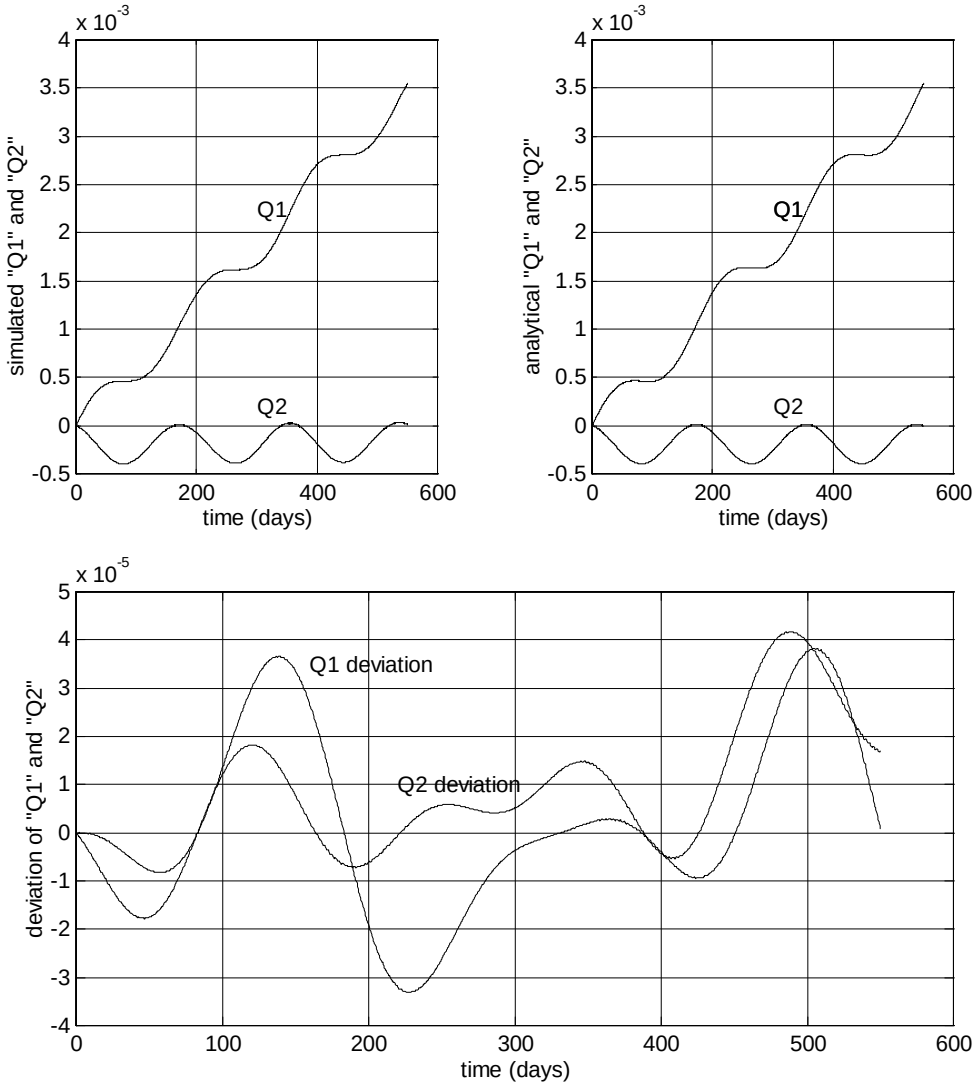

Figure B.13: Q1, Q2; Simulated, Analytical and Deviation for Test 4

The gradient of the 'Q1' plot can be used to calculate the rate of change of inclination over the period as 0.268°/year, additionally if 'Q2' is approximated to zero Ω=90° and thus the expected variation of inclination is confirmed. The expected semi-annual period is also confirmed. Again, the deviation graphs are caused mainly by the approximation $r_s=a_s$ and by neglecting higher order 'i_s' terms.

B.2.5 : Test 5: Lunar Gravity Test (Test Name : *LG*)

Summary

A simplified integration model is compared with the full orbit integration scheme to assess if the data generated from the latter is reasonable. As in the case of Solar gravity, the major Lunar gravity effects are long term in nature. The propagation has thus been performed for a 400 day period.

Expected Results

Since both Lunar and Solar gravity effects are modelled in the same way and both orbits have low inclination and eccentricity it is reasonable to expect their effects on a GEO satellite to be similar, the differences being caused mainly by the difference in orbital period and the magnitude of the acceleration perturbations (a combination of the distance from the body and the gravitational constant of the body). Consequently, the satellite elements most effected should be 'Q1' and 'Q2' which should experience: short term daily librations; mid-term (approximately 14 day or half a lunar month) oscillatory motion; and a long term linearly increasing magnitude effect. The remaining elements should experience the oscillatory effects (although the period of the mid-term oscillation will not be 14 days) without the linear gradient term.

Analytical Solution

The orbit of the Moon around the Earth varies much more than that of the Earth around the Sun in the sense that both the argument of perigee and the right ascension of the ascending node change considerable over a relatively short time period (due to perturbation effects from the Sun). Because of this it is difficult to obtain an accurate analytical solution for the equinoctial elements over time, and for this reason the verification procedure followed here differs from that used by the previous tests.

The only software difference between this test and test 4 is that in this test Lunar gravity is modelled and in test 4 Solar gravity was modelled. The program, excluding these differences, was verified for test 4 and thus only the *implementation* of the Lunar gravity

equations need to be checked here since the remainder of the program has already been proved.

Reducing the problem even further, the calculation of the perturbation accelerations in each case is identical once the position of the Moon (in this test) or Sun (in test 4) has been calculated. To verify the program with Lunar gravity effects enabled therefore it is only necessary to verify that the position of the Moon is correctly calculated at each step.

To do this the method for calculating the position of the Moon will be replaced in the propagation program by a second method obtained from a different reference source and the results compared. Although the equations can be checked in isolation this would not negate the possibility of interference (for example due to identical variable name) between the Lunar gravity model and other sections of the propagation program.

The original method involved calculating the variables; ecliptic longitude, ecliptic latitude, horizontal parallax and distance from Earth (centre to centre) and then using these to find the Lunar position vector. The equations used are listed in chapter 4 and repeated below as equations (B.15) and (B.16).

$$
\begin{aligned}
\lambda_l &= 218^o.32 + 481267^o.883\mathrm{Tu} \\
&\quad + 6^o.29\mathrm{Sin}(134^o.9 + 477198^o.85\mathrm{Tu}) + 1^o.27\mathrm{Sin}(259^o.2 - 413335^o.38\mathrm{Tu}) \\
&\quad + 0^o.66\mathrm{Sin}(235^o.7 + 890534^o.23\mathrm{Tu}) + 0^o.21\mathrm{Sin}(269^o.9 + 954397^o.70\mathrm{Tu}) \\
&\quad - 0^o.19\mathrm{Sin}(357^o.5 + 35999^o.05\mathrm{Tu}) - 0^o.11\mathrm{Sin}(186^o.6 + 966404^o.05\mathrm{Tu}) \\
\\
\phi_l &= 5^o.13\mathrm{Sin}(93^o.3 + 483202^o03\mathrm{Tu}) + 0^o.28\mathrm{Sin}(228^o.2 + 960400^o.87\mathrm{Tu}) \\
&\quad - 0^o.28\mathrm{Sin}(318^o.3 + 6003^o.18\mathrm{Tu}) - 0^o.17\mathrm{Sin}(217^o.6 - 407332^o.20\mathrm{Tu}) \qquad \text{(B.15)} \\
\\
\mathrm{h_p} &= 0^o.9508 \\
&\quad + 0^o.0518\mathrm{Cos}(134^o.9 + 477198^o.85\mathrm{Tu}) + 0^o.0095\mathrm{Cos}(259^o.2 - 413335^o.38\mathrm{Tu}) \\
&\quad + 0^o.0078\mathrm{Cos}(235^o.7 + 890534^o.23\mathrm{Tu}) + 0^o.0028\mathrm{Cos}(269^o.9 + 954397^o.70\mathrm{Tu})
\end{aligned}
$$

$$
\mathrm{r_l} = \frac{6378137}{\mathrm{Sin}\left(\mathrm{h_p}\right)}
$$

$$
\underline{\mathrm{r_l}} = \mathrm{r_l}\begin{bmatrix} \mathrm{Cos}(\phi_l)\mathrm{Cos}(\lambda_l) \\ +0.9175\mathrm{Cos}(\phi_l)\mathrm{Sin}(\lambda_l) - 0.3978\mathrm{Sin}(\phi_l) \\ +0.3978\mathrm{Cos}(\phi_l)\mathrm{Sin}(\lambda_l) + 0.9175\mathrm{Sin}(\phi_l) \end{bmatrix} \qquad \text{(B.16)}
$$

The second method originated from Duffet-Smith [39] and provides equations for Lunar variables in terms of 'D', the number of days including fractions since 00:00 hrs GMT, 31/12/1989 (or January 0.0, 1990.0). The accuracy of the two methods is comparable (maximum errors are about 0°.3 in ecliptic longitude, 0°.2 in ecliptic latitude). Differences in results greater than twice these values would indicate programming errors.

The order of calculation for the second method is as follows.

1. Calculate the mean anomaly and ecliptic longitude of the Sun from,

$$
\begin{aligned}
\mathrm{M_s} &= 0^o.985647\mathrm{D} - 3^o.365119 \\
\lambda_s &= \mathrm{M_s} + 1^o.9151687\mathrm{Sin}\left(\mathrm{M_s}\right) + 282^o.768422
\end{aligned} \qquad \text{(B.17)}
$$

2. Calculate the uncorrected mean longitude, the mean anomaly and the corrected ascending node's mean longitude for the Moon from,

$$\begin{aligned} l &= 13^o.1763966D + 318^o.351648 \\ M_m &= l - 0^o.111404D - 36^o.340410 \\ N' &= 318^o.510107 - 0^o.0529539D - 0^o.16\mathrm{Sin}(M_s) \end{aligned} \tag{B.18}$$

3. Calculate the corrected mean anomaly as,

$$M'_m = M_m + E_v - A_e - A_3 \tag{B.19}$$

where E_v is the evection correction, A_e is the annual equation and A_3 is a third correction term. Each of these are calculated as follows.

$$\begin{aligned} E_v &= 1^o.2739\mathrm{Sin}(2[l - \lambda_s] - M_m) \\ A_e &= 0^o.1858\mathrm{Sin}(M_s) \\ A_3 &= 0^0.37\mathrm{Sin}(M_s) \end{aligned} \tag{B.20}$$

4. Calculate two more correction terms and thus find the corrected longitude, l' for the Moon,

$$\begin{aligned} E_c &= 6^o.2886\mathrm{Sin}(M'_m) \\ A_4 &= 0^o.214\mathrm{Sin}(2M'_m) \\ l' &= l + E_v + E_c - A_e + A_4 \end{aligned} \tag{B.21}$$

5. Calculate the final correction and thus the Moon's true orbital longitude, l",

$$\begin{aligned} V &= 0^o.6583\mathrm{Sin}(2(l' - \lambda_s)) \\ l'' &= l' + V \end{aligned} \tag{B.22}$$

6. The ecliptic longitude and latitude can now be calculated as,

$$\lambda_m = \mathrm{Tan}^{-1}\left(\frac{\mathrm{Sin}(l''-N')\mathrm{Cos}(i_1)}{\mathrm{Cos}(l''-N')}\right) + N'$$
$$\varphi_m = \mathrm{Sin}^{-1}\left(\mathrm{Sin}(i_1)\mathrm{Sin}(l''-N')\right) \qquad \text{(B.23)}$$

where the inverse tangent ambiguity is resolved by the signs of Sin(l''-N') and Cos(l''-N') and 'i_l' is the Lunar orbit inclination measured from the ecliptic (i_l = 5.145°).

7. Since the eccentricity of the Lunar orbit is small (e_l = 0.0549) the equation of the centre can be used to calculate the true anomaly from the mean anomaly and with this the Earth Moon distance can be found thus,

$$f_l = M_m' + \frac{360}{\pi} e_l \mathrm{Sin}(M_m')$$
$$r_l = \frac{a_l\left(1-e_l^{\,2}\right)}{1+e_l\mathrm{Cos}(f_l)} \qquad \text{(B.24)}$$

where $a_l = 384\times10^6$ m.

8. The position vector in geocentric co-ordinates is now calculated using equation (B.16).

The test results will be analysed, as before, by comparing the data generated by each method.

Comparisons between Simulated Results

Comparisons between the two methods used to generate Lunar gravity effects is presented, as in the previous tests, as comparisons between equinoctial element evolution. This is done for two reasons, firstly for completeness in showing the effects of Lunar gravity on a GEO orbit, and secondly as a final check to show that both methods generate reasonable results (it is theoretically possible for both methods to be in error, and these errors to be the same).

Discussions of the variations and deviations of the actual data from that generated by the second method are included with the graphs for the six orbital elements which follow. To show more clearly the magnitude of the semi-major axis variations the graphs illustrating the change in 'a' over time have been plotted as 'a-a_G' against time.

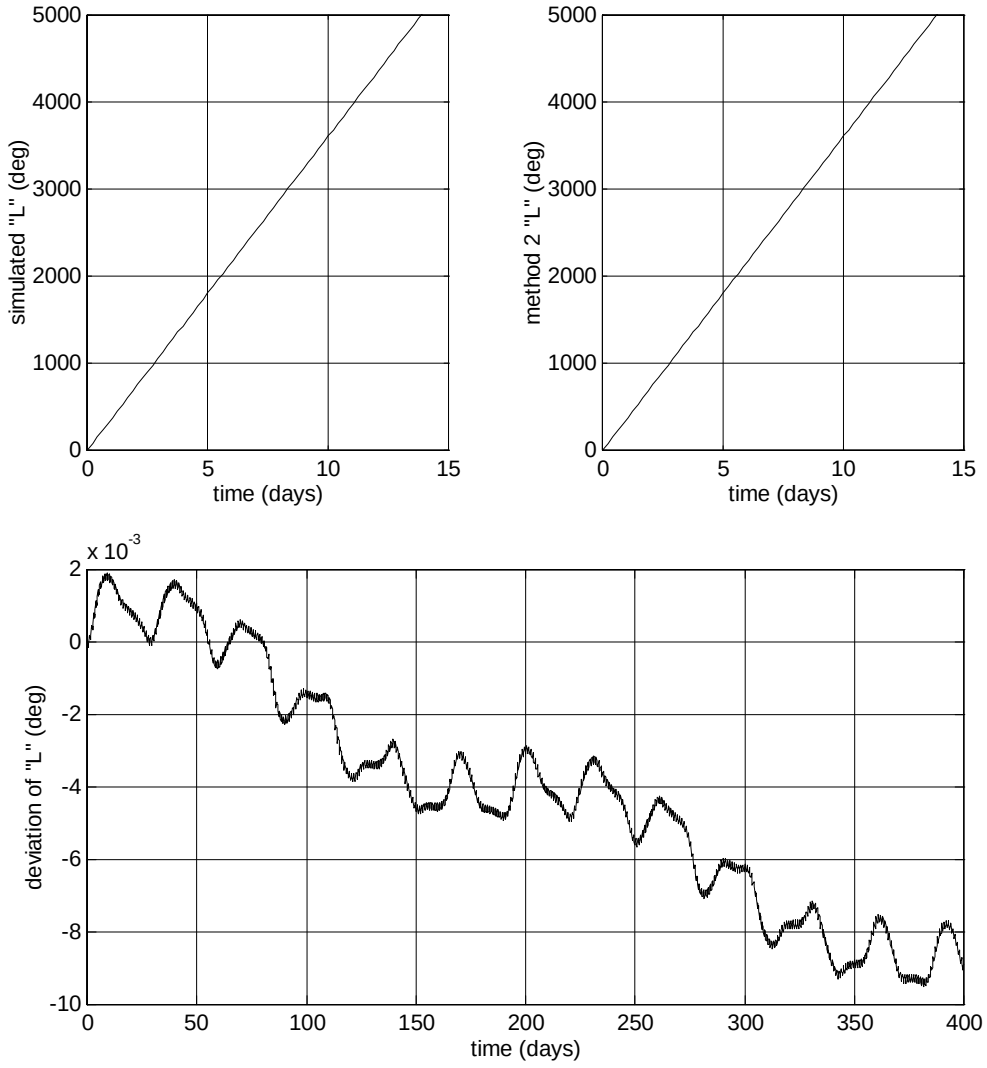

Figure B.14: True Longitude; Simulated 1, Simulated 2 and Deviation for Test 5

The graphs for true longitude have been shown over a 14 day period for clarity, however the deviation graph is shown for the test duration of 400 days. The approximately linear gradient present in the deviation graph is a result of differences between the value of the

semi-major axis of the Lunar orbit as used in the two methods. In method 1 this is not explicitly calculated, however the value in method 2 is only accurate to within 500 m. The difference over one year is negligible.

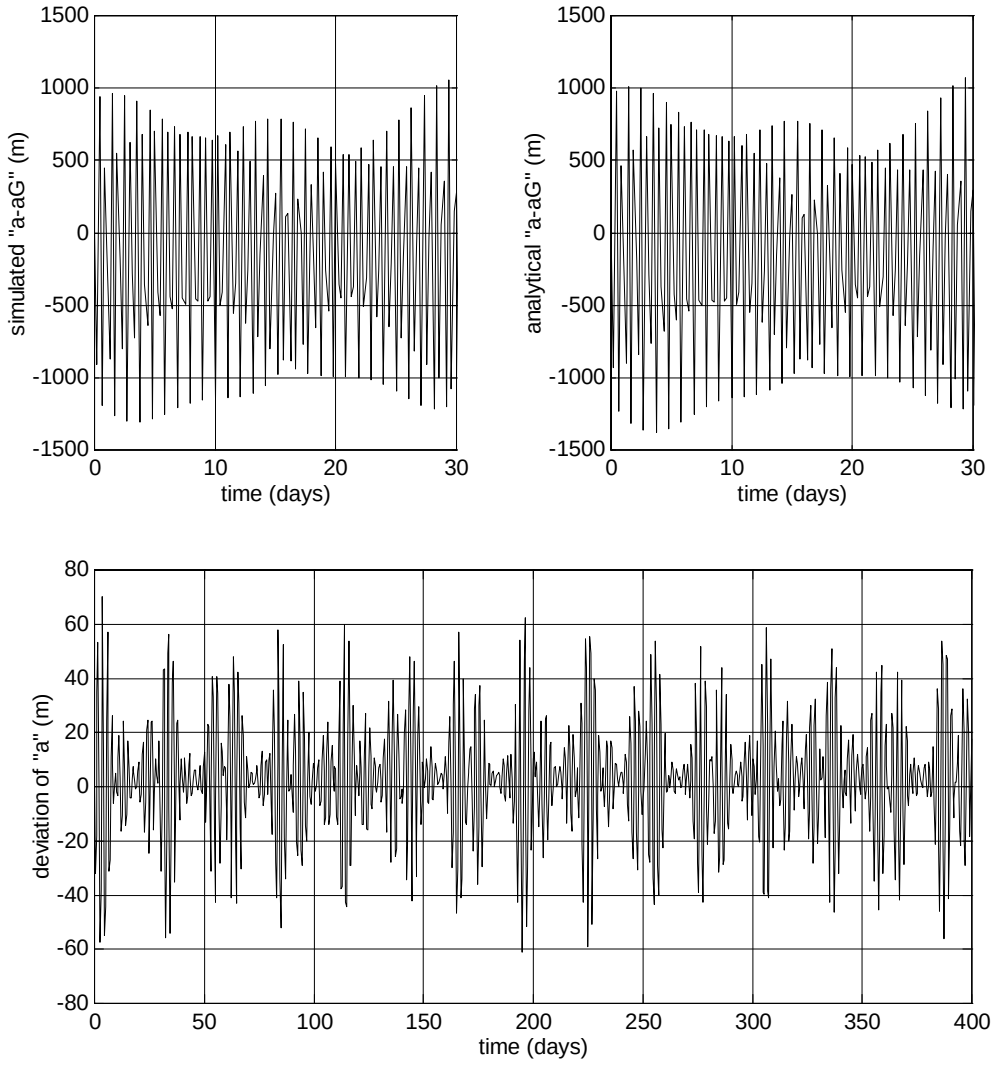

Figure B.15: Semi-major Axis; Simulated 1, Simulated 2 and Deviation for Test 5

The plots for the variation of semi-major axis show the daily oscillatory motion superimposed on which is a longer term motion, resulting from the orbital period of the Moon. The deviation graph shows no significant difference between the two methods. The apparent sinusoidal effects are due to the differences in the sinusoidal correcting

terms which are used in equations (B.15) for the first method and equations (B.20) and (B.21) for the second method.

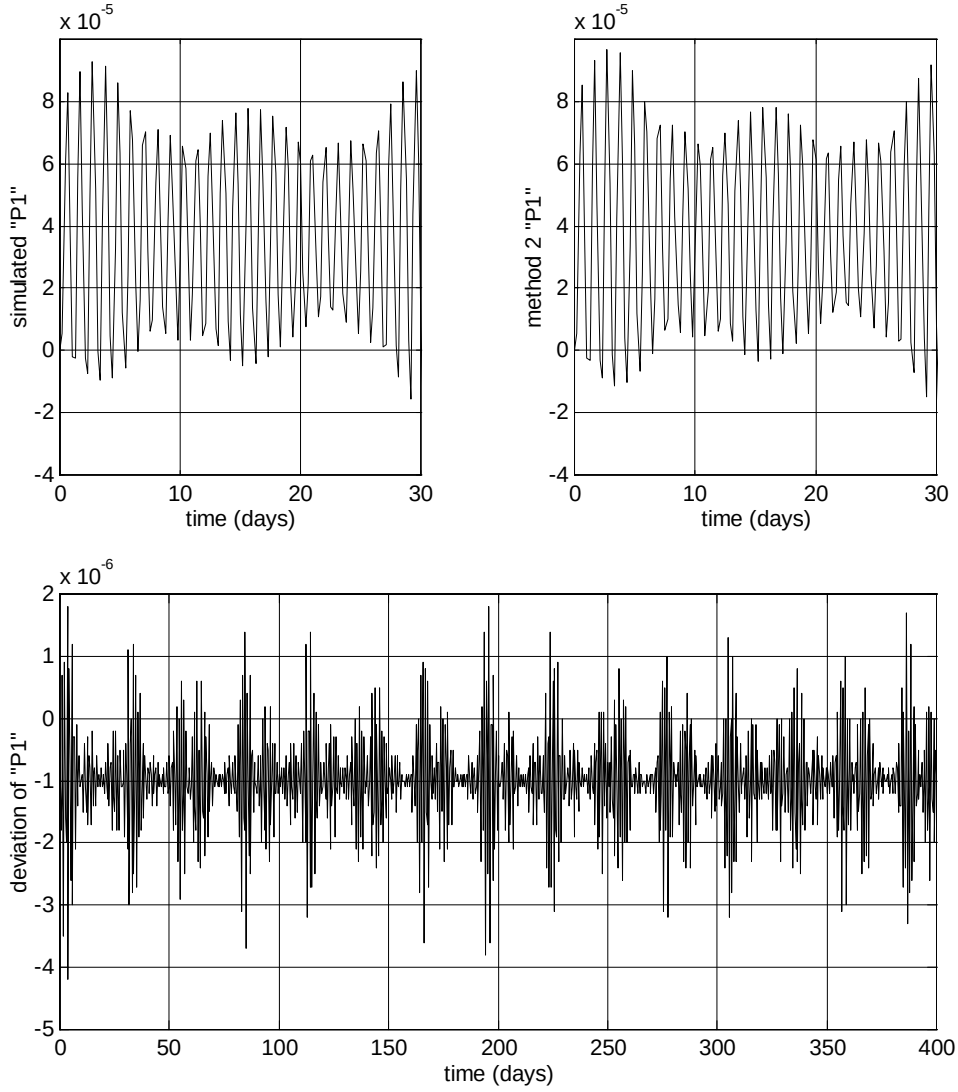

Figure B.16: P1; Simulated 1, Simulated 2 and Deviation for Test 5

The variation graphs exhibit the expected oscillatory motion. The deviation graph shows an apparent constant offset in 'P1' between methods, this is a result of the differences in Lunar semi-major axes in the two models (as noted previously) which produces a slightly different mean for 'P1'. Again the oscillatory effect is a function of the sinusoidal correction terms used to calculate the Lunar orbital variables.

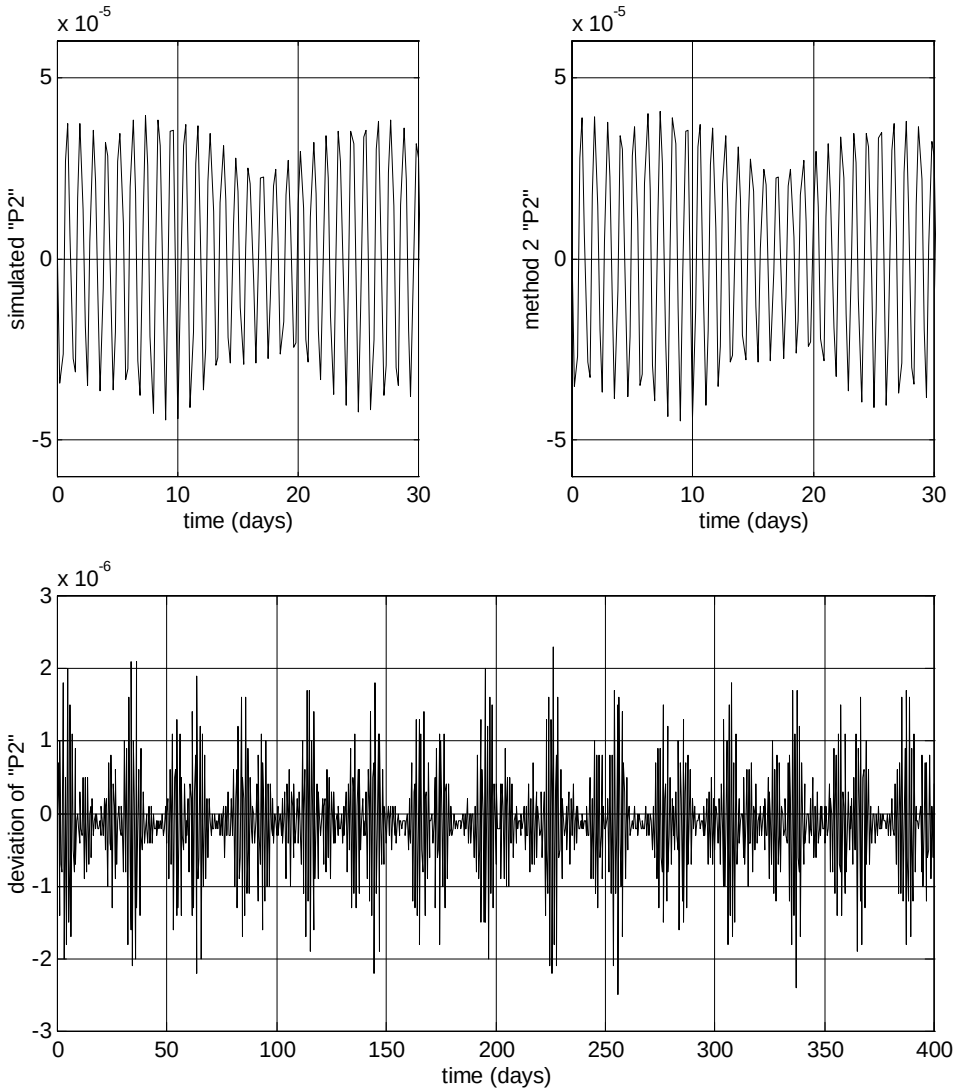

Figure B.17: P2; Simulated 1, Simulated 2 and Deviation for Test 5

The comments attached to the graphs for 'P1' are equally valid for the 'P2' graphs, although the offset in the difference between 'P2' values is less pronounced in this case.

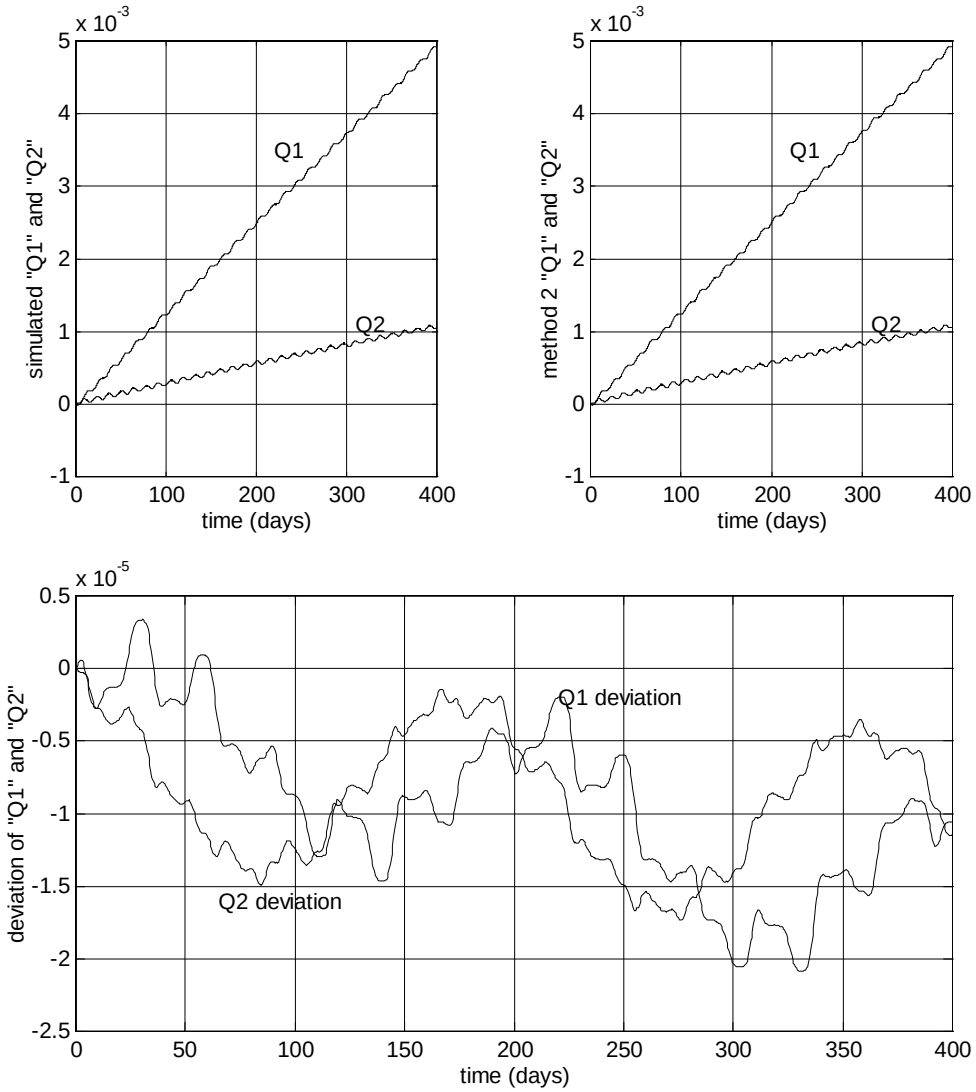

Figure B.18: Q1, Q2; Simulated 1, Simulated 2 and Deviation for Test 5

The 14 day Lunar oscillatory effect and the long term linear gradient are clearly visible from the variation graphs. Using the first variation graph and the relationship,

$$i = 2\mathrm{Tan}^{-1}\sqrt{Q1^2 + Q2^2}$$

the rate of change of inclination can be calculated as 0.531°/yr, which compares favourably with an expected value for 1994 (Agrawal [37]) of 0.533°/yr.

The deviation graph shows a possible linear gradient superimposed on which is some oscillatory motion. Again this can be accounted for by differences in the semi-major axis of the Moon between the two methods.

B.2.6 : Test 6: Solar Pressure Test (Test Name : *SP*)

Summary

The aim of this test is to validate the implementation solar pressure equations. As for tests 1 through 4 analytical solutions for the equinoctial variables are calculated based on simplified equations.

The theoretical model used for solar pressure is much simpler than those used for the other perturbations. The justification for its use is the fact that solar pressure forces are usually small and so the required accuracy of the model is low. For this reason the validation analysis will also be less accurate.

Since solar pressure effects are long term in nature a propagation has been performed for 400 days.

Expected Results

The main orbital elements effected by Solar pressure are the inplane eccentricity related variables 'P1' and 'P2'. Over the course of a year the eccentricity vector is expected to rotate 360°, describe a circle on the eccentricity plane and consequently plots of 'P1' and 'P2' against time should show sinusoidal motion. Of the remaining elements semi-major axis should be relatively unaffected; 'Q1' and 'Q2' should experience an oscillatory effect due to the out-of-orbital-plane effect of the Sun; and true longitude will be effected in so much as the rotation of the perigee of the orbit will introduce a slight linear drift rate.

Analytical Solution

The perturbation acceleration equation due to solar radiation pressure in geocentric co-ordinates described in chapter 4 is,

$$\underline{a}_{SP} \approx G\left(\frac{A}{M}\right)\left(\frac{1+R}{2}\right)\frac{\left(\underline{r}-\underline{r}_S\right)}{\left|\underline{r}-\underline{r}_S\right|} \tag{B.25}$$

for which $G=9.1\times10^{-6}$ N/m^2 is a constant and A, M, R are user inputs denoting satellite surface area, mass and surface reflectance, the values used for this test are:

$$A=25\ m^2,\ M=500\ kg \text{ and } R=0.6$$

The '$\underline{r}$' terms in equation (B.25) can be considered negligible since ($\underline{r}<<\underline{r}_s$), and thus the equation can be simplified to,

$$\underline{a}_{SP} \approx -3.64\times10^{-7}\,\underline{i}_s \tag{B.26}$$

where $\underline{i}_s$ is a unit vector pointing from the centre of the Earth to the Sun and,

$$\underline{i}_S = \begin{bmatrix} \mathrm{Cos}(L_s) \\ \mathrm{Cos}(i_s)\mathrm{Sin}(L_s) \\ \mathrm{Sin}(i_s)\mathrm{Sin}(L_s) \end{bmatrix} \approx \begin{bmatrix} \mathrm{Cos}(n_s t + L_{s0}) \\ \mathrm{Cos}(i_s)\mathrm{Sin}(n_s t + L_{s0}) \\ \mathrm{Sin}(i_s)\mathrm{Sin}(n_s t + L_{s0}) \end{bmatrix} \tag{B.27}$$

where n_s is the mean orbital rate of the Sun. Combining equations (B.26) and (B.27) and transforming to orbital axes, approximating the satellite orbit inclination to zero, gives the perturbation effect as,

$$\underline{a}_{SP} = -3.64\times10^{-7}\begin{bmatrix} \mathrm{Cos}(L)\mathrm{Cos}(n_s t + L_{s0}) + \mathrm{Sin}(L)\mathrm{Cos}(i_s)\mathrm{Sin}(n_s t + L_{s0}) \\ -\mathrm{Sin}(L)\mathrm{Cos}(n_s t + L_{s0}) + \mathrm{Cos}(L)\mathrm{Cos}(i_s)\mathrm{Sin}(n_s t + L_{s0}) \\ \mathrm{Sin}(i_s)\mathrm{Sin}(n_s t + L_{s0}) \end{bmatrix} \tag{B.28}$$

Before this is combined with equations (B.1) to find the differential equations describing the orbital elements the latter can be simplified by approximating the equinoctial elements on the right hand to constants, equal to their initial values, thus:

$$
\begin{aligned}
\frac{dl}{dt} &= n_0 - \frac{2}{n_0 a_0} a_{x_1} \\
\frac{da}{dt} &= \frac{2}{n_0} a_{y_1} \\
\frac{dP1}{dt} &= \frac{1}{n_0 a_0}\left\{-\mathrm{Cos}(L) a_{x_1} + 2\mathrm{Sin}(L) a_{y_1}\right\} \\
\frac{dP2}{dt} &= \frac{1}{n_0 a_0}\left\{\mathrm{Sin}(L) a_{x_1} + 2\mathrm{Cos}(L) a_{y_1}\right\} \\
\frac{dQ1}{dt} &= \frac{1}{2 n_0 a_0}\mathrm{Sin}(L) a_{z_1} \\
\frac{dQ2}{dt} &= \frac{1}{2 n_0 a_0}\mathrm{Cos}(L) a_{z_1}
\end{aligned}
\tag{B.29}
$$

Approximating, L=nt, equations (B.28) and (B.29) can be combined and integrated. Retaining only the dominant terms gives the analytical equations (B.30) below.

$$
\begin{aligned}
l &= n_0 t + \frac{3.64\times10^{-7}}{n_0 a_0}\left\{\frac{\left(\mathrm{Cos}(i_s)+1\right)}{n_2}\left(\mathrm{Sin}(n_2 t + c_2) - \mathrm{Sin}(c_2)\right) - \frac{\left(\mathrm{Cos}(i_s)-1\right)}{n_1}\left(\mathrm{Sin}(n_1 t + c_1) - \mathrm{Sin}(c_1)\right)\right\} \\
a &= a_0 + \frac{3.64\times10^{-7}}{n_0}\left\{\frac{\left(\mathrm{Cos}(i_s)-1\right)}{n_1}\left(\mathrm{Cos}(n_1 t + c_1) - \mathrm{Cos}(c_1)\right) - \frac{\left(\mathrm{Cos}(i_s)+1\right)}{n_2}\left(\mathrm{Cos}(n_2 t + c_2) - \mathrm{Cos}(c_2)\right)\right\} \\
P1 &= \frac{1.092\times10^{-6}}{2 n_0 n_s a_0}\left(\mathrm{Sin}(n_s t + L_{s0}) - \mathrm{Sin}(L_{s0})\right) \\
P2 &= \frac{1.092\times10^{-6}}{2 n_0 n_s a_0}\mathrm{Cos}(i_s)\left(\mathrm{Cos}(n_s t + L_{s0}) - \mathrm{Cos}(L_{s0})\right) \\
Q1 &= \frac{-3.64\times10^{-7}}{4 n_0 a_0}\mathrm{Sin}(i_s)\left\{\frac{\left(\mathrm{Sin}(n_2 t + c_2) - \mathrm{Sin}(c_2)\right)}{n_2} - \frac{\left(\mathrm{Sin}(n_1 t + c_1) - \mathrm{Sin}(c_1)\right)}{n_1}\right\} \\
Q2 &= \frac{3.64\times10^{-7}}{4 n_0 a_0}\mathrm{Sin}(i_s)\left\{\frac{\left(\mathrm{Cos}(n_1 t + c_1) - \mathrm{Cos}(c_1)\right)}{n_1} - \frac{\left(\mathrm{Cos}(n_2 t + c_2) - \mathrm{Cos}(c_2)\right)}{n_2}\right\}
\end{aligned}
\tag{B.30}
$$

where the variables n_1, n_2, c_1, c_2 are calculated from,

$$
\begin{aligned}
n_1 &= n_0 + n_s \qquad c_1 = +L_{s0} \\
n_2 &= n_0 - n_s \qquad c_2 = -L_{s0}
\end{aligned}
$$

and the initial true longitude of the Sun, L_{s0} is calculated, as in test 4, from,

$$L_{s0} = 0.985647D + 1.9151687\mathrm{Sin}(0.985647D - 3.365119) + 279.403303 \ \ \mathrm{deg}$$

('D' is the number of days from 00:00 hrs GMT, 31/12/1989).

For the purposes of comparison the mean longitude, 'l' will be approximated to the true longitude, 'L'.

Comparison between Simulated and Analytical Results

Simulated, analytical and a deviation graph of the simulated minus the analytical results are plotted in the following diagrams for each of the equinoctial elements. Discussions on the graphs are included for each element, however it is worth noting that the major differences are a result of a significant value of orbit eccentricity during part of the orbit propagation. Since 'P1' and 'P2' were approximated to zero on the right hand side of equation (B.29) this will introduce errors in all the deviation graphs which are largest when the eccentricity is large ($e = \sqrt{P1^2 + P2^2}$).

To show more clearly the magnitude of the semi-major axis variations the graphs illustrating the change in 'a' over time have been plotted as 'a-a_G' against time.

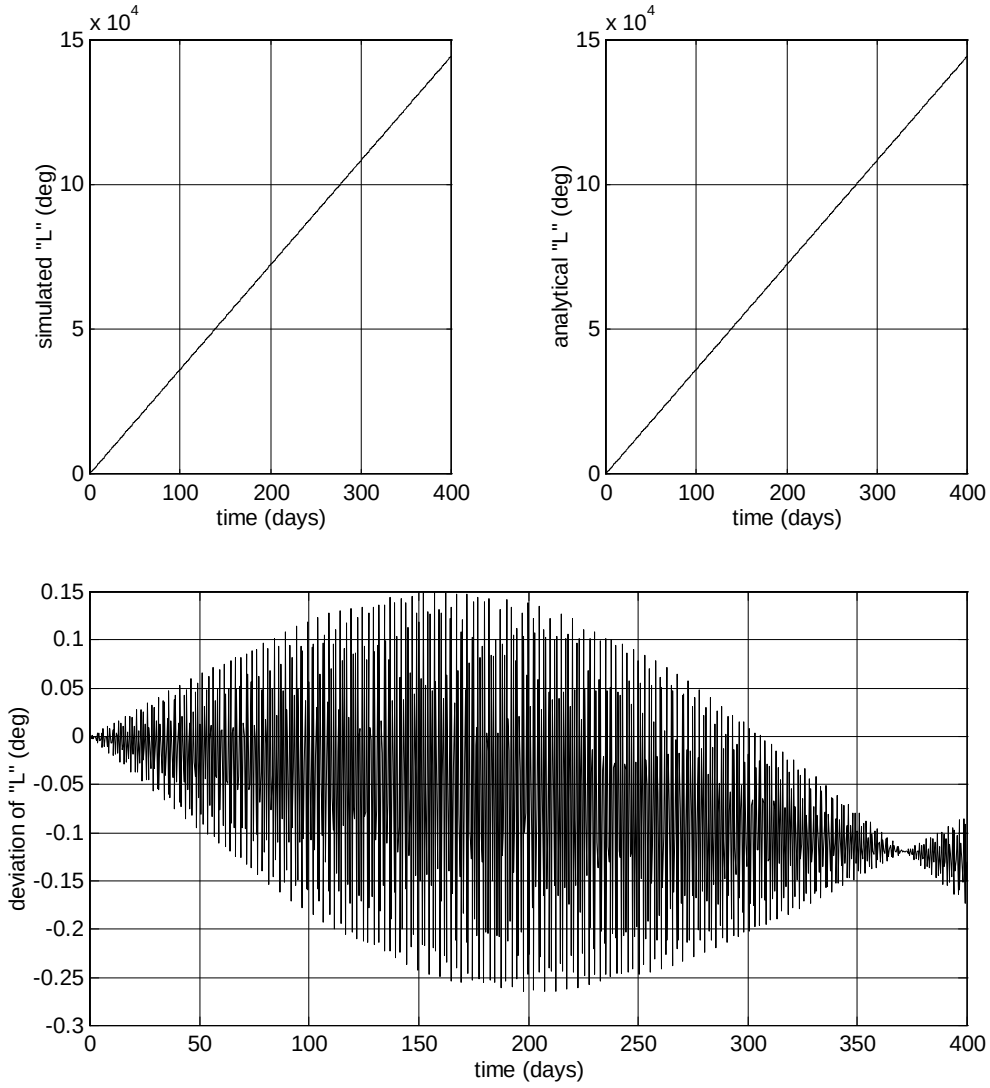

Figure B.19: True Longitude; Simulated, Analytical and Deviation for Test 6

The deviation graph shows short term oscillatory motion within an approximately sinusoidal envelope, superimposed on a linear drift rate. The oscillatory motion is a result of approximating mean longitude (unaffected by eccentricity) to true longitude (effected by eccentricity) in the analytical solution. The largest differences occur when eccentricity is largest, approximately half a year into the propagation. The short term oscillations are due to a daily libration in true longitude due to eccentricity and the long term is due to the cyclic nature of the eccentricity vector which describes one complete circle in the eccentricity plane every year. The underlying linear drift rate is due to a rotation of the orbit by solar pressure, effectively increasing the orbital rate.

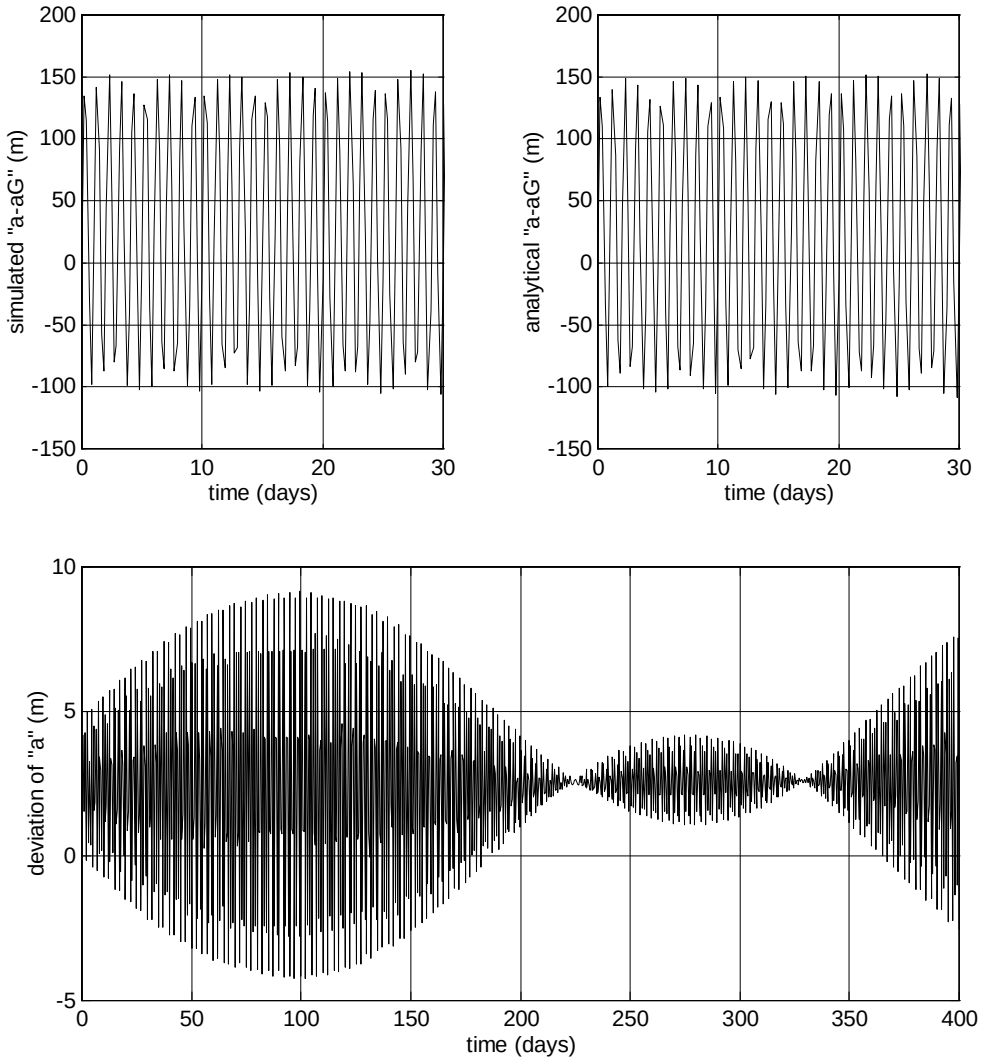

Figure B.20: Semi-major Axis; Simulated, Analytical and Deviation for Test 6

A reduced time axis has been used for the 'a-a_G' plots to clearly illustrate the daily oscillatory motion. This is the result of fitting osculating elements to a real orbit it has no physical significance. The motion shown continues for the full 400 days period with no other effects visible.

The deviation graph indicates little difference between the methods, since semi-major axis is relatively unaffected by eccentricity this can be expected.

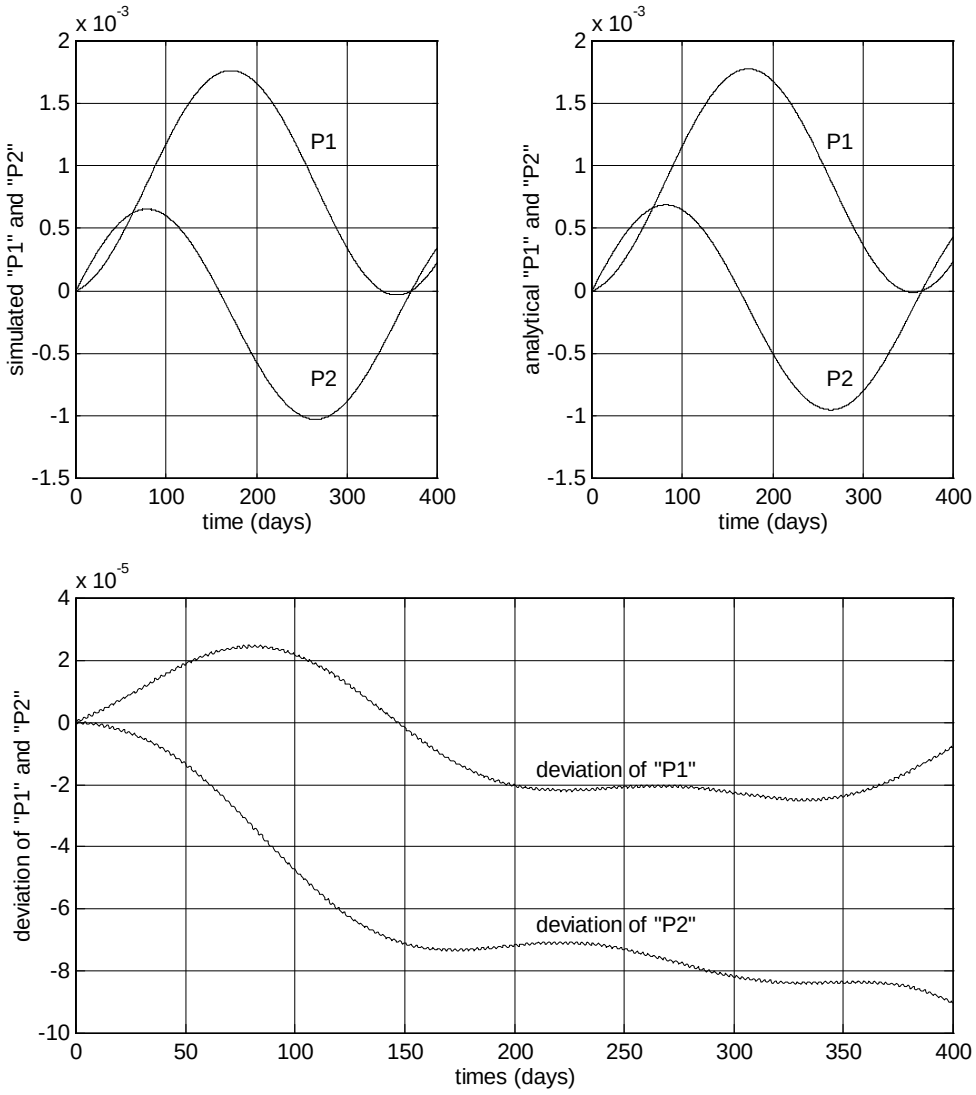

Figure B.21: P1 and P2; Simulated, Analytical and Deviation for Test 6

The deviation curves show an underlying linear drift term for both 'P1' and 'P2'. This can be explained via the approximation r=a in (B.1) which removes terms in $P1Sin^2(L)$ and $P2Cos^2(L)$, resulting from Taylor series expansions of $(Aa_{y1}+ Ba_{y2})/r$ (where 'A' and 'B' are functions of 'L'). This expansion is necessary to linearise the equations, and thus allow them to be integrated. By re-writing these terms in double angle format a constant component is introduced into the differential forms of 'P1 and 'P2', integrating this would give a linear drift effect in the two elements.

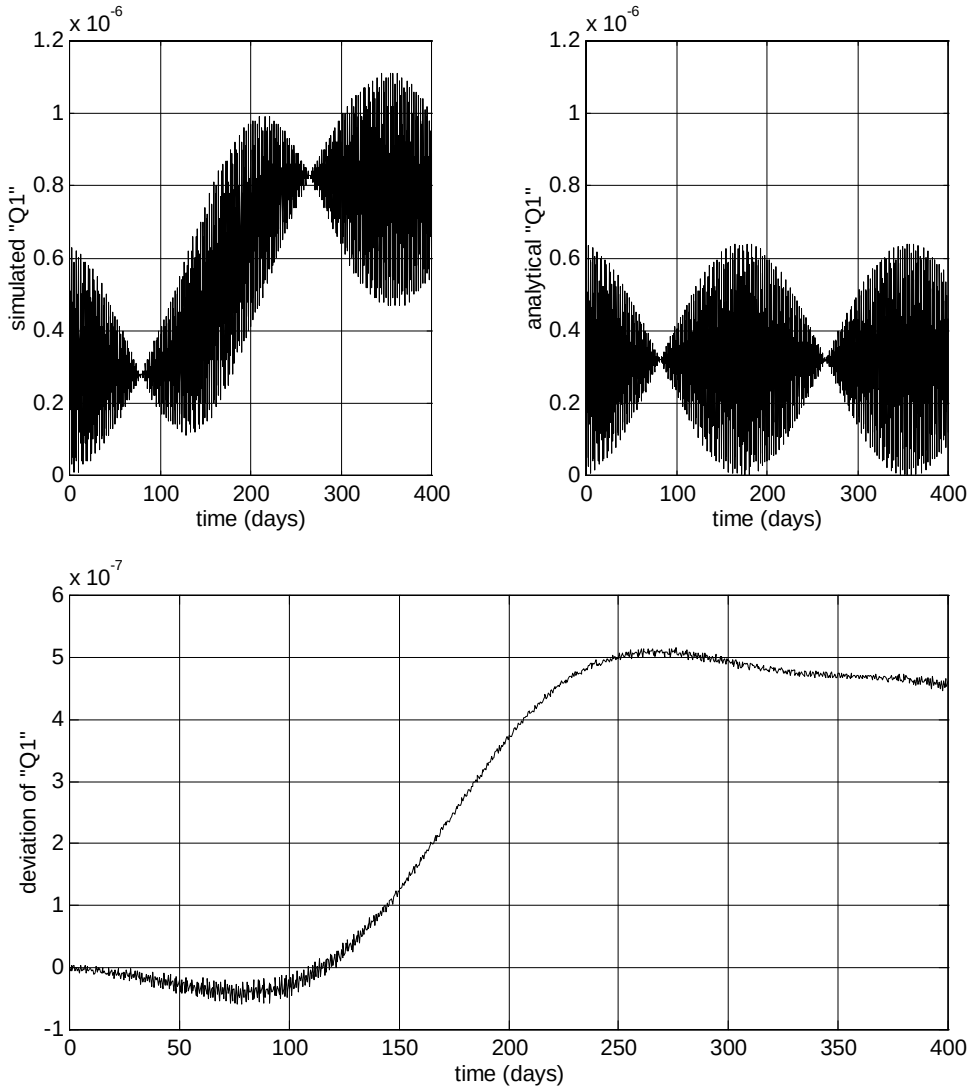

Figure B.22: Q1; Simulated, Analytical and Deviation for Test 6

The simulated and analytical graphs appear to differ significantly, however both show the same daily oscillatory motion within the same long term sinusoidal envelope. The differences between the graphs are shown more clearly on the deviation plot. Note that the rate of deviation between the two methods is greatest during the period 120 days to 240 days, which corresponds to the time when the eccentricity is largest. This leads to the largest difference in true longitude (see figure B.19), which in turn causes the errors in 'Q1' and 'Q2'. Once this period has been passed the 'Q1' deviation stabilises at a constant value (i.e. where the true longitude is again fairly accurate and the eccentricity is small).

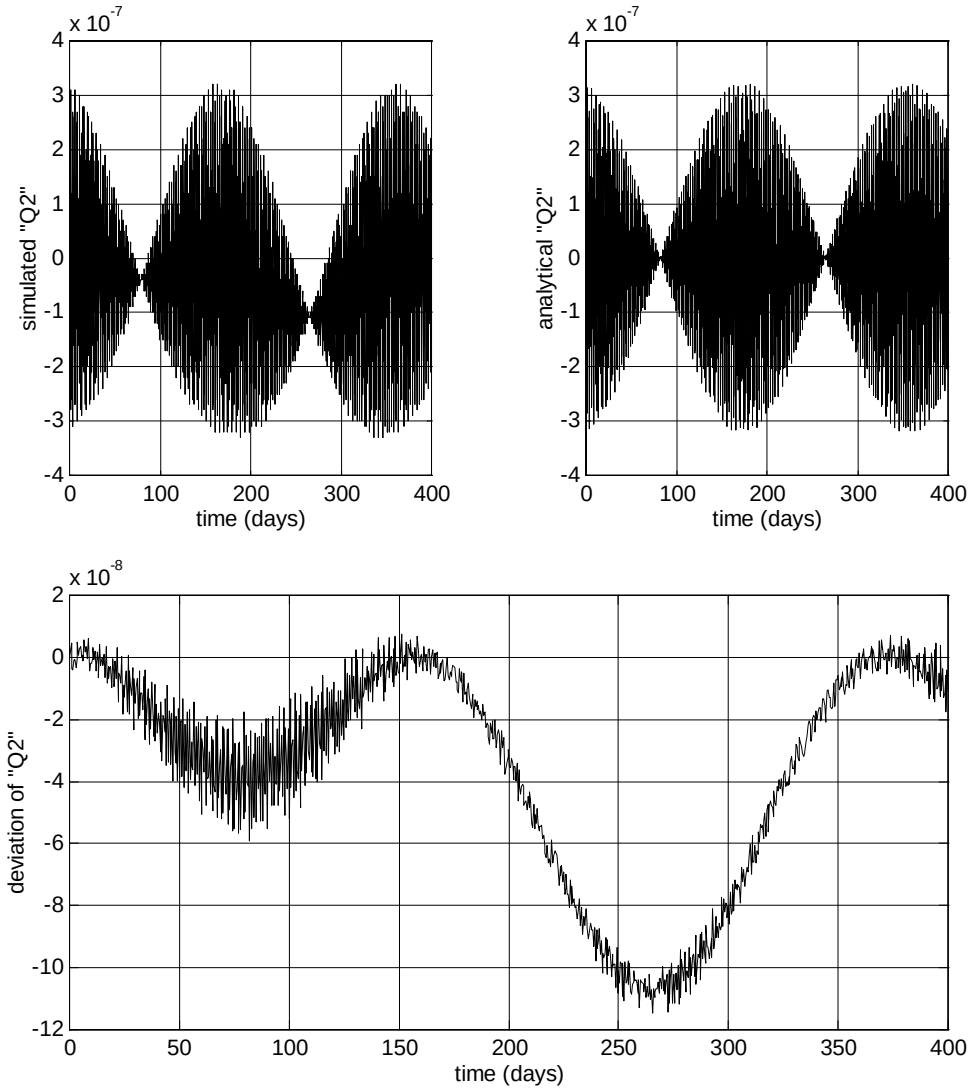

Figure B.23: Q2; Simulated, Analytical and Deviation for Test 6

The comments applied to the 'Q1' graphs are equally valid here, however due to interaction between trigonometric terms containing eccentricity variables the effect is much less pronounced.

B.3 : Comparison with Second Propagator

ESA orbit propagation data listed in Soop [31] (here-after referred to as the external data) covering a 50 day period from the 2nd March 1983 and listing one set of mean classical orbital elements every day is used for comparison purposes. The satellite area to mass ratio is not given in Soop [31], and so an estimate was made based on the radius of the 'best fit' arc passing through an eccentricity plane plot of the external data, which should equal the natural eccentricity circle radius. The corresponding effective area to mass ratio is then approximately 0.02.

The external data has been converted into equinoctial elements for comparisons however since average daily results are listed, comparisons between either true or mean longitudes would be meaningless (both have periods of about one day). Instead therefore the mean Greenwich longitude (which varies much more slowly) has been used in place of the sixth equinoctial variable.

Both sets of data are shown on the following four graphs where the external data is represented by 'O' markers and the propagator data by solid lines. A good match is evident from the graphs showing the [λ,a,Q1,Q2] elements however the [P1,P2] match is not as good. Possibly the estimate made to the area to mass ratio is a factor, but more likely this is a result of the simple Solar pressure model used in chapter 4 which does not take account of satellite eclipses or change in aspect (the non-arc like evolution of the 2D eccentricity vector $[P2,P1]^T$ in the external data graph leads to this assessment). Bearing this limitation in mind however the [P1,P2] comparisons are still acceptable.

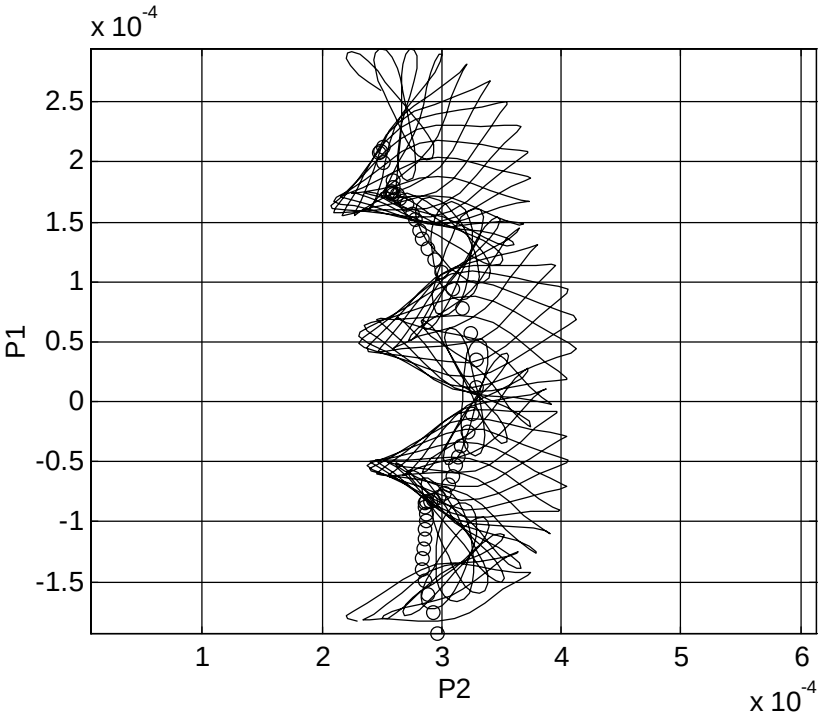

B.24 : Eccentricity Plane Comparison

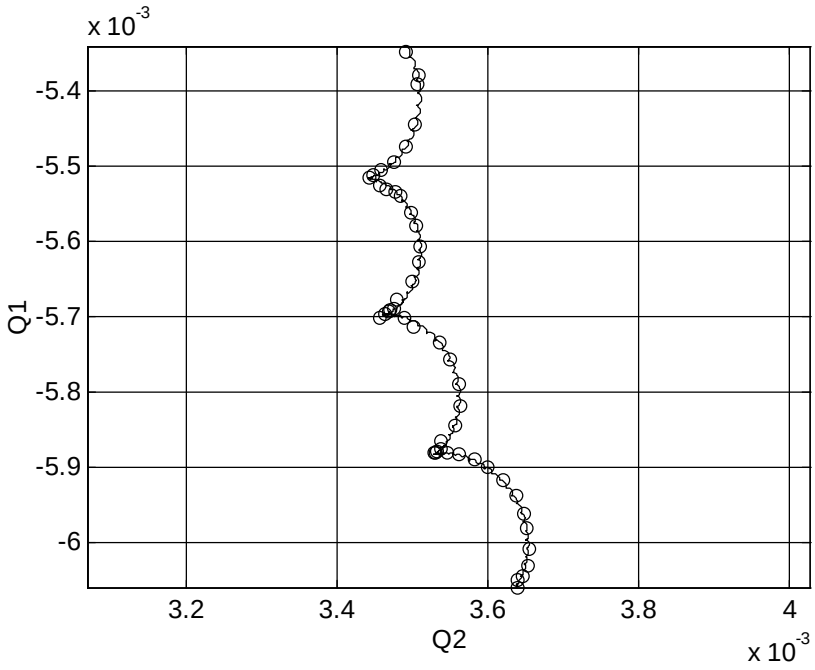

B.25 : Inclination Plane Comparison

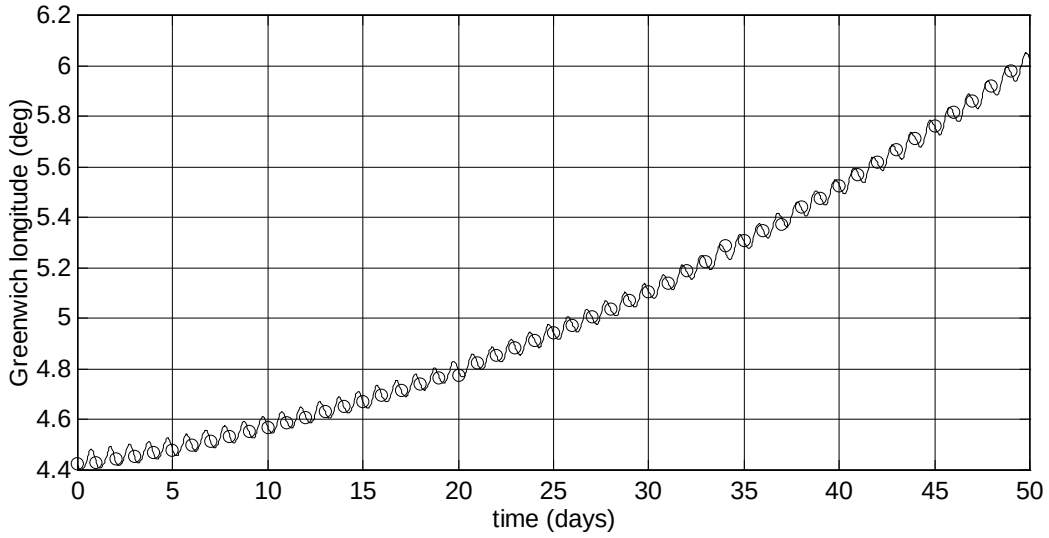

B.26 : Greenwich Longitude Evolution Comparison

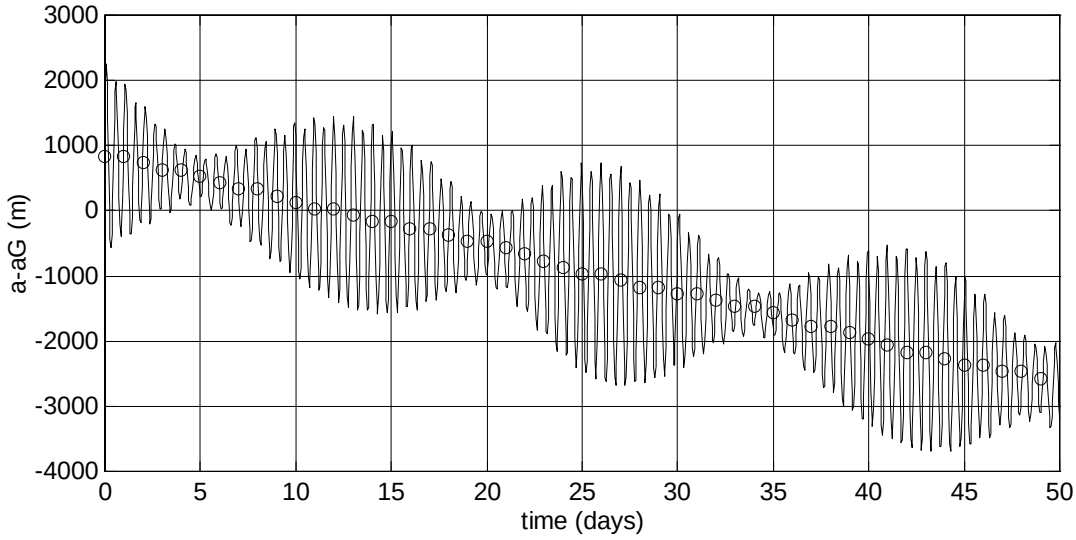

B.27 : Semi-major Axis Comparison

In the last diagram, figure B.27, '$a-a_G$' is shown for readability of the 'y' axis. Oscillations in the propagated data are a result of daily non-zero eccentricity librations which do not show up on the mean data from the Soop [31] source.

APPENDIX C : HILL'S EQUATIONS

This appendix concerns the mathematical derivation and manipulation of Hill's first order equations of relative motion. The appendix is summarised below.

- C.1 : Overview. Relative axes are defined and the use of each form of Hill's equations is explained.
- C.2 : Orbital element derivation. Starting from the equinoctial description of a satellite orbit a form of Hill's equations is derived which relates the separation between satellites to the difference in the values of the equinoctial elements.
- C.3 : Position and velocity derivation. Starting from the geocentric position and velocity vectors of two satellites a form of Hill's equations is derived which relates the separation between satellites to the differences in the elements of the geocentric positions and velocities.
- C.4 : Three Burn RL Recovery. A derivation of the required velocities along the 'L' axis for the three burn 'RL' recovery described in chapter 7 is presented.

C.1 : Overview

Analysis of the motion of one satellite relative to some reference point (which may or may not be a second satellite) is done using Hill's equations of relative motion. Different authors use different forms and so it is important to define the form used in this document.

The following three axes directions will be used for the relative co-ordinate system.

R	Radial separation (from center of Earth), positive outwards.
L	Longitudinal separation, positive Eastwards.
K	Latitudinal separation, positive Northwards.

The 'L' and 'K' components are arc lengths, however since the inter-satellite distances between colocated satellites are very small when compared to the GEO radius these will be approximately equal to straight line distances.

Two independent derivations are included. The first is based on the equinoctial orbital elements (and is a non-standard derivation) and the second, on the relative positions and velocities. The orbital element formulation is useful for separation strategy visualisation and the position-velocity formulation, for calculation of required cluster geometry recovery velocity increments. In deriving each the following assumptions were made.

1. Both the eccentricity and inclination of the individual satellite orbits are small.
2. Inter-satellite distances are small enough to make the differences in the external perturbation accelerations negligible.

For a near GEO satellite cluster, remaining within small longitude and latitude deadbands, both conditions are valid.

C.2 : Orbital Element Derivation

For near GEO orbits both the inclination and eccentricity are small and the position of a single satellite in spherical polar co-ordinates (see appendix A.2 for definition) can be written in terms of equinoctial elements approximately as,

$$\begin{aligned} r &= \frac{a\left(1-P1^2-P2^2\right)}{1+P1\mathrm{Sin}(L)+P2\mathrm{Cos}(L)} && \approx a_G+\delta a-a_G P1\mathrm{Sin}(L)-a_G P2\mathrm{Cos}(L) \\ \alpha &= \lambda+G && \approx L \\ \phi &= \mathrm{Sin}^{-1}\left(\frac{2\left(Q2\mathrm{Sin}(L)-Q1\mathrm{Cos}(L)\right)}{1+Q1^2+Q2^2}\right) && \approx 2Q2\mathrm{Sin}(L)-2Q1\mathrm{Cos}(L) \end{aligned} \qquad \text{(C.1)}$$

The approximation '$L \approx n_G(t-t_0)$' where 't_0' corresponds to 'L=0' can be used in the trigonometric terms in the first and third of these equations and the overall accuracy to first order will be unaffected. This allows 'r' and 'ϕ' to be calculated directly from the time since passage through the Vernal equinox.

To obtain a similar expression for 'α' a more complex procedure is required. Starting with the unperturbed differential form of true longitude,

$$\begin{aligned} \frac{dL}{dt} &= \frac{h}{r^2} \\ &\approx \frac{\mu}{h}\left(1+2P1\mathrm{Sin}(L)+2P2\mathrm{Cos}(L)\right) \\ &\approx n_G\left(1-\frac{3\delta a}{2a_G}\right)+2n_G P1\mathrm{Sin}\left(n_G(t-t_0)\right)+2n_G P2\mathrm{Cos}\left(n_G(t-t_0)\right) \end{aligned} \qquad \text{(C.2)}$$

where again '$L \approx n_G(t-t_0)$' can be used without a loss in overall accuracy. Equation (C.2) can now be integrated to give true longitude directly in terms of time as,

$$L = 2P1+\left(1-\frac{3\delta a}{2a_G}\right)n_G(t-t_0)-2P1\mathrm{Cos}\left(n_G(t-t_0)\right)+2P2\mathrm{Sin}\left(n_G(t-t_0)\right) \qquad \text{(C.3)}$$

Combining this with the second line of equation (C.1) the Greenwich longitude is thus,

$$\lambda = 2P1 - G_0 - \frac{3\delta a}{2a_G} n_G(t - t_0) - 2P1\mathrm{Cos}\left(n_G(t - t_0)\right) + 2P2\mathrm{Sin}\left(n_G(t - t_0)\right) \qquad \text{(C.4)}$$

where the approximation '$G \approx G_0+n_G(t-t_0)$' has been used and the first two terms in the equation represent the mean Greenwich longitude at $t = t_0$, 'λ_{m0}'.

Equation (C.1) can now be rewritten to give the satellite position in radial, longitudinal, and latitudinal terms as,

$$\begin{aligned} r &\approx a_G + \delta a - a_G P1\mathrm{Sin}\left(n_G(t - t_0)\right) - a_G P2\mathrm{Cos}\left(n_G(t - t_0)\right) \\ \lambda &\approx \lambda_0 - \frac{3\delta a}{2a_G} n_G(t - t_0) - 2P1\mathrm{Cos}\left(n_G(t - t_0)\right) + 2P2\mathrm{Sin}\left(n_G(t - t_0)\right) \\ \phi &\approx 2Q2\mathrm{Sin}\left(n_G(t - t_0)\right) - 2Q1\mathrm{Cos}\left(n_G(t - t_0)\right) \end{aligned} \qquad \text{(C.5)}$$

Consider now relative motion. Since colocated satellites must remain within a small GEO window (typically ±0.°1) the value of 'L' for each satellite in the cluster will be approximately the same and so from '$L \approx n_G(t-t_0)$' the value of 't_0' will also be similar. Using this assumption and multiplying the 'λ' and 'ϕ' equations by 'a_G' to give arc lengths, equation (C.5) can be incrementing to give the relative motion between two satellites (or one satellite and a suitable reference point) in [R,L,K] co-ordinates as,

$$\begin{aligned} R &= \Delta a - a_G \Delta P1\mathrm{Sin}\left(n_G(t - t_0)\right) - a_G \Delta P2\mathrm{Cos}\left(n_G(t - t_0)\right) \\ L &= a_G \Delta\lambda_0 - \frac{3\Delta a}{2} n_G(t - t_0) - 2a_G \Delta P1\mathrm{Cos}\left(n_G(t - t_0)\right) + 2a_G \Delta P2\mathrm{Sin}\left(n_G(t - t_0)\right) \\ K &= 2a_G \Delta Q2\mathrm{Sin}\left(n_G(t - t_0)\right) - 2a_G \Delta Q1\mathrm{Cos}\left(n_G(t - t_0)\right) \end{aligned} \qquad \text{(C.6)}$$

where 'Δa' represents the difference between the semi-major axis of the two satellites, and similar notation is used for the remaining orbital elements. It is usual to write this equation in terms of six new variables, named E_i where i=1 to 6. Equation (C.7) is the more usual form and equation (C.8) relates the E_i elements to the variables used in (C.6).

$$\begin{aligned} R &= -\frac{2}{3}E_2 + E_3\mathrm{Cos}\left(n_G(t-t_0)\right) + E_4\mathrm{Sin}\left(n_G(t-t_0)\right) \\ L &= E_1 + E_2 n_G(t-t_0) - 2E_3\mathrm{Sin}\left(n_G(t-t_0)\right) + 2E_4\mathrm{Cos}\left(n_G(t-t_0)\right) \\ K &= E_5\mathrm{Cos}\left(n_G(t-t_0)\right) + E_6\mathrm{Sin}\left(n_G(t-t_0)\right) \end{aligned} \qquad \text{(C.7)}$$

where the 'E_i' variables are found from equation (C.6) as,

$$\begin{aligned} E_1 &= a_G\Delta\lambda_0 \\ E_2 &= -\frac{3}{2}\Delta a \\ E_3 &= -a_G\Delta P2 \\ E_4 &= -a_G\Delta P1 \\ E_5 &= -2a_G\Delta Q1 \\ E_6 &= 2a_G\Delta Q2 \end{aligned} \qquad \text{(C.8)}$$

completing the orbital element derivation.

C.3 : Position and Velocity Derivation

The motion of two Earth orbiting satellites can be described by the second order differential equations given below in geocentric inertial axes.

$$\ddot{\underline{r}}_1 = -\left(\frac{\mu}{r_1^3}\right)\underline{r}_1 + \underline{f}_1 \quad ; \quad \ddot{\underline{r}}_2 = -\left(\frac{\mu}{r_2^3}\right)\underline{r}_2 + \underline{f}_2$$

The relative acceleration vector, '$\ddot{\underline{\rho}}$', is then,

$$\ddot{\underline{\rho}} = \ddot{\underline{r}}_2 - \ddot{\underline{r}}_1 = \frac{\mu}{r_1^3}\left(\underline{r}_1 - \left(\frac{r_1^3}{r_2^3}\right)\underline{r}_2\right) + \Delta\underline{f} \qquad \text{(C.9)}$$

The '$\underline{r}_2$' term in equation (C.9) can be re-written in terms of '$\underline{r}_1$' and '$\underline{\rho}$' and linearised using the fact that $\underline{\rho} << \underline{r}_1$. The process, retaining only first order terms, is detailed in equation (C.10).

$$\begin{aligned}\left(\frac{r_1^3}{r_2^3}\right)\underline{r_2} &= \frac{r_1^3\left(\underline{r_1}+\underline{\rho}\right)}{\left|\underline{r_1}+\underline{\rho}\right|^3}\\ &= \frac{r_1^3\left(\underline{r_1}+\underline{\rho}\right)}{\left(r_1^2+2\underline{r_1}.\underline{\rho}+\rho^2\right)^{\frac{3}{2}}}\\ &\approx \left(\underline{r_1}+\underline{\rho}\right)\left[1-3\left(\frac{\underline{r_1}.\underline{\rho}}{r_1^2}\right)\right]\end{aligned} \qquad \text{(C.10)}$$

Combining equations (C.9) and (C.10) gives an acceleration equation free from '$\underline{r_2}$' terms.

$$\begin{aligned}\underline{\ddot{\rho}} &= \frac{\mu}{r_1^3}\left(\underline{r_1}-\left(\underline{r_1}+\underline{\rho}\right)\left[1-3\left(\frac{\underline{r_1}.\underline{\rho}}{r_1^2}\right)\right]\right)+\underline{\Delta f}\\ &\approx \frac{\mu}{r_1^3}\left(-\underline{\rho}+3\left(\frac{\underline{r_1}.\underline{\rho}}{r_1^2}\right)\underline{r_1}\right)+\underline{\Delta f}\end{aligned} \qquad \text{(C.11)}$$

Although '$\underline{\rho}$' can be written directly in [R,L,K] co-ordinates '$\underline{\ddot{\rho}}$' (being an inertial acceleration) cannot. A second equation is therefore required, relating the inertial relative acceleration '$\underline{\ddot{\rho}}$' to the local axes relative acceleration, '$\underline{\ddot{\rho}_1}$'. Starting with the relationship between $\underline{r_1}$ and $\underline{r_2}$,

$$\begin{aligned}\underline{r_2} &= \underline{r_1}+\underline{\rho}\\ \underline{\dot{r}_2} &= \underline{\dot{r}_1}+\underline{\dot{\rho}} = \underline{\dot{r}_1}+\underline{\dot{\rho}_1}+\underline{n}\times\underline{\rho}\\ \underline{\ddot{r}_2} &= \underline{\ddot{r}_1}+\left(\underline{\ddot{\rho}_1}+\underline{n}\times\underline{\dot{\rho}_1}\right)+\left(\underline{\dot{n}}\times\underline{\rho}+\underline{n}\times\underline{\dot{\rho}}\right)\\ \underline{\ddot{\rho}} &= \left(\underline{\ddot{\rho}_1}+\underline{n}\times\underline{\dot{\rho}_1}\right)+\left(\underline{\dot{n}}\times\underline{\rho}+\underline{n}\times\left(\underline{\dot{\rho}_1}+\underline{n}\times\underline{\rho}\right)\right)\end{aligned}$$

Since the orbits are approximately GEO the angular velocity vector, '$\underline{n}$' can be assumed constant. Applying this restriction and rearranging,

$$\underline{\ddot{\rho}} = \underline{\ddot{\rho}_1}+2\left(\underline{n}\times\underline{\dot{\rho}_1}\right)+\underline{n}\times\left(\underline{n}\times\underline{\rho}\right) \qquad \text{(C.12)}$$

Where all the vector quantities on the right hand side are known in [R,L,K] axes. Using this to replace '$\ddot{\underline{\rho}}$' in equation (C.11),

$$\ddot{\underline{\rho}}_l + 2\left(\underline{n} \times \dot{\underline{\rho}}_l\right) + \underline{n} \times \left(\underline{n} \times \underline{\rho}\right) - \frac{\mu}{r_1^3}\left(\underline{\rho} - 3\left(\frac{\underline{r_1}.\underline{\rho}}{r_1^2}\right)\underline{r_1}\right) = \underline{\Delta f} \qquad \text{(C.13)}$$

Since '$\underline{r_1}$' is not present in isolation in equation (C.13) it can be approximated to the ideal GEO value without a loss in overall accuracy. The vector quantities in equation (C.13) can then be summarised in the [R,L,K] frame as,

$$\underline{\rho} = \begin{bmatrix} R \\ L \\ K \end{bmatrix} \quad ; \quad \dot{\underline{\rho}}_l = \begin{bmatrix} \dot{R} \\ \dot{L} \\ \dot{K} \end{bmatrix} \quad ; \quad \ddot{\underline{\rho}}_l = \begin{bmatrix} \ddot{R} \\ \ddot{L} \\ \ddot{K} \end{bmatrix} \quad ; \quad \underline{n} = \begin{bmatrix} 0 \\ 0 \\ n_G \end{bmatrix} \quad ; \quad \underline{r_1} \approx \begin{bmatrix} a_G \\ 0 \\ 0 \end{bmatrix} \quad ; \quad \underline{\Delta f} = \begin{bmatrix} \Delta f_R \\ \Delta f_L \\ \Delta f_K \end{bmatrix} \qquad \text{(C.14)}$$

Combining (C.13) and (C.14) yields three differential equations which describe the relative motion,

$$\begin{aligned} \ddot{R} - 2n_G\dot{L} - 3n_G^2 R &= \Delta f_R \\ \ddot{L} + 2n_G\dot{R} &= \Delta f_L \\ \ddot{K} + n_G^2 K &= \Delta f_K \end{aligned} \qquad \text{(C.15)}$$

Using the assumption already mentioned that the satellites are close enough for the difference in perturbing accelerations to be negligible, the right hand side of equations (C.15) can be set equal to zero and the equations can be solved analytically to give,

$$\begin{aligned} R &= -\frac{2}{3}E_2 + E_3\mathrm{Cos}\left(n_G\left(t - t_0\right)\right) + E_4\mathrm{Sin}\left(n_G\left(t - t_0\right)\right) \\ L &= E_1 + E_2 n_G\left(t - t_0\right) - 2E_3\mathrm{Sin}\left(n_G\left(t - t_0\right)\right) + 2E_4\mathrm{Cos}\left(n_G\left(t - t_0\right)\right) \\ K &= E_5\mathrm{Cos}\left(n_G\left(t - t_0\right)\right) + E_6\mathrm{Sin}\left(n_G\left(t - t_0\right)\right) \end{aligned} \qquad \text{(C.16)}$$

which is identical to equation (C.7) in the previous derivation. Using conditions at $t=t_0$,

$$\begin{aligned}
E_1 &= L_0 - 2\dot{R}_0/n_G \\
E_2 &= -3\dot{L}_0/n_G - 6R_0 \\
E_3 &= -3R_0 - 2\dot{L}_0/n_G \\
E_4 &= \dot{R}_0/n_G \\
E_5 &= K_0 \\
E_6 &= \dot{K}_0/n_G
\end{aligned} \tag{C.17}$$

or more generally, given the relative position and velocity at time 't',

$$\begin{aligned}
E_1 &= \left(3n_G t\dot{L} + 6{n_G}^2 tR + n_G L - 2\dot{R}\right)/n_G \\
E_2 &= -3\left(\dot{L} + 2n_G R\right)/n_G \\
E_3 &= -\left(\left[2\dot{L} + 3n_G R\right]\mathrm{Cos}\left(n_G\left(t-t_0\right)\right) + \dot{R}\mathrm{Sin}\left(n_G\left(t-t_0\right)\right)\right)/n_G \\
E_4 &= -\left(\left[2\dot{L} + 3n_G R\right]\mathrm{Sin}\left(n_G\left(t-t_0\right)\right) - \dot{R}\mathrm{Cos}\left(n_G\left(t-t_0\right)\right)\right)/n_G \\
E_5 &= \left(-\dot{K}\mathrm{Sin}\left(n_G\left(t-t_0\right)\right) + Kn_G\mathrm{Cos}\left(n_G\left(t-t_0\right)\right)\right)/n_G \\
E_6 &= \left(\dot{K}\mathrm{Cos}\left(n_G\left(t-t_0\right)\right) + Kn_G\mathrm{Sin}\left(n_G\left(t-t_0\right)\right)\right)/n_G
\end{aligned} \tag{C.18}$$

Completing the position and velocity derivation.

Equation (C.18) is particularly useful in calculating the effect of velocity increments on the relative orbit and is used for such in chapter 7.

C.4 : Three Burn RL Recovery

In chapter 7 a method by which the equations of relative motion can be used to calculate the 'L' axis velocity increments needed at the three correction points 'A', 'B, 'C' (see figure 7.1) to recover the nominal cluster geometry in the 'RL' plane is described. The solution presented involves the derivation of analytical expressions for three quantities from which the entire 'RL' recovery can be determined. The three quantities are,

'$\dot{L}_A$'	The 'L' axis velocity after the first corrective burn.
'$\dot{L}_{B2}$'	The 'L' axis velocity after the second corrective burn.
'$\left(\dot{R}_{B1} - \dot{R}_{B2}\right)$'	The change in 'R' axis velocity at point 'B'.

and for the recovery restrictions imposed in chapter 7 the last must equal zero, providing an equation that can be solved iteratively for 't_B' (the time when the second corrective burn is applied).

To solve for '$\dot{L}_A$', '$\dot{L}_{B2}$' and '$\left(\dot{R}_{B1} - \dot{R}_{B2}\right)$' the sixteen simultaneous equations listed as (7.5) to (7.7) are reduced to four simultaneous equations and then solved symbolically using MATLAB.

The details of the reduction process and the subsequent simplification of the final equations is described in this section. For clarity the simultaneous equations remaining at each step will be written in the matrix format,

$$M_i \underline{u_i} = \underline{k_i} \tag{C.19}$$

where 'M_i' is an 'i×i' matrix (composed mainly of trigonometric terms), '$\underline{u_i}$' is a column vector of the remaining unknowns, and '$\underline{k_i}$' is a known column vector.

The following notational reductions are used in the derivation.

$$n = n_G \qquad sA = \mathrm{Sin}\left(n_G\left(t_A - t_0\right)\right) \qquad sB = \mathrm{Sin}\left(n_G\left(t_B - t_0\right)\right) \qquad sC = \mathrm{Sin}\left(n_G\left(t_C - t_0\right)\right)$$

$$tA0 = t_A - t_0 \qquad cA = \mathrm{Cos}\left(n_G\left(t_A - t_0\right)\right) \qquad cB = \mathrm{Cos}\left(n_G\left(t_B - t_0\right)\right) \qquad cC = \mathrm{Cos}\left(n_G\left(t_C - t_0\right)\right)$$

$$tB0 = t_B - t_0$$

$$tC0 = t_C - t_0 \qquad cBA = \mathrm{Cos}\left(n_G\left(t_A - t_B\right)\right) \qquad cCB = \mathrm{Cos}\left(n_G\left(t_C - t_B\right)\right) \qquad cCA = \mathrm{Cos}\left(n_G\left(t_C - t_A\right)\right)$$

$$sBA = \mathrm{Sin}\left(n_G\left(t_A - t_B\right)\right) \qquad sCB = \mathrm{Sin}\left(n_G\left(t_C - t_B\right)\right) \qquad sCA = \mathrm{Sin}\left(n_G\left(t_C - t_A\right)\right)$$

Initial Equations

The sixteen simultaneous equations defining the 'RL' recovery are listed in chapter 7 as equations (7.5) to (7.7) and are repeated below.

Equations at A

$$\begin{aligned}
R_A &= -\frac{2}{3}E_2 + E_3cA + E_4sA \\
L_A &= E_1 + E_2n\left(t_A - t_0\right) - 2E_3sA + 2E_4cA \\
\dot{R}_A &= -nE_3sA + nE_4cA \\
\dot{L}_A &= E_2n - 2nE_3cA - 2nE_4sA
\end{aligned}$$

Equations at B

$$\begin{aligned}
R_B &= -\frac{2}{3}E_{2C1} + E_{3C1}cB + E_{4C1}sB \\
L_B &= E_{1C1} + E_{2C1}n\left(t_B - t_0\right) - 2E_{3C1}sB + 2E_{4C1}cB \\
\dot{R}_{B1} &= -nE_{3C1}sB + nE_{4C1}cB \\
\dot{L}_{B1} &= E_{2C1}n - 2nE_{3C1}cB - 2nE_{4C1}sB \\
R_B &= -\frac{2}{3}E_{2C2} + E_{3C2}cB + E_{4C2}sB \\
L_B &= E_{1C2} + E_{2C2}n\left(t_B - t_0\right) - 2E_{3C2}sB + 2E_{4C2}cB \\
\dot{R}_{B2} &= -nE_{3C2}sB + nE_{4C2}cB \\
\dot{L}_{B2} &= E_{2C2}n - 2nE_{3C2}cB - 2nE_{4C2}sB
\end{aligned} \qquad \text{(C.20)}$$

Equations at C

$$\begin{aligned}
R_C &= -\frac{2}{3}E_{2C2} + E_{3C2}cC + E_{4C2}sC \\
L_C &= E_{1C2} + E_{2C2}n\left(t_C - t_0\right) - 2E_{3C2}sC + 2E_{4C2}cC \\
\dot{R}_C &= -nE_{3C2}sC + nE_{4C2}cC \\
\dot{L}_C &= E_{2C2}n - 2nE_{3C2}cC - 2nE_{4C2}sC
\end{aligned}$$

where the unknowns are,

$$t_B, \dot{L}_A, R_B, \dot{R}_{B1}, \dot{R}_{B2}, L_B, \dot{L}_{B1}, \dot{L}_{B2}, \dot{L}_C,$$

$$E_{1c1}, E_{2c1}, E_{3c1}, E_{4c1}, E_{1c2}, E_{2c2}, E_{3c2}, E_{4c2}$$

Reduction to 10×10 Matrix Equation

Using the equations before and after the burn at 'B' the variables 'R_B' and 'L_B' in equations (C.20) can be eliminated, reducing the number of equations by two. Further reductions are possible by noting that '$\dot{R}_{B1}$' ,'$\dot{L}_{B1}$' and '$\dot{L}_C$' are dependant variables, and thus lines 5, 7 and 12 can be discarded. In addition if we initially assume '$\dot{R}_{B2}$' to equal '$\dot{R}_{B1}$' then both line 11 can also be discarded for the same reason. The overall result of this process is to reduce the sixteen equations to ten. Converting to matrix form the variables from equation (C.19) are,

M_{10} =

0	0	0	-2/3	cA	sA	0	0	0	0
0	0	1	nt_A	-2sA	2cA	0	0	0	0
0	0	0	0	-nsA	ncA	0	0	0	0
-1	0	0	n	-2ncA	-2nsA	0	0	0	0
0	0	0	0	0	0	0	-2/3	cC	sC
0	0	0	0	0	0	1	nt_C	-2sC	2cC
0	0	0	0	0	0	0	0	-nsC	ncC
0	0	0	-2/3	cB	sB	0	2/3	-cB	-sB
0	0	1	nt_B	-2sB	2cB	-1	$-nt_B$	2sB	-2cB
0	-1	0	0	0	0	0	n	-2ncB	-2nsB

$\underline{k}_{10}$ =

dL_A/dt
dL_B/dt
E_{1c1}
E_{2c1}
E_{3c1}
E_{4c1}
E_{1c2}
E_{2c2}
E_{3c2}
E_{4c2}

$\underline{u}_{10}$ =

R_A
L_A
dR_A/dt
0
R_C
L_C
dR_C/dt
0
0
0

By a series of row operations to eliminate the 'E_j' variables the matrix equation (C.19) can be reduced to a 4×4 matrix equation which is small enough to be solvable

analytically by MATLAB. The reduced equation at each step in the process will now be detailed.

Reduction to 9×9 Matrix Equation

Eliminate 'E_{1c1}' between lines 6 and 9 of 'M_{10}' and thus remove column 3 of matrix M_{10}. Additionally, divide lines 3 and 7 by 'n'.

M_9 =

0	0	-2/3	cA	sA	0	0	0	0
0	0	nt_A-nt_B	-2sA+2sB	2cA-2cB	1	nt_B	-2sB	2cB
0	0	0	-sA	cA	0	0	0	0
-1	0	n	-2ncA	-2nsA	0	0	0	0
0	0	0	0	0	0	-2/3	cC	sC
0	0	0	0	0	1	nt_C	-2sC	2cC
0	0	0	0	0	0	0	-sC	cC
0	0	-2/3	cB	sB	0	2/3	-cB	-sB
0	-1	0	0	0	0	n	-2ncB	-2nsB

$\underline{k_9}$ =

dL_A/dt
dL_B/dt
E_{2c1}
E_{3c1}
E_{4c1}
E_{1c2}
E_{2c2}
E_{3c2}
E_{4c2}

$\underline{u_9}$ =

R_A
L_A
$(dR_A/dt)/n$
0
R_C
L_C
$(dR_C/dt)/n$
0
0

Reduction to 8×8 Matrix Equation

Eliminate 'E_{1c2}' between lines 2 and 6 of 'M_9' and thus remove column 6 of matrix 'M_9'.

M_8 =

0	0	-2/3	cA	sA	0	0	0
0	0	nt_A-nt_B	-2sA+2sB	2cA-2cB	nt_B-nt_C	-2sB+2sC	2cB-2cC
0	0	0	-sA	cA	0	0	0
-1/n	0	1	-2cA	-2sA	0	0	0
0	0	0	0	0	-2/3	cC	sC

0	-1/n	0	0	0	1	-2cB	-2sB
0	0	0	0	0	0	-sC	cC
0	0	-2/3	cB	sB	2/3	-cB	-sB

$\underline{k_8}$ =

dL_A/dt
dL_B/dt
E_{2c1}
E_{3c1}
E_{4c1}
E_{2c2}
E_{3c2}
E_{4c2}

$\underline{u_8}$ =

R_A
L_A-L_C
$(dR_A/dt)/n$
0
R_C
0
$(dR_C/dt)/n$
0

Reduction to 7×7 Matrix Equation

Eliminate 'E_{2c1}' between lines 1,2,4 and 8 of 'M_8' (by subtracting multiples of line 4 from the other lines) and thus remove column 3 of matrix 'M_8'.

M_7 =

-(2/3)/n	0	-cA/3	-sA/3	0	0	0
$1/n(nt_A-nt_B)$	0	$-2sA+2sB+2ncA(t_A-t_B)$	$2cA-2cB+2nsA(t_A-t_B)$	nt_B-nt_C	-2sB+2sC	2cB-2cC
0	0	-sA	cA	0	0	0
-(2/3)/n	0	cB-4cA/3	sB-4sA/3	2/3	-cB	-sB
0	0	0	0	-2/3	cC	sC
0	-1/n	0	0	1	-2cB	-2sB
0	0	0	0	0	-sC	cC

$\underline{k_7}$ =

dL_A/dt
dL_B/dt
E_{3c1}
E_{4c1}
E_{2c2}
E_{3c2}
E_{4c2}

$\underline{u_7}$ =

R_A
L_A-L_C
$(dR_A/dt)/n$
0
R_C
0
$(dR_C/dt)/n$

Reduction to 6×6 Matrix Equation

Eliminate 'E_{2c2}' between lines 2,4,5 and 6 of 'M_7' (by subtracting multiples of line 6 from the other lines) and thus remove column 5 of matrix 'M_7'.

M_6 =

-2/n	0	-cA	-sA	0	0
t_A-t_B	t_B-t_C	2cA(t_A-t_B)n-2sA+2sB	2sA(t_A-t_B)n+2cA-2cB	2cB(t_B-t_C)n-2sB+2sC	2sB(t_B-t_C)n+2cB-2cC
0	0	-sA	cA	0	0
-2/n	2/n	3cB-4cA	3sB-4sA	cB	sB
0	-2/n	0	0	3cC-4cB	3sC-4sB
0	0	0	0	-sC	cC

$\underline{k_6}$ =

dL_A/dt
dL_B/dt
E_{3c1}
E_{4c1}
E_{3c2}
E_{4c2}

$\underline{u_6}$ =

R_A
L_A-L_C
$(dR_A/dt)/n$
0
R_C
$(dR_C/dt)/n$

Reduction to 5×5 Matrix Equation

Eliminate 'E_{3c2}' between lines 2,4,5 and 6 of 'M_6' (by subtracting multiples of line 6 from the other lines) and thus remove column 5 of matrix 'M_6'. Additionally, simplify using trigonometric subtraction formulae.

M_5 =

-2/n	0	-cA	-sA	0
-(t_A-t_B)sC	-(t_B-t_C)sC	-(2cA(t_A-t_B)n-2sA+2sB)sC	-(2sA(t_A-t_B)n+2cA-2cB)sC	-2sCB-2cCB(t_B-t_C)n
0	0	-sA	cA	0
2sC/n	-2sC/n	-(3cB-4cA)sC	-(3sB-4sA)sC	-cCB
0	2sC/n	0	0	-3+4cCB

$\underline{k_5}$ =

dL_A/dt
dL_B/dt
E_{3c1}
E_{4c1}
E_{4c2}

$\underline{u_5}$ =

$3R_A$
-(L_A-L_C)sC-(dR_C/dt)(2cB(t_B-t_C)n-2sB+2sC)/n
$(dR_A/dt)/n$
-(dR_C/dt)cB/n
-3R_CsC-(dR_C/dt)(3cC-4cB)/n

Reduction to 4×4 Matrix Equation

Eliminate 'E_{4c2}' between lines 2,4 and 5 of 'M_5' (by subtracting multiples of line 4 from the other lines) and thus remove column 5 of matrix 'M_5'.

M_4 =

-2/n	0	-cA	-sA
(t_A-t_B)sCcCB -2sC(-2sCB-2cCB(t_B-t_C)n)/n	-3(t_B-t_C)sCcCB -4sCsCB/n	2(cA(t_A-t_B)n-sA+sB)sCcCB -2(3cB-4cA)sC(sCB+cCB(t_B-t_C)n)	(2sA(t_A-t_B)n+2cA-2cB)sCcCB -2(3sB-4sA)sC(sCB+cCB(t_B-t_C)n)
0	0	-sA	cA
2sC(3-4cCB)/n	-2sCcCB/n -2sC*(3-4*cCB)/n	(3cB-4cA)sC(-3+4cCB)	(3sB-4sA)sC(-3+4cCB)

$\underline{k_4}$ =

dL_A/dt
dL_B/dt
E_{3c1}
E_{4c1}

$\underline{u_4}$ =

$3R_A$
sC(cCB(L_A-L_C)+2(dR_C/dt)(cCB-1)/n)
(dR_A/dt)/n
3(R_CcCBsC+(dR_C/dt)(cCBcC-cB)/n)

Solution via MATLAB is possible at this stage and the resulting expressions for '$\dot{L}_A$' and '$\dot{L}_{B2}$' after simplification are given below.

$$
\begin{aligned}
&2D \times \dot{L}a = \\
&-nR_A\left[4(3sCA - 3sBA - 4sCB) + 3n\left(4\left(t_C - t_A\right) - 3cBA\left(t_C - t_B\right) - 4cCB\left(t_B - t_A\right)\right)\right] \\
&-\dot{R}_A\left[4(1 - cCB + cCA - cBA) + 3nsBA\left(t_C - t_B\right)\right] - nR_C\left[4sCB - 3ncCB\left(t_C - t_B\right)\right] \\
&+\dot{R}_C\left[8(1 - cCB) - 3nsCB\left(t_C - t_B\right)\right] + 2n\left(L_A - L_C\right)(1 - cCB)
\end{aligned}
\qquad (C.21)
$$

$$
\begin{aligned}
&2D\dot{L}b = \\
&+nR_A(3 - 4cCB)\left[4sBA - 3cBAn\left(t_B - t_A\right)\right] + \dot{R}_A(3 - 4cCB)\left[8 - 8cBA - 3sBAn\left(t_B - t_A\right)\right] \\
&+nR_C\left[4(sCA + sCB(3 - 4cBA)) + 3cCBn\left(t_A + 3t_B - 4tC + 4cBA\left(t_C - t_B\right)\right)\right] \\
&-\dot{R}_C\left[4(sCBsBA + 7(1 - cCB)(1 - cBA)) - 3sCBn\left(t_B - t_A + 4(tC - tB)(1 - cBA)\right)\right] \\
&-n\left(L_A - L_A\right)(1 - cBA)(6 - 8cCB)
\end{aligned}
\qquad (C.22)
$$

where the common element 'D' in equation (C.21) and (C.22) is,

$$D = 4(sCA - sCB - sBA) + 3n\left(t_C - t_A - cBA\left(t_C - t_B\right) - cCB\left(t_B - t_A\right)\right) \qquad (C.23)$$

Expression for '$\left(\dot{R}_{B1} - \dot{R}_{B2}\right)$'

In formulating the 10×10 matrix 'M' the equation for '$\left(\dot{R}_{B1} - \dot{R}_{B2}\right)$' was discarded, however as explained in chapter 7 this quantity is useful in providing an iterative solution for 't_B'.

Since '$\left(\dot{R}_{B1} - \dot{R}_{B2}\right)$' is a function of the variables [E_{3c1}, E_{3c2}, E_{3c2}, E_{4c2}, t_B] it can be re-introduced at the 5×5 matrix stage, thus creating a new 6×6 matrix equation which can again be reduced to 4×4 before solving via MATLAB. The resulting equation is then,

$$\begin{aligned}
&D \times \left(\dot{R}_{b1} - \dot{R}_{b2}\right) = \\
&-\dot{R}_A\left[4\left(sCB - sCA + sBA\right) + 3n(t_C - t_B + cCA\left(t_B - t_A\right) - cBA\left(t_C - t_A\right))\right] \\
&+3n^2 R_A\left[sCA\left(t_B - t_A\right) - sBA\left(t_C - t_A\right)\right] \\
&+\dot{R}_C\left[4(sCB - sCA + sBA) + 3n\left(t_B - t_A + cCA\left(t_C - t_B\right) - cCB\left(t_C - t_A\right)\right)\right] \\
&+3n^2 R_C\left[sCA\left(t_C - t_B\right) - sCB\left(t_C - t_A\right)\right] + 2n\left(L_A - L_C\right)(sBA + sCB - sCA)
\end{aligned} \qquad (C.24)$$

APPENDIX D : ORBIT PROPAGATOR LISTINGS

D.1 : Overview

During the course of the research a significant amount of computer software was written (in excess of 6000 lines of code) and whilst it is neither possible nor desirable to list it all here there is benefit in listing the main orbit propagation segment, since it is this that the station keeping and cluster geometry control algorithms derived in chapters 5 and 7 have been 'tested' on.

As noted in the introduction the mathematically intensive programming tasks were written in *Borland Turbo Pascal for Windows 1.5* and all the listings presented here are in that programming language. The following three 'code modules' are included,

1. The variable definition module.
2. The perturbation force module.
3. The main orbit integration module.

The first defines the global variable names as used by all modules, the second contains the implementation of the perturbation force equations given in chapter 4 and the final listing is the main orbit integration module which propagates the orbit by one time step. At each step in the propagation the second module is called by the third.

None of the included listings are complete computer programs, they are sub-routines to which data is sent and from which results are recorded. The user interface code which links the modules is not relevant to orbit propagation and so is not listed, however various aspects of this are included by way of screenshots in the main text.

The following conventions used in the listings are explained below.

{TEXT} Comment lines, included for clarity.

CAPITALS TPW reserved words.

D.2 : Variable Definition Module

```
{$N+}                    {compiler directive enabling co-proccessor support}
UNIT ORBITVAR;
INTERFACE

CONST                                                    {--CONSTANTS--}
  Months :ARRAY[1..12] OF string[29] = ('January','February','March','April','May','June','July'
                                        ,'August','September','October','November','December');
  muE      = 3.986005e14;                                {gravitational constant of Earth}
  muS      = 1.32712438e20;                              {gravitational constant of Sun}
  muM      = 4.902794e12;                                {gravitational constant of Moon}
  aG       = 42164171.7145;                              {ideal GEO altitude}
  aS       = 1.49597870e11;                              {semi-major axis of Earth orbit around the Sun}
  re       =  6371000;                                   {mean radius of the Earth}
  Home_dir = 'C:\COLOCATE';                              {home directory of program components}

VAR                                                      {--GLOBAL VARIABLES--}
  St,Title,columns,BaseFileName,DateString               : string;       {output file init. strings}
  axis_polar,axis_classical,axis_inertial,axis_mfiles    : word;         {if =1 then, axis sets are required}
  EH,SG,LG,SP                  : byte;                                  {forces acting variables}
  NoSatellites,CurrSatNo                                 : integer;      {loop counter variables}
  count,maxcount,res_no                                  : longint;      {integration step variables}
  step,rec_interval                                      : extended;     {integration step variables}
  s,c,c1,pt nE                                           : extended;     {integration control variables}
  element,loop1,loop2                                    : integer;      {loop control variables}
  mass,area,reflect                                      : extended;     {satellite physical characteristics}
  Datafile                                               : text;         {input data file}
  pv                           : ARRAY[1..6, 1..5] OF extended;         {stores past dw/dt values}
  te                           : ARRAY[1..6] OF extended;               {stores present w values}

        {Output file filename variables and output files}
  EquinFile,ClassFile,PolarFile,InertFile                : ARRAY[1..2] OF string;
  ResArrayE,ResArrayC,ResArrayP,ResArrayI                : ARRAY[1..2,1..10] of string;
  resultsE,resultsP,resultsC,resultsI                    : text;         {result file variables}
  MatFileE,MatFileC,MatFileP,MatFileI                    : text;         {MATLAB result file variables}

        {Main Astrodynamical Variables}
  Y,M,D                        :  word;                                 {Year/Month/Day}
  UT,t                                                   : extended;     {Universal and simulation time}
  JD,JD_bs,G                                             : extended;     {Julian date and Greenwich angle}
  P2,P1,Q1,Q2,mL,L,a                                     : extended;     {Equinoctial variables}
  lambda,r,La                                            : extended;     {Polar variables}
  Bomega,Somega,e,i,f                                    : extended;     {Classical variables}
  Xi,Yi,Zi,dXi,dYi,dZi                                   : extended;     {Inertial variables}
  ad1,ad2,ad3                                            : extended;     {force calculation variables}

IMPLEMENTATION
END.
```

D.3 : Perturbation Force Module

```
{$N+}                                          {compiler directive enabling co-proccessor support}
UNIT Forces;
INTERFACE
USES WinCRT, Utility, OrbitVAR;                {other modules used by this module}


CONST                {EARTH HARMONIC CONSTANTS}
    J20    =  1082.6283E-6;
    J22    = -1.8083E-6;        L22 = -0.259965;
    J30    = -2.5418E-6;
    J31    = -2.1791E-6;        L31 =  0.123341;
    J32    = -3.848E-7;         L32 = -0.297313;
    J33    = -2.2132E-7;        L33 =  0.372075;
    J40    = -1.6086E-6;
    J41    = -6.7614E-7;        L41 =  3.852015;
    J42    = -1.6853E-7;        L42 =  0.546840;
    J43    = -5.9015E-8;        L43 = -0.075211;
    J44    = -7.3147E-9;        L44 =  0.515748;
VAR  sLa,sLa2,cLa,z1,z2 : extended;            {module specific variables}


                                   {INCLUDED FUNCTIONS AND PROCEDURES}
        {Earth Harmonic Perturbation Calculation Functions}
FUNCTION  fr(Lo,La,r:extended):extended;
FUNCTION  fLo(Lo,La,r:extended):extended;
FUNCTION  fLa(Lo,La,r:extended):extended;

        {Total Perturbation Calculation Procedure}
PROCEDURE PerturbingForces(L,a,P2,P1,Q1,Q2:extended);


                                   {LISTINGS OF FUNCTIONS AND PROCEDURES}
IMPLEMENTATION

FUNCTION fr(Lo,La,r:extended):extended;        {radial perturbation acceleration}
VAR  t1,t2,t3,t4,t5,t6 : extended;
BEGIN
   t1:=3/2*J20*(3*sLa2-1) + 9*J22*(1-sLa2)*cos(2*(Lo-L22));
   t2:=re/r*(2*J30*(5*sLa2-3)*sLa + 6*J31*(5*sLa2-1)*cLa*cos(Lo-L31));
   t3:=60*re/r*(J32*(1-sLa2)*sLa*cos(2*(Lo-L32)) + J33*(1-sLa2)*cLa*cos(3*(Lo-L33)));
   t4:=sqr(re/r)*(5/8*J40*(35*sLa2*sLa2-30*sLa2+3) + 25/2*J41*(7*sLa2-3)*cLa*sLa*cos(Lo-L41));
   t5:=75/2*sqr(re/r)*J42*(7*sLa2-1)*(1-sLa2)*cos(2*(Lo-L42));
   t6:=525*sqr(re/r)*(1-sLa2)*(J43*cLa*sLa*cos(3*(Lo-L43)) + J44*(1-sLa2)*cos(4*(Lo-L44)));
   fr:=z1*(t1+t2+t3+t4+t5+t6);
END;                                           {of 'fr' function}

FUNCTION fLo(Lo,La,r:extended):extended;               {longitudinal perturbation acceleration}
VAR  t1,t2,t3,t4 : extended;
BEGIN
   t1:=6*J22*cLa*sin(2*(Lo-L22)) + 45*re/r*J33*(1-sLa2)*sin(3*(Lo-L33));
   t2:=re/r*(3/2*J31*(5*sLa2-1)*sin(Lo-L31) + 30*J32*cLa*sLa*sin(2*(Lo-L32)));
   t3:=sqr(re/r)*(5/2*J41*(7*sLa2-3)*sLa*sin(Lo-L41) + 15*J42*(7*sLa2-1)*cLa*sin(2*(Lo-L42)));
   t4:=sqr(re/r)*(1-sLa2)*(315*J43*sLa*sin(3*(Lo-L43)) + 420*J44*cLa*sin(4*(Lo-L44)));
   fLo:=z1*(t1+t2+t3+t4);
END;                                           {of 'fLo' function}

FUNCTION fLa(Lo,La,r:extended):extended;       {latitudinal perturbation acceleration}
VAR  t1,t2,t3,t4,t5,t6 : extended;
BEGIN
   t1:=-3*J20*sLa*cLa + 6*J22*cLa*sLa*cos(2*(Lo-L22));
   t2:=3/2*re/r*(-J30*(5*sLa2-1)*cLa + J31*(15*sLa2-11)*sLa*cos(Lo-L31));
   t3:=re/r*(15*J32*(3*sLa2-1)*cLa*cos(2*(Lo-L32)) + 45*J33*(1-sLa2)*sLa*cos(3*(Lo-L33)));
   t4:=-5/2*sqr(re/r)*J40*(7*sLa2-3)*sLa*cLa;
   t5:=sqr(re/r)*(5/2*J41*(28*sLa2*sLa2-27*sLa2+3)*cos(Lo-L41)
        + 30*J42*(7*sLa2-4)*cLa*sLa*cos(2*(Lo-L42)));
   t6:=sqr(re/r)*(1-sLa2)*(105*J43*(4*sLa2-1)*cos(3*(Lo-L43))
```

```
        + 420*J44*cLa*sLa*cos(4*(Lo-L44)));
   fLa:=z1*(t1+t2+t3+t4+t5+t6);
END;                                        {of 'fLa' function}


PROCEDURE PerturbingForces(L,a,P2,P1,Q1,Q2:extended);
VAR                         {LOCAL VARIABLE DECLARATIONS}
   alpha,delta,c1,c2,q,Tu       : extended;     {program control variables}
   rx,ry,rz             : extended;             {satellite positional variables}
   m                    : ARRAY[1..3,1..3] OF extended;     {transformation matrix elements}
    {Earth harmonic calculation variables}
   ar,aLo,aLa                   : extended;     {acceleration components}
   c3,c4                        : extended;
    {Solar gravity and pressure calculation variables}
   irx,iry,irz,isx,isy,isz              : extended;     {unit vector components in inertial axes}
   aSx,aSy,aSz                  : extended;     {acceleration components}
   Ms,es,Cs,mLs,Ls,obliq,rs     : extended;     {solar orbit variables}
    {Lunar gravity calculation variables}
   ilx,ily,ilz                          : extended;     {unit vector components in inertial axes}
   alx,aly,alz                  : extended;     {acceleration components}
   hp,rl                        : extended;     {lunar orbit variables}

BEGIN {of 'PerturbingForces' procedure}
 ad1:=0; ad2:=0; ad3:=0;                    {initialise perturbation acceleration values}
 {------------------CALCULATIONS COMMON TO ALL PERTURBATION SOURCES-----------}
 IF (EH<>0) OR (SG<>0) OR (SP<>0) OR (LG<>0) THEN BEGIN
    {Compute 'r' vector components in Geocentric coordinates, 'r' magnitude already known}
   q        := (1+sqr(Q1)+sqr(Q2));
   c1       := 2*(Q2*s-Q1*c)/q;
   c2       := 2*(Q2*c+Q1*s)/q;
   irx      := c+Q1*c1;
   iry      := s-Q2*c1;
   irz      := c1;
   rx       := r*irx;
   ry       := r*iry;
   rz       := r*irz;
    {Compute transformation matrix elements (geocentric to orbital co-ordinates)}
   m[1,1]   := irx;
   m[1,2]   := iry;
   m[1,3]   := irz;
   m[2,1]   := -s+Q1*c2;
   m[2,2]   := c-Q2*c2;
   m[2,3]   := c2;
   m[3,1]   := 2*Q1/q;
   m[3,2]   := -2*Q2/q;
   m[3,3]   := (1-sqr(Q1)-sqr(Q2))/q;
    {Calculate number of Julian centuries since 2000.0}
   Tu       := (JD-2451545.0)/36525;
 END; {of common calculations}
 {-----------------------------------------EARTH HARMONICS CALCULATIONS-------------------------}
 IF EH<>0 THEN BEGIN
    {calculate perturbing accelerations in radial/longitude/latitude co-ordinates}
   alpha                := Arctan2(iry,irx);                    {satellite right ascension}
   lambda               := Modulus(alpha-G,2*pi);               {satellite Greenwich longitude}
   La                   := Arcsin(2*(Q2*s-Q1*c)/(1+sqr(Q1)+sqr(Q2)));   {satellite latitude}
   sLa                  := sin(La);
   sLa2     :           = sLa*sLa;
   cLa                  := cos(La);
   z1                   := muE*sqr(re/(r*r));
   ar                   := fr(lambda,La,r);                     {radial acceleration}
   aLo                  := fLo(lambda,La,r);                    {longitudinal acceleration}
   aLa                  := fLa(lambda,La,r);                    {latitudeinal acceleration}
    {calculate perturbing accelerations in orbital co-ordinates}
   c3                   := Q1*cos(alpha)-Q2*sin(alpha);
   c4                   := Q1*sin(alpha)+Q2*cos(alpha);
   ad1                  := ad1 + ar;
   ad2                  := ad2 + (cos(alpha-L)-c2*c4)*aLo + (cLa*c2-(sin(alpha-L)+c2*c3)*sLa)*aLa;
   ad3                  := ad3 - (2*c4/q)*aLo - (cLa-2*(cLa-sLa*c3)/q)*aLa;
 END; {of Earth harmonic specific calculations}
```

```
{-----------------------------------------SOLAR EFFECTS CALCULATIONS---------------------------------}
 IF (SG<>0) OR (SP<>0) THEN BEGIN
    {calculate Solar orbital elements}
   mLs                  := rad(280.46645+36000.76983*Tu+0.0003032*Tu*Tu);
   Ms                   := rad(357.52910+35999.05030*Tu-0.0001559*Tu*Tu-0.00000048*Tu*Tu*Tu);
   Cs       := rad((1.9146-0.004817*Tu-0.000014*Tu*Tu)*sin(Ms)
            +(0.019993-0.000101*Tu)*sin(2*Ms)+0.00029*sin(3*Ms));
   Ls       := Modulus(mLs+Cs,2*pi); {Sun true longitude}
   obliq    := rad(23.439291-0.013004*Tu-1.639E-7*Tu*Tu+5.03E-7*Tu*Tu*Tu);
   es       := 0.016708617-0.000042037*Tu-0.0000001236*Tu*Tu;
   rs       := aS*(1-es*es)/(1+es*cos(Ms+Cs));
    {compute unit position vector of Sun in geocentric co-ordinates}
   isx      := cos(Ls);
   isy      := cos(obliq)*sin(Ls);
   isz      := sin(obliq)*sin(Ls);
    {SOLAR GRAVITY SPECIFIC CALCULATIONS}
   IF SG<>0 THEN BEGIN
      {calculate perturbing accelerations in geocentric co-ordinates}
    z1      := muS/(rs*rs)*(r/rs);
    z2      := irx*isx+iry*isy+irz*isz;
    aSx     := z1*(3*z2*isx-irx);
    aSy     := z1*(3*z2*isy-iry);
    aSz     := z1*(3*z2*isz-irz);
      {calculate perturbing accelerations in orbital co-ordinates}
    ad1     := ad1 + m[1,1]*aSx+m[1,2]*aSy+m[1,3]*aSz;
    ad2     := ad2 + m[2,1]*aSx+m[2,2]*aSy+m[2,3]*aSz;
    ad3     := ad3 + m[3,1]*aSx+m[3,2]*aSy+m[3,3]*aSz;
   END; {of solar gravity specific calculations}
    {SOLAR PRESSURE SPECIFIC CALCULATIONS}
   IF SP<>0 THEN BEGIN
      {calculate perturbing accelerations in geocentric co-ordinates}
    z1      := 4.56E-6*area/mass*(1+reflect)/sqrt(sqr(rx-rs*isx)+sqr(ry-rs*isy)+sqr(rz-rs*isz));
    aSx     := z1*(rx-rs*isx);
    aSy     := z1*(ry-rs*isy);
    aSz     := z1*(rz-rs*isz);
      {calculate perturbing accelerations in orbital co-ordinates}
    ad1     := ad1 + m[1,1]*aSx+m[1,2]*aSy+m[1,3]*aSz;
    ad2     := ad2 + m[2,1]*aSx+m[2,2]*aSy+m[2,3]*aSz;
    ad3     := ad3 + m[3,1]*aSx+m[3,2]*aSy+m[3,3]*aSz;
   END; {of solar pressure specific calculations}
 END; {of solar effects specific calculations}
{-----------------------------------------LUNAR GRAVITY CALCULATIONS---------------------------------}
 IF LG<>0 THEN BEGIN
    {calculate Lunar orbital elements}
   alpha    := rad(218.32+481267.883*Tu+6.29*sin(rad(134.9+477198.85*Tu))
            -1.27*sin(rad(259.2-413335.38*Tu))+0.66*sin(rad(235.7+890534.23*Tu))    +0.21*sin(rad(269.9+954397.7*Tu))-
0.19*sin(rad(357.5+35999.05*Tu))
            -0.11*sin(rad(186.6+966404.05*Tu)));
   delta    := rad(5.13*sin(rad(93.3+483202.03*Tu))+0.28*sin(rad(228.2+960400.87*Tu))
            -0.28*sin(rad(318.3+6003.18*Tu))-0.17*sin(rad(217.6-407332.2*Tu)));
   hp       := rad(0.9508+0.0518*cos(rad(134.9+477198.85*Tu))+0.0095*cos(rad(259.2-413335.38*Tu))
            +0.0078*cos(rad(235.7+890534.23*Tu))+0.0028*cos(rad(269.9+954397.70*Tu)));
   rl       := 6378137/(sin(hp));
    {compute unit position vector of Moon in geocentric co-ordinates}
   ilx      := cos(delta)*cos(alpha);
   ily      := (0.9175*cos(delta)*sin(alpha)-0.3978*sin(delta));
   ilz      := (0.3978*cos(delta)*sin(alpha)+0.9175*sin(delta));
    {calculate perturbing accelerations in geocentric co-ordinates}
   z1       := muM/(rl*rl)*(r/rl);
   z2       := irx*ilx+iry*ily+irz*ilz;
   alx      := z1*(3*z2*ilx-irx);
   aly      := z1*(3*z2*ily-iry);
   alz      := z1*(3*z2*ilz-irz);
    {calculate perturbing accelerations in orbital co-ordinates}
   ad1      := ad1 + m[1,1]*alx+m[1,2]*aly+m[1,3]*alz;
   ad2      := ad2 + m[2,1]*alx+m[2,2]*aly+m[2,3]*alz;
   ad3      := ad3 + m[3,1]*alx+m[3,2]*aly+m[3,3]*alz;
 END; {of lunar specific calculations}
```

```
END;    {of 'PerturbationForces' procedure}

END. {of 'FORCES.PAS' module}
```

D.4 : Main Orbit Integration Module

The listing for the main orbit integration loop is given below. Unlike the previous two listings the 'MAINLOOP' procedure is part of the main program code (the previous listings are modules which are 'called' by the main code).

```
PROCEDURE MAINLOOP;
CONST
     {array containing maximum permissible errors per step in the equinoctial elements}
    max_error_array : ARRAY[1..6] OF extended = (1e-12,1e-8,1e-12,1e-12,1e-12,1e-12);

     {procedure specific variables}
VAR
    sigma,max_error,limit,min_step          : extended;          {PC5 error control variables}
    k1,k2,k3,k4,k5,k6,w,w1                  : extended;          {RK5 integration variables}
    c1,Kold,Knew,mLold                      : extended;          {constants over step interval}
    iteration_error                         : integer;           {crash avoidance variable}
    need_new_step                                  : boolean;           {should step size change ?}

  {dw/dt=fn(t,w) where 'w' is the current element (to be integrated) and 'fn' is the function: }
 FUNCTION fn(tnew,w:extended)           : extended;
 VAR    L,p,h,store,mlnew               : extended;
 BEGIN
  store                 := te[element];                                 {temporary store for element value}
  te[element]           := w;
  p                     := te[1]*(1-te[8]*te[8]-te[20]*te[20]);         {a*(1-e*e)}
  h                     := sqrt(abs(p)*muE);                            {orbit angular momentum}
  c1                    := sqrt(p/te[1]);                               {b/a}
   {calculate true longitude 'Lnew' from mean longitude 'mlnew'}
  mlnew                 := mlold+sqrt(muE/te[1])/te[1]*(tnew-t);        {lold+n*(time step)}
  Knew                  := mlnew;                                       {first guess for eccentric longitude}
  iteration_error       :=0;
  REPEAT
   iteration_error      := iteration_error+1;
   Kold                 := Knew;
   Knew                 :=Knew-(Knew-mlnew+te[20]*cos(Knew)
                        -te[8]*sin(Knew))/(1-te[20]*sin(Knew)-te[8]*cos(Knew));
  UNTIL (abs(Knew-Kold)<1e-6) OR (iteration_error=100);
  r         := te[1]*(1-te[20]*sin(Knew)-te[8]*cos(Knew));          {calculate 'r'}
  s         := te[1]/r*((1-1/(1+c1)*sqr(te[8]))*sin(Knew)+1/(1+c1)*te[20]*te[8]*cos(Knew)-te[20]);
  c         := te[1]/r*((1-1/(1+c1)*sqr(te[20]))*cos(Knew)+1/(1+c1)*te[20]*te[8]*sin(Knew)-te[8]);
  L         := arctan2(s,c);                                                {where s=sin(L) and c=Cos(L)}
  {check for program crashing, if true find out why}
  IF (p<0) OR (r<=re) OR (iteration_error=100) THEN BEGIN
   program_crashed  := true;
   crash_code                   := 1;
   IF p<0 THEN crash_code:=crash_code*2;                          {non-ellipse}
   IF r<=re THEN crash_code:=crash_code*3;                        {collided with Earth}
   IF (iteration_error=100) THEN crash_code:=crash_code*5;        {'K' failed to converge}
  END; {of program crash checking}
  JD        := JD_bs+(tnew-t)/86400;
  G         := GreenwichAngle(UT+tnew-t);
  PerturbingForces(L,te[1],te[8],te[20],te[22],te[10]);   {call procedure from FORCES.PAS}
   {element=[1,2,3,4,5,6]=[mL,a,P2,P1,Q1,Q2]}
  CASE element OF
   1 :      fn:= sqrt(muE/te[1])/te[1] - r/h*(
           +(1/(1+c1)*p/r*(te[20]*s+te[8]*c)+2*c1)*ad1
           +1/(1+c1)*(1+p/r)*(te[20]*c-te[8]*s)*ad2
           +(te[22]*c-te[10]*s)*ad3);
   2 :      fn:= 2*te[1]*te[1]/h*((te[8]*s-te[20]*c)*ad1+p/r*ad2);
   3 :      fn:= r/h*(p/r*s*ad1+(te[8]+(1+p/r)*c)*ad2+te[20]*(te[22]*c-te[10]*s)*ad3);
   4 :      fn:= r/h*(-p/r*c*ad1+(te[20]+(1+p/r)*s)*ad2-te[8]*(te[22]*c-te[10]*s)*ad3);
```

```
    5 :     fn:= r/(2*h)*(1+te[22]*te[22]+te[10]*te[10])*s*ad3;
    6 :     fn:= r/(2*h)*(1+te[22]*te[22]+te[10]*te[10])*c*ad3;
  END;
  te[element]          :=store;  {restore element to former value}
 END;   { of function fn }

{-----------------------------------------MAINLOOP PROPER-----------------------------------------------------}
BEGIN
  {assign temporary array, 'te' elements to equal equinocital elements to avoid step mis-match}
 te[11]:=mL;te[1]:=a;te[8]:=P2;te[20]:=P1;te[22]:=Q1;te[10]:=Q2;
FOR loop1:=1 TO 6 DO new_step[loop1]:=step;          {reset step values to last value of step}
mLold                 := mL;                         {store value of mean longitude at beginning of step}
 need_new_step        := false;
  {integrate each element in turn using 'te' values throughout to avoid step mis-match}
 FOR element:=1 TO 6 DO
 BEGIN
  IF (pv[element,5]=-1) THEN
  BEGIN                          {use RK5 if less than 5 equally spaced data points available}
   k1      := step*fn(t,te[element]);
   k2      := step*fn(t+step/4,te[element]+k1/4);
   k3      := step*fn(t+3/8*step,te[element]+3/32*k1+9/32*k2);
   k4      := step*fn(t+12/13*step,te[element]+1932/2197*k1+7200/2197*k2+7296/2197*k3);
   k5      := step*fn(t+step,te[element]+439/216*k1-8*k2+3680/513*k3-854/4104*k4);
   k6      := step*fn(t+step/2,te[element]-8/27*k1+2*k2-3544/2565*k3+1859/4104*k4-11/40*k5);
   w       := te[element] + 16/135*k1 + 6656/12825*k3 + 28561/56430*k4 - 9/50*k5 + 2/55*k6;
  END ELSE BEGIN                 {use PC5 if 5 equally spaced points available}
   w1:=te[element]+step/720*(1901*pv[element,1]-2774*pv[element,2]+2616*pv[element,3]
          -1274*pv[element,4]+251*pv[element,5]);
   w :=te[element]+step/720*(251*fn(t+step,w1)+646*pv[element,1]-264*pv[element,2]
          +106*pv[element,3]-19*pv[element,4]);
    {check error tolerance is not exceed and store 'new_step' variable if it is}
   max_error          := max_error_array[element];
   sigma              := abs(w-w1)/(10*step);
   IF ((sigma<max_error/10) OR (sigma>max_error)) THEN BEGIN
    IF (sigma<>0) THEN new_step[element]:=step*sqrt(sqrt(max_error/(2*sigma)))
    ELSE new_step[element]:=rec_interval;
    IF new_step[element]>rec_interval THEN new_step[element]:=rec_interval;
    IF abs(new_step[element]-step)>1 THEN need_new_step:=true;
   END; {of error checking}
  END; {of element integration}

  {assign new value to variable currently being integrated}
  CASE element OF
   1 :     mL         := Modulus(w,2*pi);
   2 :     a          := w;
   3 :     P2         := w;
   4 :     P1         := w;
   5 :     Q1         := w;
   6 :     Q2         := w;
  END;
   {update past value,'pv', array, which stores last 5 element data points (for PC5 use)}
  FOR loop1:=4 DownTo 1 DO pv[element,loop1+1]:=pv[element,loop1];
  pv[element,1]:=fn(t+step,w);
 END; {of numerical integration loop}
 {Calculate true longitude from mean longitude}
 Knew  := mL;                                                    {first guess}
 iteration_error:=0;
 REPEAT
  iteration_error:=iteration_error+1;
  Kold     := Knew;
  Knew     := Knew-(Knew-mL+P1*cos(Knew)-P2*sin(Knew))/(1-P1*sin(Knew)-P2*cos(Knew));
 UNTIL (abs(Knew-Kold)<1e-6) OR (iteration_error=100);
 c1          := sqrt(1-P1*P1-P2*P2);                          {b/a}
 r           := a*(1-P1*sin(Knew)-P2*cos(Knew));              {recalculate r for new L}
 s           := a/r*((1-1/(1+c1)*P2*P2)*sin(Knew)+1/(1+c1)*P1*P2*cos(Knew)-P1);
 c           := a/r*((1-1/(1+c1)*P1*P1)*cos(Knew)+1/(1+c1)*P1*P2*sin(Knew)-P2);
 L           := arctan2(s,c);
  {update time dependant variables for next loop}
 t           := t+step;
```

```
  UT          := Modulus(UT+step,86400);
  JD_bs       := JD_bs+step/86400;
  JD          := JD_bs;
  G           := GreenwichAngle(UT);
    {Find min. step size specified by elements and change step size to this value if required}
  IF need_new_step THEN BEGIN
    min_step          := new_step[11];
    FOR element       := 2 TO 6 DO IF new_step[element]<min_step THEN min_step:=new_step[element];
    IF (min_step<=rec_interval) AND (min_step<>step) THEN BEGIN
      step := min_step;
      FOR loop1:=1 TO 6 DO FOR loop2:=1 TO 5 DO pv[loop1,loop2]:=-1;
    END;
  END; {of step size adjustment}
END; {of 'MAINLOOP' procedure}
```